Analysis of Fluctuating Static Pressure Measurements in the National Transonic Facility

William B. Igoe
Langley Research Center • Hampton, Virginia

Contents

iv

Symbols

$A_{\max}$	model maximum cross-sectional area, ft^2
A_n	polynomial fit area, ft^2
A_x	model cross-sectional area, ft^2
A_T	test section throat cross-sectional area, ft^2 (66.77 ft^2 for NTF)
a	slope of least-squares straight line
b	intercept of least-squares straight line
C_x	longitudinal buoyancy-force coefficient, $\dfrac{F_x}{qS}$
c	speed of sound, fps
$\bar{c}$	wing mean aerodynamic chord, ft
c_t	stagnation speed of sound, fps
d_1, d_2	cavity depth of outer and inner chambers, respectively, of dual Helmholtz resonator, in., (fig. A14)
e	base of Naperian logarithms (2.71828. . .)
F_x	longitudinal buoyancy force, lb
f	frequency, Hz
f_p	calculated fundamental frequency of slotted wall-plenum resonance, Hz
f_s	characteristic slot frequency, Hz
g	gravitational acceleration, ft/sec^2
h	test section height at throat, ft (8.202 ft for NTF)
i	ith data point
J	highest order exponent in polynomial fit to area distribution
j	upper limit of summation for least-squares straight-line fit
k_1	model blockage area ratio, $\dfrac{A_{\max}}{A_T}$
k_2	wing area to test section area ratio, $\dfrac{S}{A_T}$
k_3	model length to test section height ratio $\dfrac{l}{h}$
L	lip-to-wedge gap distance for edge tone geometry, in.
l	length of model, ft
M	test section free-stream Mach number, $\dfrac{V}{c}$
m	stage number for edge tone frequencies
N	amplification factor; logarithmic exponent of disturbance growth ratio
n	exponent in polynomial fit to area distribution
OA_1, OA_2	open area ratio of perforated liner for outer and inner chambers, respectively, of dual Helmholtz resonator (fig. A14)
P	static pressure measurement, psi (fig. C1)
P_i	static pressure measurement at ith point, psi (fig. C1)
p	static pressure, psi
p_i	true static pressure at ith point, psi

p_{max}	maximum amplitude range of pressure sensor, psi
p_t	free-stream stagnation pressure, psi
$\tilde{p}$	root-mean-square value of fluctuating component of static pressure (with the mean subtracted), psi
$(\tilde{p}/q)^2$	power spectral density function of the fluctuating static pressure coefficient, per Hz
q	test section free-stream dynamic pressure, psf
q_{sc}	dynamic pressure in settling chamber, psf
R	Reynolds number
$R_{\bar{c}}$	Reynolds number based on wing mean aerodynamic chord
S	model wing area; other reference area, ft^2
St	Strouhal number
T_{aw}	adiabatic wall temperature, °F
T_t	free-stream stagnation temperature, °F
T_w	wall temperature, °F
T_∞	free-stream static temperature, °F
u_c	streamwise convection velocity, fps (appendix E)
$u_c(x)$	measured overall streamwise convection velocity, fps
V	free-stream velocity, fps
v	volume, ft^3
x	longitudinal distance (positive downstream), ft
α_{rf}	reentry flap angle (positive away from flow), deg
γ	lag factor in edge tone feedback emittance
Δ	increment or change in a quantity or variable
Δa	error in least-squares straight-line slope a
δ	root sum squares of δ_i, psi
δ_i	deviation between measured pressure P_i and least-squares straight-line fit at ith point, psi (fig. C1)
$\tilde{\delta}_{msw}$	model support wall angle (positive away from flow), deg
ε_i	error in measured pressure P_i, psi
θ_{tsw}	test section wall divergence angle (positive away from flow), deg
ϕ	phase angle, deg

Abbreviations:

AEDC	Arnold Engineering and Development Center
BPF	blade passage frequency
dia.	diameter
DRA	Defence Research Agency (formerly RAE)
ESP	electronically scanned pressure
FM	frequency modulation
freq.	frequency

GN$_2$	gaseous nitrogen
ID	inner diameter
IGV	inlet guide vane
IRIG	Inter-Range Instrumentation Group
LaRC	Langley Research Center
LHS	left-hand side
LN$_2$	liquid nitrogen
max.	maximum
min.	minimum
NASA	National Aeronautics and Space Administration
NBS	National Bureau of Standards
NIST	National Institute of Standards and Technology (formerly NBS)
NLR—HST	National Aerospace Laboratory—High-Speed Tunnel
NTF	National Transonic Facility
OD	outer diameter
RAE	Royal Aerospace Establishment
re	with respect to
RHS	right-hand side
rms	root mean square
rss	root sum square
TPT	Transonic Pressure Tunnel

Summary

Dynamic measurements of fluctuating static pressure levels were taken with flush-mounted, high-frequency response pressure transducers at 11 locations in the circuit of the National Transonic Facility (NTF) across the complete operating range of this wind tunnel. Measurements were taken at test-section Mach numbers from 0.1 to 1.2, at pressures from 1 to 8.6 atm, and at temperatures from ambient to $-250°F$, which resulted in dynamic flow disturbance measurements at the highest Reynolds numbers available in a transonic ground test facility. Tests were also made by independent variation of the Mach number, the Reynolds number, or the fan drive power while the other two parameters were held constant, which for the first time resulted in a distinct separation of the effects of these three important parameters.

This report contains a description of the NTF and emphasizes flow quality features; details of instrument calibration; results of measurements with the test section slots covered and the downstream choke; effects of liquid nitrogen injection and gaseous nitrogen venting; comparisons between air and nitrogen modes of operation; isolation of the effects of Mach number, Reynolds number, and fan drive power; and identification of the sources of significant flow disturbances. The results indicate that primary sources of flow disturbance in the NTF may be edge tones generated by test section sidewall reentry flaps and the venting of nitrogen gas from the return leg of the tunnel circuit between turns 3 and 4 in the cryogenic mode of operation. The tests to isolate the effects of Mach number, Reynolds number, and fan drive power indicate that Mach number effects predominate. A comparison with other transonic wind tunnels shows that the NTF has low levels of test section fluctuating static pressure, especially in the high-subsonic Mach number range of 0.7 to 0.9.

1. Introduction

A wind tunnel is primarily a means of creating a flow over a model or body to determine the influence of one on the other. With the exception of specialized wind tunnels for the study of specific fluid dynamic problems, the principal objective of the wind tunnel is to study the flow about configurations while duplicating full-scale, free-flight conditions to the fullest extent possible. Wind tunnels such as the National Transonic Facility (NTF) fulfill the full-scale condition by achieving full-scale Reynolds numbers. In general, the free-flight condition is addressed in a variety of ways. The interference created by the test section walls is alleviated by wall ventilation such as slots or perforations; adaptive walls are sometimes used in an attempt to remove the interference more completely. The interferences created by model supports

are minimized by support of the models from the rear by stings or blades; the interference can be removed more completely by the use of magnetic suspension. To date, the uniformity and steadiness of the flow has not been completely resolved. Few wind tunnels, if any (especially transonic wind tunnels), can approach the relatively quiescent conditions of free air. Therefore, examination of the disturbance levels of wind tunnels is necessary to assess their capability to perform diverse research roles.

1.1. Background

The influence of flow disturbances such as velocity fluctuation and noise on aerodynamic phenomena has long been widely recognized; in recent years, the dynamic flow quality of wind tunnels has received close attention. Lately, efforts to develop natural laminar flow, laminar flow control airfoils, and other aerodynamic surfaces for use on commercial aircraft have increased the interest in the magnitude and the frequency characteristics of flow disturbances in wind tunnels.

In the early 1900's, an example of the effect of dynamic flow quality on wind tunnel measurements by Prandtl (1914) involved the discrepancy in sphere drag data measured under comparable test conditions in the wind tunnels of Prandtl and Eiffel. Here of course, the discrepancy was resolved after recognition that higher velocity turbulence levels in the Eiffel wind tunnel had caused transition of the sphere boundary layer farther upstream, which resulted in the sphere having more resistance to flow separation and lower drag. An important byproduct of discovering the cause of the sphere drag discrepancy was that wind tunnel investigators should proceed with caution when applying the results of measurements taken in turbulent wind tunnel airstreams to aircraft in nominally quiescent free air.

As used by Mabey (1976), the term wind tunnel unsteadiness is a general one which refers to fluctuations in velocity, pressure, and temperature. Timme (1973) distinguished between acoustic (i.e., noise) disturbances, which show wave forms with a phase velocity corresponding to the speed of sound and turbulence, which has stochastic fluctuations with a phase velocity that is some fraction of the flow velocity. However, Timme noted that the difference between the two may not always be distinct. Figure 1, adapted from Mabey (1971), shows many of the sources of flow unsteadiness identified by Mabey in transonic wind tunnels.

Although flow disturbances may have an effect on all measurements taken in wind tunnels, the effects are more pronounced in certain types of aerodynamic research. As indicated by Timme (1973) and Mabey (1976), those research areas that can be most affected by

wind tunnel unsteadiness include boundary layer transition from laminar to turbulent flow, turbulent boundary layer development, shock-wave–boundary-layer interaction, separated flows and wakes, flow reattachment, inlet and control surface buzz, buffeting, and flutter.

In wind tunnels, fluctuations in velocity have been generally considered to have the greatest influence on dynamic flow quality. Prandtl (1914) proposed that the abrupt change with Reynolds number in the drag coefficient of a sphere be used to indicate a measure of the velocity fluctuations. However, as discussed by Dryden and Abbott (1948), spheres were not reliable indicators for low-turbulence wind tunnels at turbulence levels below approximately 0.5 percent. Also, because of the effects of compressibility, Robinson (1937) showed that spheres were not suitable for high-speed wind tunnels at Mach numbers greater than ≈0.35. Because of these limitations, the sphere drag test became less useful as a turbulence indicator.

As described by Dryden and Abbott (1948), the hot-wire anemometer became the standard instrument for the measurement of velocity fluctuations. Kovásznay (1950, 1953) developed the application of hot-wire measurement techniques for supersonic flow. Spangenberg (1955) showed that typical hot-wire sensitivities were a function of both Mach number and Knudsen number. Morkovin (1956) improved and extended Kovásznay's techniques, but the application for high-subsonic compressible flow and transonic flow remained in question. Horstman and Rose (1977) and Rose and McDaid (1976) applied the supersonic flow hot-wire techniques to transonic flow with the assumption that the hot-wire sensitivities for velocity and for density changes were equal. However, Stainback, Johnson, and Basnett (1983) and Jones (1991) have shown that the velocity and density sensitivities for hot-wires are not equal. A three-wire technique of Stainback, Johnson, and Basnett and of Jones was developed to separate the effects of velocity, density, and temperature changes but has not yet received universal acceptance. The velocity and density fluctuations measured with this technique appear unusually large, and the reasons for these results have not been determined.

As shown by Meyers and Wilkinson (1982), laser velocimeters have been used to measure velocity fluctuation and have indicated reasonable comparisons with hot-wire technique results for the streamwise component of velocity fluctuation. However, the high-speed burst counter technique of Meyers and Wilkinson has a high-amplitude threshold of detection of approximately 0.5 percent. Meyers and Clemmons (1987) indicated that this threshold of detection can be lowered to approximately 0.2 percent by using a frequency domain signal

processor, but even this amplitude threshold is not sufficiently sensitive for low-turbulence wind tunnel measurements.

The length of the laminar boundary layer run before the transition to turbulence occurs is considered a sensitive measure of flow quality. In a review of the influence of flow disturbances, Michel (1988) has indicated that, although the boundary layer transition process is primarily sensitive to velocity fluctuations, aerodynamic sound can control the transition process below a minimum threshold value of approximately 0.2 percent. Dougherty (1980) has used a cone having an included angle of revolution of 10° to evaluate the relationship of boundary layer transition sensitivity and wind tunnel flow quality in a large number of wind tunnels. The Arnold Engineering and Development Center (AEDC) 10° transition cone was instrumented with a traversing surface probe to detect the location of transition and with surface-mounted microphones or pressure transducers to measure the fluctuating static pressure on the cone surface. This cone has been used to determine the dynamic flow quality in 23 wind tunnels in both this country and Europe. In addition to wind tunnel tests, Dougherty and Fisher (1980) describe flight tests of the cone on the nose of an F-15 fighter airplane. With so much test history in so many research environments, the cone has attained the status of a calibration standard. The 10° cone tests provided a distinct opportunity to obtain dynamic flow quality information in a large number of different test facilities with identical hardware and instrumentation, which assured comparability of all measurements. Unfortunately, the AEDC 10° cone is not compatible with a cryogenic environment either in materials or in operational capability; thus, it could not be tested in the nitrogen mode of the NTF.

The initial analysis by Dougherty (1980) of the variation of the transition Reynolds number with the measured fluctuating static pressure coefficient of the AEDC 10° cone showed apparent correlation between the fluctuating pressure coefficient and the transition Reynolds number based on either the beginning or the end of transition. However, the transition data show considerable scatter when data from one facility are compared with that from another. Spangler and Wells (1968) have further shown that the effectiveness of sound in promoting transition is highly dependent on the frequency of the excitation. The correlation between the root-mean-square (rms) noise level and the location of transition is difficult because both the frequency spectrum of the noise and the receptivity of the boundary layer are involved. The apparent correlation by Dougherty of the data from the AEDC 10° cone has been challenged by an analysis of the data by Murthy and Steinle (1985, 1986) in which they attempted to account

for the effects of Mach number in the correlation. They concluded that there was no acceptable data correlation for the AEDC 10° cone between the transition Reynolds number and the fluctuating pressure coefficient, at least at low-noise levels.

The sensitivity of an initially laminar boundary layer to flow disturbances which cause transition to turbulence based on a comparison of the boundary layer transition locations calculated by the e^N method of the linear compressible stability theory with those locations actually measured in a wind tunnel has been used by Elsenaar (1990) as a measure of dynamic flow quality. The comparison yielded representative N factors which are characteristic of the flow for specific configurations. On a two-dimensional laminar flow airfoil in the National Aerospace Laboratory—High-Speed Tunnel (NLR—HST), Elsenaar obtained N factors of 6 to 12, depending on Mach number and Reynolds number; high-N factors close to free-flight values were associated with good dynamic flow quality.

Both Timme (1973) and Mabey (1976) have described the difficulties of measuring velocity fluctuations at transonic speeds and have indicated that flow unsteadiness in transonic wind tunnels is usually estimated from measurement of the fluctuating static pressure. Elsenaar (1990) has also indicated that the measurement of the fluctuating static pressure in the test section provides a first indication of the dynamic flow quality in a wind tunnel.

By comparing the static pressure fluctuation measured on a body of revolution on the tunnel center-line with that on a sidewall, Mabey (1971) concluded that the pressure fluctuations were almost the same and that the pressure fluctuation field was approximately one-dimensional. Dolling and Dussauge (1989) also indicated that fluctuating pressures measured on a wall are dependent on the surrounding flow and reflect the salient features of that flow; the wall measurements have the additional advantage of being essentially nonintrusive.

Siddon (1969) has cautioned that measurements in the free stream of fluctuating static pressures with probes can result in significant error. The interaction between the probe and the fluctuating flow can result in errors that are either positive or negative, which depends on whether the scale of a typical eddy size in the flow is smaller or larger, respectively, than the dimensions of the probe. Eckelmann (1990) has also indicated that pressure probe measurements within turbulent flows are not reliable because velocity fluctuations in the flow produce random pressure fluctuations on the probe, which would not occur if the probe were not present.

In addition to the fluctuations occurring in the free stream, wall pressure measurements include contributions from disturbance levels generated within the turbulent boundary layer itself. Within the turbulent boundary layer, interactions of the turbulence with the mean shear and of the turbulence with itself occur. However, Mabey (1971) has indicated that the latter contribution to wall pressure measurements represents only a small correction at high frequency and is frequently approximated as a constant as was shown by Lowson (1968).

Because of the difficulties associated with other means of determining wind tunnel dynamic flow quality and the advantages associated with the wall measurement of fluctuating static pressures as cited previously, the wall pressure approach was adopted for the preliminary assessment of dynamic flow quality in the NTF.

1.2. Dynamic Measurements in NTF

Because the NTF is a wind tunnel which operates at high Reynolds numbers, verification of dynamic flow quality was considered essential to gain confidence that the NTF would be suitable for laminar flow research and for dynamic aeroelastic research such as flutter and buffet testing. The cryogenic feature of this wind tunnel, which contributes so importantly to its high Reynolds number capability, also introduces additional factors which affect the flow quality and complicate its measurement. To obtain these measurements, high-frequency response pressure transducers were installed flush with the surface at 11 locations in the NTF circuit. Dynamic measurements were made of the fluctuating static pressure levels across the complete operating range of the NTF at test section Mach numbers M from 0.1 to 1.2, at pressures p from 1 to 8.6 atm at temperatures T_t from ambient to $-250°F$, and at a maximum unit Reynolds number of approximately 146×10^6 ft^{-1}. These combinations of test conditions resulted in data at the highest Reynolds numbers available in a transonic ground test facility.

The capability to test across a wide range of temperatures permitted measurements of fluctuating static pressures to be made at variable Mach number while keeping Reynolds number and fan drive power constant by appropriate variation of temperature and pressure. Similarly, additional tests were made at variable Reynolds number while keeping Mach number and fan drive power constant, and at variable fan drive power while keeping Mach number and Reynolds number constant, which for the first time resulted in a distinct separation of the effects of these important parameters.

The importance of the fan drive system as a source of wind tunnel noise has been described in several papers including Williams (1977), Michel and Froebel (1988),

and Chiu and Lauchle (1989). As indicated by Williams, the wind tunnel fan drive system represents one of the primary sources of background noise in the test section. According to Chiu and Lauchle, the fan aerodynamic noise has a broadband spectrum, which sometimes includes a series of discrete frequency peaks associated with the fan blade passage frequency and its harmonics. The major broadband noise sources include blade vortex shedding from the blade trailing edge, blade-to-blade vortex interaction, flow separation from the blade upper surface, and random fluctuating blade forces caused both by the blade boundary layer and by blade interaction with inflow turbulence. The discrete frequency peaks are primarily due to inflow distortion where the blades interact with wakes from upstream obstructions. This unsteady interaction causes fluctuating pressure fields, which in a compressible medium radiate as dipole sound sources.

When comparing broadband dipole fan noise under similar operating conditions, Williams (1977) indicated that the fan overall sound power is approximately proportional to the cube of the fan tip speed times the fan aerodynamic shaft power times one minus the fan aerodynamic efficiency. To isolate the effect of blade tip speed from that of fan drive power, the NTF was operated across the same wind tunnel speed and fan drive power ranges and either fan speed change or inlet guide vane angle change was used to load the fan and change wind tunnel speed.

2. Test Apparatus

Before beginning a description of the NTF, a brief review of the cryogenic concept may be worthwhile. Historically, the use of modest cooling to increase Reynolds number was first proposed by Margoulis (1921), and the potential benefits of further temperature reduction were later pointed out by Smelt (1945). Many years were to pass by before the cryogenic concept would be successfully demonstrated at Langley Research Center (LaRC) by Kilgore (1974). (Also, see Goodyer and Kilgore (1972).)

2.1. Benefits of Cryogenic Concept

The benefits of the cryogenic approach can best be illustrated in figure 2, which are taken from Kilgore, Adcock, and Ray (1974) and shown for a Mach number of 1. In figure 2(a), the variation of the gas properties with temperature is shown with reference to the properties at 120°F. As shown in figure 2, the density increases, and both the viscosity and speed of sound decrease with decreasing temperature. The Reynolds number depends on density in the numerator and viscosity in the denominator, and the variation of Reynolds number with temperature is shown in figure 2(b), again in relative terms.

In the extreme, an increase of sixfold or more in Reynolds number can be obtained, although the temperature is rarely taken this low in actual testing. The difficulty arises in approaching the gas condensation boundary too closely. A more realistic factor for the increase of Reynolds number with temperature reduction would be four to five. Because the speed of sound is reduced with reduced temperature, the velocity to achieve a given Mach number is also reduced so the required fan drive power is reduced. All this is obtained with no change in dynamic pressure. This demonstrates why the cryogenic concept is an attractive way to obtain high Reynolds numbers. Any further increase of Reynolds numbers would normally be obtained by increasing the stagnation pressure with the accompanying increase in dynamic pressure and fan drive power.

Some additional benefits of the cryogenic concept were pointed out by Kilgore, Adcock, and Ray (1974) and are shown in figures 3–5. These figures are conceptual and do not represent actual performance of the NTF. Figure 3 shows that, at a constant Mach number, dynamic pressure and hence model loads and deflections can be held constant while the Reynolds number is varied; conversely, Reynolds number can be held constant while dynamic pressure is varied for pure aeroelastic studies. Figure 4 shows that at a constant Reynolds number, Mach number can be varied while dynamic pressure is held constant, or dynamic pressure can be varied while Mach number is held constant. Figure 5 shows that, at a constant dynamic pressure, either Mach number or Reynolds number can be varied independently. Thus, this feature of the cryogenic concept permits pure Mach number, pure Reynolds number, or pure aeroelastic studies to be made while the other parameters are held constant. Later in this paper, some additional benefits of the cryogenic concept for dynamic flow quality testing will be presented, which show that the effects of fan drive power can be separated from those of Mach number and Reynolds number.

2.2. Description of NTF

The NTF characteristics have been amply described as has the wind tunnel evolved during planning, design, construction, and initial operation. Howell and McKinney (1977), Igoe (1980), and Bruce (1985) are typical sources of information on the NTF and cite many other references. A brief description of the NTF is presented here; a more detailed description, which includes those components that influence the dynamic flow quality, is presented in appendix A. These descriptions, which are essentially a review of the previously mentioned sources, draw material freely from them and their other cited references.

In most respects, the NTF is a rather conventional wind tunnel with only a few unconventional features. The circuit lines and overall dimensions of the wind tunnel are shown in figure 6. The tunnel circuit is approximately 200 ft long and 48.6 ft wide between centerlines, which results in an internal circuit length of approximately 497 ft and enclosed volume of approximately 230000 ft^3. It was constructed on the site of the deactivated 4-Foot Supersonic Pressure Tunnel, and incorporated the induction drive motors as well as some of the other equipment from that tunnel. The plane of the tunnel circuit is tilted approximately 9° with the center-line of the fan at a lower elevation than the centerline of the test section. The fan and test section centerlines lie in horizontal planes, and the walls of the test section are oriented horizontally and vertically. The reason for the tilt was to accommodate the fan driveshaft centerline positioning with respect to the existing induction drive motors and to minimize extensive below-grade excavation requirements in the test section-plenum region.

The wind tunnel has two basic modes of operation: one at near-ambient temperatures with air as the test gas and the other at cryogenic temperatures with nitrogen as the test gas. In the air mode of operation, cooling is accomplished by a conventional water cooled heat exchanger inside the tunnel circuit. For cryogenic operation, cooling is accomplished by spraying liquid nitrogen directly into the tunnel circuit. The minimum Mach number is 0.1, the maximum is 1.2, and the maximum unit Reynolds number is about 146×10^6 ft^{-1} at a Mach number of about 1.0.

2.3. Instrumentation

2.3.1. Pressure Transducer Characteristics

The fluctuating pressures were measured with miniature electrical pressure transducers. The transducer casing was 0.092 in. in diameter by 0.5 in. long with a differential pressure range of ±10 psi. They had an aniso-tropically etched silicon diaphragm 0.05 in. in diameter with an active four-arm piezoresistive bridge diffused into the diaphragm. The diaphragm was recessed below the surface of the transducer under a 0.03-in-diameter orifice with a dead volume of 0.000015 in^3. The specified resonant frequency of the diaphragm was 130 kHz; the sensitivity to acceleration was 0.00015 psi/g. Temperature compensation for bridge resistance change with temperature is accomplished with integral hybrid electrical circuitry. The transducers were temperature-compensated across a temperature range of approximately −280°F to 150°F. The excitation voltage for both the data measurement and the bench calibration was 10 V and was continuously monitored during measurements.

2.3.2. Pressure Transducer Calibration

The primary calibration of the pressure transducers was done in a laboratory environment with calibration standards traceable to the National Institute of Standards and Technology (NIST), formerly the National Bureau of Standards (NBS). Calibrations were performed both statically and dynamically at an excitation voltage of 10 V.

2.3.2.1. Static calibration. The pressure transducers were calibrated statically over their full pressure range of ±10 psi at 2 psi pressure increments at temperatures from 135°F to −280°F to span the expected NTF operating temperature range of 120°F to −250°F. The individual calibration data at each temperature were fitted with a least-squares straight line. The slopes of the straight-line fits for one of the pressure transducers (64RY), which was used in the NTF test section sidewall at station 13 on the right-hand side, are shown in figure 7(a). The dashed line through the data points is a least-squares straight line versus temperature. The variation of calibration sensitivity with temperature was fitted this way for all the pressure transducers used in this investigation. The static calibration sensitivities were used to reduce the data from the dynamic pressure transducers because they were considered the most reliable.

2.3.2.2. Dynamic check-calibration. The pressure transducers were dynamically check-calibrated with a microphone calibrator. The output of the calibrator was verified with a 1/2-in. microphone as a standard. The pressure transducers were check-calibrated at a constant frequency of 1 kHz with input amplitudes varying from 0.001 to 0.1 psi and at a constant input amplitude of 0.05 psi at frequencies ranging from 50 Hz to 2 kHz. These dynamic calibrations were only performed at room temperature. The results of the constant frequency and constant amplitude dynamic calibrations for transducer 64RY are shown in figures 7(b) and 7(c). The variation in sensitivity of all pressure transducers with either amplitude or frequency variation was within the ±1/2-dB band normally expected from this type of calibration. The ordinate scale ranges in figures 7(b) and 7(c) (34 to 38 mV/psi and 33 to 37 mV/psi, respectively) correspond approximately to a ±1/2-dB range. In addition to the laboratory calibration, all transducer outputs were verified in position in the wind tunnel with a portable calibrator at a signal amplitude of 0.0015 psi and a frequency of 2 kHz.

2.3.2.3. Resonant frequency. Because of the high resonant frequency (130 kHz) of the pressure transducers and the frequency limitation of the spectral analyzer which was used (100 kHz at the maximum digital sampling rate of 256 kHz in the single-channel mode of

operation), the resonant peaks of these transducers do not show up in any of the power spectra plots. However, frequency counting on an oscilloscope trace yielded a frequency of approximately 137 kHz, which because of its proximity to the resonant frequency of 130 kHz specified for the transducers, is probably the actual resonant frequency.

2.3.3. Pressure Transducer Installation

Before the pressure transducers were installed in the tunnel circuit, they were first mounted in brass instrument plugs as shown in figure 8. Brass was chosen as the material for the plugs because it is easy to machine, braze, or solder, and its thermal coefficient of expansion is similar to that of the aluminum structure of the wind tunnel to which they were attached. This method of installation was utilized for all the transducers except for the two that will be described later. With guidance from the results of Coe (1969) and the recommendations of Hanly (1975), the pressure transducers were mounted either flush or slightly below (0.001 in.) the surface of the brass plug to minimize transducer-generated flow disturbances. A static pressure orifice and a copper-constantan thermocouple were included in the instrument plug. The static pressure orifice was connected to the reference pressure side of the pressure transducer through a 100-ft coil of 0.04-in-inside-diameter flexible pressure tubing to provide damping of the reference pressure. A short length ($\approx$1/2 in.) of 0.01-in-inside-diameter stainless steel tubing connected the flexible pressure tubing and the reference side of the pressure transducer. The thermocouple was used to monitor the temperature of the pressure transducer environment. The pressure transducers were potted in place in the plugs with an instrument-grade silicone rubber compound. Prior to cryogenic operation, the reference pressure tubes were purged with dry nitrogen gas.

Eight instrumented brass plugs were installed in the NTF circuit flush with the local surface, at the tunnel station mid-height, and with the thermocouple oriented downstream. The locations are shown in figure 9 and are as follows: one on the left-hand side (LHS) when looking upstream at station 6.5 and another opposite to it on the right-hand side (RHS), three closely spaced (2.25 in. apart streamwise) on the RHS at station 13, one on the RHS at station 16, one on the LHS in the high-speed diffuser at station 68, and one on the RHS just downstream of turn 1 and adjacent to the liquid nitrogen injectors. An additional instrumented brass plug was installed in the plenum on the RHS at station 0 near the plenum wall and at the same height as the test section top wall.

Because of space limitations, the pressure transducer installed in the settling chamber was first potted into a drilled 1/4"-20 stainless steel bolt and then installed flush on the RHS of the settling chamber wall at station −52, 1 ft downstream of the last screen and approximately 30° up the wall from bottom center. The reference pressure for the transducer was supplied from an adjacent static pressure orifice and again damped through a 100-ft coil of flexible pressure tubing. The temperature environment for this transducer was assumed to be equal to the wind tunnel stagnation temperature. A conventional pitot-static pressure probe was installed downstream of the heat exchanger to measure the local flow conditions in the settling chamber.

During this investigation, the test section was nominally empty; that is, there was no test model installed in the test section. To cover up the blunt centerbody on the model support arc-sector strut, a conical fairing with an included angle of 10.6° was installed as shown in figure 10. Most of the rearward section of the fairing was made of fiberglass-reinforced plastic. The tip section of the fairing was made of stainless steel and is shown in figures 11 and 12. The apex of the cone was blunted with a 0.06-in-radius tip. The machined surface of the cone front section was estimated to have a 32-µin. finish.

A flush-mounted dynamic pressure transducer was installed on the cone surface 10.4 in. downstream of the blunted cone tip. Because the transducer had a flat 0.092-in-diameter face and was mounted in a conical surface with a radius of 1.03 in. at that point, the so-called flush mounting was not really flush. The philosophy, which was followed in mounting the pressure transducer in the cone, was to avoid any forward-facing surfaces or other protrusions of the transducer. Although the installation was as clean as could be under the circumstances, it still represented some discontinuity in the cone surface. When installed in the tunnel, the cone tip was on the test section centerline at station 16.74. The transducer was on the RHS and faced the test section RHS wall at station 17.60. A copper-constantan thermocouple was installed in the cone on the side opposite of the pressure transducer. The reference pressure for the transducer was the plenum static pressure and was supplied to the transducer through a 100-ft coil of flexible pressure tubing. The plenum static pressure is nearly the same as the free-stream static pressure in the test section across the entire operating range of the wind tunnel.

2.3.4. Signal Conditioners

The signal conditioners used for the dynamic pressure transducers were all silicon, solid-state, feedback amplifiers with gain settings of 0 to 60 dB (equivalent to a linear scale of 1 to 1000). The filter settings ranged from 10 Hz to 100 kHz (wideband setting) with a

12-dB/octave Bessel filter characteristic. The input impedance was 100 MΩ.

Before the signal conditioners were installed for this investigation, they were carefully matched so that signal pairs that were to be analyzed with respect to phase angle, and cross-correlation were connected to amplifiers with similar phase shift characteristics. For example, the signal conditioners for the two adjacent pressure transducers at station 13, for which phase angle and cross-correlation information are presented, had a phase shift within 1° of each other across the entire range of gain settings of the signal conditioners.

The amplifiers were operated in the manual gain-setting mode but the gain settings were acquired automatically on the NTF steady-state data acquisition system. During the entire investigation, all of the filters were set at the wideband setting which exceeded the upper limit of the frequency response of the FM data tape recorder.

2.3.5. Dynamic Data Acquisition

All of the dynamic pressure transducer data signals were recorded on magnetic tape with a 28-track FM tape recorder. The tape recorder was operated in the wideband 1 mode so that, at the tape recording speed of 60 ips, the resultant bandwidth was 40 kHz. All data signals were continuously monitored on-line with oscilloscope displays, and the signal conditioner amplifier gain settings were manually adjusted to keep the recorded signal amplitude as high as possible without exceeding ±1 V peak to peak. A time code generator signal was synchronized with the NTF steady-state data acquisition system clock and was also recorded on the FM tape.

Some selected data signals were also simultaneously acquired on-line with a four-channel spectral analyzer. The analyzer digitized the input signal, performed a fast Fourier transform on the digital data, and computed power spectra or other frequency domain or time domain statistical quantities, which were then stored on a computer disk. The dynamic data acquisition instrumentation in the NTF control room and a simplified wiring block diagram of the system are shown in figures 13 and 14, respectively.

2.3.6. NTF Steady-State Data System

The current configuration of the NTF steady-state data system utilizes four 16-bit, serial processor, digital computers each with 2 MB of memory and a 167-MB hard disk drive. The computers are linked together and share four magnetic tape drives. Each computer supports specific operations in the NTF: one computer is dedicated to research data acquisition and processing, another supports data management and communication, a third serves as a process monitor for operation of the NTF, and a fourth is dedicated to wind tunnel control. Descriptions of the data acquisition system are given by Fuller (1981), Boyles (1986), and Foster and Adcock (1987).

Because the NTF operates at high pressures in the air mode and at high pressures and low temperatures in the nitrogen mode, the test gas can depart significantly from perfect gas behavior. Adcock (1976), Adcock and Johnson (1980), and Hall and Adcock (1981) have shown that imperfect gas effects can be adequately accounted for with Beattie-Bridgman-type equations of state solved iteratively for the appropriate gas flow parameters. The most serious departures from perfect gas behavior in the NTF occur at low temperatures as the gas condensation boundary is approached.

All of the steady-state gas flow parameters for this investigation were computed with imperfect gas effects taken into account as indicated by Foster and Adcock (1987). As noted previously, the amplifier gain settings from the signal conditioners for the dynamic pressure transducers were acquired on the steady-state data acquisition system. In addition, the outputs of the thermocouples and the monitor signals of the excitation voltages of the dynamic pressure transducers were also acquired on that system along with all the usual steady-state flow parameter measurements for the wind tunnel.

2.4. Data Accuracy

The uncertainty expected in the fluctuating static pressure data will be considered in three categories. The first category includes the free-stream parameters and other wind tunnel-related data. The second category includes the actual measurement of the fluctuating static pressure. The third category includes the statistical reliability of the spectral data derived from statistical analysis of the fluctuating static pressure measurements.

2.4.1. Free-Stream Parameters

On the basis of information presented on the NTF instrumentation by Kern, Knight, and Zasimowich (1986), on the NTF data acquisition system by Foster and Adcock (1987), and on the NTF static wind tunnel calibration (private communication from M. Susan Williams and Jerry B. Adcock of the NTF staff), the estimated uncertainties for the free-stream parameters for this investigation are as follows:

M ....±0.002

R, ft^{-1}..±0.2 × 10^6

q, percent value ....±0.1

V, fps ....±2

p_t, percent value .... ±0.025

T_t, °F .... ±0.1

Fan rotational speed, rpm .... ±2

q_{sc}, percent value .... ±5

2.4.2. Fluctuating Static Pressure

The static calibration of the pressure transducers yielded least-squares straight-line fits (sensitivities) with a maximum deviation of less than ±1 percent of full scale and, generally, less than ±0.5 percent, which indicates good linearity and very little hysteresis. The variations in sensitivity with temperature were fitted with least-squares straight lines with a maximum deviation of less than ±1 percent for all the pressure transducers.

The dynamic check-calibrations show basically that no significant anomalies existed in the dynamic performance of the pressure transducers, at least over the range covered by the dynamic check-calibrations. The variations in performance which were indicated by the dynamic check-calibrations are primarily a characteristic of the dynamic calibrator system which was used and are not a characteristic of the pressure transducers (private communication from John J. Chapman of the LaRC Instrument Research Division staff).

Dolling and Dussauge (1989) list several sources of errors in fluctuating static pressure measurements with wall-mounted pressure transducers. For transducers with diaphragm sensors mounted in cavities beneath orifices, diaphragm and cavity resonances exist that are to be avoided. For the pressure transducers used in this investigation, the diaphragm resonance was about 137 kHz and the cavity Helmholtz resonance was estimated to be approximately 75 kHz under no-flow conditions. Both of these frequencies are well above the 20 kHz upper cutoff frequency used for the analysis of the rms fluctuating static pressure coefficient data.

For turbulent boundary layers, Dolling and Dussauge (1989) indicated that a typical frequency for energy containing eddies is of the order of the velocity at the outer edge of the boundary layer divided by the thickness of the boundary layer. They stated that a safe upper cutoff frequency would be on the order of five times this typical frequency for energy containing eddies. This criterion was developed for velocity fluctuations but was also assumed to apply to pressure fluctuations. The test section sidewall turbulent boundary layer at station 13 in the NTF has been found by measurement to vary from approximately 2.5 to 4 in. in thickness; the thickness depends on Reynolds number and Mach number (private communication from Jerry B. Adcock of the NTF staff). For an average wall boundary layer thickness of 3 in., the upper frequency cutoff criterion for the flow conditions of this investigation would be approximately 20 kHz.

The effect of orifice size on the spatial resolution of the measurement is another source of error discussed by Dolling and Dussauge (1989). Disturbances whose scales are small compared with the orifice diameter tend to be averaged out, and the spectrum is therefore underestimated at the higher frequencies. By using the previously noted upper frequency cutoff criterion, these authors concluded that an orifice diameter less than 0.04 times the boundary layer thickness should be adequate. By applying this criterion to an average 3-in-thick boundary layer, the orifice diameter would be about 0.12 in., which is large when compared with the actual diameter of 0.03 in. of the NTF transducers.

By using empirically determined relationships for the one-dimensional longitudinal and lateral cross-spectral density for the wall turbulent boundary layer, Corcos (1963, 1967) developed a correction procedure for the power spectral density as a function of a non-dimensionally (similarity) reduced frequency. The correction gives the ratio of the measured to actual power spectral density at a given reduced frequency caused by the averaging effect of the finite size of the transducer orifice. However, both Willmarth and Roos (1965) and Schewe (1983) indicate that the Corcos correction may not be adequate at high frequencies.

Schewe (1983) measured the wall fluctuating static pressures beneath turbulent boundary layers with pressure transducers of different sizes, and the results showed increased spatial resolution as a function of the reduced diameter of the pressure transducer diaphragm expressed in terms of wall coordinates (i.e., essentially the Reynolds number of the diaphragm diameter based on the friction velocity). Schewe concluded that a diaphragm diameter of approximately 20 wall coordinates was adequate to resolve the pressure structures in a turbulent boundary layer. For the NTF, Schewe's criterion for transducer diameter would impose an unusually stringent requirement for the pressure transducers. For the NTF sidewall installation, the orifice diameter in wall coordinates was estimated to vary from approximately 50 to greater than 6000. Only the settling chamber pressure transducer with an estimated orifice diameter in wall coordinates of approximately 13 could even approach Schewe's criterion and then only at the lowest free-stream Reynolds number. The conclusion was that no realistically sized orifice diameter for the NTF pressure transducers could have satisfied Schewe's criterion at the NTF test conditions. For the NTF data, no corrections have been made to the spectra for the turbulent boundary

layer fluctuations or for the size of the transducer relative to the boundary layer.

The data channels for the test section RHS sidewall station 13 and the 10.6° cone were two of the four channels analyzed on-line with the spectral analyzer. The mean-square data and the 20-kHz bandwidth spectra for these two channels on the spectral analyzer had a maximum dynamic range of 76 dB. All other data were analyzed off-line and were limited to the maximum signal-to-noise ratio of 47 dB characteristic of the playback performance of the 28-track FM tape recorder.

2.4.3. Statistical Reliability

Bendat and Piersol (1980) list several factors affecting errors in the statistical analysis of random data. Among these factors are measurement transducers, signal conditioners, magnetic tape recorders, analog-to-digital conversion, preanalysis data conditioning, stationarity (i.e., ergodicity), finite sample length, random error, and bias (i.e., systematic) error. The latter few factors are those of importance in statistical analysis errors. For the NTF data, stationarity is obtained by holding all of the test conditions which are subject to control as nearly constant as possible during the time interval of the data sample. A long sample length on the order of 30 sec was used for most of the data analyses; however, even longer samples on the order of several minutes were sometimes used when advantageous to do so (e.g., for some of the cross-correlation analyses).

With certain simplifying assumptions, Bendat and Piersol (1980) indicated that the normalized random error for a power spectral density estimate is inversely proportional to the square root of the number of distinct averages used in the computation. For most analyses, 100 averages were used, which resulted in a normalized random error on the order of 10 percent for the NTF power spectral density data and on the order of 5 percent for the rms data. A Hanning window was used for all the spectral analyses. For the type of random data analyzed herein, the normalized bias error is expected to be small compared with the random error and, because of being frequency specific, cannot be stated in general terms.

2.4.4. Data Repeatability

During the nitrogen mode of testing, a nominal test condition (except for the wall-to-gas temperature ratio) at $M = 0.8$ and $R = 40 \times 10^6 \text{ ft}^{-1}$ was repeated to give a total of five data points. The repeatability of these test conditions and the rms fluctuating pressure coefficient on the test section RHS sidewall station 13 was as follows:

M .... ±0.001

R, ft^{-1} ....±0.5 × 10^6

q, percent value ....±0.3

V, fps ....±3

p_t, percent value ....±0.1

T_t, °F..±1.5

$\tilde{p}/q$, percent value ....±2

3. Test Conditions

With the exception of some preliminary tests which were performed during the steady-state calibration with a centerline calibration probe in the test section, the dynamic investigation was performed with the test section empty; as noted previously, a 10.6° cone fairing covered the model support strut centerbody. The NTF steady-state calibration was done only with the test section slots open, and the plenum static pressure was the calibration reference pressure. With two exceptions, dynamic measurements were taken with the test section geometry variables of wall divergence, reentry flap angle, and model support wall angle at the settings developed during the NTF steady-state calibration to obtain minimum longitudinal static pressure gradients. The two exceptions occurred when the effects of variation in wall divergence, flap angle, and model support wall angle were being investigated and when the slots were covered. The slot covers changed the test section static pressure gradient and also rendered the plenum pressure unusable as a reference. For the latter case with the slots covered, special steps were necessary not only to obtain a satisfactory reference pressure but also to ascertain the effects of the slot covers on the static pressure gradient.

3.1. Static Pressure Gradient

The longitudinal static pressure gradients in the test section are of interest because gradients tend to promote interaction between the turbulent fields of fluctuations in velocity, pressure, and temperature and can distort the power spectra at high frequencies. For the dynamic measurements to be representative of aerodynamic research conditions, these measurements must be taken at the same flow conditions as are encountered during the aerodynamic research.

Generally, for aerodynamic research purposes, as small a gradient as possible is desirable as a means of more closely duplicating free-air conditions. When longitudinal static pressure gradients are encountered in aerodynamic research (e.g., force test models), the gradients are usually accounted for by introduction of longitudinal buoyancy corrections to the force data. Because the NTF is capable of variable wall divergence, the longitudinal buoyancy in the NTF can be hypothetically reduced to an extremely small amount but is seldom ever actually

accomplished. One of the objectives in the NTF steady-state calibration was to determine the sensitivity of the longitudinal static pressure gradient to wall divergence angle. In a solid wall test section, the sensitivity is high and only small wall angle changes are needed to cancel gradients. However, in a ventilated wall test section, the flow is in intimate communication with the plenum, which is a uniform pressure reservoir. As a consequence, the longitudinal gradients are naturally very small but are also less sensitive to a change of the wall angle.

If consideration is restricted to a linear change of static pressure with longitudinal distance and if some further simplifying assumptions are invoked, some general results on buoyancy effects are obtained as indicated in appendix B. These results are based on the maximum recommended size limits for models in transonic testing as indicated by Baals and Stokes (1971) and Monti (1971). The results are shown in figure 15 as a test section longitudinal static pressure gradient that would cause one count (defined as 0.0001) of buoyancy-induced incremental drag coefficient on a large model. Other gradients are obtained by linearly scaling up or down according to the chosen allowable level of buoyancy drag. Figure 16 shows the same gradient expressed in terms of Mach number.

For the steady-state calibration, an extensive distribution of 25 static pressure orifices was available in the centerline calibration probe. The individual pressures for each orifice were determined with an electronically scanned pressure (ESP) unit with a maximum pressure range of ±2.5 psi and a specified error of no more than ±0.15 percent of full range. Appendix C shows that a least-squares straight-line fit to the longitudinal static pressure variation determined with the ESP instrumentation has similar accuracy to the lower dashed line shown in figure 15 for the gradients determined with the centerline calibration probe. To determine the static pressure gradients with the slots covered, static pressure orifices in the walls were used. The same ESP unit was used, but only 13 orifices were available, which resulted in the somewhat degraded accuracy shown in figure 15 by the upper dashed line. The same gradient error information is shown is figure 16 in terms of Mach number.

3.2. Air Mode Tests

The NTF performance envelope for air mode operation (private communication from Jerry B. Adcock of the NTF staff) is shown in figure 17. The boundaries are formed on the bottom by the minimum operating pressure of about 1 atm, on the LHS by the minimum Mach number of about 0.1, on the RHS by the maximum fan speed, on the top left by the maximum pressure limit of the shell of 130 psi, and on the top right by the cooling

capacity of the water-cooled heat exchanger. The symbols shown in this figure indicate the test conditions at which dynamic data were obtained. These conditions include Mach number variations along the minimum pressure boundary, along the maximum performance boundary, and at a constant $R = 6 \times 10^6$ ft^{-1} as well as Reynolds number variations at a constant Mach number of 0.5.

At a constant $R = 6 \times 10^6$ ft^{-1}, the effect of changing Mach number by adjustment of the inlet guide vanes with a constant fan rotational speed of 550 rpm was investigated at $M = 0.6$ to 1.0. A comparison was made at the same Reynolds number, but the Mach number was changed by varying the fan rotational speed and keeping the inlet guide vanes fixed at 0°. In addition, $R = 6 \times 10^6$ ft^{-1} and $M = 0.8$, the effects of variable test section wall geometry (i.e., test section wall divergence from −0.3° (converged) to 0.3° (diverged), reentry flap deflection from −1.5° (toward flow) to 2° (away from flow), and test section wall to model support wall step height from 4.0 to 6.2 in. (0.08 to 0.13 as a fraction of test section half-height)) were investigated. Some of the NTF test section geometry variables are shown in figure A10.

The effect of slot covers was investigated along the minimum pressure boundary $M = 0.2$ to 0.9. The slot covers are shown in place in figure 18. The effect of a downstream choke, as shown in figures 18 and A10, was investigated both with slots open and slots covered at $M = 0.8$. On the 10.6° cone, the effect of free transition was investigated at $M = 0.1$ to 0.8.

At $M = 0.5$, the effect of Reynolds number variation from $R = 2.9 \times 10^6$ to 19×10^6 ft^{-1} by variation in total pressure was investigated with boundary layer transition both fixed and free on the 10.6° cone. For all other tests, the transition on the cone was fixed by a transition strip near the tip. The transition strip consisted of No. 80 grit sparsely distributed in a 0.1-in-wide band 2 in. downstream of the tip. The choice of grit size and location was guided by the criteria given by Braslow and Knox (1958) and by Braslow, Hicks, and Harris (1966).

3.3. Nitrogen Mode Tests

Data point coverage within the performance envelope of the NTF in the nitrogen mode of operation is shown in figure 19. The symbols indicate the test conditions at which dynamic measurements were obtained. As shown at the bottom of the figure, the Mach number was varied from $M = 0.2$ to 1.05 at $R = 6 \times 10^6$ ft^{-1}. This test was done in warm nitrogen to correspond to the similar test in the air mode and provide a direct comparison between results in air and in nitrogen. The test points in the nitrogen mode were taken at the same temperature as

those in the air mode, and the pressure was adjusted to give the same Reynolds number for each Mach number. In retrospect, a better procedure might have been to adjust the temperature to give the same stagnation speed of sound as in air and then adjust the pressure to match the Reynolds number. This will be examined further when the results are discussed. (See section 4.3.)

The other test points shown in figure 19 were chosen to cover the operating envelope as completely as possible under the circumstances of limited resources of liquid nitrogen. At stagnation pressure $p_t = 43.2$ psi and stagnation temperature $T_t = -250°F$, the Mach number was varied from $M = 0.2$ to 1.0. A single point was taken at $M = 0.8$ and $p_t = 80$ psi at the same $T_t = -250°F$. The points at high Reynolds numbers were taken at near-maximum pressure and $T_t = -250°F$. A single point was taken at $M = 1.2$, $p_t = 20$ psi, and $T_t = -158°F$.

As mentioned previously, the special cryogenic features of the NTF permitted isolation of effects such as variations in Mach number, Reynolds number, and fan drive power. In a conventional wind tunnel, the operating temperature is usually fixed within relatively narrow limits, and Reynolds number changes are obtained by pressure changes with an accompanying change in fan drive power. Generally, Mach number variations are also accompanied by a change in fan drive power. However, in a cryogenic wind tunnel such as the NTF, Mach number can be varied while holding Reynolds number and fan drive power constant by appropriate variation of the pressure and temperature. Similarly, Reynolds number can be varied while holding Mach number and fan drive power constant, or to vary fan drive power while holding Mach number and Reynolds number constant. These latter two variations are indicated in figure 20, which shows an operating envelope (private communication from Jerry B. Adcock of the NTF staff) for $M = 0.8$. The Reynolds number variation at constant power is shown along a constant power line of 30 MW. The fan drive power variation is shown for $R = 40 \times 10^6$ ft^{-1}. The Mach number variation at constant Reynolds number and fan drive power can be visualized as occurring normal to the page and going through successive points at different Mach numbers, all at $R = 40 \times 10^6$ ft^{-1} and a fan drive power of 30 MW. In addition, figure 20 shows a variation of Reynolds number by pressure variation while temperature is held constant at $T_t = -230°F$ and by temperature variation while pressure is held constant at $p_t = 43.2$ psi. Note that all of these variations pass through a common point at $M = 0.8$, $R = 40 \times 10^6$ ft^{-1}, fan drive power of 30 MW, $p_t = 43.2$ psi, and $T_t = -230°F$. This point was repeated each time but was usually approached from different conditions so that the wall temperatures were not in thermal equilibrium with the gas temperature, which permitted a limited study of the

effect of hot wall or cold wall on the measured wall pressure fluctuations.

The effects of hot wall and cold wall were studied further during the initial cooldown of the NTF from near-ambient temperature to cryogenic temperatures. One of the design requirements for the structure of the NTF was that it be able to withstand the thermal effects of a rapid cooldown or warmup of 80°F. This rapid change of temperature was done at $M = 0.8$ and $p_t = 25$ psi, which produced fairly large differences in wall temperature when compared with the adiabatic wall temperature. For these hot wall and cold wall tests, the adiabatic wall temperature was calculated by ignoring imperfect gas effects and assuming a recovery factor equal to the cube root of the Prandtl number.

During the steady-state calibration of the NTF, some preliminary dynamic measurements with a centerline calibration probe in the test section were attempted. If the requirements for both the steady-state and the dynamic measurements could have been satisfied at the same time, an efficient use of tunnel test time and of liquid nitrogen resources would have resulted. These preliminary measurements are presented and discussed in appendix D.

4. Discussion of Results

The dynamic data are presented in the form of a dynamic pressure coefficient $\tilde{p}/q$, where $\tilde{p}$ is the root-mean-square (rms) value of the fluctuating static pressure readings with the mean subtracted. The fluctuating pressure coefficients were computed for all outputs of the dynamic pressure transducers from the dynamic pressure in the test section except for the transducer in the settling chamber where the local flow conditions were measured with a pitot-static probe. For the pressure coefficients of this transducer, the dynamic pressure in the settling chamber was used.

The fluctuating pressure components were recorded in analog form on FM magnetic tape and were played back into a spectral analyzer, four channels at a time. The analyzer had an upper frequency limit of 20 kHz per channel as a result of the maximum digital sampling rate of 51.2 kHz per channel when four channels are analyzed simultaneously. The mean-square values were obtained by integration of the power spectra from 0 to 20 kHz. The power spectra presented in figure 21 show some of the consequences of terminating the integration of the spectra at 20 kHz. One of the power spectra (fig. 21(a)) is for the transducer in the test section sidewall at station 13. The other (fig. 21(b)) is for the transducer in the 10.6° cone. Both power spectra are from ambient temperature air mode tests at $M = 0.801$ and $R = 38 \times 10^6$ ft^{-1}, which corresponds to the minimum

pressure boundary in air. The numbers at the top of the grid in figure 21 are the rms fluctuating pressure coefficients corresponding to the integrated mean-square values when the integration is terminated at that frequency. There is a 1- to 1.5-percent reduction in the coefficient as the integration range is shortened from 40 kHz to 20 kHz. The dB levels which are included in figure 21 for reference are with respect to the standard 20 μPa.

As indicated by Mabey (1971), disturbances propagating upstream from the extraction region (where the test section flow which has entered the plenum through the slots is returned to the mainstream) and the high-speed diffuser are major sources of high levels of fluctuating static pressure in slotted transonic test sections at high-subsonic speeds. Data presented by Mabey show that the disturbance levels are a strong function of the longitudinal location of the measurement; the levels are highest near the downstream end of the test section and diminish sharply toward the upstream end. A similar variation occurred in the NTF test section as shown in figure 22 where RHS sidewall data at stations 6.5, 13, and 16 are shown with data from the 10.6° cone at station 17.6 for a $M = 0.8$. Mabey's results were obtained from the reduction in magnitude of a particular spectral peak. However, the results in figure 22 are for overall rms magnitudes and therefore show a less pronounced variation. Because of the variation of disturbance level with location in the test section and because station 13 corresponds with the center of the calibrated region of the test section and is the center of pitch rotation for models tested at angle of attack, data for this station are used to represent the test section disturbance levels for the NTF.

4.1. Effect of Hot Wall and Cold Wall

Whenever the test gas temperature is changed, the wind tunnel structure thermally lags the gas temperature; the greater and more rapid the temperature change, the greater the lag. When the NTF is cooled down from ambient temperature to cryogenic temperatures, the cooling process can take 4 to 5 hr to avoid large temperature differences in the structure and the thermal strains which accompany them. During this cooling process, the wind tunnel flows are just high enough to promote satisfactory heat transfer without consumption of too much liquid nitrogen in the process. However, when gas temperature changes are made at research conditions, the liquid nitrogen flow rates can be much greater, and any delays in stabilizing test conditions can be very costly in terms of nitrogen consumption. During the dynamic investigation, the concern was whether differences between wall temperature and gas temperature would have a significant effect on the measured fluctuating pressures. Because temperature differences affect the wall shear stress and the thickness and stability of the boundary

layer, the question was to what extent the fluctuating pressures would be similarly affected.

Fluctuating pressure data obtained on the test section RHS sidewall at station 13 during the NTF initial cooldown for this investigation are shown by the square symbols in figure 23. There is a tendency for the cold wall data to have greater fluctuations than the hot wall data but the differences are slight except for the point on the extreme right in the figure. The temperature differences obtained during the cooldown were greater than those encountered during the normal research test conditions. The data point shown in figure 20 for $M = 0.8$, $R = 40 \times 10^6$ ft^{-1}, $p_t = 43.2$ psi, and $T_t = -230°$F was repeated several times, which resulted in the pressure fluctuation data shown plotted with the circles in figure 23. The temperature differences encountered for these data are more typical of what occurred during the dynamic investigation. Across this more limited range, the effects appear quite small and indicate that wall temperature differences can be ignored in the dynamic data.

4.2. Effect of Fixing Boundary Layer Transition on 10.6° Cone

The fluctuating pressure coefficient measured on the 10.6° cone with fixed and free boundary layer transition is shown in figure 24(a). These data were taken along the minimum Reynolds number boundary in the air mode of operation at ambient temperature and $p_t = 15$ psi. As described earlier, the transition strip consisted of No. 80 grit sparsely distributed in a 0.1-in-wide band 2 in. downstream of the tip of the cone. With free transition at low Mach numbers from $M = 0.1$ to 0.4, the cone apparently had a laminar boundary layer extending past the location of the cone pressure transducer at 10.4 in. from the tip. Boundary layer transition from laminar to turbulent flow was detected in time history traces of the 10.6°-cone pressure transducer signal on an oscilloscope by observation of the occurrence of intermittent pressure spikes. At $M = 0.5$, the boundary layer was transitional at the pressure transducer and continued to be so up to $M = 0.7$, the point at which the boundary layer was fully turbulent and developed trends similar to the results for fixed transition. For the free-transition case, very low levels (as low as 0.001) of fluctuating pressure coefficient were measured beneath the laminar boundary layer and very high levels (as high as 0.023) were measured beneath the transitional boundary layer.

Further effects of fixing boundary layer transition on the 10.6° cone are shown in figure 24(b) for $M = 0.5$ and $R \approx 3 \times 10^6$ to 20×10^6 ft^{-1}. For $R > 6 \times 10^6$ ft^{-1}, the results for free transition are very close to those for fixed transition, which indicate that the boundary layer is fully turbulent in this range. However, at $R = 3 \times 10^6$ ft^{-1}, the

results for free transition are influenced by a transitional boundary layer. The lack of agreement for the repeat points here and in figure 24(a) is indicative of how sensitive the transitional boundary layer is to minor variations in test conditions. To avoid this sensitivity and such wide and abrupt variations in transducer response as shown in figure 24, the dynamic investigation was performed mostly with the boundary layer transition fixed on the 10.6° cone.

Measurements beneath a laminar boundary layer would ordinarily be preferable because they would be uncontaminated by the higher pressure fluctuation levels associated with a turbulent boundary layer and would thereby more closely represent the fluctuation levels occurring in the free stream. However, such measurements were not possible across most of the operating range of the NTF because of the minimum physical size of the pressure transducers and the high unit Reynolds number of the wind tunnel flow.

4.3. Comparison of Air and Gaseous Nitrogen Results

Because air is roughly 78-percent nitrogen and both gases behave as diatomic perfect gases at standard conditions, measurements in the two media could reasonably be expected to compare well. Results for air and gaseous nitrogen, as measured on the test section RHS sidewall at station 13, are shown in figure 25 for $R = 6 \times 10^6$ ft^{-1}. Power spectra (0 to 20 kHz) for the rms data in figure 25 are shown in figure 26. The differences between the power spectra of the air and nitrogen mode tests are primarily broadband in nature with the exception of the power spectra for $M = 0.2$ and 0.7 in figures 26(a) and 26(f), respectively. At $M = 0.2$, the power spectrum for nitrogen shows a peak at about 3.2 kHz. As discussed later in section 4.9, this peak is thought to be due to an acoustic standing wave associated with the heat exchanger in the settling chamber. At $M = 0.7$, both the air and the nitrogen power spectra show a peak at about 850 Hz. Reduced bandwidth (0 to 2 kHz) power spectra for this Mach number are shown in figure 27. The improved frequency resolution in this bandwidth shows that the peak in air is at 840 Hz and in nitrogen at 855 Hz. These frequencies appear proportional to velocity and both have approximately the same reduced frequency, which suggests that they are possibly aerodynamic in origin.

Although the Mach numbers and Reynolds numbers were the same for the air and nitrogen data, the velocities were not the same. This mismatch in velocity was a consequence of the way the test conditions were reproduced. As mentioned previously, the Mach numbers and the stagnation temperatures were matched, and the stagnation pressures were adjusted to match the Reynolds numbers. Because of the difference in gas constants, which are nominally 1716 ft^2/sec^2-°R for air and 1775 ft^2/sec^2-°R for nitrogen, the velocities are approximately mismatched by the square root of the ratio of the two gas constants. If the stagnation speed of sound had been matched instead of the temperatures, the velocities would then have been matched. The importance of matching velocity lies in the fact that the frequencies of aerodynamic disturbances such as vortex shedding or edge tones are proportional to velocity; to reproduce these aerodynamic disturbances faithfully, the velocity should be matched as well as Mach number and Reynolds number. The large difference in amplitude between the two peaks in figure 27 raises the possibility that the aerodynamic disturbance may be coupling with another disturbance that is sensitive to resonance conditions and may be sharply tuned.

Power spectra for the settling chamber, plenum, high-speed diffuser, and liquid nitrogen injection station are shown in figure 28 at ambient temperature for air and nitrogen at $M = 0.7$. Stations in the settling chamber upstream of the test section, in the high-speed diffuser, and at the liquid nitrogen injectors downstream of the test section do not show peaks in the 850 Hz frequency range, which indicate that the source of this disturbance is apparently localized in the vicinity of the test section and the plenum. The disturbance is present in the test section at the same Mach number with the slots covered as shown by the power spectrum in figure 29, which indicates that the disturbance is not directly connected with the slots or the extraction region where the flow entering the plenum through the slots is reintroduced into the mainstream. However, there may be an indirect connection with the extraction region because various mechanical gaps exist even with the slots covered, and many possible sources (e.g., edge tones) remain and cannot be eliminated from consideration.

The phase angle and coherence between adjacent pressure transducers spaced 2.25 in. apart streamwise on the test section RHS sidewall at station 13 are shown in figures 30(a) and 30(b), respectively, as a function of frequency in the range from 0 to 2 kHz at $M = 0.7$ for both air and nitrogen. The phase angle is shown for the downstream transducer signal with respect to the upstream transducer signal; a positive phase shift indicates that the downstream signal is leading the upstream signal, and therefore, the disturbance is propagating in the upstream direction. Further comment on the source of the 850 Hz disturbance will be reserved until the Mach number effects at constant Reynolds number and fan drive power are discussed in section 4.6.1.

4.4. Effect of Fan Drive Power Variation at Constant Mach Number and Reynolds Number

Mach number, Reynolds number, and fan drive power are three of the most influential factors affecting the disturbance level in wind tunnels. The test matrix shown in figure 20 illustrates the way in which either Reynolds number or fan drive power can be varied while the other two parameters are held constant. Although not shown in figure 20, the same can be done for Mach number. The significance of this test technique is that it separates the effects of the three variables, something not possible before the advent of the cryogenic wind tunnel.

As indicated in figure 20, the fan drive power was varied from approximately 24 MW to 53 MW for $M = 0.8$ and $R = 40 \times 10^6$ ft^{-1}. The results of this test are shown in figure 31 for the test section RHS sidewall at station 13. The variation of fluctuating pressure coefficient is mostly flat with a slight tendency to rise with increased power. The results indicate that, for these test conditions, the disturbance level as measured by the fluctuating static pressure coefficient on the test section sidewall is relatively insensitive to variations in fan drive power. The variable power data in figure 31 were taken with the fan drive system at a constant synchronous speed of 360 rpm. The effect of blade tip speed will be examined in section 4.6.3.3.

4.5. Variation of Fluctuating Pressure Coefficient With Reynolds Number

4.5.1. Effect of Constant Stagnation Pressure, Stagnation Temperature, or Fan Drive Power

The matrix of test points shown in figure 20 includes Reynolds number variations along three paths: constant pressure, constant temperature, and constant fan drive power. The results of these three variations are shown in figure 32 for the test section RHS sidewall at station 13 for $M = 0.8$. For $R > 40 \times 10^6$ ft^{-1}, the disturbance levels are all about the same with a coefficient value of approximately 0.0095. At lower Reynolds numbers, the high levels or low levels of disturbance are associated with the presence or absence of discrete frequency peaks in the respective power spectra. The three data points at $R = 40 \times 10^6$ ft^{-1} are all essentially repeat test data at the same values of $p_t = 43.2$ psi, $T_t = -230°$F, fan drive power of 30 MW, and $M = 0.8$. As mentioned in the discussion of hot wall and cold wall effects, the disturbance levels could be affected by the different wall temperatures which occur as the data points were approached from the prior run warmer or colder temperature level. However, the differences in disturbance level are slight.

The variation of disturbance level with Reynolds number at constant fan drive power shown in figure 32 is

of particular significance because, as has already been indicated, this type of data has not been previously available. A principal result of this test series is that the variation of disturbance level with Reynolds number at constant fan drive power for $M = 0.8$ is relatively flat from $R = 20 \times 10^6$ to 50×10^6 ft^{-1}. Note that peak disturbance levels generally occur around $M = 0.8$ (e.g., fig. 25), and that these peak disturbance levels (fig. 32) appear relatively insensitive to Reynolds number variation.

4.5.2. Effect of Reynolds Number in Air

The variation of the fluctuating pressure coefficient with Reynolds number on the test section RHS sidewall at station 13 is shown in figure 33 for $M = 0.5$ in air at ambient temperature. The Reynolds number range of $R \approx 3 \times 10^6$ to 20×10^6 ft^{-1} was obtained by the variation of stagnation pressure from $p_t = 15$ to 105 psi. As a consequence, the fan drive power varied from 7.7 to 41.4 MW. The disturbance level on the sidewall decreased monotonically with increasing Reynolds number in this range of test variables.

The disturbance level measured on the 10.6° cone with fixed transition at these same test conditions has already been shown in figure 24(b). Except at the lowest Reynolds number, the trend of the disturbance level is upward with increasing Reynolds number. This, of course, is opposite to what was observed previously on the test section sidewall. However, the boundary layers in these two instances are noticeably very different; the boundary layer on the cone is undoubtedly very thin compared with that on the sidewall. On the cone, the distance from the origin of the boundary layer to the location of the orifice is less than 1 ft. For the test section sidewall, the virtual origin for the boundary layer probably lies somewhere in the upstream section of the contraction as far as 50 ft from the transducer. Therefore, the Reynolds numbers based on the turbulent boundary layer lengths of the wall and cone differ by approximately 50 to 1 and may not be comparable at all with each other.

4.6. Variation of Fluctuating Pressure Coefficient With Mach Number

4.6.1. Effect of Mach Number at Constant Reynolds Number and Fan Drive Power

As mentioned in the description of the tests, appropriate variation of pressure and temperature will result in a variation of Mach number if Reynolds number and fan drive power are held constant. The significance of this test technique is that it permits an isolation of the effects of Mach number from those of Reynolds number and fan

drive power, which have already been noted as being three of the most influential factors in wind tunnel disturbances. The fluctuating pressure coefficients measured on the test section RHS sidewall at station 13 are shown in figure 34 for constant $R = 40 \times 10^6$ ft^{-1} and fan drive power of 30 MW for $M = 0.6$ to 1.0. The disturbance level variation with pure Mach number variation is similar to that shown previously in figure 25 and confirms that, for these and all other test section results, the disturbance level typically peaks at high-subsonic Mach numbers near 0.8 and falls off as a Mach number of 1.0 is approached. The falloff $M > 0.8$ may be at least partially due to a choking effect that prevents downstream disturbances from propagating upstream into the test section. At near-sonic speeds, all results tend to converge to a lower level of the fluctuating pressure coefficient of approximately 0.0055.

The behavior of the fluctuating pressure coefficient at $M = 0.7$ to 0.8 in figure 34 is similar to what was shown in figure 25 in the air-nitrogen comparison. The reasons are again found in the power spectra that are shown in figure 35. Frequency peaks in the 0.8- to 1.0-kHz range occur in almost all data sets, particularly at 860 Hz for $M = 0.694$, at 900 Hz for $M = 0.742$, and somewhat less prominently at 960 Hz for $M = 0.793$ in figures 35(b), 35(c), and 35(d), respectively. For these Mach numbers, the phase shift between adjacent pressure transducers at station 13, which is shown in figure 36(a) along with the coherence in figure 36(b), again indicated an upstream propagation of disturbances at these frequencies. Figure 35(g) for $M = 0.992$ also shows a disturbance at 960 Hz, which indicates that the disturbances at these frequencies were not being choked off and therefore probably did not originate downstream of the test section. The disturbances did not appear in the power spectra for the settling chamber, which supported the indications that the source is probably localized in the test section or plenum. The most likely area of origin is the extraction region at the downstream end of the test section.

The reduced frequencies shown in figure 35 are not constant. The lack of constancy may be associated with test conditions which required that constant Reynolds number and constant fan drive power be achieved simultaneously. Both the temperature and the pressure had to be varied across a fairly wide range, the pressure from 71 to 34 psi and the temperature from -174°F to -250°F. The temperature changes cause thermally induced changes in the dimensions of the test section; the pressure changes can contribute to dimensional changes as well. Thus, if the extraction region of the test section is involved in the disturbances, then the dimensional changes can be responsible for changes in frequency, especially if the disturbances are associated with edge

tone effects. As in the case of the air-nitrogen comparison and in the absence of more information, the probable source of these disturbances is speculative.

An estimation of possible edge tone frequencies associated with the geometry of the sidewall reentry flaps at the downstream end of the test section near station 20 is presented in appendix E. While not conclusive, the frequency estimation can be viewed as supportive of the possibility that the disturbance peaks in the power spectra of figures 27 and 35 are caused by edge tones.

Within the range of the three variables considered here (i.e., Mach number, Reynolds number, and fan drive power), Mach number has the greatest effect on the fluctuating pressure coefficients. This result should not be interpreted as indicating that Reynolds number and fan drive power are unimportant in affecting disturbance levels but rather that the coefficient formed by dividing the rms fluctuating pressure by the dynamic pressure serves to collapse some of these effects, particularly in the case of fan drive power. This collapsing influence of the dynamic pressure also occurs on the Mach number effects as would become apparent if the coefficient were formed by dividing by the static pressure instead of the dynamic pressure as is sometimes done.

4.6.2. Nitrogen Mode Performance Envelope Results

The fluctuating pressure coefficients measured on the test section RHS sidewall at station 13 for the test points in figure 19 for the nitrogen mode of operation are shown in figure 37. The data for the maximum Reynolds number boundary and for a constant $p_t = 43.2$ psi were obtained at a constant $T_t = -250$°F. The data in figure 25 for $R = 6 \times 10^6$ ft^{-1} at ambient temperatures are included here for comparison. A single data point obtained at $M = 1.2$ and $R = 14.3 \times 10^6$ ft^{-1} is also included.

To show frequency content, power spectra for the high Reynolds number data in figure 37 are presented in figures 38 and 39. For those Mach numbers where comparable data exist, the power spectra for the maximum Reynolds number boundary and $p_t = 43.2$ psi are very similar. Figure 38 shows power spectra from 0 to 20 kHz; figure 39 shows the same data across a reduced bandwidth of 0 to 2 kHz. For $M = 0.2$ and 0.4, the frequency peak at about 2 kHz is thought to result from an acoustic standing wave associated with the heat exchanger in the settling chamber and will be discussed later in section 4.9. At $M = 0.6$ and 0.7, the frequency peaks at about 800 Hz are thought to be associated with edge tones originating at the sidewall reentry flaps.

The previously shown insensitivity of the disturbance coefficient levels to fan drive power and Reynolds

number at a $M = 0.8$ is reflected in the results shown in figure 37. The data for the constant $p_t = 43.2$ psi and for the maximum Reynolds number boundary show close agreement at a $M = 0.8$ despite a fan drive power increment from 26.7 to 76.6 MW and a Reynolds number increment from 46.0×10^6 to 132.4×10^6 ft^{-1}. The closeness of agreement across the rest of the Mach number range prompts speculation that the demonstrated insensitivity may not be limited to just $M = 0.8$ but may occur more widely. Note that the peak fluctuating pressure coefficient $\tilde{p}/q = 0.0953$ at $M = 0.8$ and $R = 132.4 \times 10^6$ ft^{-1} corresponds to a peak sound pressure level of 161.4 dB re 20 μPa.

One result of the apparent insensitivity of the NTF flow disturbance level to Reynolds number may be the possible absence of what is referred to by Elsenaar, Binion, and Stanewsky (1988) as a pseudo-Reynolds number effect. (Also, refer to the discussion by Bobbitt (1981) on unit Reynolds number effects.) This effect is attributed to the variation of the wind tunnel disturbance level with wind tunnel Reynolds number. As already noted, the wind tunnel disturbance level can alter the location of the boundary layer transition and cause false results if the disturbance level varies when the wind tunnel Reynolds number is varied. Elsenaar, Binion, and Stanewsky indicate that this pseudo-Reynolds number effect occurs most readily if the location of the boundary layer transition is not fixed; however, it can also occur when the boundary layer transition is fixed. The apparent insensitivity of the flow disturbance level to Reynolds number in the NTF does not completely ensure that pseudo-Reynolds number effects will not occur in this wind tunnel but is clearly a favorable indicator.

4.6.3. Air Mode Performance Envelope Results

The fluctuating pressure coefficients have been measured as a function of Mach number in the air mode at the Reynolds number ranges indicated in the performance envelope in figure 17. The results for the minimum and maximum Reynolds number boundaries are presented in figure 40 for the test section RHS sidewall at station 13. There is a tendency for more separation of the data with Reynolds number in the air mode than was observed in figure 37 for the nitrogen mode, and the overall level near the peak at $M = 0.8$ is lower. Further, in contrast with the nitrogen mode results, the maximum Reynolds number boundary results for the air mode are everywhere lower than those for the minimum Reynolds number boundary. Generally, the Mach number effects are quite similar to what has been observed previously.

4.6.3.1. Effect of test section slot covers. Ventilated wall test sections tend to be much noisier than comparable solid wall test sections. Overall, slotted wall test sections tend to be quieter than perforated wall test sections. In perforated wall test sections, the primary additional noise source tends to be edge tones associated with the perforation holes. In slotted wall test sections, the primary additional noise sources are the free-shear layers in the slots and the extraction region of the test section where plenum flow reenters the mainstream. By covering the slots, both of these additional noise sources are eliminated. The slot covers that were used are shown in place in the test section in figure 18.

With the slots covered and the choke off, the test section wall divergence angle was set at 0.1° on the top and bottom walls; the sidewalls remained parallel. These wall settings resulted in a slight positive static pressure gradient. Quantitatively in terms of Mach number, the gradients varied from $dM/d(x/h) = -0.00010$ to -0.00595, or in terms of equivalent buoyancy-induced drag coefficient increments in figure 16, from less than a half count (0.00005) to somewhat more than four counts (0.0004) of negative buoyancy drag coefficient in the Mach number range of 0.2 to 0.9. For reference, the normal operating conditions for the NTF with slots open result in less than one count of buoyancy-induced drag coefficient across the entire operating range.

The fluctuating pressure coefficients measured on the test section RHS sidewall at station 13 with the slots covered are shown in figure 41. The data were taken from $M = 0.2$ to 0.9 along the minimum Reynolds number boundary in air. Data taken along the same boundary with the slots open are also shown for comparison. The reduction in disturbance level with slots covered occurs only at the high-subsonic Mach numbers ($M > 0.6$). This characteristic may be connected with incomplete wave reflection at the slotted wall-plenum interface, which allows test section disturbances to pass through into the plenum and become dissipated at $M < 0.618$. As noted previously in the discussion of the air-nitrogen comparison, the power spectrum with the slots covered (fig. 29) shows a disturbance peak at 850 Hz. The presence of these disturbances with the slots covered eliminates any direct connection between these disturbance peaks and the slot flow or the reentry process in the extraction region. This result is supportive of the probability that edge tone effects associated with the sidewall reentry flaps are responsible for the large peaks occurring in the power spectra in figures 27 and 35.

Power spectra (0 to 20 kHz) with the slots open and the slots covered are shown in figure 42 at the tunnel conditions plotted in figure 41. For $M \leq 0.6$, the power spectral densities with the slots open are slightly higher than with the slots covered at low frequencies but are lower at high frequencies. For $M > 0.6$, the power spectral densities at low frequencies for the slots open are

significantly higher than with the slots covered but are still lower at the high frequencies. The most significant difference in power spectra apparently occurs from $M = 0.7$ to 0.9 at the low frequencies from 0 to ≈ 1 kHz where the power spectral densities with slots open are much higher than with slots covered.

4.6.3.2. Effect of downstream choke. A major contributor of broadband noise at low frequencies is the noise propagating upstream from the diffuser and model support sections into the test section. To investigate the effect of a downstream choke, the variable geometry features of the NTF test section were used to create a minimum flow area at the downstream end of the test section. As shown in figure A10, the minimum flow area was located at the hinge line of the top and bottom wall reentry flaps, which created a two-wall choke at station 25. The area was sized to choke the flow at this location when the test section $M \approx 0.8$. Although the test section geometry is capable of being fully variable while the tunnel is running, the test section wall angle, the model support wall angle, and the reentry flap angles were all preset before tunnel start-up and were not varied during the choke runs. The choke geometry was set both for slots-open and slots-covered conditions. Because of differences in test section wall boundary layer growth with the slots open and covered, the preset wall geometry was not identical for the two conditions. The test section wall divergence angle was set to accommodate the calculated boundary layer growth for the closed wall configuration to minimize the longitudinal static pressure gradient, and the reentry flap angles were set to blend with the test section wall. The wall geometry settings for the different runs are summarized in table I. The wall geometry at the downstream end of the test section is shown in figure 43. The settings are pictured for the slots-open condition. The photograph was taken when the wall geometry settings were rehearsed prior to the actual dynamic investigation. The sting configuration shown in the photograph was for a model test which was in preparation at the time and was removed for the dynamic investigation.

The effect of the downstream choke is shown in figure 41 with the flagged solid symbols. In operation with the choke in place, the wind tunnel speed was increased until further increases in fan drive power did not result in any further increase in wind tunnel speed as shown in figure 44. The relatively small decrease in disturbance level with the choke deployed (on the order of 0.001 in coefficient) may be an indication that disturbances originating downstream of the test section do not contribute greatly to the disturbance level in the test section. The power spectra for the configuration with the slots open, both choked and unchoked, are shown in figure 45 for $M = 0.8$. The reduction in disturbance levels due to the choke occurs mainly at the low frequencies between 0 and 5 kHz. From the data shown in figures 41 and 45, the use of a two-wall downstream choke to reduce flow disturbance levels in the NTF test section resulted in only marginal improvements. However, a different choke configuration might have been more effective.

4.6.3.3. Effect of fan speed or inlet guide vane variation for velocity change. As described in appendix A, the NTF tunnel has two relatively independent means of changing tunnel speed. In normal wind tunnel operation, when only the power of the induction motors is required and the synchronous motor is not energized, the wind tunnel speed can be changed by either fan speed or inlet guide vane (IGV) angle variation; the method depends upon circumstances. The preferred mode of operation is to select a fixed fan speed that can be maintained while wind tunnel speed is varied over the desired range using IGV variation. This is especially true when the wind tunnel is operated automatically under computer control. Wind tunnel speed changes can be made much more rapidly by using IGV variation than by using fan speed variation. When the additional power of the synchronous motor is required and the fan speed is fixed at synchronous speed, then IGV variation must be used for wind tunnel speed changes.

A brief test was made to determine if the test section disturbance level would be affected by operation in either one or the other of the wind tunnel speed-changing modes. At $R = 6 \times 10^6$ ft^{-1} in the air mode, the wind tunnel speed was changed from $M = 0.2$ to 1.0 with fan speed variation from 160 to 595 rpm with the IGV fixed at $0°$ (neutral position). At the same test conditions, the

Table I. NTF Test Section Wall Geometry Variables

Test section configuration		Wall angle, deg, at—		Reentry flap angle, deg	Mach number range
Slots	Choke	Test section	Model support section		
Covered	On	0.1	−4.23	0.87	0.2 to 0.8
Covered	Off	0.1	−3.79	−0.1	0.2 to 0.9
Open	On	0	−4.23	1.86	0.2 to 0.8
Open	Off	0	−1.76	0	0.2 to 1.05

wind tunnel speed was also varied from $M = 0.6$ to 1.0 with IGV variation from $25°$ (fan unloaded) to $-20°$ (fan loaded) at a fan speed of 550 rpm. The results are shown in figure 46 for the test section RHS sidewall at station 13. The close agreement between the two sets of results would indicate that fluctuating static pressure level is not dependent upon the method of wind tunnel speed changes or the combinations of IGV settings and fan speed settings used to set a particular Mach number.

The results of this IGV versus fan speed investigation also provide some information on the noise characteristics of the NTF fan system. As noted previously, fan sound power is usually considered proportional to the fan power times the cube of the blade tip speed. Although the inflow velocities at the fan were not measured, they should be essentially a function of Mach number for the test conditions in figure 46 and be fairly similar for both the variable speed and the variable IGV data points. Because the blade tip speed is obtained by a vector resolution of the fan rotational speed and the inflow velocity, its variation over the Mach number range is different for the variable speed and the variable IGV data points. For data points in figure 46 at $M < 0.9$, the blade tip speed would be higher for the variable IGV data compared with the variable speed data, and the opposite is true for $M > 0.9$. However, the data for the disturbance levels do not show a similar tendency. From the results in figures 31 and 46, the disturbance level in the NTF test section appears to be insensitive to variations in either the blade tip speed or the shaft power of the NTF fan drive system.

4.6.3.4. Comparison with other wind tunnels. The fluctuating pressure coefficients measured on the NTF test section RHS sidewall at station 13 for the minimum Reynolds number boundary in air (atmospheric stagnation pressure and ambient temperature) and plotted in figure 40 are replotted in figure 47. Data from Jones (1991) for the Langley 8-Foot Transonic Pressure Tunnel (8-Foot TPT) at similar test conditions are shown for comparison. The Langley 8-Foot TPT data are from a pressure transducer located on the test section LHS sidewall at a station corresponding to the location of test models. The LHS sidewall of the Langley 8-Foot TPT, which is downstream of the inside corner of turn 4 is similarly positioned to the RHS sidewall of the NTF.

No test model was in the Langley 8-Foot TPT at the time of Jones' (1991) measurements, but a nose cone supporting five probes was mounted on the centerline model support system of the wind tunnel. This model support system regularly utilizes a pair of guy wires downstream of the model location to provide lateral restraint for the sting support system. A frequency spike caused by vortex shedding from these guy wires was

identified by Jones in the spectra of the Langley 8-Foot TPT fluctuating pressure data. Because guy wires are normally present for conventional model testing in the Langley 8-Foot TPT, their influence is a normal part of the flow disturbance measurements in that wind tunnel. Jones did not indicate to what extent the guy wire interference may have affected the overall level of the measurements.

The data for the Langley 8-Foot TPT sidewall show the same characteristics as observed for the NTF data, that of peaking at high-subsonic Mach numbers near 0.8 and falling off steeply as sonic speeds are approached. Both wind tunnels show similar disturbance levels on the order of 0.6 percent at low-supersonic speeds. At the peak near $M = 0.8$, the level is approximately 1.5 percent for the Langley 8-Foot TPT and 0.8 percent for the NTF.

For reference, the fluctuating pressure coefficient data measured in the NLR—HST by Ross and Rohne (1973) are also shown in figure 47. The NLR—HST data were measured on the AEDC $10°$ cone which is described by Dougherty (1980). The HST data appear to represent a maximum envelope of disturbance level for the test conditions in that wind tunnel. These data may not be directly comparable with the Langley 8-Foot TPT or NTF data because of the differences in the methods of measurement. However, all three wind tunnels appear to have relatively quiet flows. The peak level for the NLR—HST is approximately 1 percent. On the basis of the data in figure 47, the NTF has low levels of test section fluctuating static pressure as measured on the test section sidewall, especially in the high-subsonic Mach number range from 0.7 to 0.9.

As mentioned previously, wall pressure fluctuations measured beneath a turbulent boundary layer are influenced by disturbance levels generated within the turbulent boundary layer itself. There is an interaction of the turbulence with the mean shear and an interaction of the turbulence with itself. These disturbance levels represent a floor or minimum level that can be measured on a wall. Lowson (1968) has derived the empirical expression for estimating this minimum level for attached equilibrium turbulent boundary layers of

$$\frac{\tilde{p}}{q} = \frac{0.006}{1 + 0.14M^2} \tag{1}$$

which is also shown in figure 47. Most of the wind tunnel data are above this line.

4.7. Effect of Test Section Geometry Variables

As indicated in figure A10, the NTF test section geometry variables consist of variable top and bottom test section wall divergence angles, variable reentry flap

angles, and variable top and bottom model support section wall angles. The role of the test section wall divergence in controlling longitudinal static pressure gradients has already been mentioned. The reentry flaps can similarly control pressure gradients near the downstream end of the test section. The model support section wall angle variation was used in the downstream choke test to form a minimum flow area at the location of the reentry flap hinge line. All three variables affect the wind tunnel power consumption. The results of the steady-state calibration (private communication from M. Susan Williams and Jerry B. Adcock of the NTF staff) were used to select settings of these geometry variables for normal operation of the wind tunnel, and these settings were used for the dynamic measurements as well.

The effect that the test section geometry variables have on the disturbance level in the test section was investigated briefly by varying each setting through a small range while the other two were held fixed. The results are shown in figure 48 for the test section RHS sidewall at station 13 for $M = 0.8$ and $R = 6 \times 10^6$ ft^{-1}. With the exception of the test section wall divergence angle of 0.3°, all the effects are slight. Broadband (0 to 20 kHz) power spectra for the rms data in figure 48 are shown in figure 49. For the data point at 0.3° wall divergence in figure 48(a), the power spectrum in figure 49(a) does not show any frequency spikes, only a small broadband increase in disturbance level in the frequency range from ≈100 Hz to ≈2 kHz. Figure 48 shows that the lowest levels of disturbance are obtained at test section wall angles from parallel to slightly converged, reentry flap angles away from the flow, and model support wall angles toward the flow.

4.8. Effect of Liquid Nitrogen Injection

A process capable of spraying as much as 1000 lb/sec of volatile liquid in a confined space has the potential of having a significant influence on the test section disturbance levels. Tests in the air mode and in the nitrogen mode provided an opportunity to compare the disturbance levels at the liquid nitrogen station both with and without injection but at otherwise substantially the same test conditions. This comparison is shown in figure 50 at $R = 6 \times 10^6$ ft^{-1}. The pressure coefficient data are plotted as a function of the test section Mach number. Because the liquid nitrogen injection station is downstream of the test section, the choke effect at the test section does not tend to reduce the disturbance levels as test section sonic speeds are approached, and the disturbance levels continue to rise as the Mach number is increased. Power spectra for the rms data in figure 50 are shown in figure 51.

At $M > 0.6$, the disturbance levels are greater in nitrogen than in air. A comparison of the power spectra for these conditions (figs. 51(e)–51(l)) showed that the increase was primarily broadband with no apparent particular frequency selectivity. The frequency peaks that were so prominent in the power spectra of the test section pressure transducers at these test conditions (figs. 26 and 27) were not evident in the power spectra at the liquid nitrogen injection station.

To gain further insight into the effect of liquid nitrogen injection, the output of the dynamic instrumentation was continuously recorded as the injection process was abruptly turned off. The initial test conditions for the cutoff test were $M = 0.8$, $R = 12.6 \times 10^6$ ft^{-1}, $p_t = 20$ psi, and $T_t = -160°$F. A playback of the continuously recorded data is shown in figure 52 for the settling chamber, the test section RHS sidewall at station 13, the high-speed diffuser, and the liquid nitrogen injection station. The initiation and completion times for the cutoff of injection are shown on the upper grid line. The total cutoff time from initiation to completion took about 12 sec. The time for a disturbance to propagate by convection completely around the tunnel circuit at this test condition has been estimated to be slightly less than 7 sec. The effects of the nitrogen cutoff are so imperceptible in figure 52, and the moment of cutoff is nearly impossible to detect from the transducer signals. As will be discussed in section 4.9, the settling chamber disturbance level may be influenced by the gaseous nitrogen exhaust which is automatically controlled by the wind tunnel control process to maintain stagnation pressure when the nitrogen injection is stopped.

During the cutoff procedure, the wind tunnel control system maintained the Mach number and the stagnation pressure. The stagnation temperature increased rapidly and the test was terminated after a temperature increase of 25°F. Because the Mach number was being held constant, the velocity increased with the temperature. Because of the rapid increase in temperature and velocity following the nitrogen cutoff, the test conditions were no longer completely constant, and the statistical analysis methods used herein were no longer strictly appropriate. However, because the disturbance amplitude did not show drastic changes as seen from the time history traces in figure 52, a short relatively stationary time sample of about 10 sec before and after cutoff was analyzed for power spectral content and rms level. The power spectra are shown in figure 53 for the same four wind tunnel stations whose time traces are shown in figure 52. The rms levels listed on the power spectra indicate that the settling chamber disturbance level decreased slightly when the liquid nitrogen injection was stopped and either

remained the same or increased slightly for the other three stations. Sound pressure levels in dB re 20 µPa are also shown in figure 53.

The apparent lack of influence of the liquid nitrogen injection process on the level of flow disturbances detected in the test section may be associated with the presence of suspended droplets in the liquid nitrogen spray. Such a droplet suspension could be inhibiting the upstream propagation of broadband fan noise similar to the attenuation of sound propagation in atmospheric fog and partially offsetting any direct noise created by the injection process.

4.9. Fluctuating Pressure Coefficient in Settling Chamber

The fluctuating pressure coefficients for the settling chamber at the test conditions along the maximum Reynolds number boundary in the nitrogen mode are shown in figure 54. In this and subsequent figures showing the settling chamber disturbance levels, the fluctuating pressure coefficients are formed by using the dynamic pressures in the settling chamber and are plotted as a function of the Mach number or Reynolds number in the test section. Although the coefficient levels are higher in the settling chamber, a significant resemblance exists between figure 54 and figure 37, which showed the disturbance level in the test section for the same test condition. For the settling chamber, a sharp drop-off of the fluctuating pressure coefficient occurs from approximately 0.275 at $M = 0.8$, to approximately 0.125 as sonic speeds are approached in the test section. The similar characteristics shown in figures 37 and 54 suggest that the disturbance levels in the settling chamber are strongly affected by the levels in the test section, which indicate that these disturbances may originate in the test section or further downstream and propagate upstream from the test section into the settling chamber. This supposition is further supported by the effect of the downstream choke, which is shown for the minimum Reynolds number boundary in air in figures 55(a) and 55(b) with the test section slots open and covered, respectively. When the downstream second minimum cross section is actively choking flow, the fluctuating levels drop to the same level as when sonic speeds are approached, which mirror the results of the test section. (See fig. 41.) However, there is a significant difference between the levels for the maximum Reynolds number boundary (fig. 54) and the minimum Reynolds number boundary (fig. 55(a)), which raises the question of whether other influences (e.g., possibly fan noise and other disturbances caused by the wide-angle diffuser, the heat exchanger, and the screens) are present in the settling chamber as well and bias the results from minimum to maximum Reynolds number.

Some possible sources of disturbance will be examined next to see if they could be responsible for the large differences between the rms data in figures 54 and 55. The settling chamber power spectra for the maximum and minimum Reynolds number boundary at $M = 0.8$ are shown in figure 56. A comparison of the power spectra shows that at frequencies above ≈2 kHz, the higher levels of disturbance for the maximum Reynolds number boundary are primarily broadband. However, the contribution at these frequencies to the overall power is slight. The major differences between the maximum and minimum Reynolds number boundary power spectra are in three broad peaks with most of their power concentrated below ≈1.2 kHz. The lowest of the three broad peaks contains a small peak at the blade passage frequency of 150 Hz and another small peak at 110 Hz, which is probably associated with vortex shedding from the tubes of the heat exchanger. The small peak at 35 Hz is probably associated with vortex shedding from some of the heat exchanger support structure, which consists of vertical plates on either side of the individual tube bundles in the heat exchanger. The minor peak at 2165 Hz is probably associated with vortex shedding from the screen wires. The tentative frequency identifications just referred to and that follow are based on the assumed Strouhal number for the vortex-shedding characteristics of each component.

At the maximum Reynolds number boundary test condition, the fan was operated at its synchronous speed of 360 rpm. The 25 blades of the fan produce disturbances at the fundamental blade passage frequency (BPF) of 150 Hz and harmonics at integral multiples of that frequency. Except for the fundamental tone at 150 Hz, none of the blade passage harmonic frequencies are apparent in the spectrum for the maximum Reynolds number boundary. At the minimum Reynolds number boundary test condition, the fan was operated at its maximum speed of 600 rpm. The fundamental BPF of 250 Hz is barely evident among other minor peaks in that frequency range. The first, second, and third harmonics of the BPF at 500 Hz, 750 Hz, and 1000 Hz are evident but higher harmonics are not.

For the rest of the low Reynolds number boundary power spectrum, the only peaks which can be tentatively identified are again the following vortex-shedding frequencies: at 50 Hz from the support structure of the heat exchanger, at 210 Hz from the heat exchanger tubes, and at 3420 Hz from the screen wires. These tentatively identified sources for the minimum and maximum Reynolds number boundaries represent only a small fraction of the total power in the respective spectra. If the source identifications are correct, these sources cannot by themselves be responsible for the differences in the disturbance levels, and some other as yet undetermined

source must be a factor. Note that disturbances from the wide-angle diffuser have not been eliminated from consideration, but these disturbances would likely be broadband in nature and not cause the discrete peaks which have been observed. Another possibility is the venting region in the crossleg between turns 3 and 4. For the minimum Reynolds number boundary in air, the vent valves are normally closed. However, the valves are open for the maximum Reynolds number boundary in nitrogen and vent a mass flow at a rate equal to the liquid nitrogen injection rate.

The tests of air versus nitrogen provide an opportunity to compare the settling chamber disturbance levels both with and without venting at otherwise similar test conditions. The fluctuating pressure coefficients in the settling chamber for these two tests are shown in figure 57 for a test section $R = 6 \times 10^6$ ft^{-1}. Power spectra at selected Mach numbers for the test points in figure 57 are shown in figure 58. Because the test conditions for the air and the nitrogen mode tests are nearly identical, the differences between the tests should be directly attributable to the nitrogen injection process and the accompanying venting. The data in figure 50 showed that the injection process did not have much effect at the liquid nitrogen injection station. The injection process can be assumed to have even less effect at the settling chamber, so the differences that are observed can be attributed primarily to the venting.

The fluctuating pressure coefficient data in figure 57 show an increase in the disturbance level across the Mach number range for the nitrogen test. At $M \geq 0.6$, the power spectra in figure 58 show both narrowband and broadband increases. At $M = 0.2$ in the nitrogen mode (fig. 58(a)), the peak at 3.2 kHz is thought to be due to an acoustic standing wave associated with the heat exchanger in the settling chamber. This tentative identification is based on the observation that the frequency did not vary with velocity changes but did vary approximately with the square root of the absolute temperature, and the lateral spacing of the heat exchanger tubes was about right for a standing wave of this frequency. At $M = 0.2$ and 0.4, the air mode test data show major frequency peaks at 14.8 kHz and 15.3 kHz, respectively, which are not present in the nitrogen mode test data. No information is currently available on the noise characteristics of the vent region on which to base any further comment. This area of the wind tunnel circuit and the venting process require further study.

Figure 59 shows comparative data taken at two different test conditions in the nitrogen mode: one at constant $R = 40 \times 10^6$ ft^{-1} and constant fan drive power of 30 MW and the other at constant $p_t = 43.2$ psi and constant $T_t = -250°$F. The fluctuating pressure coefficients

in the settling chamber are relatively insensitive to the differences in the test conditions in this intermediate Reynolds number range. Data taken across a broad range of Reynolds numbers at $M = 0.8$ are shown in figure 60 for three test conditions: constant drivepower of 30 MW, constant stagnation temperature of $-230°$F, and constant stagnation pressure of 43.2 psi. These data are also relatively insensitive to the difference in the three test conditions but show an increasing level of disturbance with increasing Reynolds number. The effect of the variation of fan drive power is shown in figure 61 for $M = 0.8$ and $R = 40 \times 10^6$ ft^{-1}. The disturbance levels are relatively insensitive to changes in fan drive power with only a slight tendency to decrease with increasing fan drive power. Figures 59–61 show that the settling chamber responses are similar to those observed in the test section where disturbance levels are a strong function of Mach number and relatively insensitive to fan drive power. Although still slight, the effects of Reynolds number appear more distinct in the settling chamber.

4.10. Fluctuating Pressure Coefficient in High-Speed Diffuser

The pressure transducer in the high-speed diffuser was installed on the LHS at midheight, about halfway downstream at station 68. The fluctuating pressure coefficient was formed with the dynamic pressure in the test section, and the coefficients were plotted as a function of test section Mach number. Data for the comparison tests in air and in nitrogen at ambient temperatures are shown in figure 62 for $R = 6 \times 10^6$ ft^{-1}. Just as with the liquid nitrogen injection station data, the disturbance levels continue to rise as sonic speeds in the test section are approached and exceeded because the measuring station is downstream of the test section; there is no tendency for the choke effect at the test section to reduce the disturbance levels as test section sonic speeds are approached. In fact, the tendency is for the disturbance levels to rise more steeply for $M > 0.8$ probably as a result of the formation of unsteady shocks between the end of the test section and the beginning of the diffuser with their attendant increase in noise levels.

4.11. Fluctuating Pressure Coefficient in Plenum

The pressure transducer in the plenum was installed on the RHS at station 0, near the plenum wall, and at the same height as the test section top wall. The fluctuating pressure coefficients calculated with the test section dynamic pressure are shown as a function of the test section Mach number in figure 63. The test conditions represented in figure 63 are the comparison tests for air and nitrogen at $R = 6 \times 10^6$ ft^{-1} and the minimum and maximum Reynolds number boundaries, respectively. The disturbance levels in the plenum for these test

conditions are very low and increase from about 0.001 to 0.002 with an increase in Mach number from 0.2 to 1.05. There is very little difference between the air and the nitrogen mode test results at $R = 6 \times 10^6$ ft^{-1} or between the minimum and maximum Reynolds number boundaries.

Power spectra for the minimum Reynolds number boundary data for $M = 0.2$ to 0.642 are shown in figure 64 for a frequency bandwidth from 0 to 1 kHz. At $M = 0.2$ (fig. 64(a)), line frequency interference peaks at multiples of 60 Hz are quite evident. The somewhat elevated disturbance level shown for the rms fluctuating pressure coefficient at this Mach number in figure 63(b) may partially result from the line interference present in the measurement. Note that this is an exceptional condition where an already quiet signal from the plenum is measured at the lowest operating condition of the tunnel. At most other conditions, the data signal is of sufficient magnitude that the small line frequency interference is not an appreciable part of the measurement. At $M = 0.3$ (fig. 64(b)), the line frequency interference is still evident but not nearly so intrusive as at the lower Mach number. At the higher Mach numbers, the line frequency interference is still identifiable in some places but is not a significant part of the measurement.

All of the power spectra in figure 64 show that many disturbance peaks affect the plenum. Few, if any, of the peaks can be positively identified as to source except, of course, the line frequency interference. Another possible exception is the fan BPF, which is known fairly accurately. The BPF is noted on each of the power spectra. A careful examination of the power spectra shows peaks at or very near this frequency. For instance, at $M = 0.6$ to 0.642 (figs. 64(e)–64(g)), the BPF is 227 Hz. There is a modest peak in the power spectra at 221 Hz. The frequency resolution in the power spectra is approximately 1 Hz so this peak is not close enough in frequency to be identified as the BPF. However, the peak at 221 Hz is distorted on the high-frequency side as though a second peak might be there as well. A higher resolution power spectrum in figure 65 for $M = 0.6$, which corresponds to the power spectrum of figure 64(e), shows a separate peak of about 225 Hz, which probably corresponds to the fan blade passage frequency peak.

Mabey (1976) has indicated that the slots themselves can be sources of regular disturbances with characteristic slot frequencies having Strouhal numbers in the range of 0.03 to 0.04 based on slot width. If a slot Strouhal number of 0.035 is assumed, then the characteristic slot frequencies f_s for the NTF slots are as indicated on the power spectra in figure 64. Positive correlation of these frequencies with frequency peaks in the power spectra

was not possible and evidence of their existence in the power spectra is not strong.

Multiple acoustic resonances can exist in the plenum, but these disturbances have not been considered in the present analysis. However, wind tunnel models subject to unsteady load are, therefore, sources of excitation and can be affected by one particular kind of resonance associated with the ventilated test section walls and the plenum. For this kind of resonance, the model is the source of the excitation either through forced oscillation or aeroelastic vibration response such as flutter or buffet. In this test section plenum resonance, transverse waves from the test section are partially transmitted through the test section plenum boundary, travel outward into the plenum, and are reflected from the outer plenum walls back to the ventilated wall interface. If the returning wave is in phase with the outgoing wave, resonance will occur.

This kind of resonance problem has been studied by Mabey (1978), Barger (1981), and Mokry (1984) who developed analytical solutions; more recently, Lee and Baik (1991) extended a finite element numerical solution to include the slotted wall boundary conditions. For resonance frequency estimates in the NTF, the closed form results of Barger were applied because that analysis used accurate boundary conditions for the slotted walls. The calculated fundamental frequencies for the test section plenum resonance f_p are indicated in the power spectra in figures 64(a)–64(e) up to $M = 0.6$. For $M > 0.618$, the solution changes character, the reflection from the slotted boundary is complete, and the influence of the plenum is greatly diminished.

The presence of the test section plenum resonance peaks cannot be confirmed in the power spectra in figure 64. In the absence of discrete excitation as might be provided by an oscillating or vibrating test model, this particular form of resonance is not considered to be a problem in the NTF. Apparently, flow unsteadiness by itself is not sufficient to excite this resonance to detectable levels.

From the power spectra in figure 64, the excitation associated with fan blade passage frequencies, characteristic slot frequencies, and slotted wall plenum resonances do not contribute significantly to the level of disturbance measured in the plenum.

4.12. Convection Velocities

In a shear layer, disturbance patterns are transported with the stream at some fraction of the free-stream velocity, which depends on the scale of the disturbance and its location within the shear layer. The magnitude of the transport velocity generally depends on the frequency of

the disturbance and on the separation distance over which it is measured.

In the NTF, the overall streamwise convection velocity $u_c(x)$ was measured in the test section. Three pressure transducers were spaced 2.25 in. apart streamwise on the test section RHS sidewall at station 13. Cross correlations of unfiltered signals from an adjacent pair of these transducers were used to obtain the transit time between the two transducers for disturbances convecting downstream. A sample cross-correlation plot is shown in figure 66 for $M = 0.998$ and $R = 6.1 \times 10^6$ ft^{-1}. This measurement was made in the nitrogen mode at ambient temperatures. For this test point, an overall streamwise convection velocity ratio $u_c(x)/V = 0.746$ was computed. Data for this and other Mach numbers from 0.2 to 1.05 are shown in figure 67 for comparison with similar data measured in air. The agreement between the two sets of data is sufficient to indicate that there are no significant differences in convection velocities in the two test gases. Although the convection velocity ratio is relatively constant across the Mach number range at ≈ 0.76, there is a slight tendency for the level to rise with increasing Mach number.

A similar comparison is shown in figure 68 for slots open compared with slots covered. These data were measured in the air mode along the minimum Reynolds number boundary. Again, comparative data indicate no significant difference between slots open and slots covered. The overall convection velocity ratio of 0.74 at minimum Reynolds numbers is slightly lower than for $R = 6 \times 10^6$ ft^{-1} with a slight tendency for the level to rise with increasing Mach number. Because Reynolds number increases with increasing Mach number along the minimum Reynolds number boundary, the apparent increase of convection velocity ratio with Mach number may really be a Reynolds number effect.

The effects of hot wall versus cold wall on the convection velocity are shown in figure 69 for $M = 0.8$. There is a tendency for the convection velocities to be higher for the hot wall condition than for the cold wall condition; overall, the convection velocity ratio is ≈ 0.77. The Reynolds numbers are not constant for these data and range from $\approx 7.5 \times 10^6$ ft^{-1} for the cold wall data to $\approx 10 \times 10^6$ ft^{-1} for the hot wall data. The tendency in the convection velocity data has been for the level to increase slightly as the Reynolds number is increased, which might partially account for the apparent effect of the hot wall in figure 69.

The effect of Reynolds number mentioned previously is somewhat more apparent in the data in figure 70 where the convection velocity ratios for the maximum Reynolds number boundary are shown as a function of Mach number. The data for the minimum Reynolds number boundary (air mode with slots open) are repeated from figure 68 for comparison. The convection velocity ratios for intermediate Reynolds numbers at $p_t = 43.2$ psi are also shown. There is a positive increment of about 0.05 in convection velocity ratio from the minimum to the maximum Reynolds number boundary with most of the increment occurring between the low and intermediate Reynolds numbers.

5. Conclusions

Dynamic measurements of the fluctuating static pressure levels have been made at 11 locations in the circuit of the NTF across the complete operating range, which resulted in flow disturbance measurements at the highest Reynolds numbers available in a transonic ground test facility. Tests were made with independent variation of Mach number, Reynolds number, and fan drive power; for each test, two of the three parameters were kept constant, which for the first time allowed a distinct separation of the effect of these important parameters. Tests were also made with independent wind tunnel speed variation by either fan speed or inlet guide vane angle variation. An analysis of these dynamic flow disturbance measurements has led to the following conclusions:

1. The results of tests to isolate the effects of Mach number, Reynolds number, and fan drive power on flow disturbance levels indicate that Mach number effects predominate. The flow disturbance levels appear relatively insensitive to Reynolds number and fan drive power variations.

2. One of the primary sources of noise in the NTF appears to be flow surface gaps associated with the sidewall reentry flaps at the downstream end of the test section. The gaps appear capable of producing edge tones at some flow conditions.

3. The downstream second minimum flow area formed on the top and bottom walls to choke the flow at subsonic test section Mach numbers produces only marginal reduction in the flow disturbance levels in the test section at a choke $M = 0.8$.

4. The effects on flow disturbance level of intentional differences in temperature between the wall boundaries and the test gas are small with a tendency for the cold wall to have a slightly higher disturbance level than the hot wall. Smaller incidental temperature differences during the tests show an almost negligible effect on the data.

5. Although in general agreement, a comparison between results in air and in nitrogen show differences that are thought to be caused at least in part by a mismatch in velocity between the two tests.

6. The liquid nitrogen injection process does not contribute significantly to the level of flow disturbance in the test section.

7. Flow disturbance levels in the settling chamber appear to be adversely affected by the gas-venting process, which occurs during cryogenic operations with nitrogen.

8. Tests with the slots covered show reductions in the test section sidewall static pressure fluctuation levels only at $M > 0.6$.

9. Test section sidewall static pressure fluctuation levels are relatively independent of the test section geometry settings of wall divergence, reentry flap angle, and model support wall angle.

10. Wind tunnel speed changes can be obtained with either fan speed changes or inlet guide vane angle changes with no significant difference in test section flow disturbance levels.

11. Fan blade passage frequency peaks are not a significant contribution to the flow disturbance levels in the wind tunnel at most operating conditions. These frequency peaks are only apparent in the power spectra at low tunnel operating conditions (i.e., low-Mach number, low-stagnation pressure, and low fan drive power) when the background level of disturbance is sufficiently low. The disturbances associated with the characteristic slot frequencies and slotted wall-plenum resonances are also insignificant.

12. Overall streamwise convection velocity ratios $u_c(x)/V$ measured with the use of unfiltered pressure transducer signals on the test section sidewall are relatively unaffected by the change in test gas from air to nitrogen, by open or covered test section slots, or by differences in wall-to-gas temperature. The convection velocity ratios increase slightly with increasing Reynolds number.

13. A comparison with other transonic wind tunnels shows that the NTF has low levels of test section fluctuating static pressure especially in the high-subsonic Mach number range from 0.7 to 0.9.

Some additional comments on the measured data beyond those specifically enumerated are included here.

From comments by Mabey (1991), the weak sensitivity of the measured flow disturbances to Reynolds number variation in the NTF may indicate that the flow disturbances being measured could be due primarily to aerodynamic noise sources that are controlled by turbulent eddy viscosity effects. Such effects are typically dependent on velocity and eddy sizes and independent of Reynolds number. Mabey's theory specifically considers the noise that emanates from the extraction region at the downstream end of the test section where flows, which have entered the plenum through the slots, reenter the mainstream. The results in this report do not specifically confirm Mabey's theory, but the comparison at high-subsonic Mach numbers between slots open and slots covered (fig. 41) is consistent with it.

The lower flow disturbance levels in the test section at $M < 0.6$ with the slots open compared with slots covered may be connected with the partial transmission of waves at the slotted wall-plenum interface, which allows test section disturbances to pass through into the plenum at $M < 0.618$. Waves that enter the plenum may be subject to dissipation effects through multiple reflections from the thermal insulation surface on the interior of the pressure shell or may become trapped by plenum structural elements. At $M > 0.618$, the reflection of waves from the slotted boundary is complete, and the attenuating influence of the plenum could be greatly diminished.

Although considered separately in the list of conclusions, the effect of fan drive power variation and the comparison of fan speed versus inlet guide vane angle for changing wind tunnel speed, when taken together, indicate that the flow disturbance levels in the NTF test section are insensitive to either the fan blade tip speed or the fan shaft power. The relationship, if any, between this apparent insensitivity and the extensive noise attenuation treatment of the fan nacelle nose cone and tail cone was not determined.

The apparent lack of influence of the liquid nitrogen injection process on the level of flow disturbance detected in the test section may be associated with the presence of suspended droplets in the liquid nitrogen spray. Such a droplet suspension could be inhibiting the upstream propagation of broadband fan noise similar to the attenuation of sound propagation in atmospheric fog, which would partially offset any direct noise created by the injection process.

NASA Langley Research Center
Hampton, VA 23681-0001
October 23, 1995

Appendix A

Detailed Description of NTF

The National Transonic Facility (NTF) is a single-return pressurized transonic cryogenic wind tunnel with a slotted square test section and can operate at Mach numbers up to 1.2, pressures up to 130 psi, and temperatures down to −320°F. Specific components of the wind tunnel are described in this appendix.

Thermal Insulation

Thermal insulation for the wind tunnel (shown shaded in fig. 6) is internal rather than external to the pressure shell. The internal insulation shields the pressure shell from large temperature changes as the wind tunnel temperature is varied during the cryogenic mode of operation. Because the pressure shell with its large thermal inertia is not directly subjected to changes in gas temperature, liquid nitrogen consumption is reduced and thermal cycling of the pressure shell is avoided.

The insulation is a closed-cell, high-density, rigid foam of modified polyurethane material varying in thickness from ≈6.0 to 7.5 in. and is attached to the inside of the pressure shell as shown in figure A1. Its excellent fire-retardant property is an important feature for any material used in a wind tunnel such as the NTF, which can be pressurized to 130 psi in air. As shown in figure 6, the insulation is completely isolated from the flow by an internal aerodynamic liner in the high-speed section of the wind tunnel from the beginning of the wide-angle diffuser downstream to the end of the high-speed diffuser. Except for the fan shroud region, the insulation in the remainder of the wind tunnel circuit is separated from the flow stream by a relatively thin liner as shown in figure A1. For economy of fabrication, the liner plates shown in figure A2 are flat aluminum panels installed in a 24-sided polygon cross-sectional shape in the wind tunnel essentially from turn 1 to turn 4.

Principal Components

The principal components of the NTF circuit are shown in figure A3. As previously mentioned, the cryogenic mode of operation uses nitrogen as the test gas with cooling accomplished by the injection of liquid nitrogen directly into the flow stream. The liquid nitrogen injection nozzles are located upstream of the fan nacelle. Adcock (1977) has shown that liquid nitrogen injection upstream of the fan results in lower power requirements and lower liquid nitrogen flow rates when compared with downstream injection. This location may also be more favorable for complete evaporation of the injected liquid, attenuation of upstream moving fan noise by liquid nitrogen spray droplets, and reduction in the injection noise levels which reaches the test section.

The aerodynamic design of the NTF has been strongly influenced by the need for economy of operation. The cryogenic concept permits the achievement of high Reynolds numbers at relatively low energy consumption levels compared with other high Reynolds number ground test facility concepts. However, even for the cryogenic wind tunnel, the overall consumption of energy is high and must be carefully managed. The principal energy requirement of the NTF in the cryogenic mode of operation is the energy consumed to produce the liquid nitrogen used for cooling. To minimize the cost of nitrogen required to pressurize the tunnel and to reduce the cost of the pressure shell, the internal volume of the NTF circuit was designed to be as small as practical. Within this limitation, the settling chamber was made with as great a length as the economics of the pressure shell and the internal fill volume would permit.

The corners of the NTF circuit are mitered to form 90° turns. The turning vanes in these corners have an arithmetically progressive spacing, which was introduced initially by Dimmock (1950) for gas turbine research and used in other wind tunnels such as the LaRC 0.3-Meter Transonic Cryogenic Tunnel and the Defence Research Agency (DRA) (formerly Royal Aerospace Establishment (RAE)) 5 Metre Pressurized Low Speed Wind Tunnel.

Wide-Angle Diffuser

The wide-angle diffuser shown in figure A4 is located immediately upstream of the settling chamber. The use of a wide-angle diffuser at this location minimized the diameter of the return duct of the tunnel circuit but still permitted a large settling chamber and a high-contraction ratio with its attendant benefits on wind tunnel performance and flow quality. The wall curvature in the wide-angle diffuser was designed in the manner described by Küchemann and Weber (1953) for a nearly constant static pressure along the walls in the streamwise direction. This desired pressure gradient with its reduced tendency for boundary layer separation is obtained by proper curvature of the walls. The centrifugal force acting on the flow as it follows the curved wall contour is balanced by the stream pressure gradient as the flow is slowed by the increased area of the wide-angle diffuser. At the downstream end, the flow must be returned toward the axial direction. In the NTF, the turning is accomplished by the finned tube heat exchanger, which also contributes to the downstream pressure loss required to prevent flow separation from the diffuser walls. The heat exchanger cooling water tubes are elliptical in cross section and are oriented vertically. The plate-like fins

attached to the tubes are oriented horizontally. The aerodynamic and gravity loads on the heat exchanger are supported by a truss with radial and annular elements located near the downstream end of the wide-angle diffuser. The annular elements have been shaped to conform to the flow field curvature in the streamwise direction. The wide-angle diffuser has an exit-to-inlet area ratio of 2.08:1, a length-to-inlet diameter ratio of 0.465:1, and an exit wall angle of about 61°.

Turbulence Damping Screens

The exit of the wide-angle diffuser is followed by a settling chamber approximately 19 ft long. There are four turbulence damping screens in the settling chamber that are spaced 2 ft apart with the last screen approximately 5 ft from the beginning of the contraction. The four screens are identical; the square-mesh wire cloth is woven of 0.032-in-diameter wires at a spacing of 6 wires/in. with a resulting porosity of approximately 0.65. Because of the large diameter (35.7 ft) of the settling chamber and the high pressure (130 psi) at which the NTF can operate, the limiting factor in the selection of the screens was the stress in the screen wires under load. The 18-ft-wide rolls of screen cloth are joined together at their edges by butt-welding the individual wires thereby producing aerodynamically clean seams. The screens are installed preslacked to allow them to deflect about 2 ft downstream under maximum load as a means of reducing the screen wire stress.

Contraction Section

The contraction section has an area ratio 14.95 to 1 and was designed to produce uniform flow at the throat under choke conditions (i.e., to have an essentially straight sonic line). The prescribed area distribution for the contraction was calculated by a streamline curvature method developed by Barger (1973) for axially symmetrical flow with the use of the exact equations for an inviscid compressible flow.

The NTF contraction consists of the three subsections shown in figure A5. The first subsection is axially symmetrical with the prescribed area distribution matched exactly. The second subsection is a transition of the cross-sectional shape from round to flat-sided with radial corner fillets of progressively shorter radius and arc length. Here, the prescribed area distribution is matched only approximately. The third subsection is a continuation of the essentially square cross section with corner fillets; the corner fillet shape changes from circular arc to flat approximately 9 ft upstream of the test section.

The length of the contraction is approximately 48 ft. An upstream 39-ft-long section of the contraction is a movable structure that can be detached from the rest of the contraction and moved upstream within the pressure shell to permit deployment of one of two isolation valves that seal the test section and plenum from the rest of the circuit. The isolation valves permit access to the test section without depressurizing the entire tunnel circuit.

Test Section

A plan view of the NTF test section is shown in figure A6. The design of the NTF test section closely resembles that of the Langley 8-Foot Transonic Pressure Tunnel, especially in the flow reentry region at the downstream end of the test section. The cross section is nominally 8.2 by 8.2 ft square with flat corner fillets at 45°, which results in a test section throat cross-sectional area of 66.77 ft^2. There are six longitudinal slots in each of the horizontal (top and bottom) walls and provision for two slots in each of the vertical (side) walls.

The NTF slot shape for the top and bottom walls is shown in figure A7. In the test section length normally occupied by test models, the slots are of constant width (i.e., open area ratio of 6 percent). The upstream length of the slots is contoured to obtain a uniform Mach number distribution at a Mach number of 1.2. The contour shape was designed with a modified method of characteristics developed by Ramaswamy and Cornette (1980). The side wall slots are currently blanked off which provides a solid side wall. Because the current configuration of the test section is only slotted on the top and bottom walls, the overall wind tunnel open area ratio is then 3 percent.

The length of the slotted region is approximately three test section widths. The side walls are parallel to each other, but the top and bottom walls have flexures at the upstream end which permit variation in wall angle from approximately 0.5° converged to 1.0° diverged. As shown in the sketches of figures A8 and A9, the side-walls have provision for three large windows for flow field observations; smaller ports are located in the top, bottom, and side walls for lighting and viewing.

Remotely adjustable reentry flaps equal to 20-percent slot length are located at the downstream ends of the slots. The angle of these flaps can be varied to control test section flow gradients and to minimize power consumption. The range of flap angle adjustment is from 4° toward the flow to 15° away from the flow on the top and bottom walls and from 0° to 15° away from the flow on the side walls.

Model Support Section

The model support section, which is located immediately downstream of the test section, is rectangular in

cross section with corner fillets that are tapered in the streamwise direction. The side walls adjacent to the model support strut are indented to relieve strut blockage. The top and bottom walls in this section are attached to flexures at their downstream ends. The angle of inclination of these walls can be varied from 0° (walls parallel to tunnel centerline) to approximately 4.5° inward (leading edge toward flow). The vertical height offset between the top and bottom test section walls and the model support section walls is independently variable from an offset near zero to approximately 8 in. This vertical height offset can be varied as a function of wind tunnel flow conditions to accommodate varying reentry flow requirements and, thus, to minimize wind tunnel power consumption. Generally, test models are sting supported from a circular arc strut as shown in figure A9. The elevation sketch in figure A10 shows the NTF test section geometry variables including the geometry for the downstream choke.

High-Speed Diffuser

The high-speed diffuser shown in figure A11, is located immediately downstream of the model support section. It consists of two sections: a three-stage transition section and a conical section. The three stages of the transition section approximate the area distribution of a cone with a half-angle of approximately 2.6°, the same angle as the actual conical section. The transition cross-sectional shape progresses from a rectangular section with flat corner fillets to a fully round section in three stages of nearly equal length. The flat corner fillets are faired out within the first stage of the transition. Except for these fillets, the shapes in the transition section consist of flat panels joined at the corners of the cross section by quarter-round conical sections. The diffuser, which includes the model support section, has an overall area ratio of 2.92 to 1. As is the contraction, the high-speed diffuser is also a movable structure. It can be detached from the model support section and moved downstream within the pressure shell to permit deployment of the downstream isolation valve. (See fig. A9.)

Fan Drive System

The fan is located 29 ft downstream of turn 2. As shown in figure A12, the upstream fan nacelle fairing is bent through that corner. The single-stage fan has 25 fixed-pitch blades fabricated of fiberglass-reinforced plastic, and the fan load is changed by either the angle of the 24 variable inlet guide vanes (IGV) upstream of the fan or rotational speed. There are 26 fixed stators downstream.

Flat acoustic panels are located on the fan nacelle and the adjacent wind tunnel walls at the nose and tail cones of the nacelle. These panels are shown in figures A13(a) and A13(b) for the nose and tail cone of the nacelle, respectively. These panels are intended to attenuate the fan noise propagating upstream and downstream from the fan. As described by Lassiter (1981), the design uses a dual Helmholtz resonator concept and provides approximately 13-dB reduction of fan noise at the test section. The geometry of the two-layer perforated sheet honeycomb lining that forms the dual Helmholtz resonator acoustic panels is shown in figure A14.

The fan is powered by two variable-speed, wound-rotor induction motors and a synchronous motor with maximum power ratings of 66 000 hp (49.2 MW) and 60 000 hp (44.8 MW), respectively. As mentioned previously, the induction motors were salvaged from the 4-Foot Supersonic Pressure Tunnel that was originally located on the NTF site. As shown in the upper part of figure A15, the introduction motors are coupled to the fan driveshaft through a two-speed gear box with gear ratios (motor-to-fan speed) of 835:360 in low gear and 835:600 in high gear. The purpose of the two-speed gear box is to provide a better match of the available motor torque with the required fan torque at different operating temperatures. The synchronous motor is in line with the fan driveshaft and rotates at fan speed at all times.

The maximum shaft power available from the drive motor combination as a function of fan rotational speed is shown in the lower part of figure A15 for both the high- and low-gear ratios. The synchronous motor is operated at the fan shaft speed corresponding to the maximum speed of the induction motors in the low-gear ratio, and is brought up to synchronous speed by the induction motors. The rotational speed of the induction motors is controllable within ±0.25 percent over the entire range with a modified Kraemer drive control system.

Under high-power conditions, when both the induction and synchronous motors are required, the fan is rotated at the synchronous motor speed of 360 rpm (6 Hz), and wind tunnel speed control is accomplished by variation of the inlet guide vane angles. At low-power conditions when only the induction motor power is required, tunnel wind speed can be varied either by inlet guide vane angle variation or motor rotational speed variation.

Because cooling in the air mode of operation is accomplished with the water-cooled heat exchanger, the maximum usable power is limited by the design capacity of the heat exchanger cooling towers; this limit is approximately 55 000 hp (41 MW).

Exhaust System

When the NTF is operating in the cryogenic mode, liquid nitrogen is continuously introduced into the circuit to maintain temperature. To maintain pressure and constant mass flow, an equal amount of gaseous nitrogen must be removed from the circuit. As seen in figure A3, the exhaust ports are in the crossleg between turns 3 and 4; a sketch of the exhaust muffler and vent stack is shown in figure A16. The maximum flow rate of liquid nitrogen into the circuit is on the order of 9000 gpm or approximately 1000 lb/sec. The muffler and vent stack are sized to exhaust an equal mass flow rate of gaseous nitrogen. The exhaust system is also used to vent the tunnel pressure in either the air mode or nitrogen mode of operation.

Three layers: insulation, adhesive, and fiberglass

Aluminum liner

Epoxy-glass pultrusion rib and cap strip

Tab and link system

Shell

Pultrusion

Liner

Flow

Links

Shell
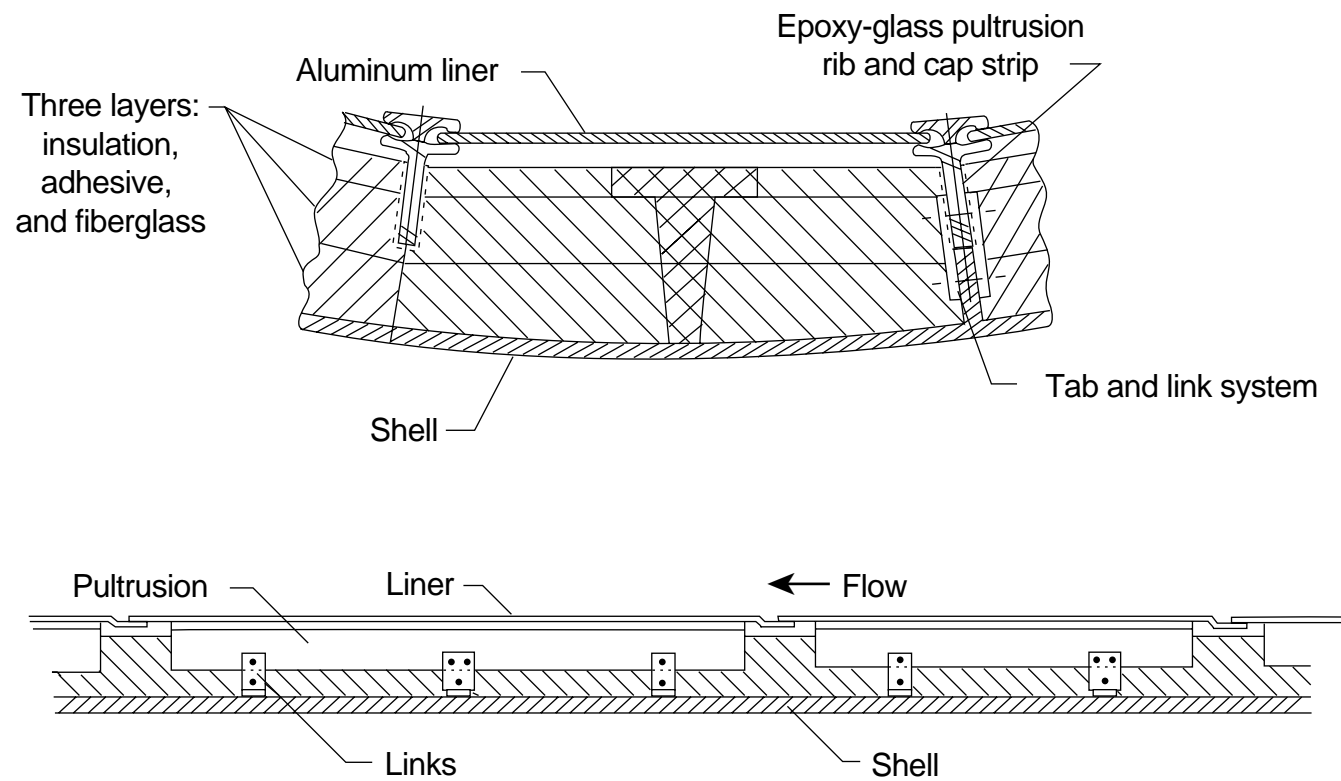
Figure A1. Thermal insulation and liner in NTF.

Figure A2. Return leg of the NTF circuit with aluminum liner plate flow surface.

Turning vanes
Screen support section
Downstream nacelle
Upstream and fan containment shroud
Downstream shroud
Upstream nacelle
GN$_2$ exhaust ports
Acoustic panels
LN$_2$ injectors
Truss support for heat exchanger
Heat exchanger
Test section windows
Model support
Wide-angle diffuser
Contraction section
Fixed contraction, test, and model support section
High-speed diffuser

Figure A3. Principal components of NTF circuit.
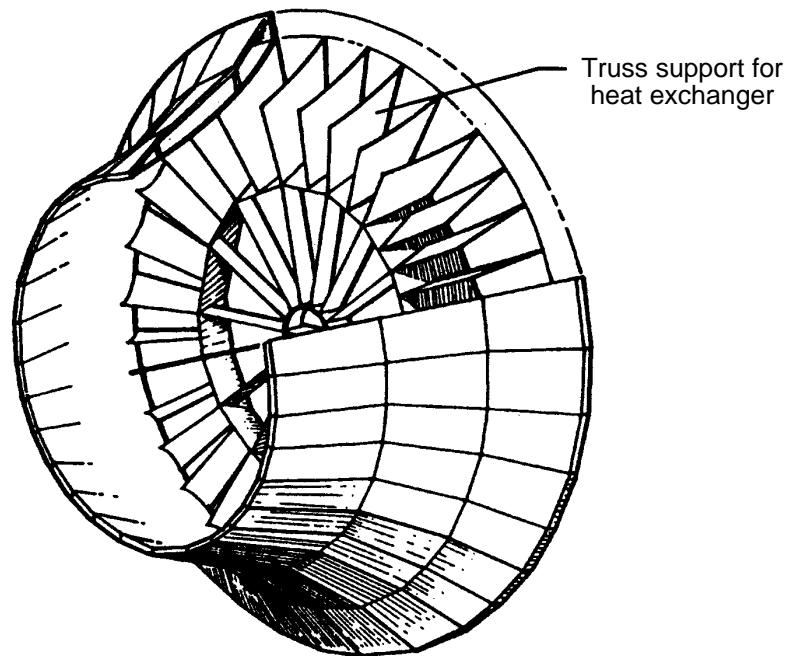
Figure A4. NTF wide-angle diffuser.
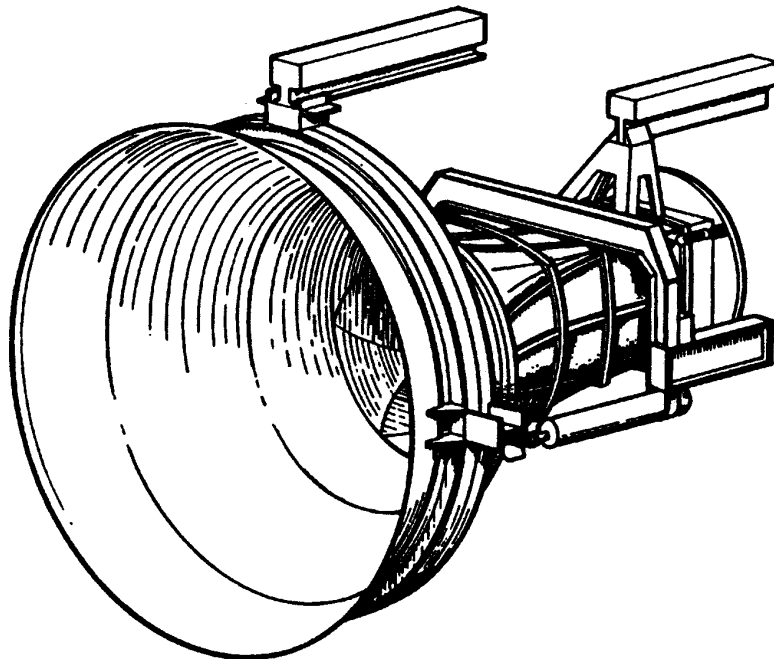
Figure A5. NTF contraction section.
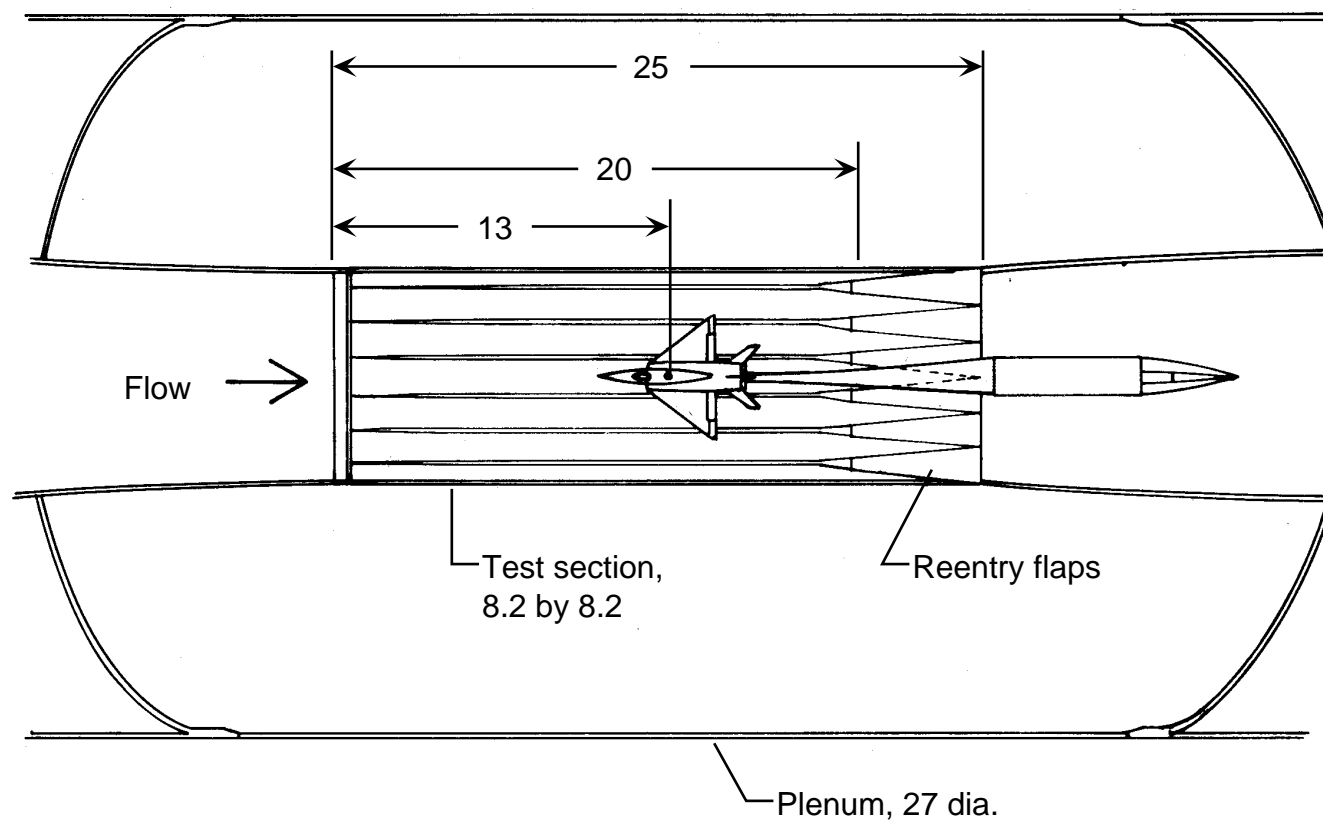
Figure A6. Plan view of NTF test section. All dimensions are in feet.
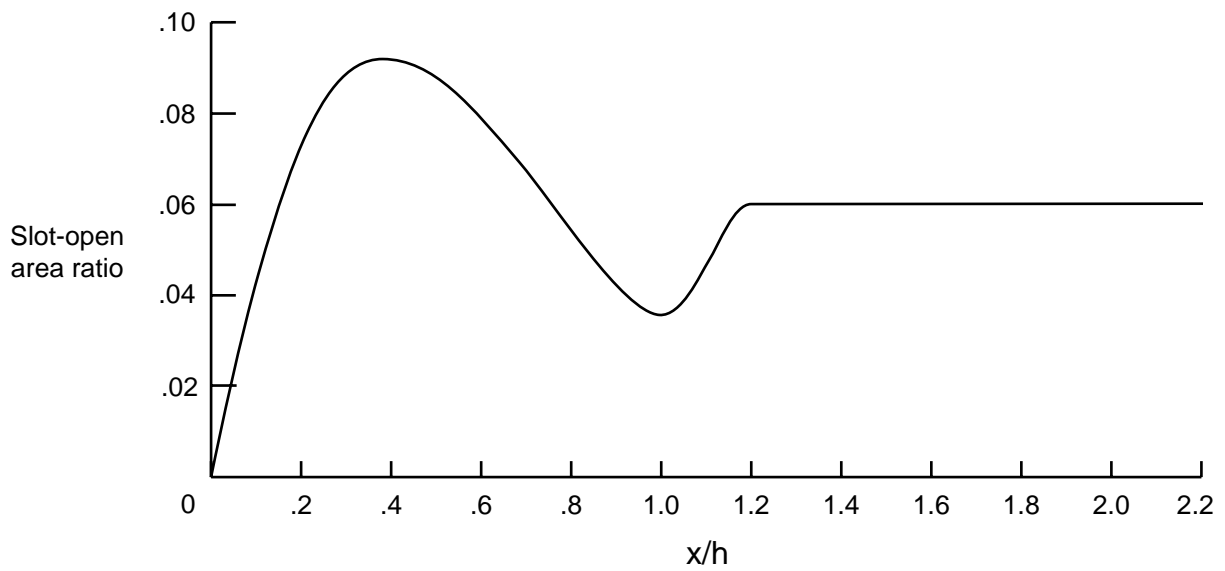
Figure A7. NTF slot shape for top and bottom walls.
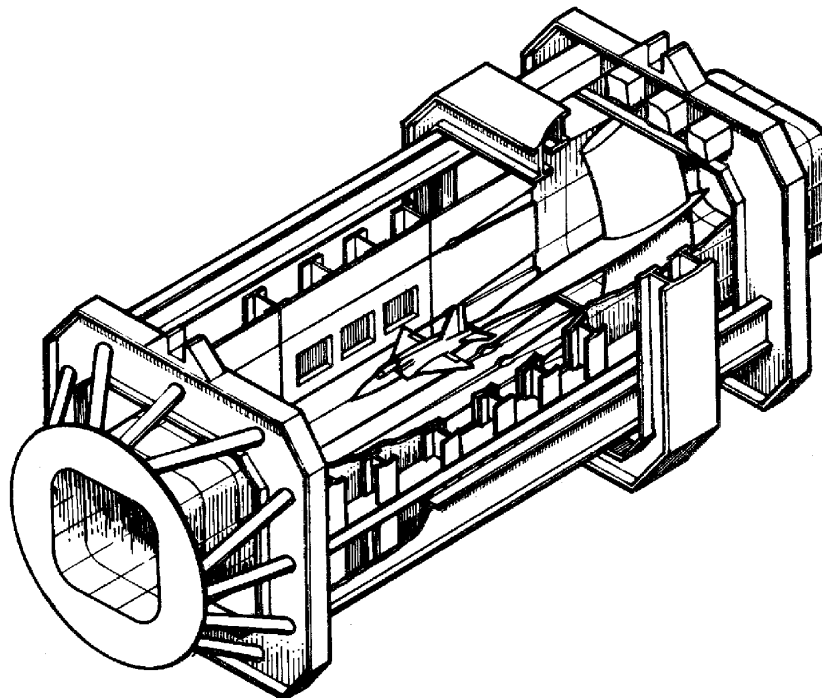
Figure A8. NTF test section.
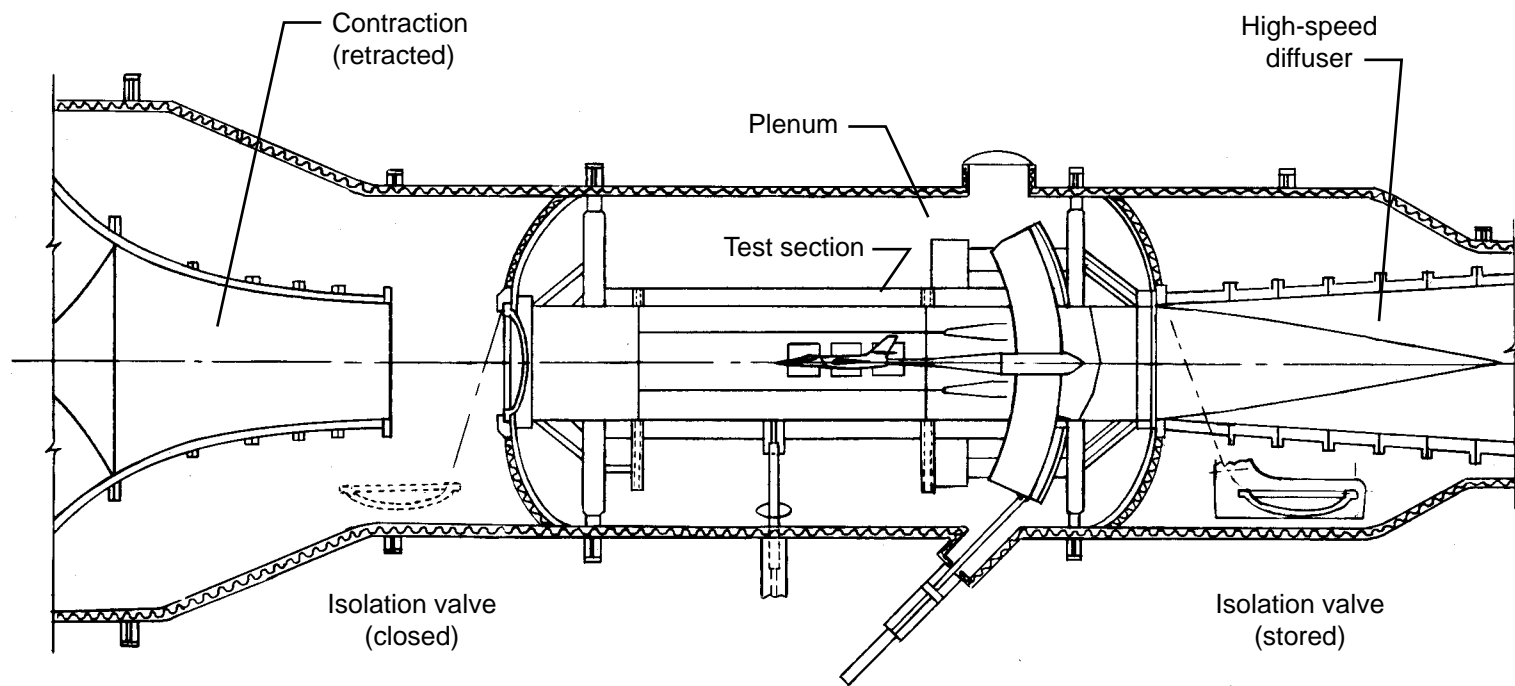
Figure A9. Elevation of NTF test section.

Tunnel
centerline

Model center
of pitch rotation
(station 13)

Flow

———— Choke off

– – – – Choke on

Choke station

Bottom test section wall
(slots open)

Flex plate

Contraction

Reentry
flap

Plenum

Flap
hinge line

Model support
section wall

Flex plate

| −5 | 0 | 5 | 10 | 15 | 20 | 25 | 30 | 35 |

Tunnel station, ft
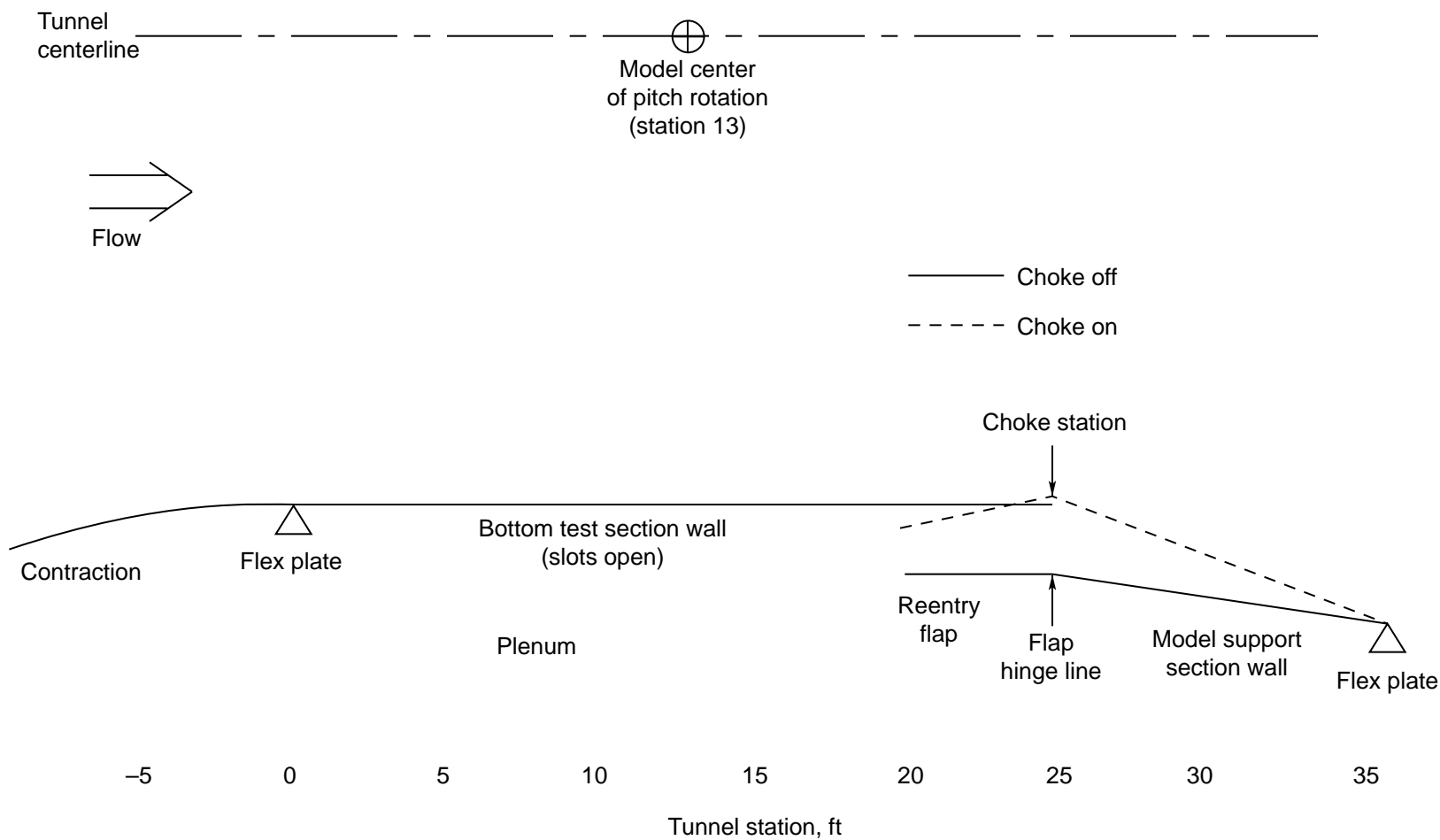
Figure A10. Elevation of NTF test section geometric variables (not to scale).
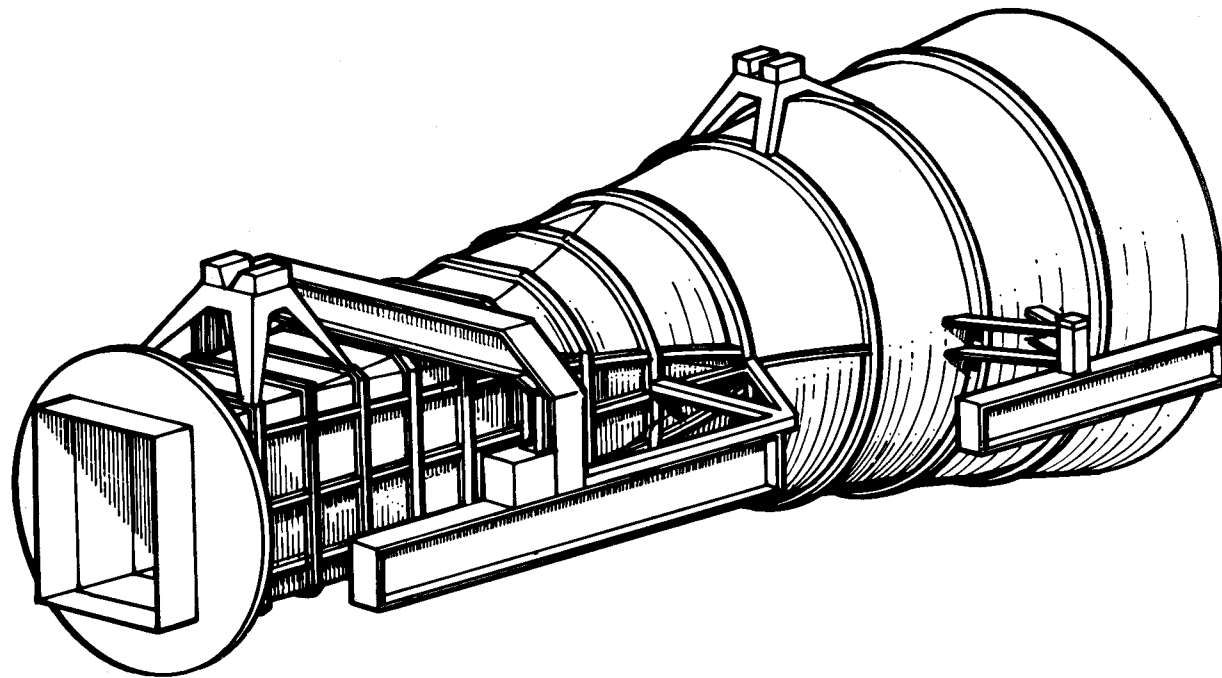
Figure A11. NTF high-speed diffuser.

Fan

Outlet stators

Inlet guide
vanes

Acoustic
liners

Shaft main
radial bearing

Guide vane
actuator ring

Acoustic liners

Flow
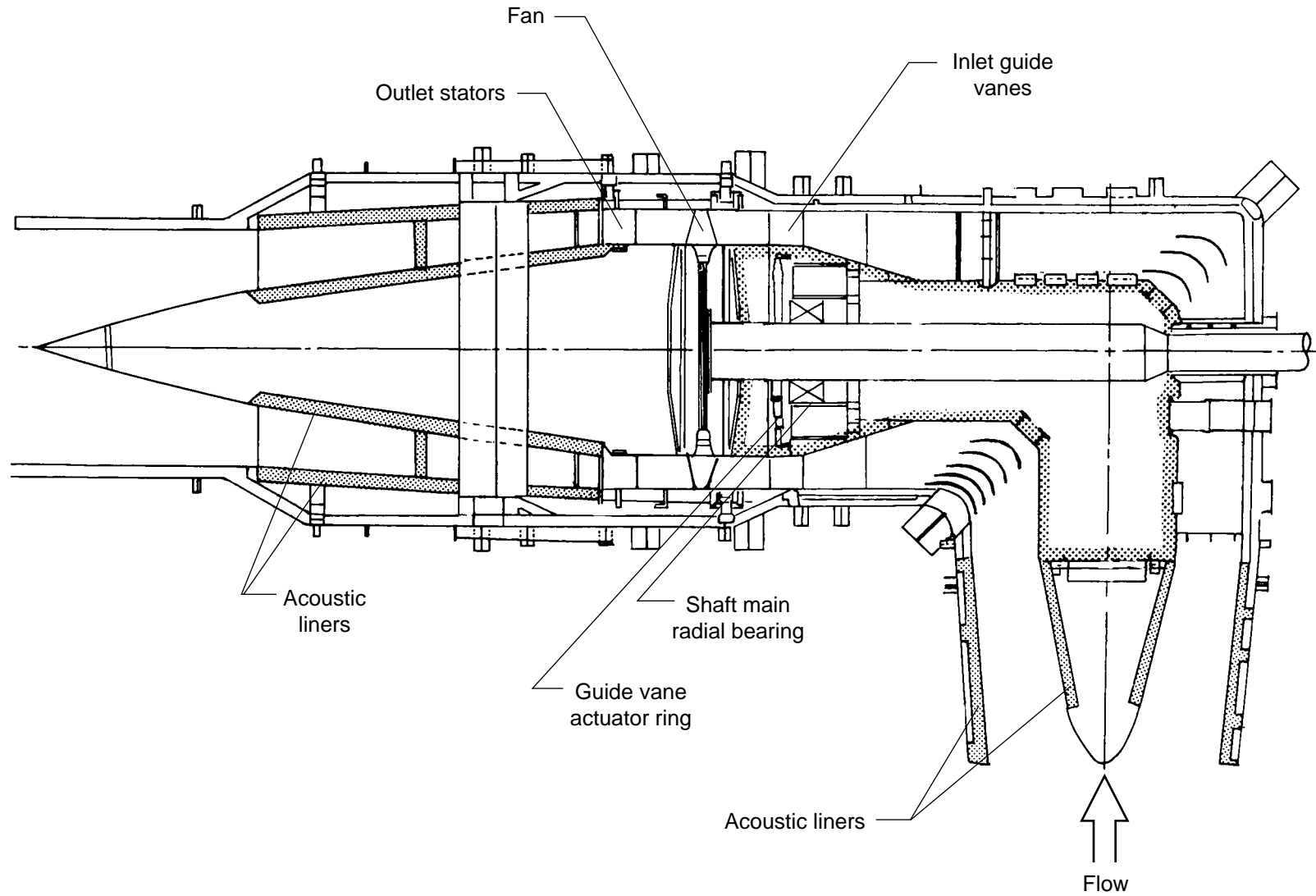
Figure A12. NTF fan section assembly.
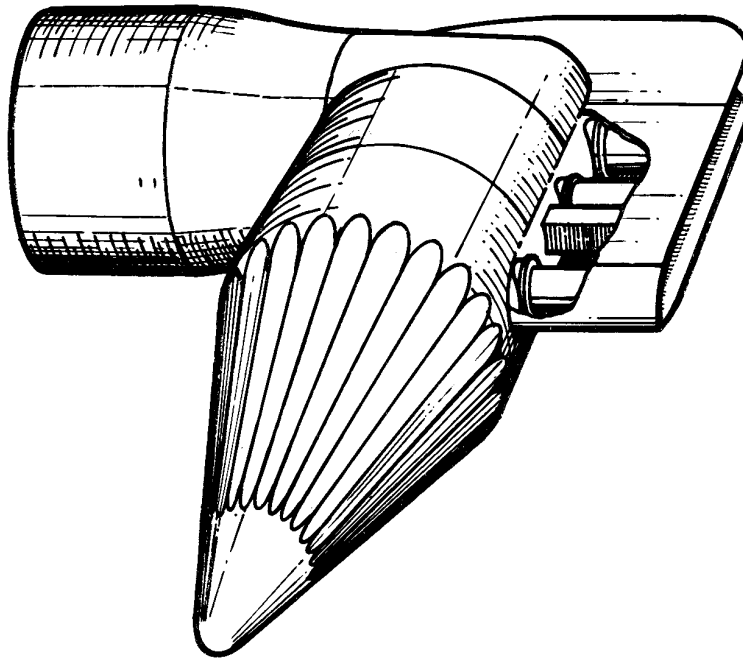
(a) Nacelle nose cone.
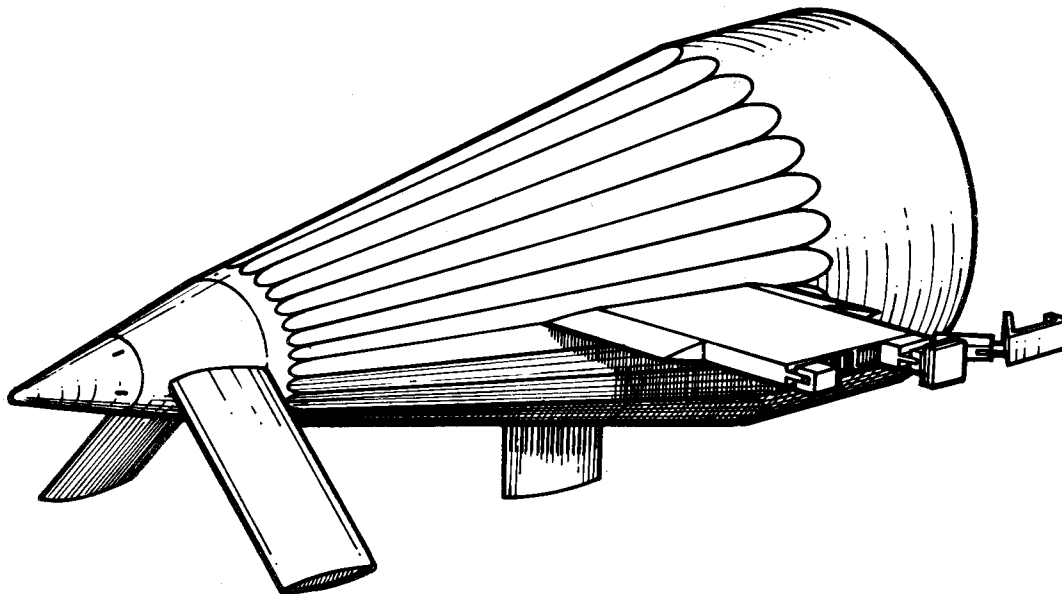
(b) Nacelle tail cone.

Figure A13. NTF nacelle fairings with artist's conception of flat acoustic liner panels.
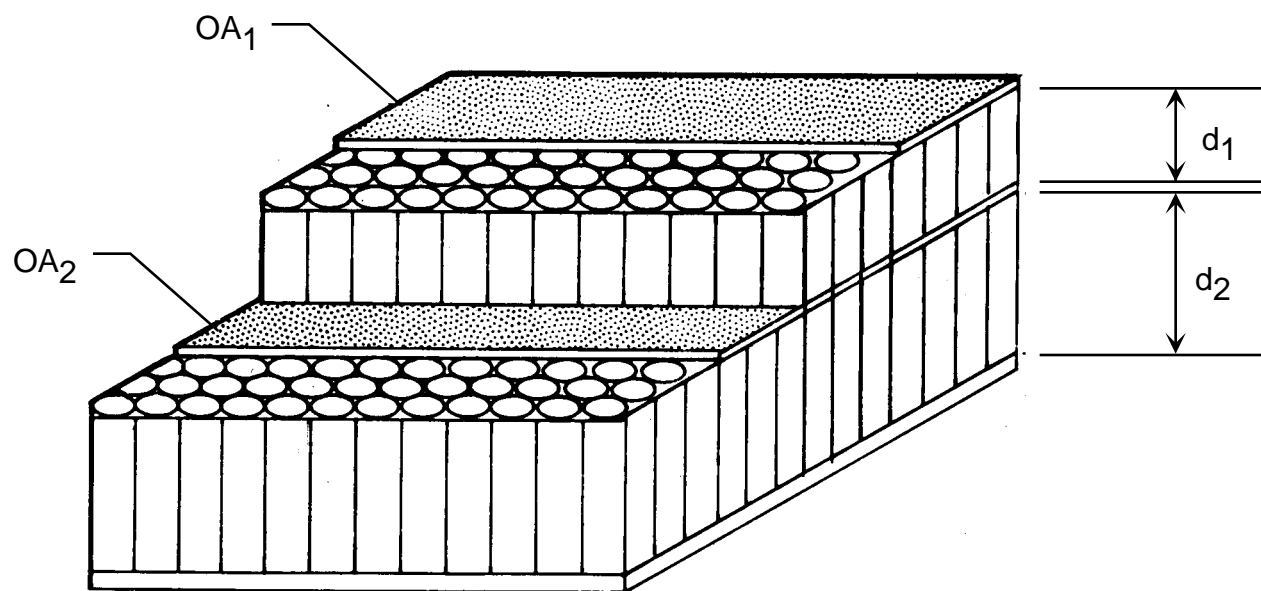
Nacelle cone	Open area—		Cavity depths—	
	OA_1, percent	OA_2, percent	d_1, in.	d_2, in.
Nose	5.5	4.5	1.3	4.6
Tail	5.5	4.5	2.5	7.5

Figure A14. NTF fan nacelle acoustic panel dual Helmholtz resonator concept.
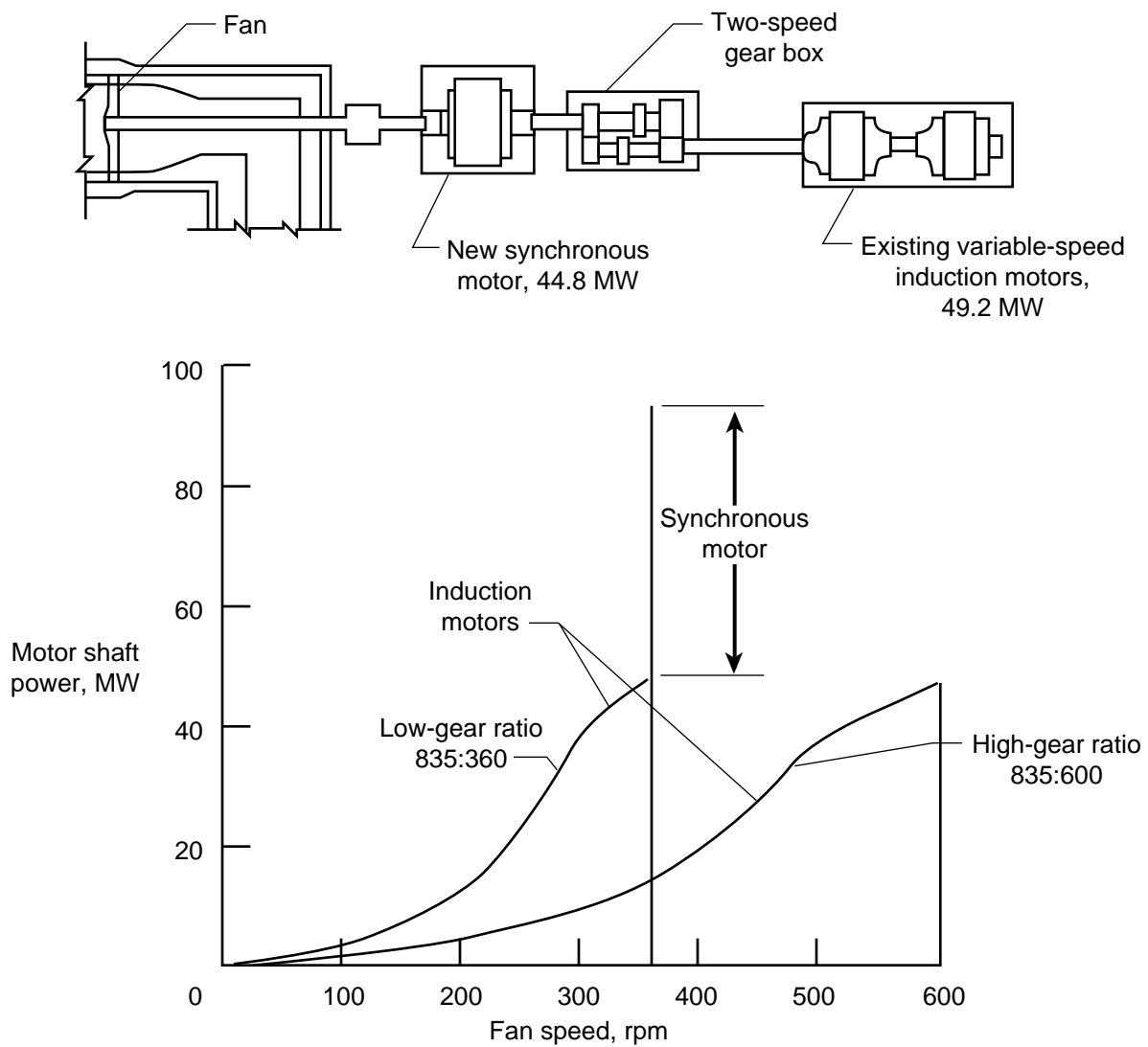
Figure A15. NTF fan drive system power 10-min. rating.
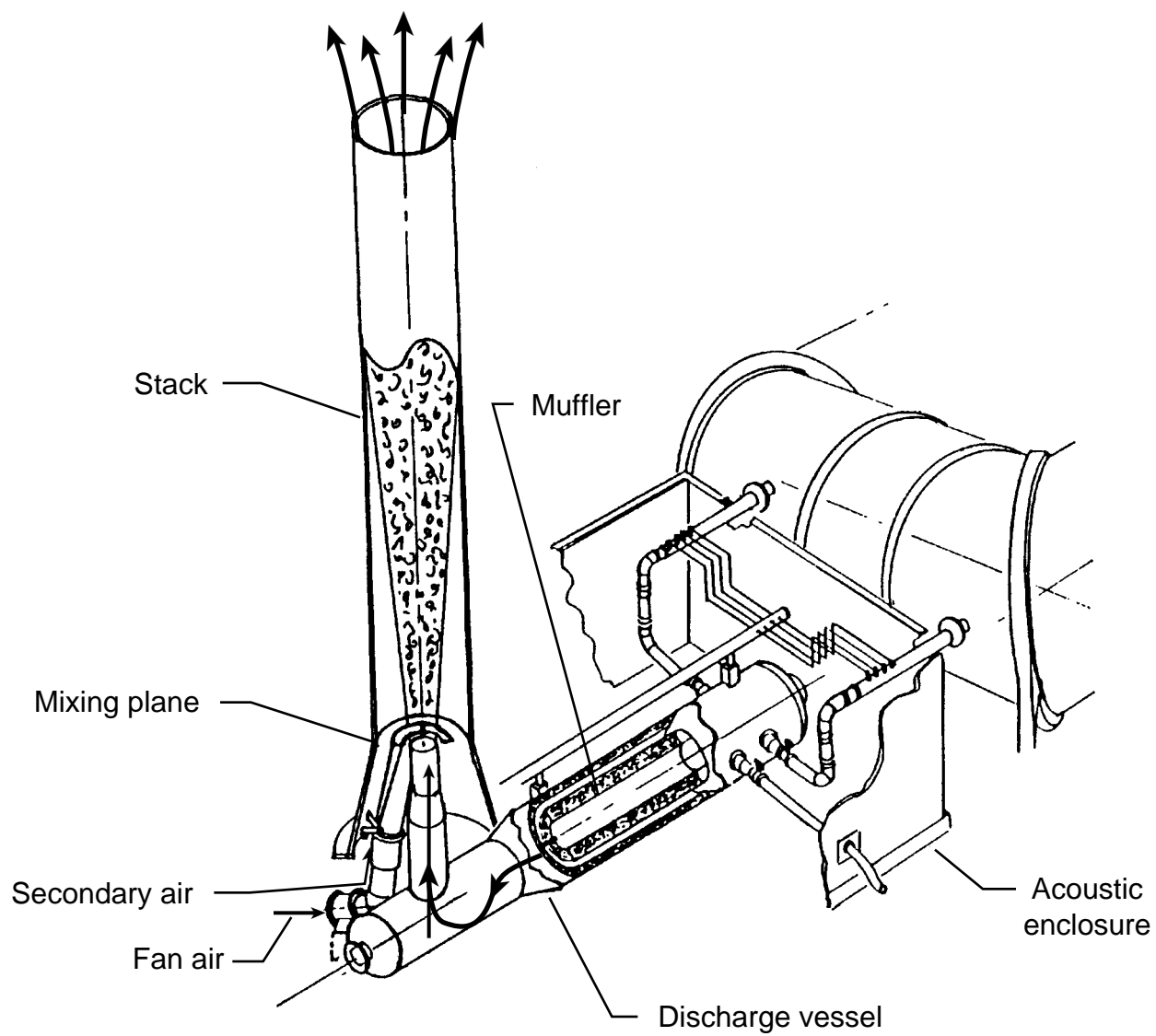
Figure A16. NTF exhaust muffler and vent stack.

Appendix B

Longitudinal Static Pressure and Mach Number Gradients

The longitudinal buoyancy force induced on a body by a static pressure gradient is

$$\Delta F_x = \int_0^l \frac{dp}{dx} A_x d_x \qquad (B1)$$

which, for a linear change in static pressure with longitudinal distance, simplifies to

$$\Delta F_x = \frac{dp}{dx} V \qquad (B2)$$

where the volume is

$$V = \int_0^l A_x d_x \qquad (B3)$$

A somewhat idealized cross-sectional area distribution of a representative transport aircraft model is shown in figure B1. A polynomial fit to the area distribution can be expressed as

$$\frac{A_x}{A_{max}} = \sum_{n=0}^{J} A_n \left(\frac{x}{l}\right)^n \qquad (B4)$$

For simplicity, the polynomial in equation (B4) is limited to its second order as shown in figure B1

$$\frac{A_x}{A_{max}} = 4\frac{x}{l}\left(1 - \frac{x}{l}\right) \qquad (B5)$$

Substitution of equation (B5) into equation (B3) results in the volume for the second-order polynomial fit

$$v = \frac{2}{3}lA_{max} \qquad (B6)$$

After substitution of this result into equation (B2), the longitudinal force is obtained from

$$\Delta F_x = \frac{2}{3}\frac{dp}{dx}lA_{max} \qquad (B7)$$

If a coefficient form is introduced into equation (B7), then

$$\Delta C_x = \frac{\Delta F_x}{qS} = \frac{2}{3}\frac{dp}{dx}\frac{l}{qS}A_{max} \qquad (B8)$$

and the various terms are nondimensionalized as

$$\Delta C_x = \frac{2}{3}\frac{1}{q/p_t}\frac{dp/p_t}{dx/h}\frac{l/h}{S/A_T}\frac{A_{max}}{A_T} \qquad (B9)$$

The following geometrical ratios, which relate the model size to the test section dimensions, can then be recognized:

1. $k_1 = \dfrac{A_{max}}{A_T}$, model blockage ratio

2. $k_2 = \dfrac{S}{A_T}$, wing area to test section area ratio

3. $k_3 = \dfrac{l}{h}$, model length to test section height ratio

Then

$$\Delta C_x = \frac{2}{3}\frac{1}{q/p_t}\frac{dp/p_t}{dx/h}\frac{k_1 k_3}{k_2} \qquad (B10)$$

To avoid significant test section wall interferences, the recommended maximum limits for these ratios are given as follows:

$$k_1 \le 0.005 \ (\text{Baals and Stokes (1971)})$$

$$k_2 \le 0.05 \ (\text{Monti (1971)})$$

$$k_3 \le 0.6 \ (\text{Baals and Stokes (1971)})$$

No firm criteria exist for what constitutes an acceptable pressure gradient. In reality, the pressure gradient is practically never exactly zero; even when it is quite small, higher order effects because of nonlinearity may assume some importance. One possible approach is to examine the magnitude of a gradient, which would cause an increment in drag coefficient of ±0.0001 (i.e., ±1 drag count in the terminology of wind tunnel experimentalists). The nondimensionalized pressure gradient is obtained from equation (B10) as

$$\frac{dp/p_t}{dx/h} = \frac{3}{2}\Delta C_x \frac{q}{p_t}\frac{k_2}{k_1 k_3} \qquad (B11)$$

and substitution of the previous values of ΔC_x, k_1, k_2, and k_3 results in

$$\frac{dp/p_t}{dx/h} = 0.0025 \frac{q}{p_t} \qquad (B12)$$

If perfect gas relations are assumed, q/p_t is solely a function of Mach number, and the nondimensional static pressure gradient can be plotted as shown in figure 15 where the allowable gradients under present assumptions are those that fall below the line. Perfect gas relations are adequate in this instance because the results are to be applied to air mode tests with the test section slots covered, the stagnation pressure near atmospheric, and the stagnation temperature near ambient.

Test section gradients are often expressed in terms of Mach number instead of static pressure. With the assumption of perfect gas relations and the ratio of

specific heats of 1.4, equation (B12) can be rewritten in terms of Mach number as

$$\frac{dM}{dx/h} = 0.00125M(1 + 0.2M^2) \qquad (B13)$$

and is shown plotted in figure 16. The question of accuracy of the measurement of the local static pressures that make up the pressure gradient and the effect of this accuracy on the computed magnitude of that gradient is addressed in appendix C.
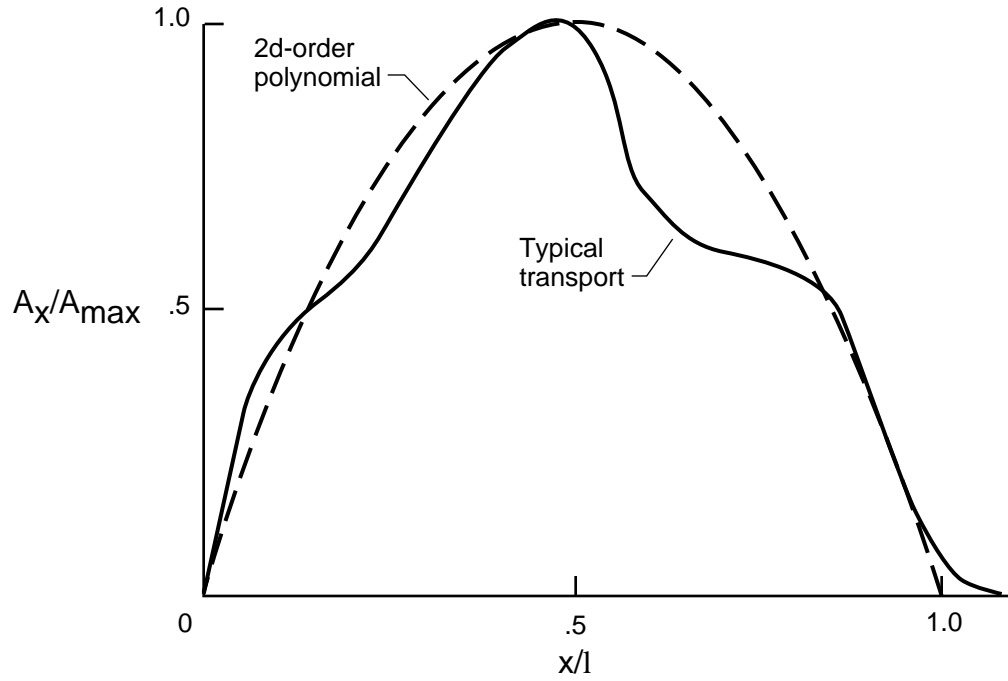
Figure B1. Cross-sectional area distribution for typical transport model.

Appendix C

Accuracy of Test Section Pressure Gradients by Least-Squares Method

The accuracy of individual pressure measurements required for least-squares slopes of a given accuracy will be evaluated here. First, the usual equations for a least-squares straight-line fit will be shown. In figure C1, the deviation between the ith data point and the least-squares straight line is

$$\delta_i = P_i - (ax_i + b) \tag{C1}$$

The sum of the squares of these deviations is to be minimized by

$$\delta^2 = \sum_{i=1}^{j} \delta_i^2 = \sum_{i=1}^{j} [P_i - (ax_i + b)]^2 = \text{min.} \tag{C2}$$

where the values of the slope a and the intercept b are to be chosen to obtain the minimization

$$\frac{\partial \delta^2}{\partial a} = -2\Sigma x_i[P_i - (ax_i + b)] = 0 \tag{C3}$$

$$\frac{\partial \delta^2}{\partial b} = -2\Sigma[P_i - (ax_i + b)] = 0 \tag{C4}$$

The summation is now understood to be on i from 1 to j.

$$\Sigma x_i P_i - a\Sigma x_i^2 - b\Sigma x_i = 0 \tag{C5}$$

$$\Sigma P_i - a\Sigma x_i - jb = 0 \tag{C6}$$

Equations (C5) and (C6) are solved simultaneously for a and b

$$a = \frac{j\Sigma x_i P_i - \Sigma x_i \Sigma P_i}{j\Sigma x_i^2 - (\Sigma x_i)^2} \tag{C7}$$

$$b = \frac{\Sigma x_i \Sigma x_i P_i - \Sigma x_i^2 \Sigma P_i}{(\Sigma x_i)^2 - j\Sigma x_i^2} \tag{C8}$$

Equations (C7) and (C8) are the standard equations to determine the slope and intercept for a least-squares straight-line fit to the data points P_i. A simplification is conveniently introduced here such that

$$\Sigma x_i = 0$$

which would be true, for instance, if the distribution of the points x_i were symmetrical about $x = 0$. In the present case, the simplification is justified because the origin for the x_i coordinates is at the midpoint of the distribution and the value of the intercept is to be used as the Mach number at the midpoint. With this simplification equations (C7) and (C8) become

$$a = \frac{\Sigma x_i P_i}{\Sigma x_i^2} \tag{C9}$$

$$b = \frac{1}{j}\Sigma P_i \tag{C10}$$

In equation (C9), note that the influence of a particular data point P_i depends on its position x_i in the distribution and on the total number of points.

Now, errors ε_i are introduced in the data points P_i such that

$$P_i = p_i + \varepsilon_i \tag{C11}$$

then

$$a + \Delta a = \frac{\Sigma x_i(p_i + \varepsilon_i)}{\Sigma x_i^2} = \frac{\Sigma x_i p_i}{\Sigma x_i^2} + \frac{\Sigma x_i \varepsilon_i}{\Sigma x_i^2} \tag{C12}$$

where the first term on the right may be associated with the true value of a and the second term with the error. A root-sum-square (rss) version of this latter term is

$$\Delta a_{\text{rss}} = \frac{\left[\Sigma(x_i \varepsilon_i)^2\right]^{1/2}}{\Sigma x_i^2} \tag{C13}$$

For the National Transonic Facility (NTF) steady-state calibration, the error in pressure measurement was

$$\varepsilon_i = \pm 0.003 p_{\text{max}}$$

then

$$\Delta a_{\text{rss}} = \frac{0.003 p_{\text{max}}}{(\Sigma x_i^2)^{1/2}} \tag{C14}$$

Also, for the distribution of static pressure orifices in the NTF centerline calibration tube, 25 orifices were spaced 3 in. apart in a length of 6 ft centered on test section station 13, so

$$\frac{1}{h}\left(\Sigma x_i^2\right)^{1/2} = 1.099$$

and

$$\left(\frac{dp/p_t}{dx/h}\right)_{\text{error}} = \frac{0.003}{1.099}\frac{p_{\text{max}}}{p_t} \tag{C15}$$

45

The electronically scanned pressure (ESP) unit used for the steady-state calibration had a maximum pressure range of ±2.5 psi; if a worst case (lowest) value of total pressure is taken as 15 psi, then the static pressure gradient error term becomes

$$\left(\frac{dp/p_t}{dx/h}\right)_{\text{error}} = 0.000455 \tag{C16}$$

The gradient error can be expressed in terms of Mach number again with the assumption of perfect gas relations and the ratio of specific heats of 1.4 to get

$$\left(\frac{dM}{dx/h}\right)_{\text{error}} = 0.000325\frac{\left(1 + 0.2M^2\right)^{9/2}}{M} \tag{C17}$$

During the dynamic investigation with the slots covered, the longitudinal static pressure gradient was determined by a distribution of 13 test section wall static pressure orifices in a length of 7.5 ft centered on test section station 13. In this case

$$\frac{1}{h}\left(\Sigma x_i^2\right)^{1/2} = 0.892$$

and because the same ESP unit for pressure measurement was used, the pressure gradient error term equivalent to equation (C16) becomes

$$\left(\frac{dp/p_t}{dx/h}\right)_{\text{error}} = 0.00056 \tag{C18}$$

The Mach number gradient error term then increases to

$$\left(\frac{dM}{dx/h}\right)_{\text{error}} = 0.00040\frac{\left(1 + 0.2M^2\right)^{9/2}}{M} \tag{C19}$$

This indicates that the accuracy of the determination of test section longitudinal gradients for the configuration with the slots covered was slightly degraded compared with that for the steady-state calibration. Equations (C16) and (C18) and equations (C17) and (C19) are included in figures 15 and 16, respectively, for reference.
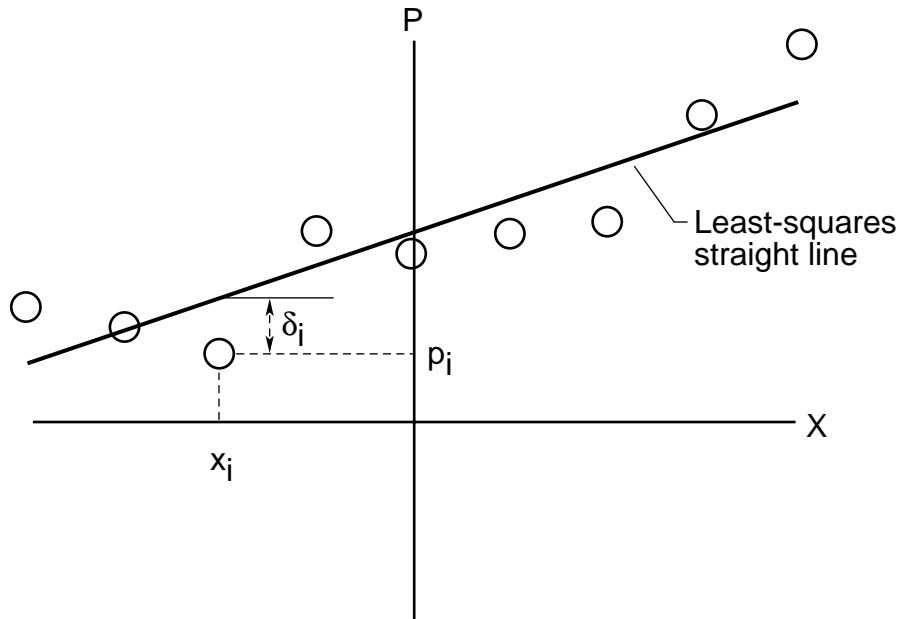
Figure C1. Least-squares straight-line fit to points P_1, ..., P_n.

Appendix D

Preliminary Test Results With Steady-State Calibration Probe Installed in Test Section

As mentioned in section 3.3 on nitrogen mode tests prior to the start of the present dynamic investigation and while the steady-state calibration investigation was being planned, simultaneous testing for both the steady-state and the dynamic characteristics of the tunnel was considered possible as an efficient use of the tunnel test time and of liquid nitrogen resources if the requirements for both sets of measurements could be satisfied concurrently. For steady-state calibration purposes, a long slender survey probe containing several hundred static pressure orifices was installed on the tunnel centerline; the probe stretched the entire length of the test section and extended well upstream into the contraction where it was secured with support cables as shown in figure D1. At the downstream end, the survey probe was mounted in the arc-sector centerbody, and the junction was aerodynamically faired with the same fiberglass-reinforced plastic conical fairing as was used for this investigation.

Fluctuating static pressure data were taken at some of the test conditions covered in the steady-state calibration. The test points for the power spectra shown in figure D2 are for test conditions near the maximum Reynolds number boundary in the nitrogen mode (105 psi $< p_t <$ 125 psi and $T_t = -250°$F). The data are for the test section RHS sidewall at station 13. A large peak exists in the unfiltered power spectra and ranges in frequency from $\approx$1.5 kHz at $M = 0.2$ to $\approx$5.2 kHz at $M = 1.0$.

To help identify the source of this peak, observe that the peak frequency changes with Mach number and therefore with velocity, which indicates that the source is likely aerodynamic. Further, observe that the source is not choked off at $M = 1.0$, which indicates that the source is not downstream of the test section. With these readily obvious clues, the probe upstream support cables would be a reasonable suspect. To substantiate this suspicion, the vortex-shedding frequency of the cables was estimated by assuming a Strouhal number of 0.2 and is shown as a function of test section Mach number in figure D3 for test conditions corresponding to the ambient temperature, low-pressure air mode tests. The frequencies of the peaks in the power spectra at these same test conditions are also shown for comparison, which indicate a reasonable probability that support cable vortex shedding is the source.

To determine the magnitude of the added disturbance, a notch or band-reject filter consisting of a combination of low-pass and high-pass filters was used to filter the suspect peak. Filtered results were obtained for all of the power spectra and are shown by the dashed lines in figure D2. The integrated rms fluctuating pressure coefficients for these power spectra are shown in figure D4. The large reduction due to filtering (as much as 25 percent at $M = 0.5$ and 0.6) indicates the importance of obtaining dynamic data with all extraneous interferences removed. These preliminary results led to the decision to obtain dynamic data under dedicated conditions with the test section empty. The actual empty test section disturbance levels were even lower than those indicated by the filtered data.
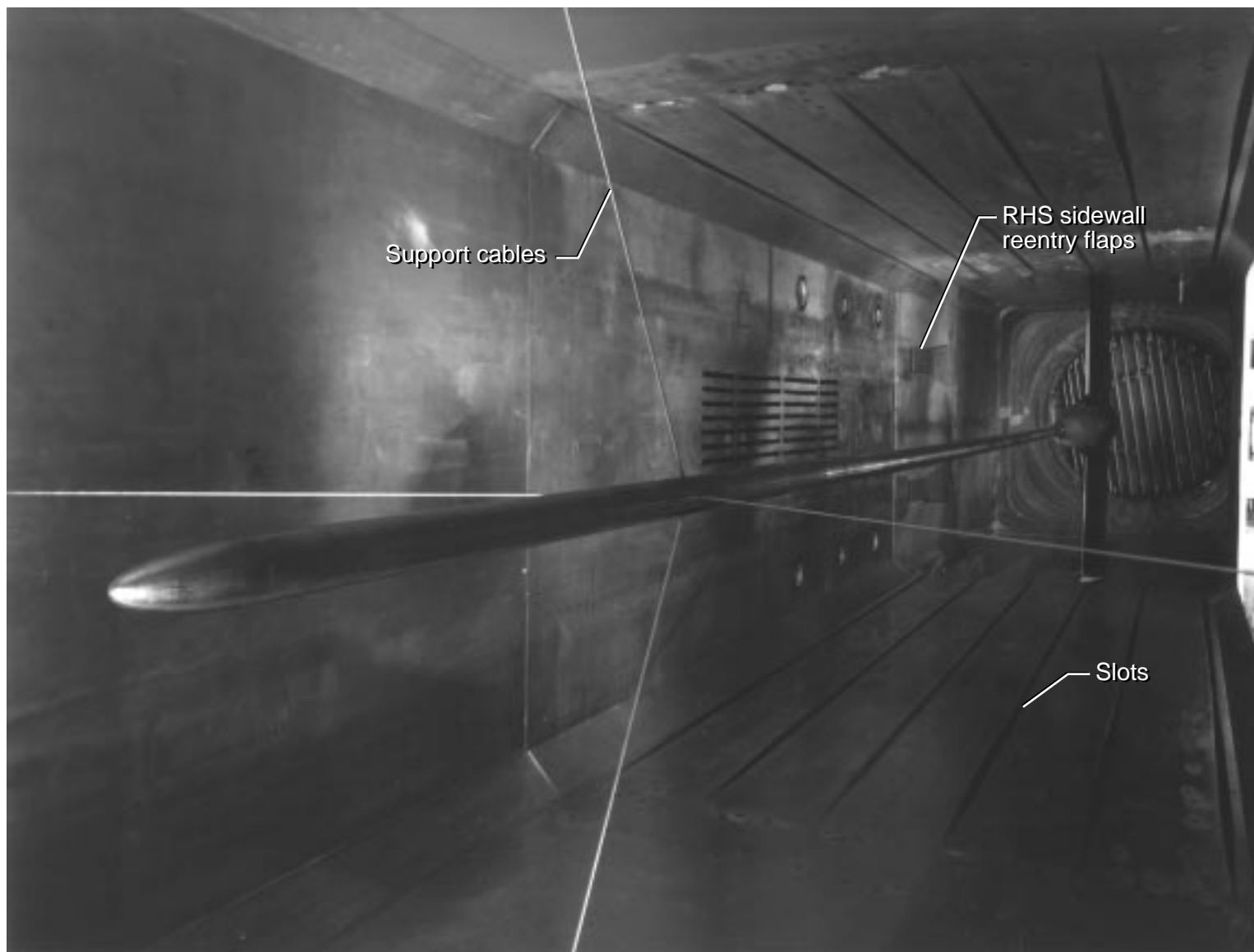
L-90-3430

Figure D1. Centerline calibration probe with support cables in NTF test section.
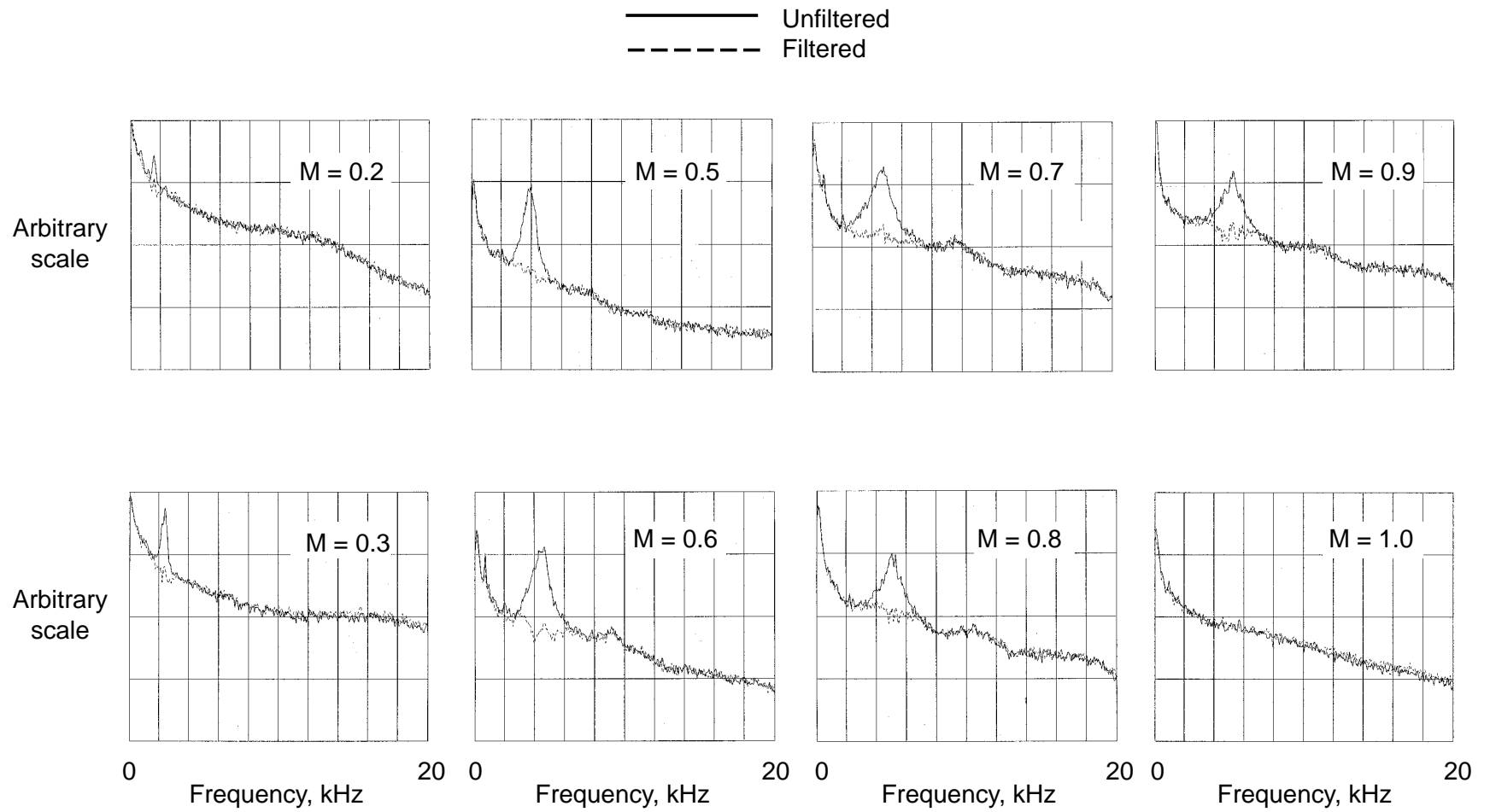
Figure D2. Power spectra obtained with centerline calibration probe in test section; test section RHS sidewall at station 13; 105 psi $< p_t <$ 125 psi; $T_t = -250°$F.
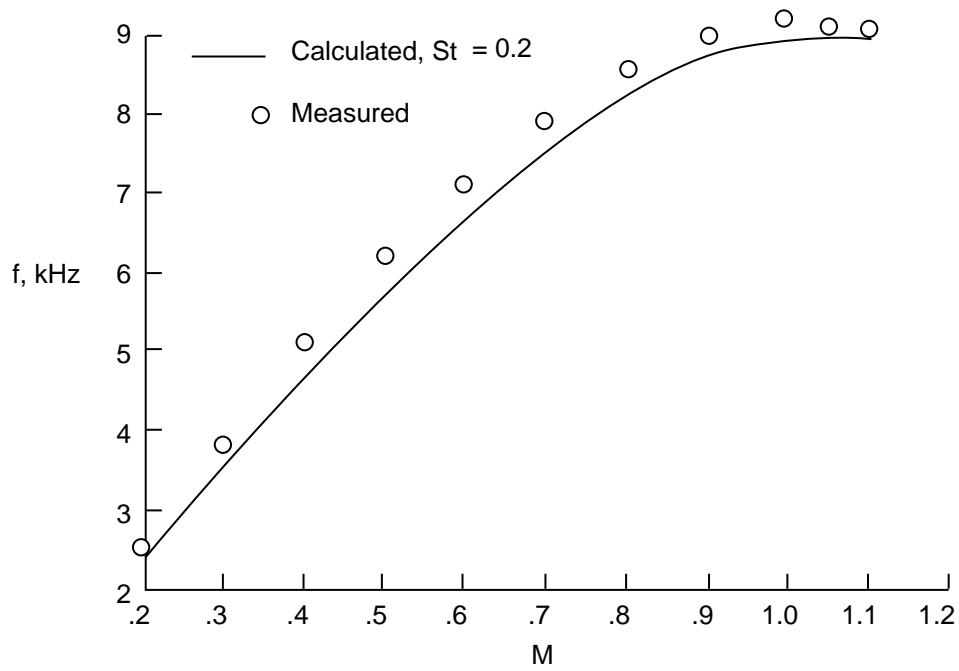
Figure D3. Calculated and measured vortex-shedding frequencies of centerline probe cables. $p_t = 17$ psi; $T_t = 120°F$; air mode.
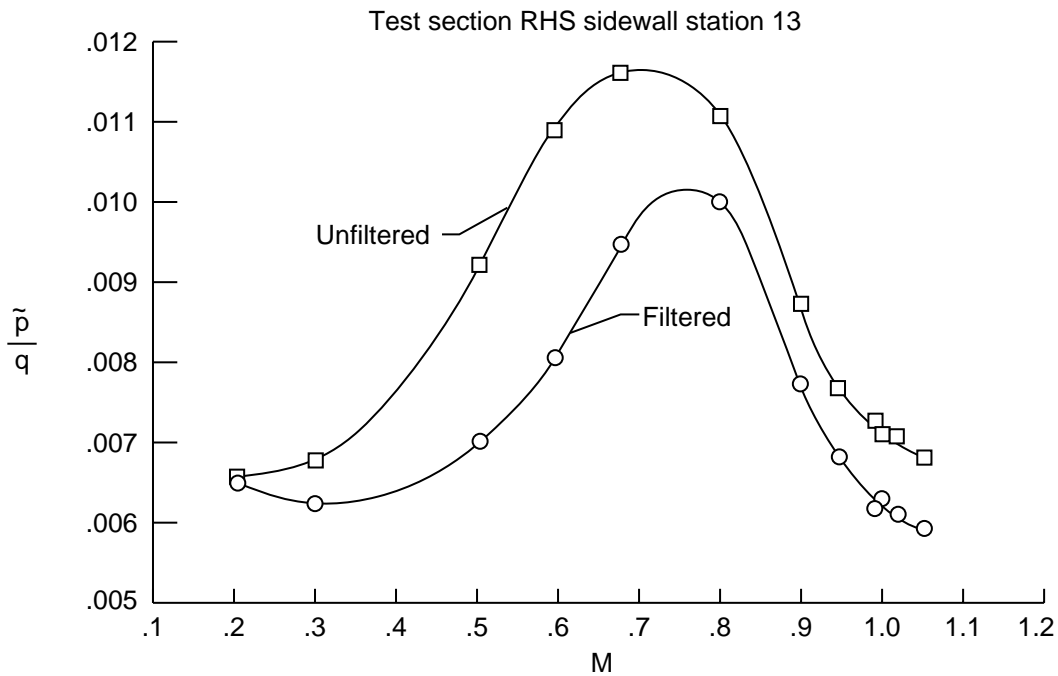
Figure D4. Effect of filtering centerline calibration probe support cable vortex-shedding frequency on fluctuating pressure coefficient.

Appendix E

Estimation of Edge Tone Frequency in Free-Shear Layer

The subject of edge tones has been extensively studied as indicated, for example, by the survey paper on jet-wedge edge tones by Karamcheti et al. (1969) and by the introductory paper on free-shear layer edge tones by Hussain and Zaman (1978). The purpose here is not to analyze the edge tone generation characteristics of free-shear layers but rather to investigate the plausibility that edge tones occur in the National Transonic Facility (NTF) test section. Attention is concentrated on aerodynamic gaps that exist at the downstream end of the test section wall surface. These gaps are on the test section sidewall immediately upstream of the leading edges of the sidewall reentry flaps and are visible in figure 43.

A sketch of the gap profile is shown in figure E1. The upstream lip is considered to act as the point of separation of the wall boundary layer to form a free-shear layer between the lip and the downstream wedge, which is formed by the leading edge of the sidewall reentry flap. As shown in the sketch, a vortex is considered to be periodically shed from the lip, to travel downstream in the free-shear layer, and to impact on the wedge, which creates an edge tone; an acoustic feedback signal is assumed to travel through the quiescent region on the plenum side of the free-shear layer and sustain the tone.

This tone phenomenon appears similar to what is encountered in open cavities. An expression for the frequency of periodic disturbances found with open cavities was given by Rossiter (1964) as

$$f \; = \; \frac{V}{L} \, \frac{m - \gamma}{V/u_c + M} \tag{E1}$$

where m is the stage number for the periodic disturbance, and γ is a factor for the lag between the interaction of the vortex with the downstream edge and the emittance of the associated acoustic feedback disturbance. Equation (E1) can be rewritten as

$$f \; = \; \frac{m - \gamma}{(L/u_c) + (L/c)} \tag{E2}$$

The denominator in equation (E2) can be recognized as the sum of the time required for the shed vortex to travel the length of the gap L downstream at a convection velocity u_c in the free-shear layer and the time for an acoustic disturbance emitted by the interaction of the vortex with the downstream edge to travel back to the lip at an acoustic velocity c through the quiescent region.

The acoustic velocity in equation (E2) has been assumed to be equal to the free-stream speed of sound. Heller, Holmes, and Covert (1971) have shown that better agreement between predicted and measured frequencies for cavities is obtained if the stagnation speed of sound is used. This modified form of the Rossiter (1964) equation is then written as

$$f \; = \; \frac{m - \gamma}{(L/u_c) + (L/c_t)} \tag{E3}$$

or in reduced frequency form as

$$\frac{fL}{V} \; = \; \frac{m - \gamma}{(V/u_c) + (V/c_t)} \tag{E4}$$

The value for the convection velocity ratio u_c/V used by Rossiter was 0.57. The lag factor γ has been shown by Rossiter to be a function of the length-to-depth ratio of the cavity and diminishes nearly linearly from a value of 0.54 at a length-to-depth ratio of 8:1 to a value of 0.25 at a length-to-depth ratio of 4:1. The gap profile of figure E1 is considered to represent an open cavity with a length-to-depth ratio approaching zero because the plenum wall is on the order of 9.0 ft from the test section sidewall.

Reduced frequencies calculated from equation (E4) for the test conditions of figures 27 and 35 are shown in table E1 and figure E2. For these calculations, the convection velocity ratio u_c/V was assumed as 0.6 (which is appropriate for a free-shear layer) the lag factor γ was taken as 0, and the velocity V was taken as the free-stream velocity in the test section.

The measured frequency results (lower at the low Reynolds numbers and higher at the high Reynolds numbers) are listed in table E1 and shown in figure E2 to bracket the calculated values. The agreement is considered good enough to support the possibility that the measured frequency peaks are caused by free-shear layer edge tones, which are generated at the gap upstream of the sidewall reentry flaps under certain flow conditions and are detectable in the test section.

Table E1. Free-Shear Layer Edge Tone Frequency Data

							fL/V—	
Gas type	M	R, ft^{-1}	V, fps	c_t, fps	T_t, °F	f, measured, Hz	measured	calculated
Air	0.695	6.0×10^6	764	1151	91.4	840	0.36	0.43
Nitrogen	.695	6.0	777	1172	92.2	855	.36	.43
Nitrogen	.598	39.9	481	834	−174.0	890	.60	.45
Nitrogen	.694	39.9	519	784	−206.2	860	.54	.43
Nitrogen	.742	39.8	538	764	−218.6	900	.54	.42
Nitrogen	.793	39.8	558	747	−228.7	960	.56	.41
Nitrogen	.839	39.8	576	734	−236.2	(1410)[a]	(.80)[a]	(.82)[a]
Nitrogen	.892	39.9	601	725	−241.4	960	.52	.40
Nitrogen	.992	40.1	644	710	−250.2	960	.48	.39

[a]Quantities in parentheses are possible second-stage frequencies.
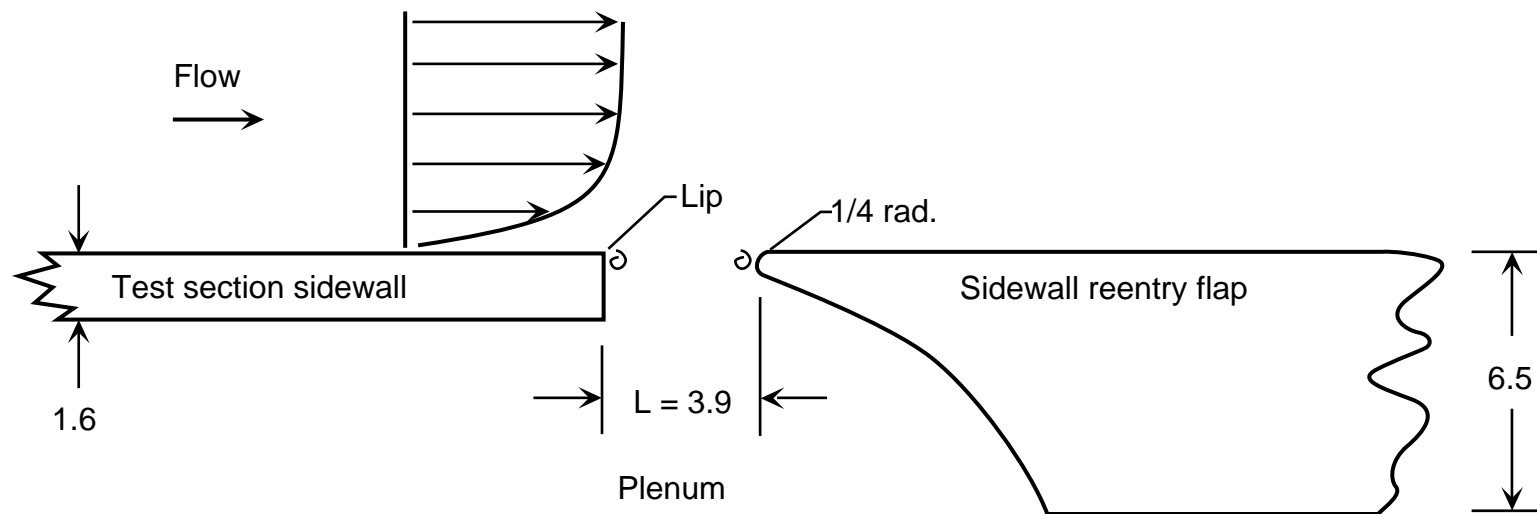
Figure E1. Gap profile between NTF test section sidewall and reentry flap. All dimensions are in inches.
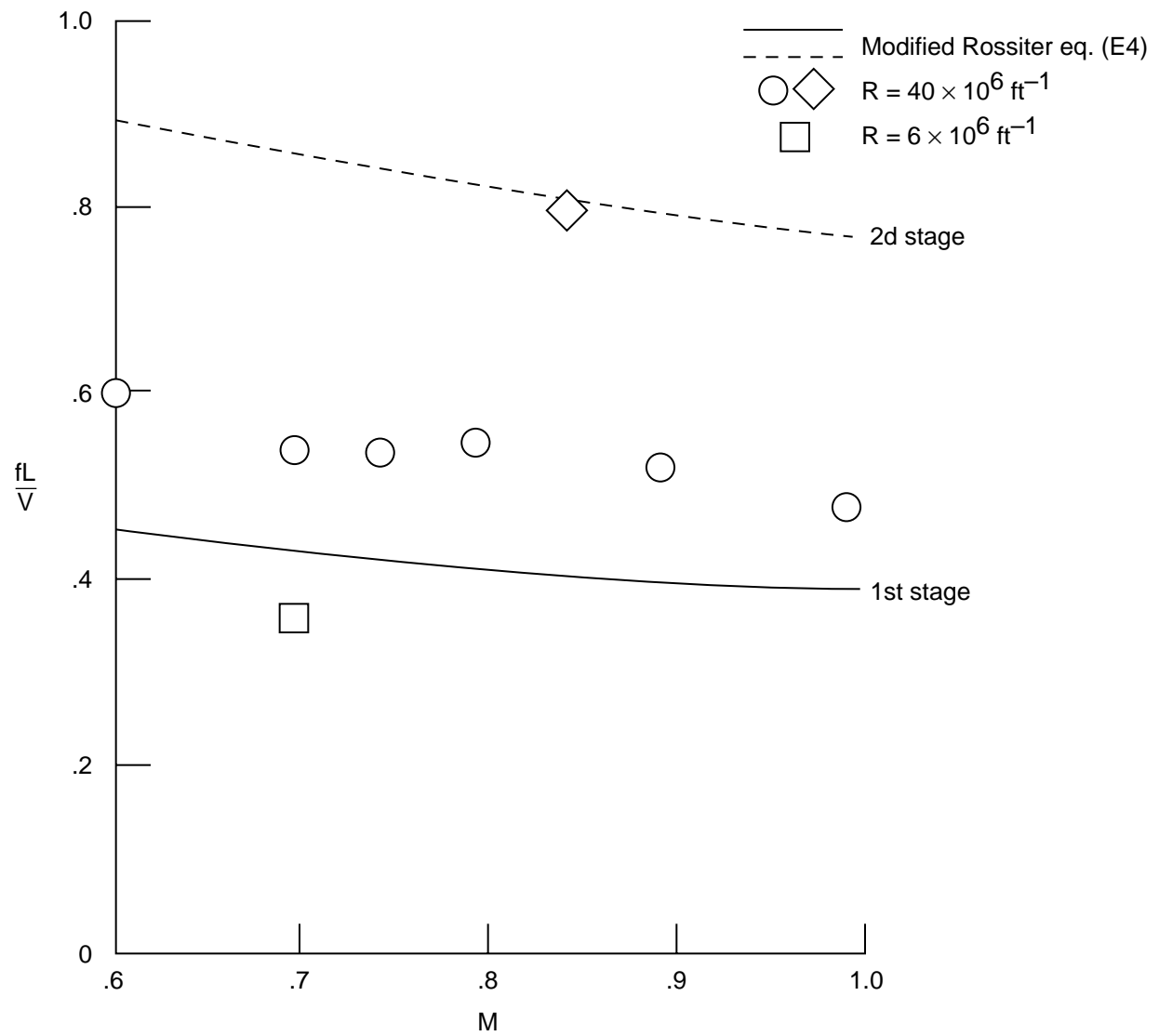
Figure E2. Comparison of measurement-reduced frequencies with free-shear layer edge tone-reduced frequencies calculated from the modified Rossiter equation.

References

Adcock, Jerry B. 1977: *Effect of LN₂ Injection Station Location on the Drive Fan Power and LN₂ Requirements of a Cryogenic Wind Tunnel.* NASA TM X-74036.

Adcock, Jerry B. 1976: *Real-Gas Effects Associated With One-Dimensional Transonic Flow of Cryogenic Nitrogen.* NASA TN D-8274.

Adcock, Jerry B.; and Johnson, Charles B. 1980: *A Theoretical Analysis of Simulated Transonic Boundary Layers in Cryogenic-Nitrogen Wind Tunnels.* NASA TP-1631.

Baals, Donald D.; and Stokes, George M. 1971: A Facility Concept for High Reynolds Number Testing at Transonic Speeds. *Facilities and Techniques for Aerodynamic Testing at Transonic Speeds and High Reynolds Number*, AGARD CP No. 83, pp. 28-1–28-12.

Barger, Raymond L. 1973: *Streamline Curvature Design Procedure for Subsonic and Transonic Ducts.* NASA TN D-7368.

Barger, Raymond L. 1981: *Theory for Predicting Boundary Impedance and Resonance Frequencies of Slotted-Wall Wind Tunnels, Including Plenum Effects.* NASA TP-1880.

Bendat, Julius S.; and Piersol, Allan G. 1980: *Engineering Applications of Correlation and Spectral Analysis.* John Wiley & Sons, Inc.

Bobbitt, Percy J. 1981: Report of the Panel on Fluid Dynamics. *High Reynolds Number Research—1980*, L. Wayne McKinney and Donald D. Baals, eds., NASA CP-2183, pp. 169–195.

Boyles, George B., Jr. 1986: Description and Operational Status of the National Transonic Facility Computer Complex. AIAA-86-0383.

Braslow, Albert L.; Hicks, Raymond M.; and Harris, Roy V., Jr. 1966: *Use of Grit-Type Boundary-Layer-Transition Trips on Wind-Tunnel Models.* NASA TN D-3579.

Braslow, Albert L.; and Knox, Eugene C. 1958: *Simplified Method for Determination of Critical Height of Distributed Roughness Particles for Boundary-Layer Transition at Mach Numbers From 0 to 5.* NACA TN-4363.

Bruce, Walter E., Jr. 1985: The U.S. National Transonic Facility—II. *Special Course on Cryogenic Technology for Wind Tunnel Testing*, AGARD-R-722, pp. 15-1–15-10.

Chiu, Wen-Shyang; and Lauchle, Gerald C. 1989: Subsonic Axial Flow Fan Noise and Inflow Velocity Disturbance. *Inter-Noise 89—Engineering for Environmental Noise Control, Proceedings of the 1989 International Conference on Noise Control Engineering*, George C. Maling, Jr., ed., Volume 1, pp. 133–138.

Coe, Charles F. 1969: Surface-Pressure Fluctuations Associated With Aerodynamic Noise. *Basic Aerodynamic Noise Research*, Ira R. Schwartz, ed., NASA SP-207, pp. 409–424.

Corcos, G. M. 1963: Resolution of Pressure in Turbulence. *J. Acoust. Soc. America*, vol. 35, no. 2, pp. 192–199.

Corcos, G. M. 1967: The Resolution of Turbulent Pressures at the Wall of a Boundary Layer. *J. Sound & Vib.*, vol. 6, no. I, pp. 59–70.

Dimmock, N. A. 1950: The Development of a Simply Constructed Cascade Corner for Circular Cross Section Ducts. National Gas Turbine Establ. Memo. No. 78, British Ministry Supply.

Dolling, D. S.; and Dussauge, J. P. 1989: Fluctuating Wall-Pressure Measurements. *A Survey of Measurements and Measuring Techniques in Rapidly Distorted Compressible Turbulent Boundary Layers*, H. H. Fernholz, P. J. Finley, J. P. Dussauge, A. J. Smits, and Eli Reshotko, eds., AGARD-AG-315. (Available from DTIC as AD A211 107.)

Dougherty, N. Sam, Jr. 1980: *Influence of Wind Tunnel Noise on the Location of Boundary-Layer Transition on a Slender Cone at Mach Numbers From 0.2 to 5.5, Volume I—Experimental Methods and Summary of Results.* AEDC-TR-78-44-VOL-1, U.S. Air Force. (Available from DTIC as AD A083165.)

Dougherty, N. S., Jr.; and Fisher, D. F. 1980: Boundary-Layer Transition on a 10-Deg Cone: Wind Tunnel/Flight Correlation. AIAA-80-0154.

Dryden, Hugh L.; and Abbott, Ira H. 1948: *The Design of Low-Turbulence Wind Tunnels.* NACA Rep. 940.

Eckelmann, Helmut 1990: A Review of Knowledge on Pressure Fluctuations. *Near–Wall Turbulence—1988 Zoran Zari'c Memorial Conference*, S. J. Kline and N. H. Afgan, eds., Hemisphere Publishing Corp., pp. 328–347.

Elsenaar, A. 1990: The Windtunnel as a Tool for Laminar Flow Research. *ICAS Proceedings—1990*, pp. 174–185. (Available as ICAS-90-6.1.1.)

Elsenaar, A.; Binion, T. W., Jr.; and Stanewsky, E. 1988: *Reynolds Number Effects in Transonic Flow.* AGARD-AG-303.

Foster, Jean M.; and Adcock, Jerry B. 1987: *User's Guide for the National Transonic Facility Data System.* NASA TM-100511.

Fuller, Dennis E. 1981: *Guide for Users of the National Transonic Facility.* NASA TM-83124.

Goodyer, Michael J.; and Kilgore, Robert A. 1972: The High Reynolds Number Cryogenic Wind Tunnel. AIAA Paper No. 72-995.

Hall, Robert M.; and Adcock, Jerry B. 1981: *Simulation of Ideal-Gas Flow by Nitrogen and Other Selected Gases at Cryogenic Temperatures.* NASA TP-1901.

Hanly, Richard D. 1975: Effects of Transducer Flushness on Fluctuating Surface Pressure Measurements. AIAA-75-534.

Heller, H. H.; Holmes, D. G.; and Covert, E. E. 1971: Flow-Induced Pressure Oscillations in Shallow Cavities. *J. Sound & Vib.*, vol. 18, no. 4, pp. 545–553.

Horstman, C. C.; and Rose, W. C. 1977: Hot-Wire Anemometry in Transonic Flow. *AIAA J.*, vol. 15, no. 3, pp. 395–401.

Howell, Robert R.; and McKinney, Linwood W. 1977: The U.S. 2.5-Meter Cryogenic High Reynolds Number Tunnel. *High*

Reynolds Number Research, Donald D. Baals, ed., NASA CP-2009, pp. 27–51.

Hussain, A. K. M. F.; and Zaman, K. B. M. Q. 1978: The Free Shear Layer Tone Phenomenon and Probe Interference. *J. Fluid Mech.*, vol. 87, pt. 2, pp. 349–383.

Igoe, William B. 1980: Characteristics and Status of the U.S. National Transonic Facility. *Cryogenic Wind Tunnels*, AGARD-LS-111, pp. 17-1–17-11.

Jones, Gregory Stephen 1991: The Measurement of Wind Tunnel Flow Quality at Transonic Speeds. Ph.D. Diss., Virginia Polytech. Inst. & State Univ.

Karamcheti, K.; Bauer, A. B.; Shields, W. L.; Stegen, G. R.; and Woolley, J. P. 1969: Some Features of an Edge-Tone Flow Field. *Basic Aerodynamic Noise Research*, Ira R. Schwartz, ed., NASA SP-207, pp. 275–304.

Kern, F. A.; Knight, C. W.; and Zasimowich, R. F. 1986: National Transonic Facility Mach Number System. *ISA Trans.*, vol. 25, no. 2.

Kilgore, Robert Ashworth 1974: The Cryogenic Wind Tunnel for High Reynolds Number Testing. Ph.D. Thesis, Univ. of Southampton. (Available as NASA TM X-70207.)

Kilgore, Robert A.; Adcock, Jerry B.; and Ray, Edward J. 1974: Flight Simulation Characteristics of the Langley High Reynolds Number Cryogenic Transonic Tunnel. *J. Aircr.*, vol. 11, no. 10, pp. 593–600.

Kovásznay, Leslie S. G. 1950: The Hot-Wire Anemometer in Supersonic Flow. *J. Aeronaut. Sci.*, vol. 17, no. 9, pp. 565–572, 584.

Kovásznay, Leslie S. G. 1953: Turbulence in Supersonic Flow. *J. Aeronaut. Sci.*, vol. 20, no. 10, pp. 657–674, 682.

Kuchemann, Dietrich; and Weber, Johanna 1953: *Aerodynamics of Propulsion*, First ed. McGraw-Hill Book Co., Inc.

Lassiter, William S. 1981: Design Predictions for Noise Control in the Cryogenic National Transonic Facility. *Noise Control Eng.*, pp. 76–84.

Lee, In; and Baik, Ki-Young 1991: Resonance Prediction for Slotted Circular Wind Tunnel Using Finite Element. *AIAA J.*, vol. 29, no. 12, pp. 2266–2269.

Lowson, M. V. 1968: *Prediction of Boundary Layer Pressure Fluctuations*. AFFDL-TR-67-167, U.S. Air Force. (Available from DTIC as AD 832 715.)

Mabey, D. G. 1971: *Flow Unsteadiness and Model Vibration in Wind Tunnels at Subsonic and Transonic Speeds*. CP No. 1155, British ARC.

Mabey, D. G. 1978: *The Resonance Frequencies of Ventilated Wind Tunnels*. R. & M. No. 3841, British ARC.

Mabey, D. G. 1991: *A Semi-Empirical Theory of the Noise in Slotted Tunnels Caused by Diffuser Suction*. Tech. Rep. 91023, British RAE.

Mabey, D. G. 1976: *Some Remarks on the Design of Transonic Tunnels With Low Levels of Flow Unsteadiness*. NASA CR-2722.

Margoulis, W. 1921: *A New Method of Testing Models in Wind Tunnels*. NACA TN-52.

Meyers, James F.; and Clemmons, James I., Jr. 1987: Frequency Domain Laser Velocimeter Signal Processor—A New Signal Processing Scheme. NASA TP-2735.

Meyers, James F.; and Wilkinson, Stephen P. 1982: A Comparison of Turbulence Intensity Measurements Using a Laser Velocimeter and a Hot Wire in a Low Speed Jet Flow. Presented at International Symposium on Applications of Laser-Doppler Anemometry to Fluid Mechanics.

Michel, Roger 1988: Boundary Layer Development and Transition. *Boundary Layer Simulation and Control in Wind Tunnels*, AGARD-AR-224, pp. 217–249.

Michel, U.; and Froebel, E. 1988: Lower Limit for the Velocity Fluctuation Level in Wind Tunnels. *Exp. Fluids*, vol. 6, pp. 49–54.

Mokry, M. 1984: Prediction of Resonance Frequencies For Ventilated Wall Wind Tunnels. *Wind Tunnels and Testing Techniques*, AGARD-CP-348, pp. 15-1–15-10.

Monti, R. 1971: Wall Corrections for Airplanes With Lift in Transonic Wind Tunnel Tests. *Report of the AGARD Ad Hoc Committee on Engine-Airplane Interference and Wall Corrections in Transonic Wind Tunnel Tests*, AGARD-AR-36-71, pp. III-1–III-13. (Available from DTIC as AD 729 568.)

Morkovin, Mark V. 1956: *Fluctuations and Hot-Wire Anemometry in Compressible Flows*. AGARDograph 24.

Murthy, S. V.; and Steinle, F. W. 1985: On Boundary Layer Transition in High-Subsonic and Transonic Flow Under the Influence of Acoustic Disturbances and Free-Stream Turbulence. AIAA-85-0082.

Murthy, Sreedhara V.; and Steinle, Frank W. 1986: Effects of Compressibility and Free-Stream Turbulence on Boundary Layer Transition in High-Subsonic and Transonic Flows. *A Collection of Technical Papers—AIAA 14th Aerodynamic Testing Conference*, pp. 242–250. (Available as AIAA-86-0764.)

Prandtl, L. 1914: Der Luftwiderstand von Kugleln. Nachrichten der Königlichen Gesellschaft d. Wiss. zu Göttingen. *Math.-Phys. K1.*, no. 2, pp. 177–190.

Ramaswamy, M. A.; and Cornette, E. S. 1980: Supersonic Flow Development in Slotted Wind Tunnels. *A Collection of Technical Papers—AIAA 11th Aerodynamic Testing Conference*, pp. 165–172. (Available as AIAA-80-0443.)

Robinson, Russell G. 1937: Sphere Tests in the N.A.C.A. 8-Foot High-Speed Tunnel. *J. Aeronaut. Sci.*, vol. 4, no. 5, pp. 199–201.

Rose, William C.; and McDaid, Edward P. 1976: Turbulence Measurement in Transonic Flow. *Proceedings—AIAA 9th Aerodynamic Testing Conference*, pp. 267–271.

Ross, R.; and Rohne, P. B. 1973: Noise Environment in the NLR Transonic Windtunnel HST. NLR TR-74128 U, Natl. Aerosp. Lab. (NLR).

Rossiter, J. E. 1964: Wind-Tunnel Experiments on the Flow Over Rectangular Cavities at Subsonic and Transonic Speeds. R. & M. No. 3438, British ARC. (Supersedes RAETR 64037.)

Schewe, Günter 1983: On the Structure and Resolution of Wall-Pressure Fluctuations Associated With Turbulent Boundary-Layer Flow. *J. Fluid Mech.*, vol. 134, pp. 311–328.

Siddon, Thomas E. 1969: *On the Response of Pressure Measuring Instrumentation in Unsteady Flow (An Investigation of Errors Induced by Probe-Flow Interaction)*. AFOSR 68-2466, U.S. Air Force. (Available from DTIC as AD 682 296.)

Smelt, R. 1945: *Power Economy in High-Speed Wind Tunnels by Choice of Working Fluid and Temperature*. Rep. No. Aero. 2081, British RAE.

Spangenberg, W. G. 1955: *Heat-Loss Characteristics of Hot-Wire Anemometers at Various Densities in Transonic and Supersonic Flow*. NACA TN-3381.

Spangler, J. G.; and Wells, C. S., Jr. 1968: Effects of Freestream Disturbances on Boundary-Layer Transition. *AIAA J.*, vol. 6, no. 3, pp. 543–545.

Stainback, P. Calvin; Johnson, Charles B.; and Basnett, Constance B. 1983: Preliminary Measurements of Velocity, Density and Total Temperature Fluctuations in Compressible Subsonic Flow. AIAA-83-0384.

Timme, Adalbert 1973: Effects of Turbulence and Noise on Wind-Tunnel Measurements at Transonic Speeds. *Fluid Motion Problems in Wind Tunnel Design*, AGARD-R-602, pp. 5-1–5-12.

Williams, John 1977: Appendix 4—Aeroacoustic Requirements for Model Noise Experiments in Subsonic Windtunnels. *A Further Review of Current Research Related to the Design and Operation of Large Windtunnels*, AGARD-AR-105, pp. 61–91.

Willmarth, W. W.; and Roos, F. W. 1965: Resolution and Structure of the Wall Pressure Field Beneath a Turbulent Boundary Layer. *J. Fluid Mech.*, vol. 22, pt. 1, pp. 81–94.
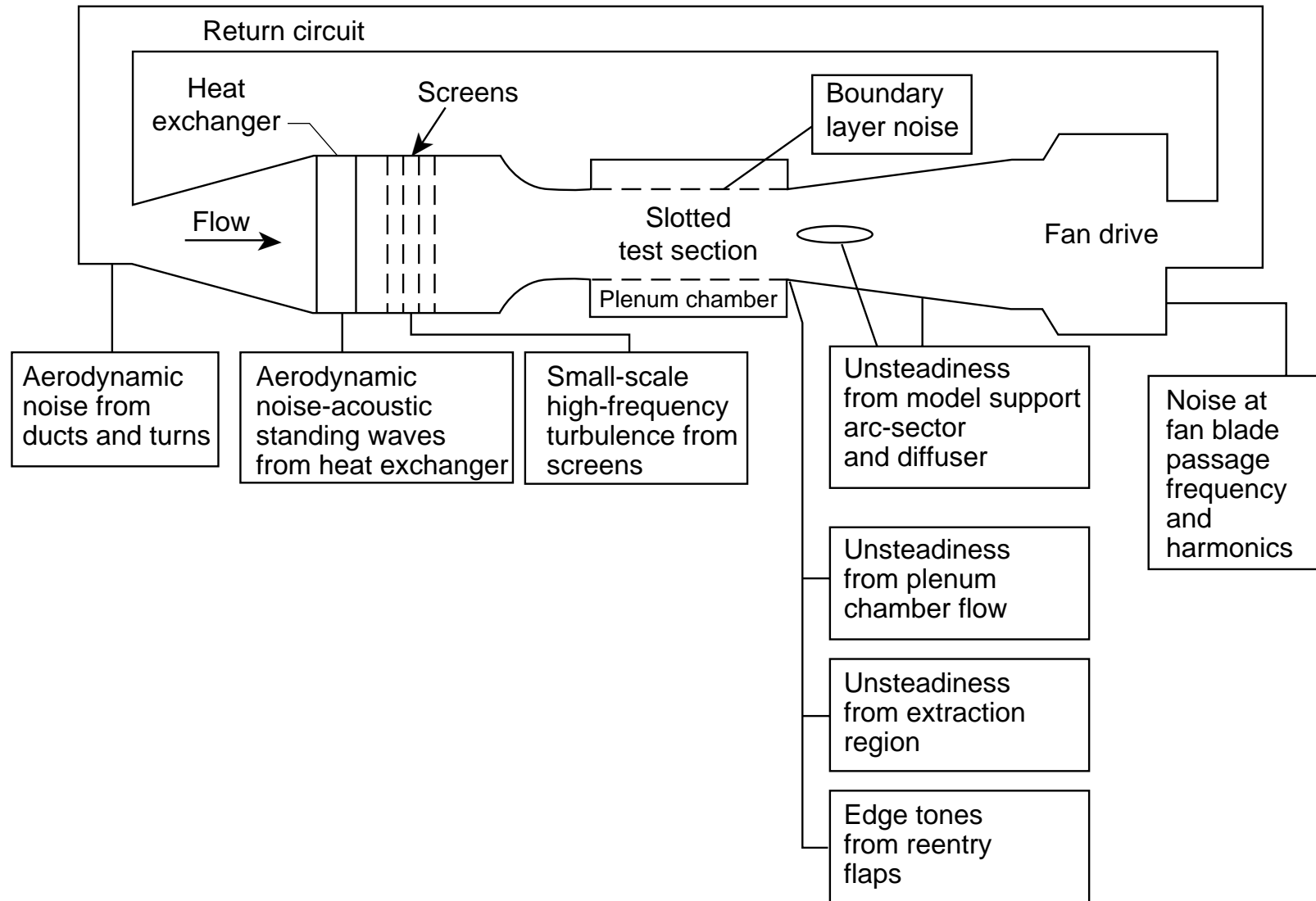
Figure 1. Sources of unsteadiness in transonic wind tunnels adapted from Mabey (1971).
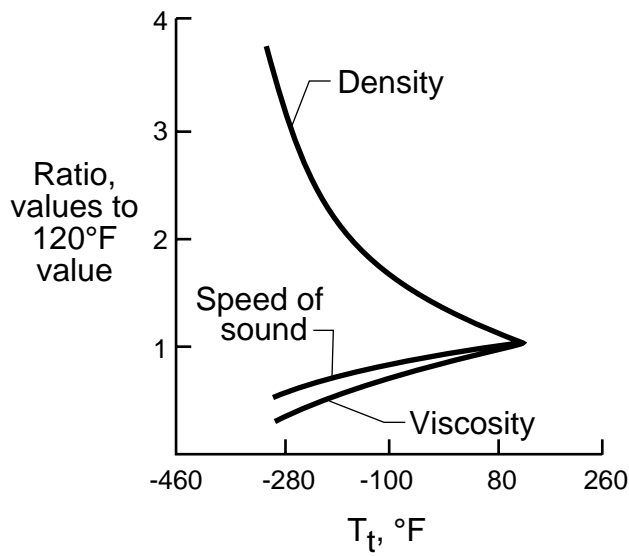
(a) Gas properties.
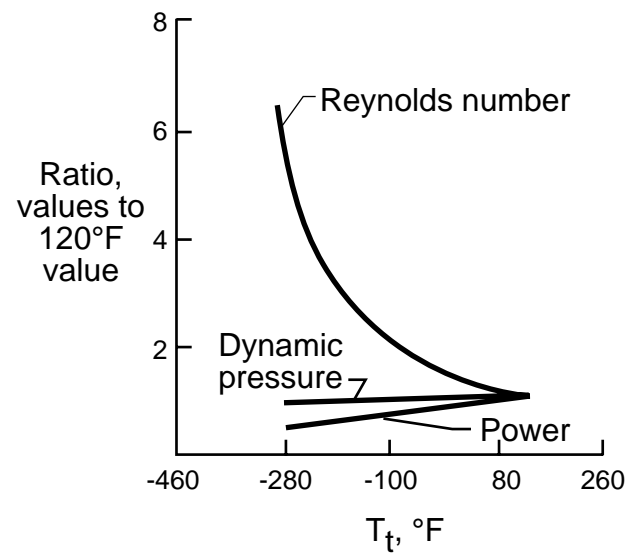
(b) Test conditions and fan drive power.

Figure 2. Variation of gas properties and wind tunnel conditions with temperature. $M = 1.0$; constant p_t; and wind tunnel size.
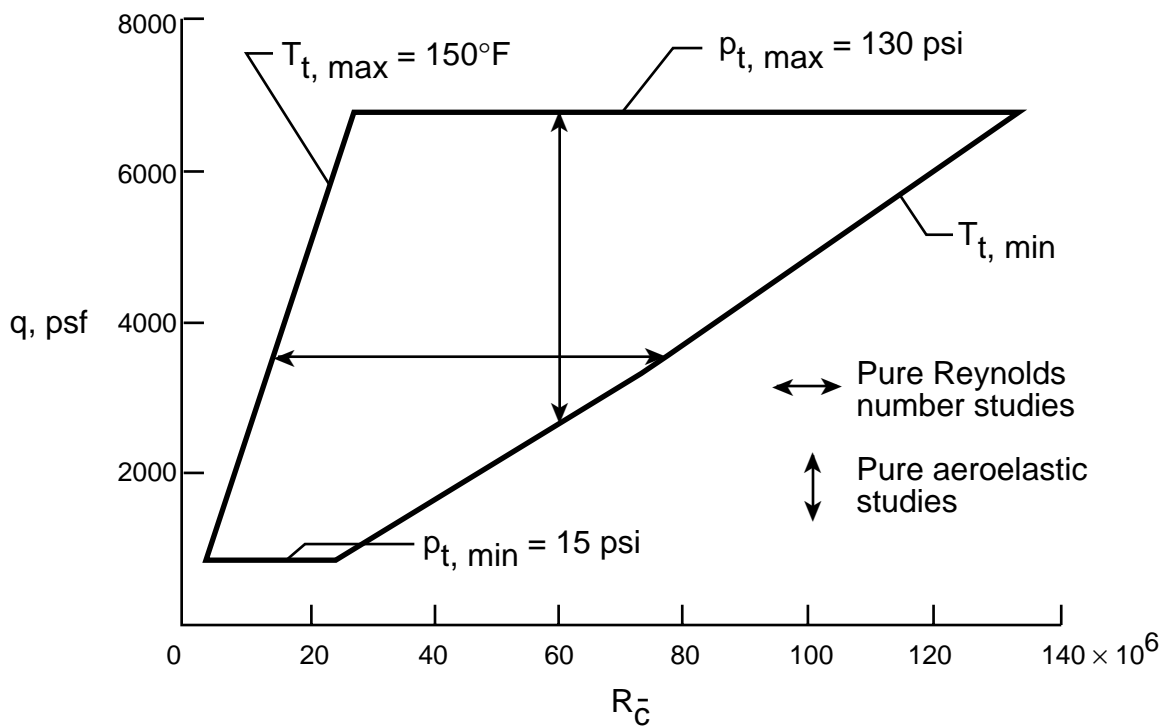
Figure 3. Operating envelope at constant Mach number. $M = 1.0$; $\bar{c} = 0.82$ ft.
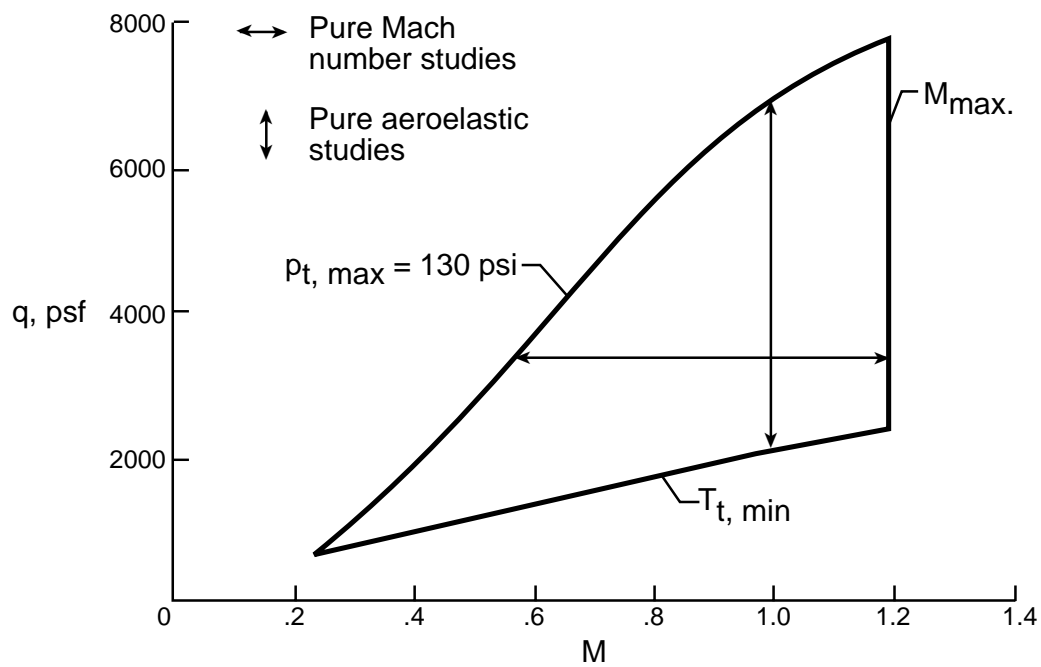
Figure 4. Operating envelope at constant Reynolds number. $R_{\bar{c}} = 50 \times 10^6$; $\bar{c} = 0.82$ ft.
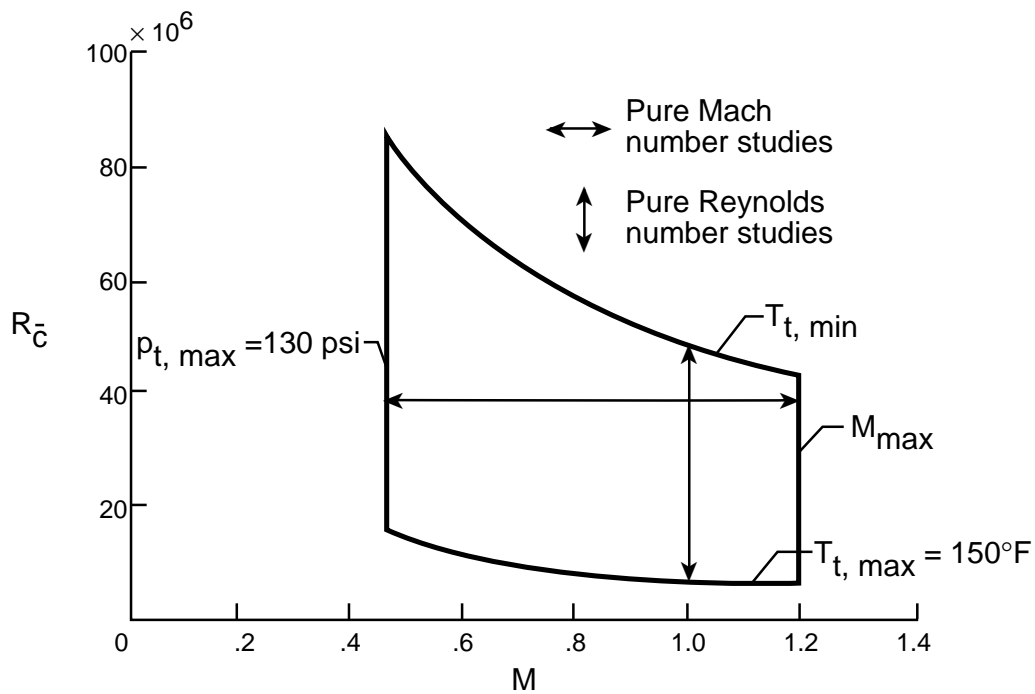
Figure 5. Operating envelope at constant dynamic pressure. $q = 2089$ psf; $\bar{c} = 0.82$ ft.
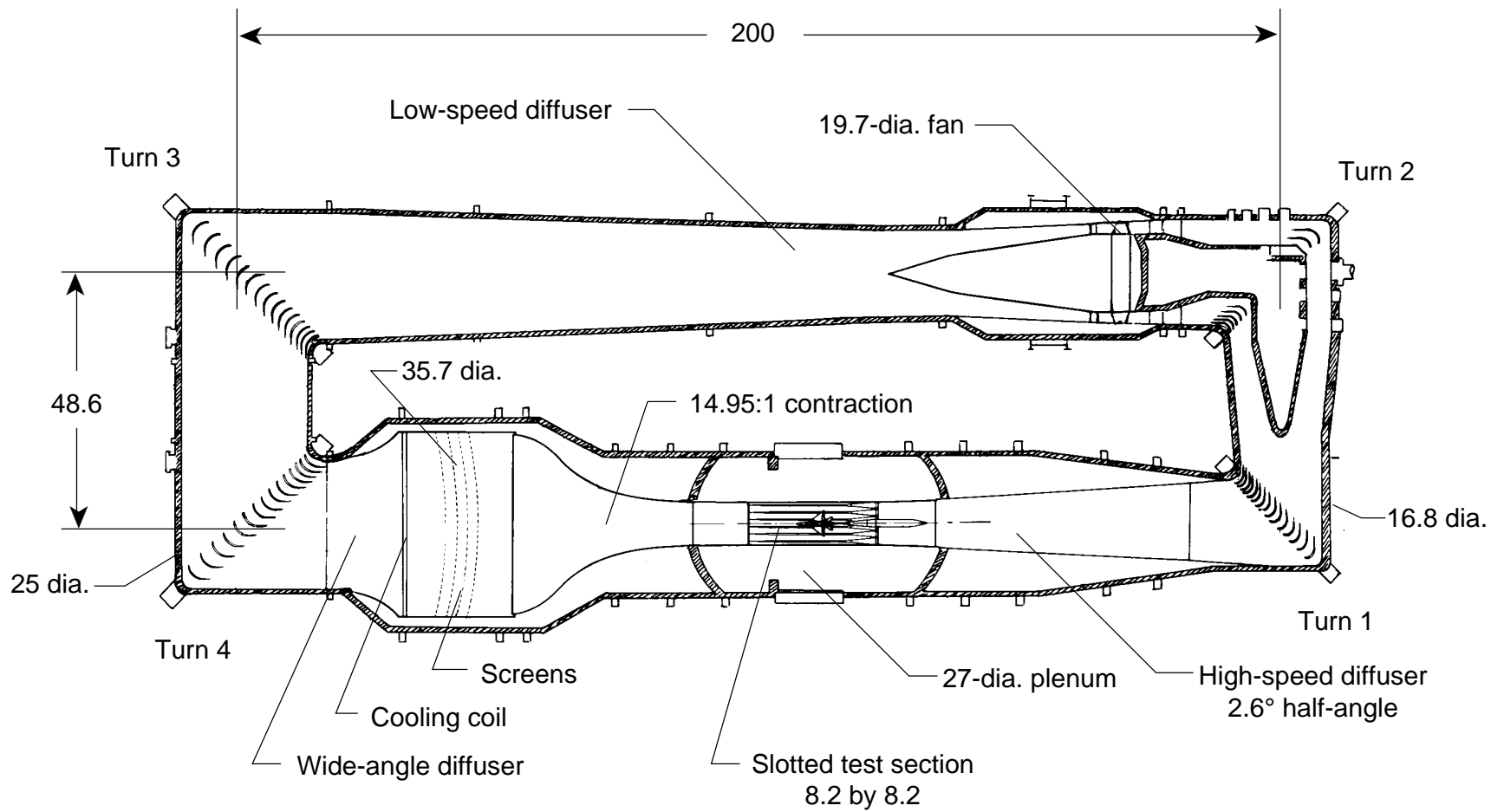
Figure 6. Plan view of NTF tunnel circuit. All linear dimensions are in feet.
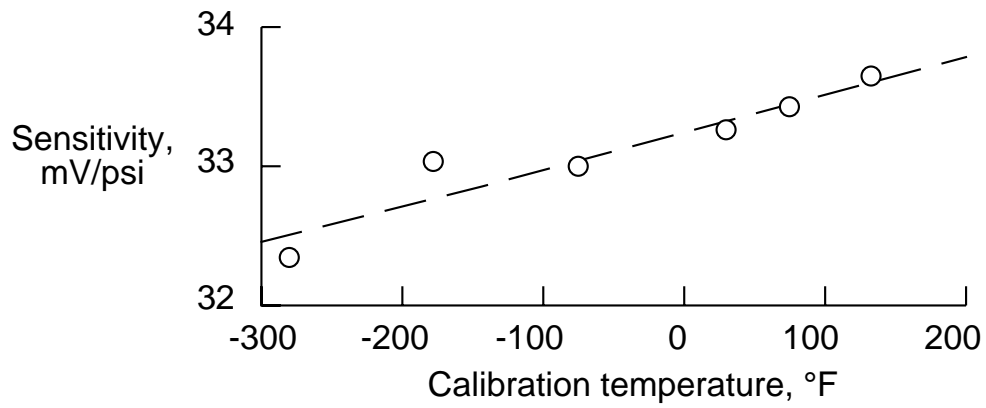
(a) Static calibration sensitivity versus temperature.
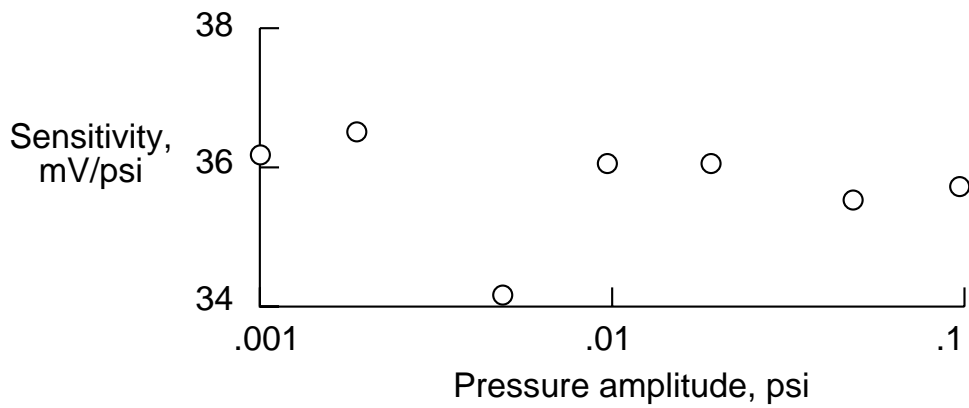
(b) Dynamic range at 1 kHz.
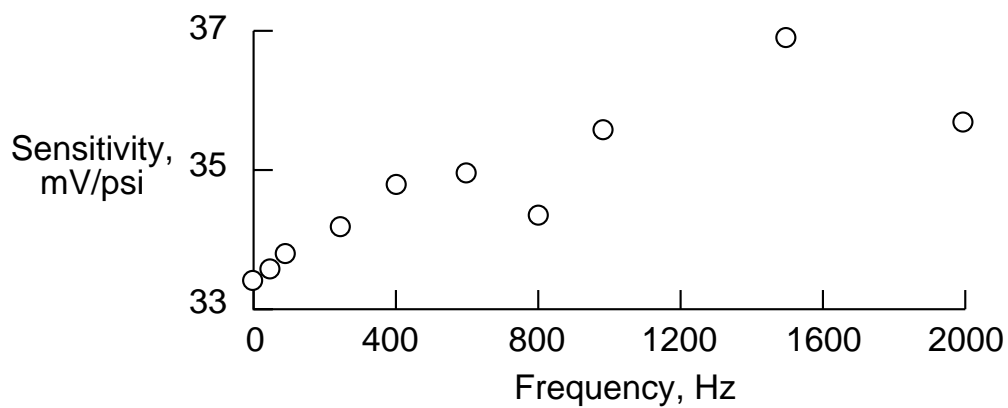
(c) Frequency response at 0.05-psi amplitude.

Figure 7. Pressure transducer 64RY static and dynamic calibration sensitivities.
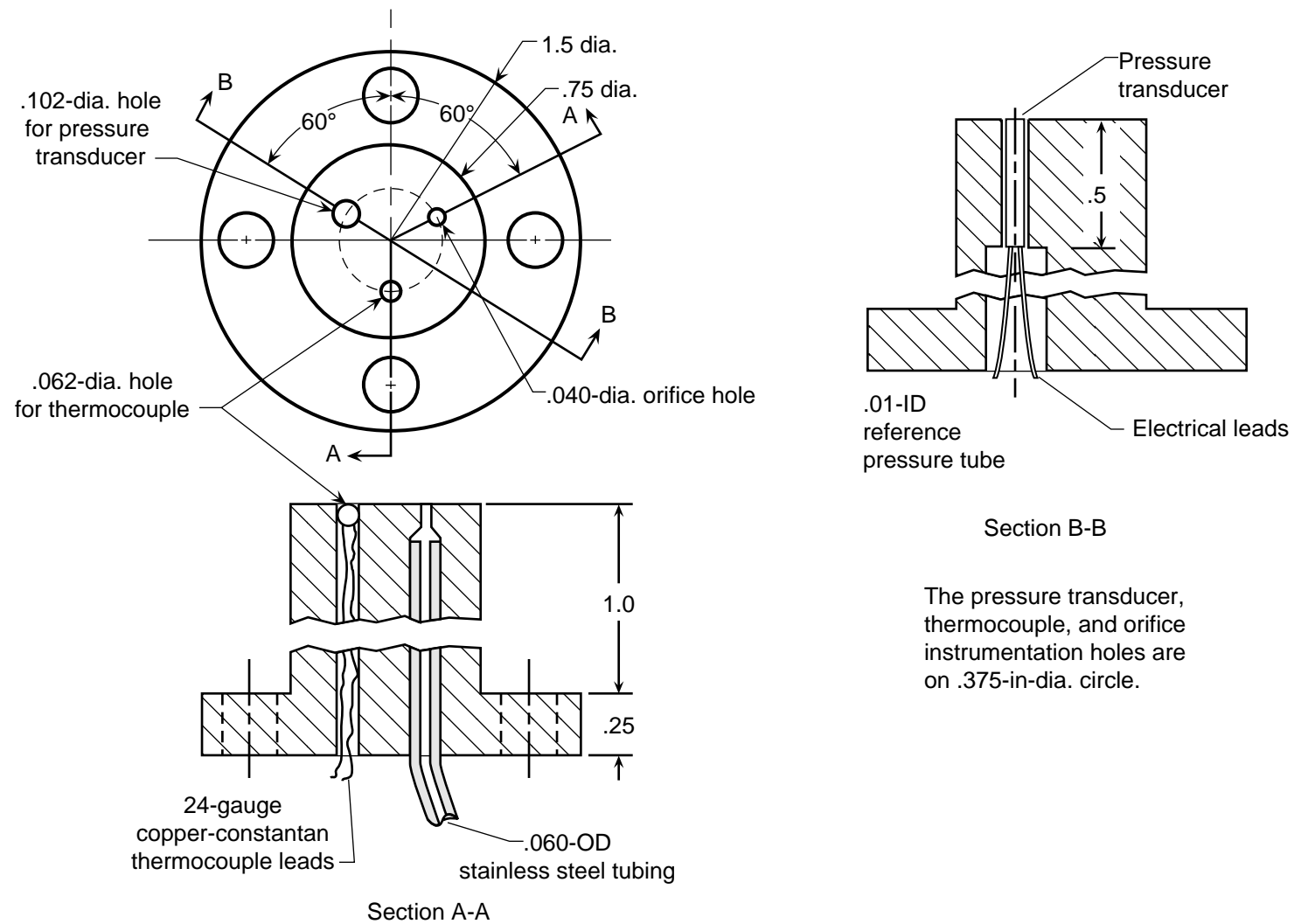
Figure 8. Pressure transducer instrumentation plug. All linear dimensions are in inches.
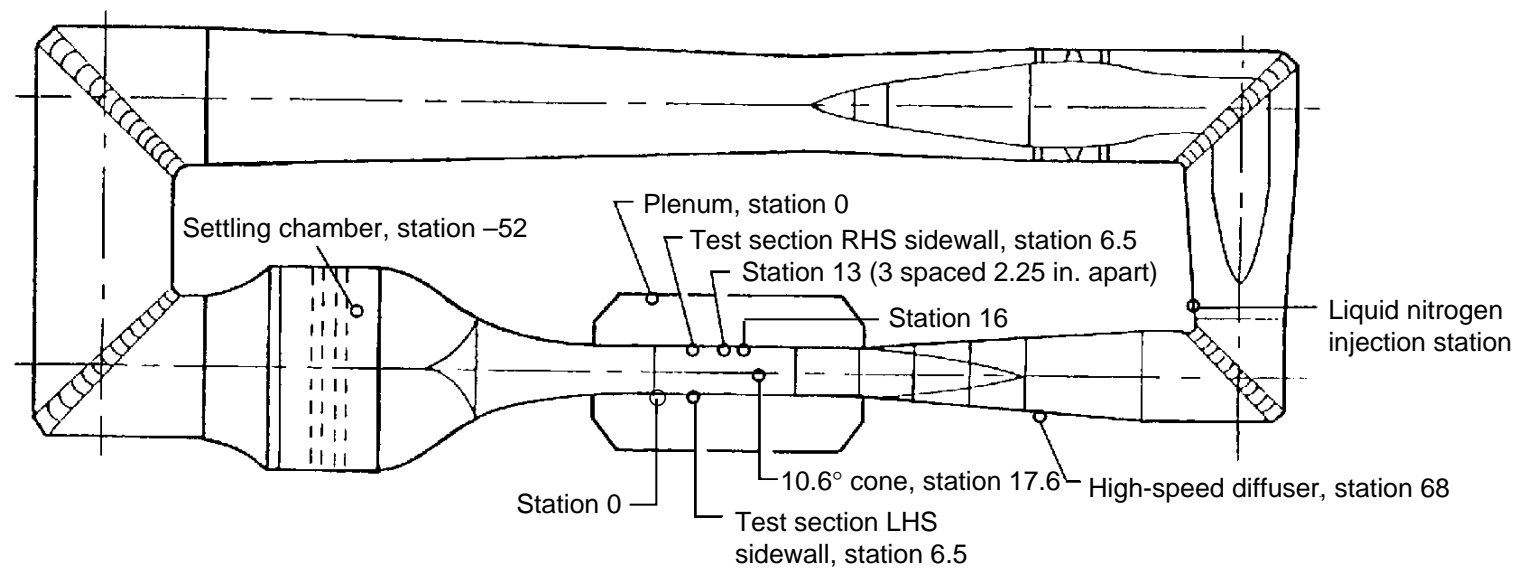
Figure 9. Locations of dynamic pressure transducers installed in NTF circuit.
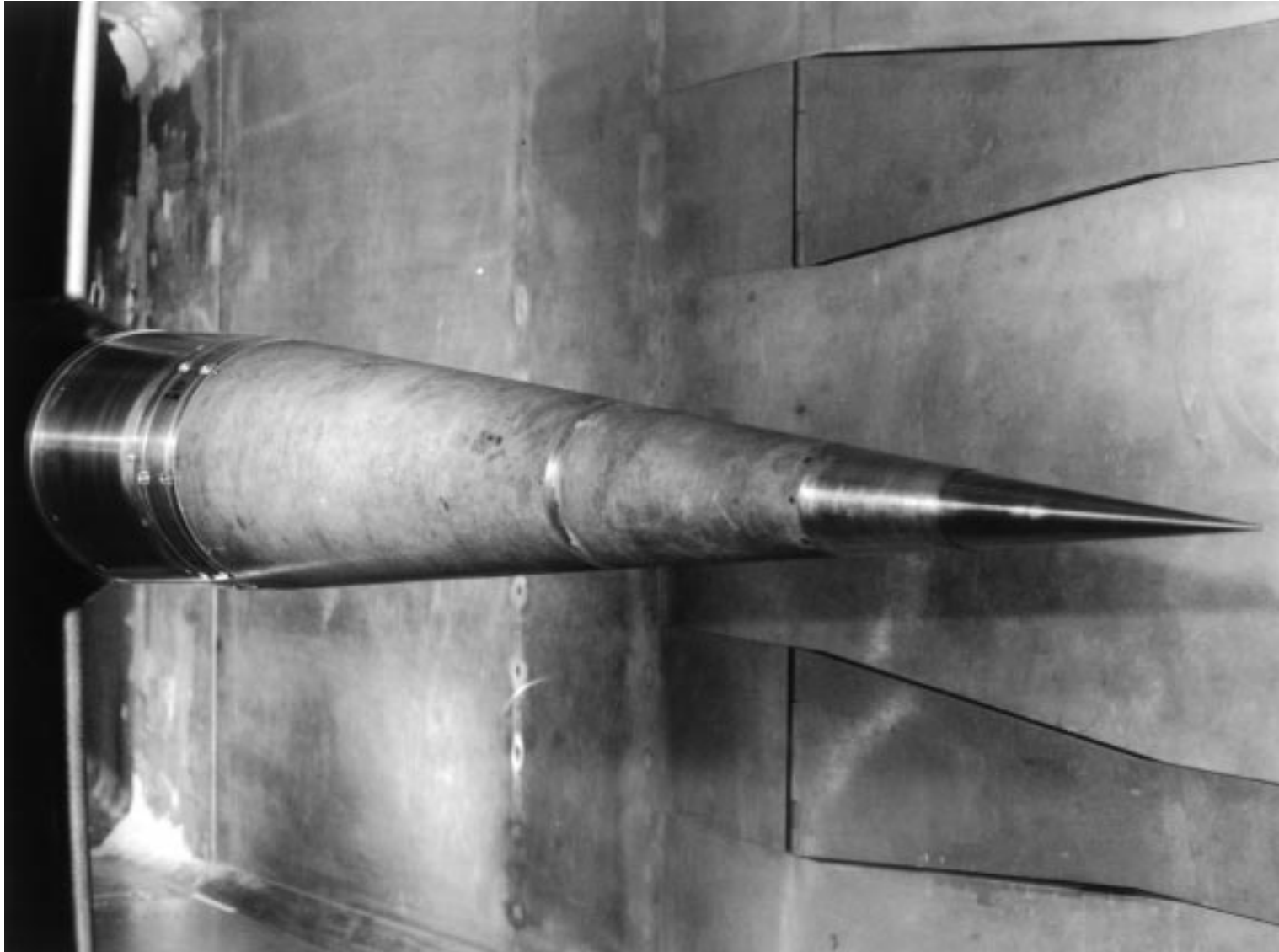
L-90-13688

Figure 10. NTF model support strut center body with 10.6° conical fairing.
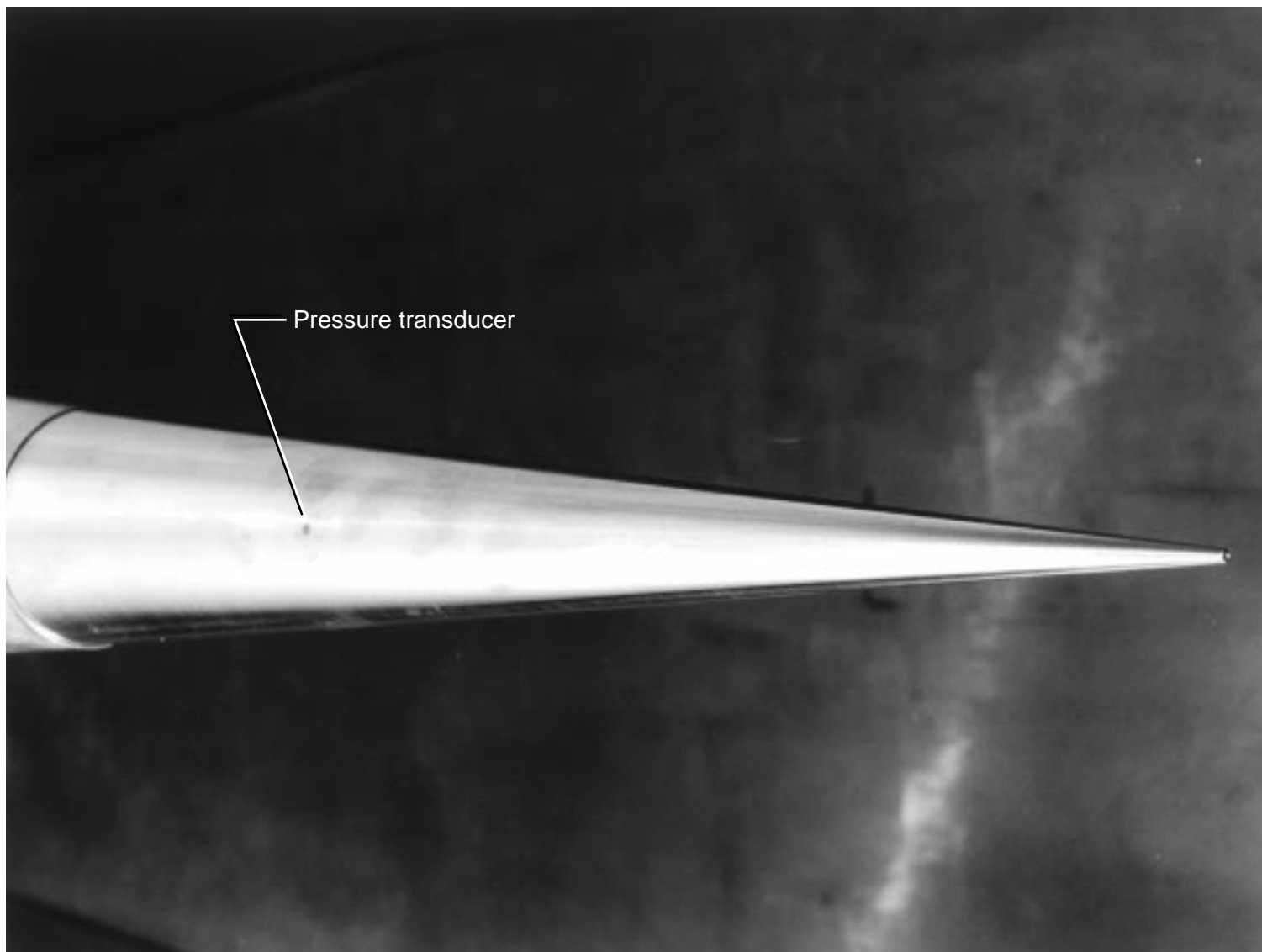
L-90-13687

Figure 11. Tip of 10.6° conical fairing with dynamic pressure transducer installed.
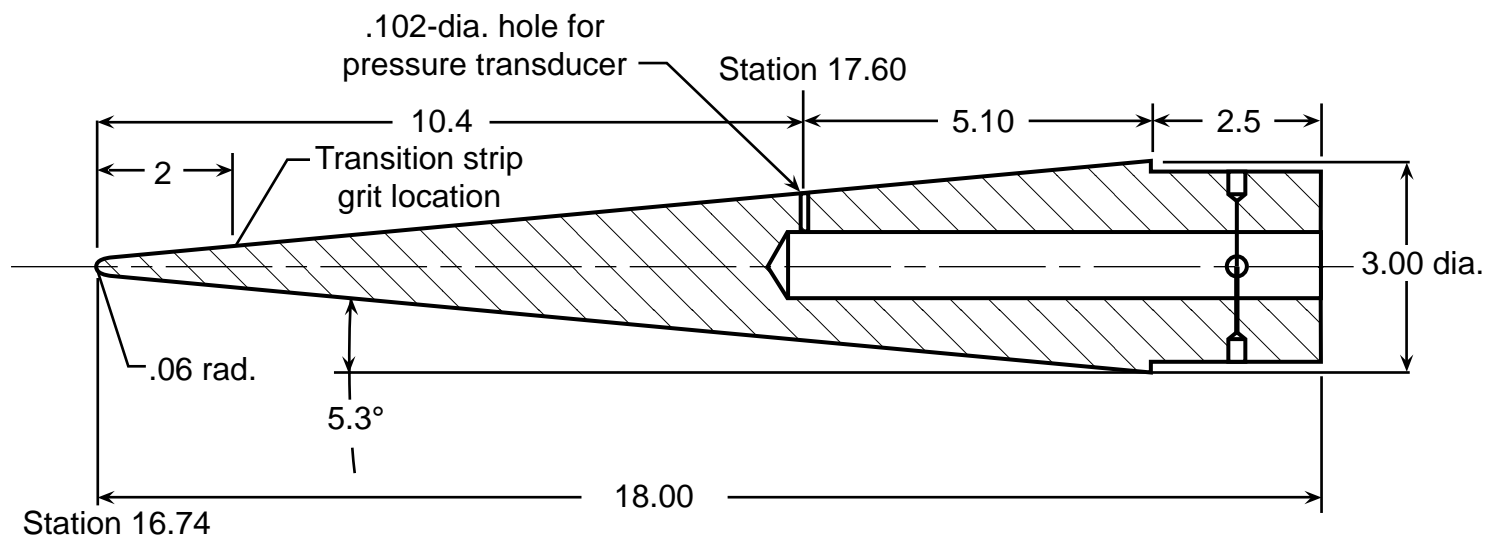
Figure 12. Tip of 10.6° cone fairing. All linear dimensions are in inches except wind tunnel stations which are in feet.
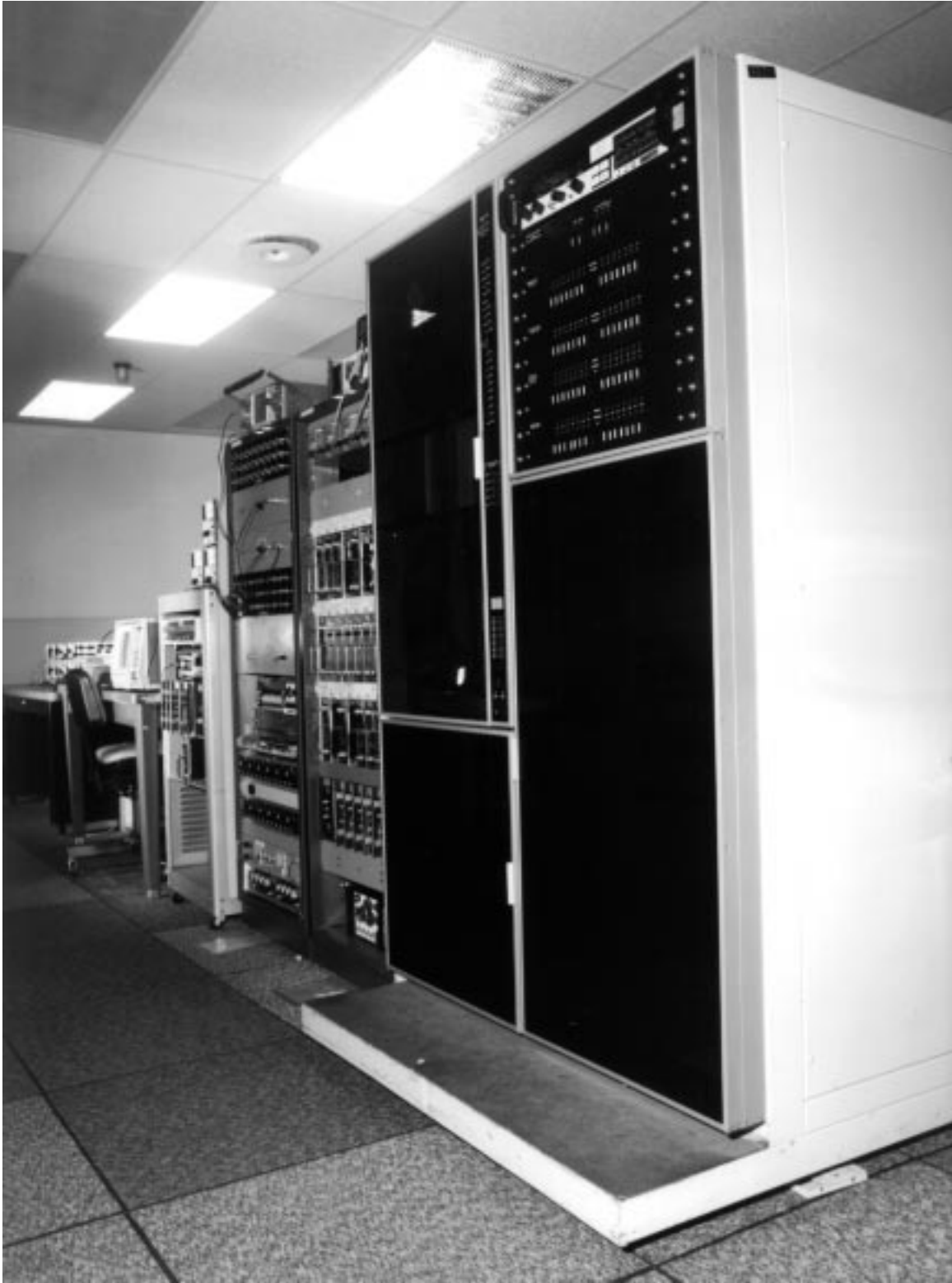
L-91-06638

Figure 13. Dynamic data acquisition instrumentation in NTF control room.
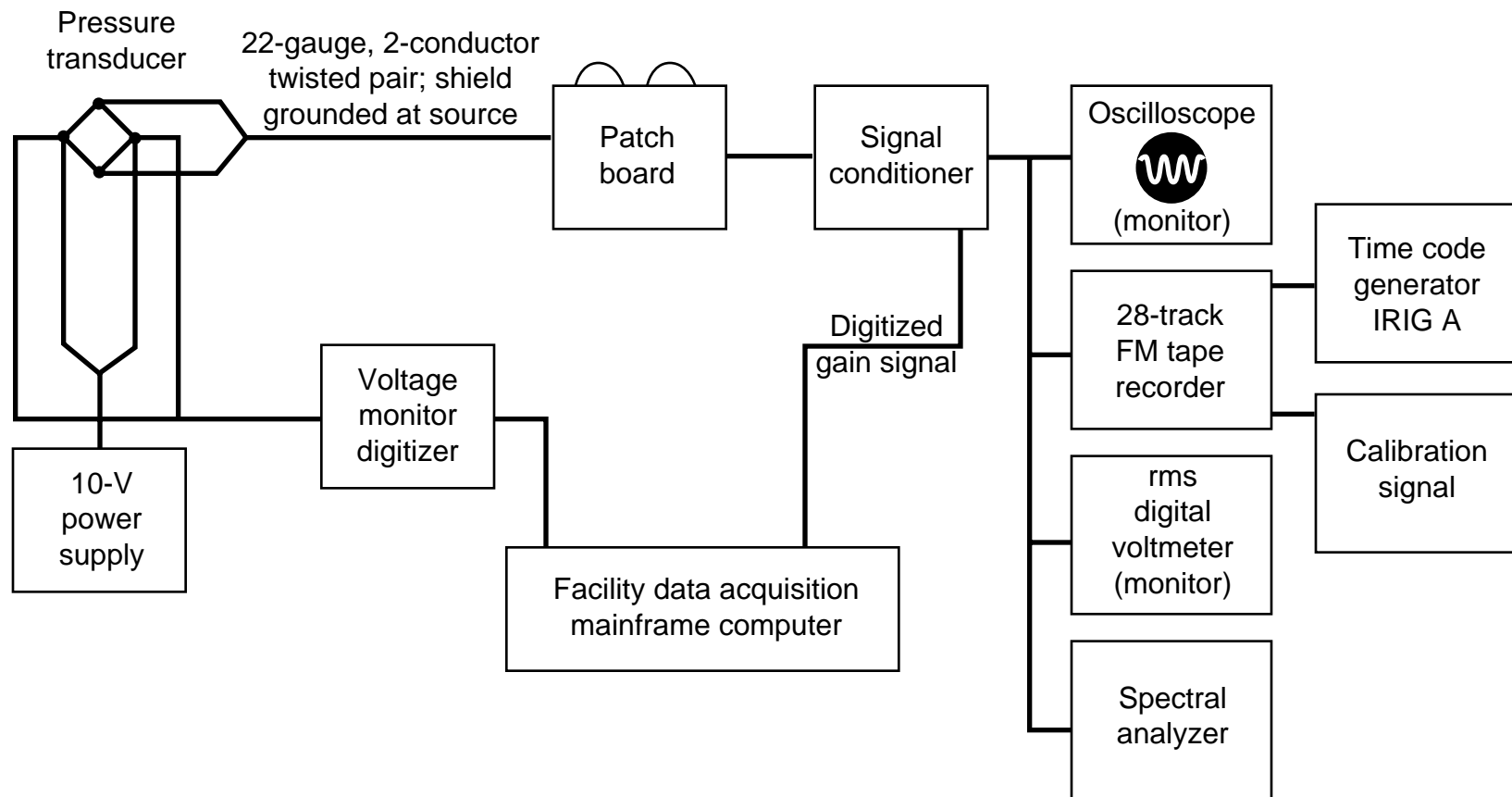
Figure 14. NTF dynamic data acquisition system wiring block diagram.
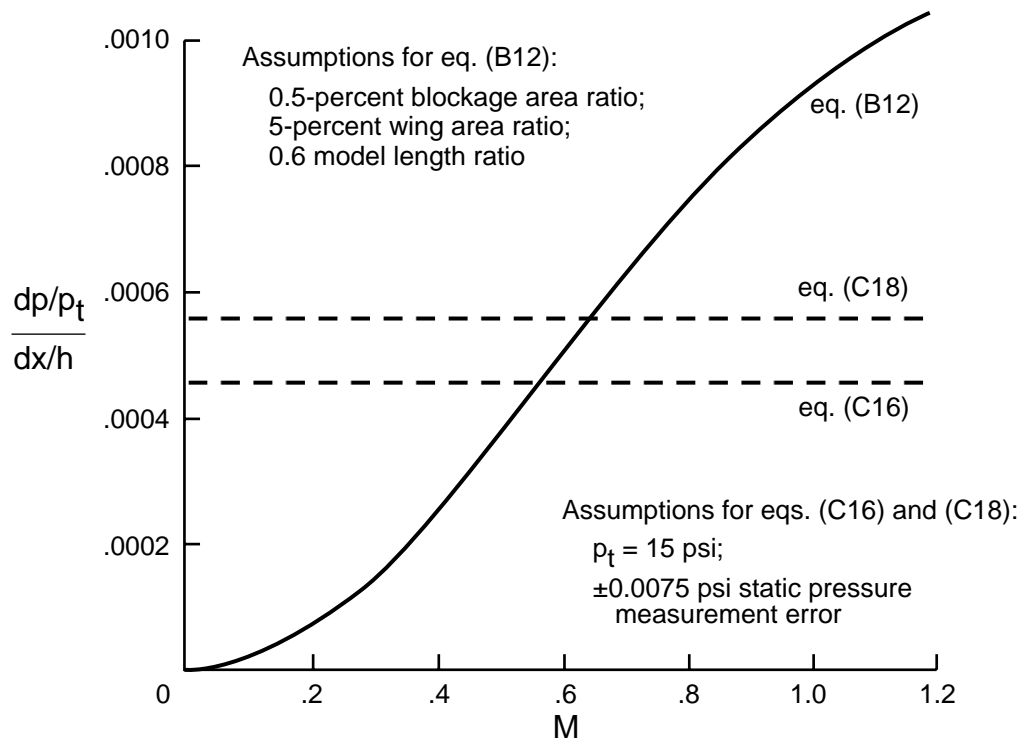
Figure 15. Longitudinal static pressure gradient for 1 count (0.0001) of buoyancy-induced drag coefficient.
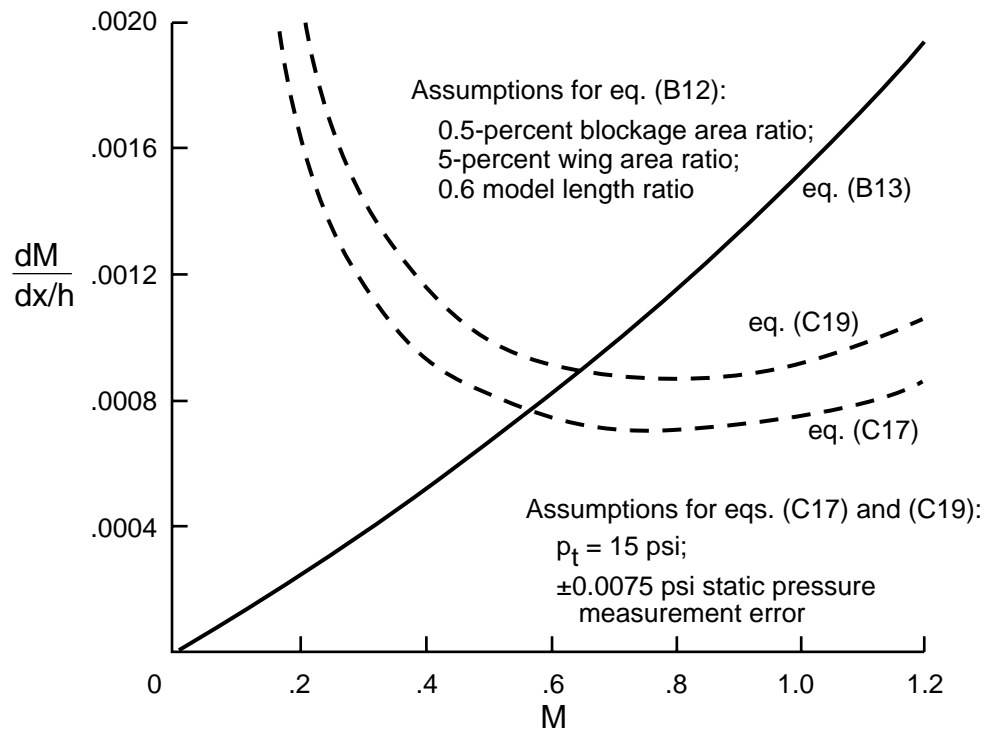
Figure 16. Longitudinal Mach number gradient for 1 count (0.0001) of buoyancy-induced drag coefficient.
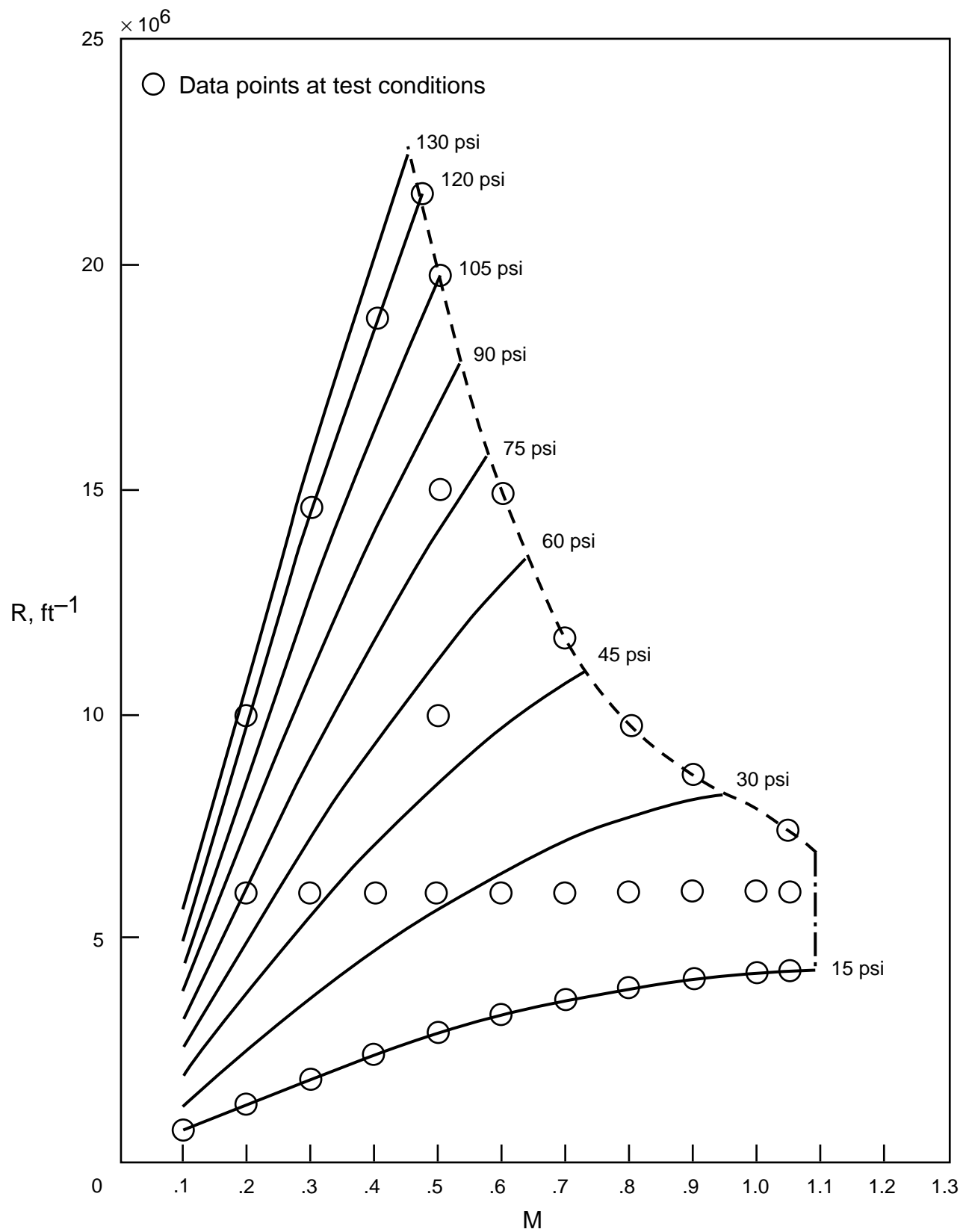
Figure 17. NTF performance envelope in air mode. $T_t = 120°F$.
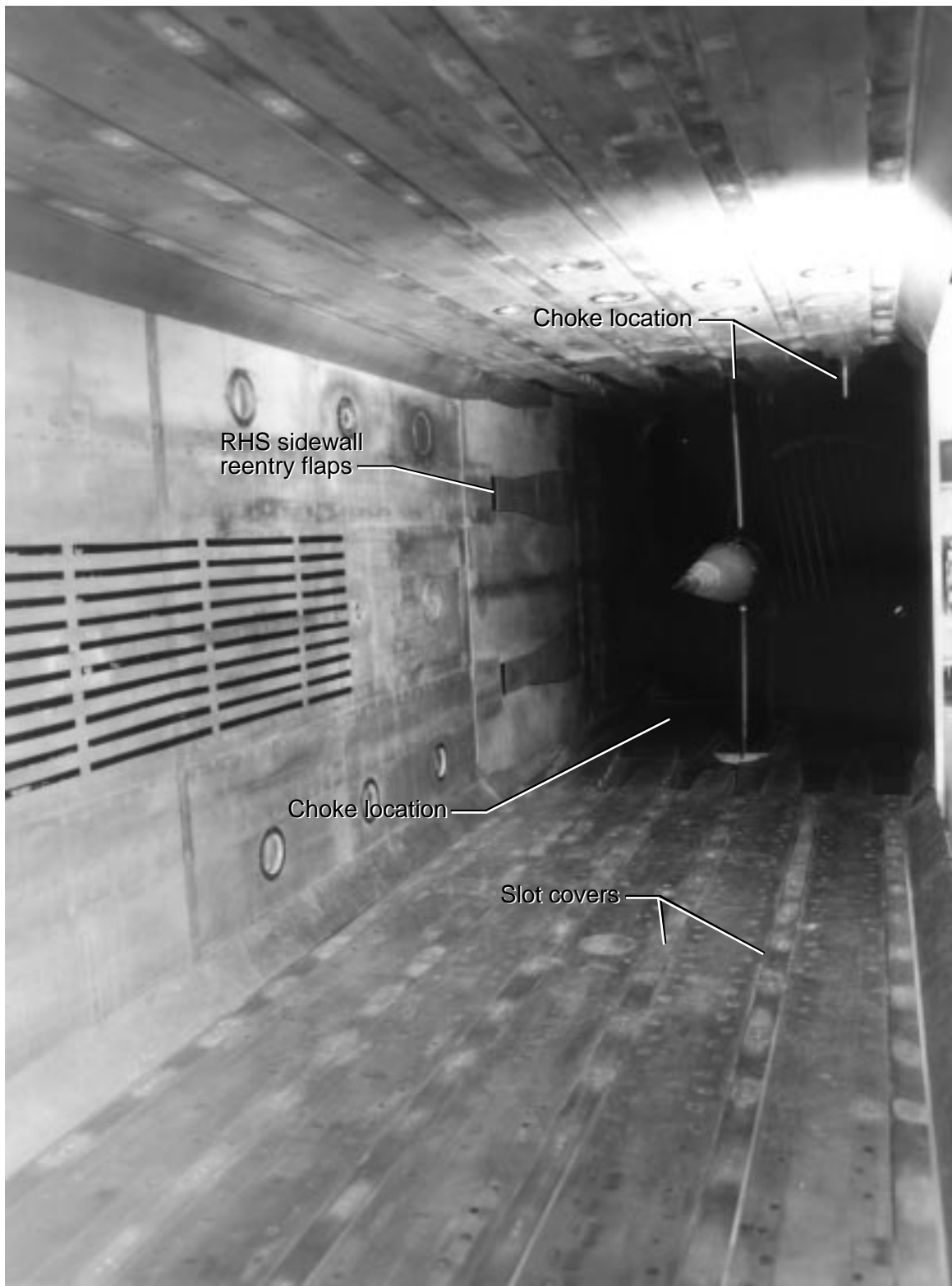
Figure 18. NTF test section walls with slot covers in place.
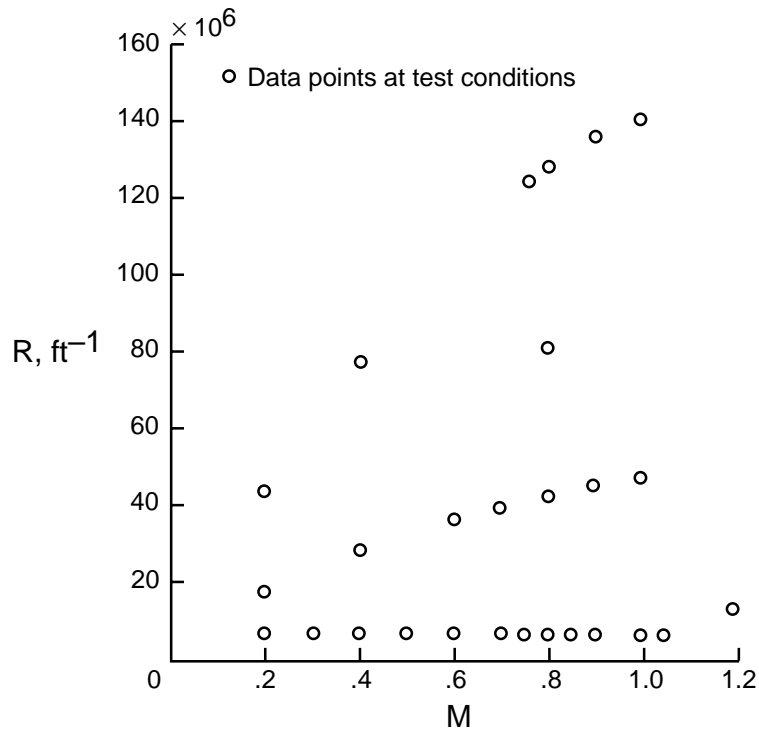
Figure 19. NTF performance envelope in nitrogen mode.
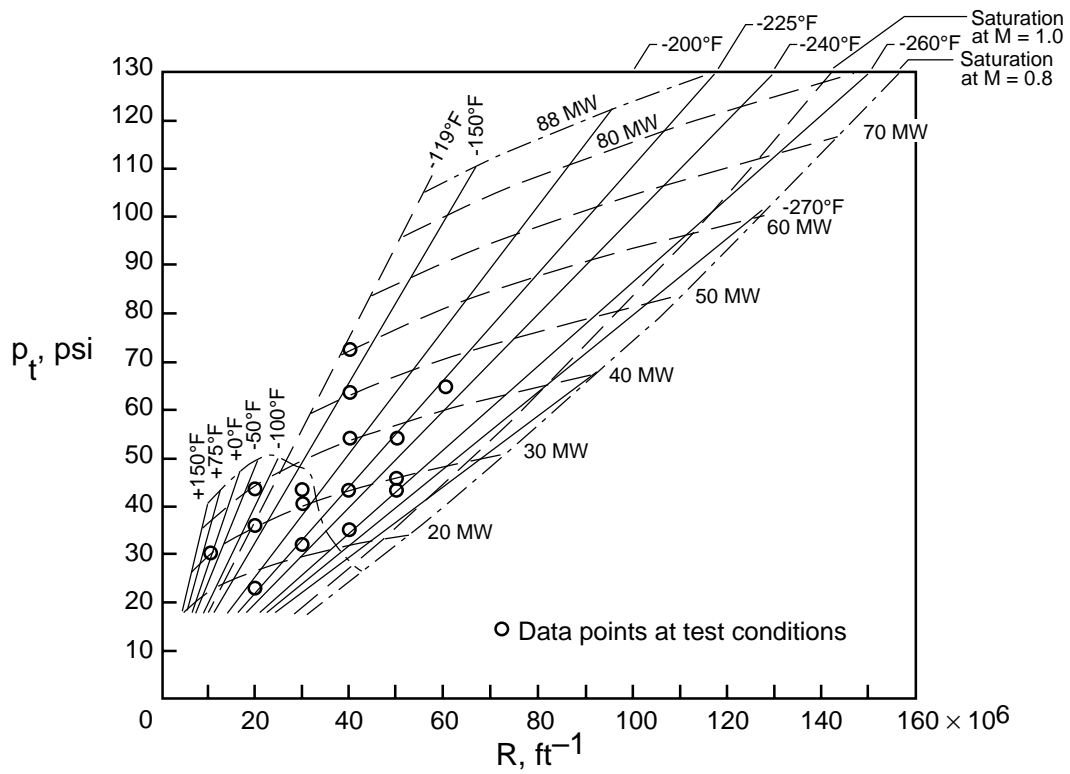
Figure 20. NTF operating envelope for $M = 0.8$.
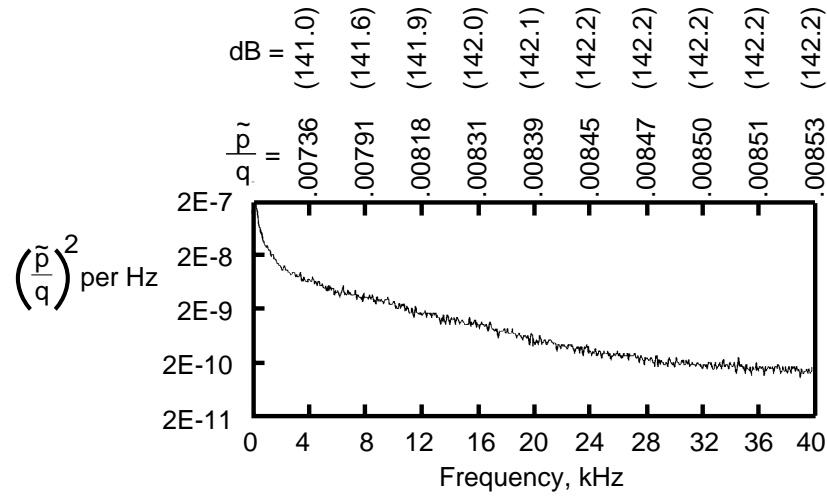
(a) Test section RHS sidewall station 13.
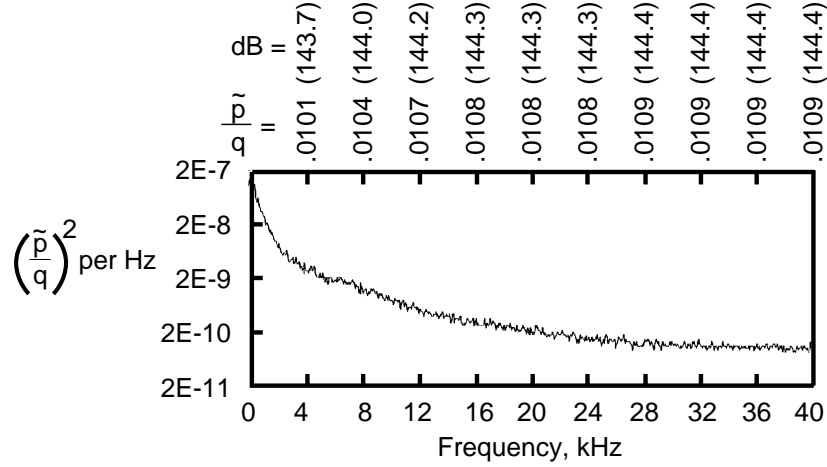
(b) 10.6° cone.

Figure 21. Power spectral density function versus frequency for fluctuating static pressure coefficient. $M = 0.801$; $R = 3.8 \times 10^6$ ft^{-1}; $p_t = 14.92$ psi; $T_t = 121.1°$F; air; dB re 20 μPa.
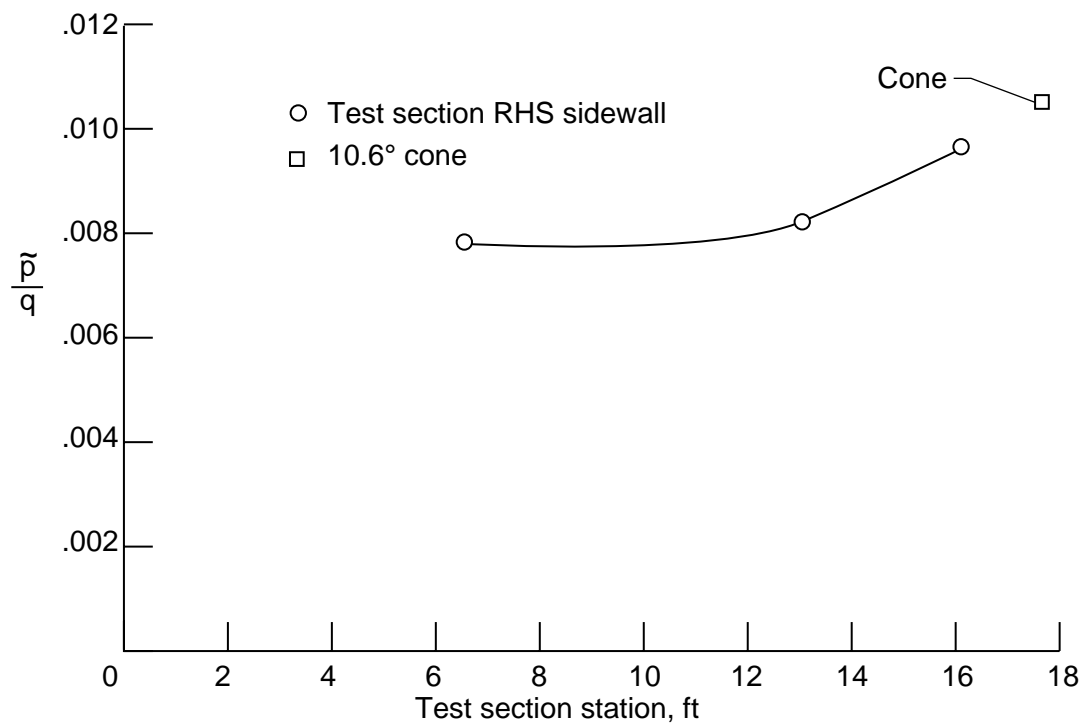
Figure 22. Variation of fluctuating pressure coefficient with streamwise location in test section. $M = 0.8$; $R = 3.8 \times 10^6$ ft^{-1}; minimum R boundary; air mode.
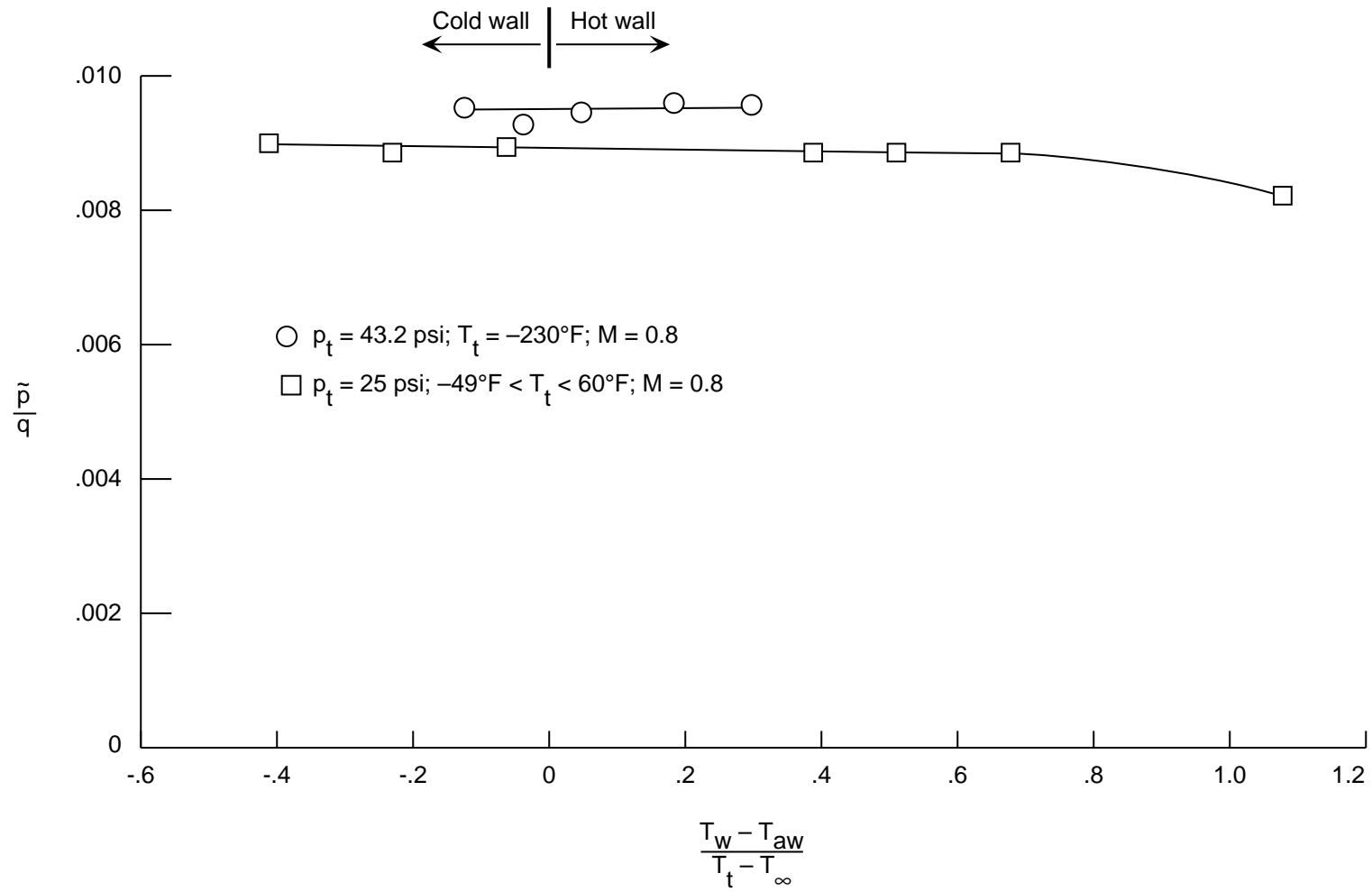
Figure 23. Effect of hot wall and cold wall on fluctuating pressure coefficients at test section RHS sidewall station 13.
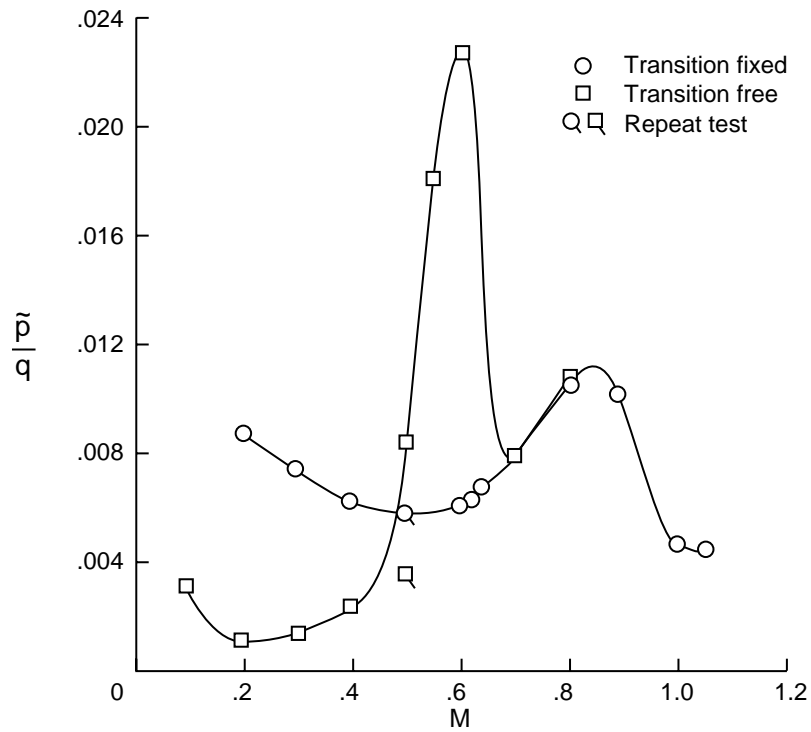
(a) $p_t = 15$ psi; ambient temperature; minimum Reynolds number boundary; air mode.
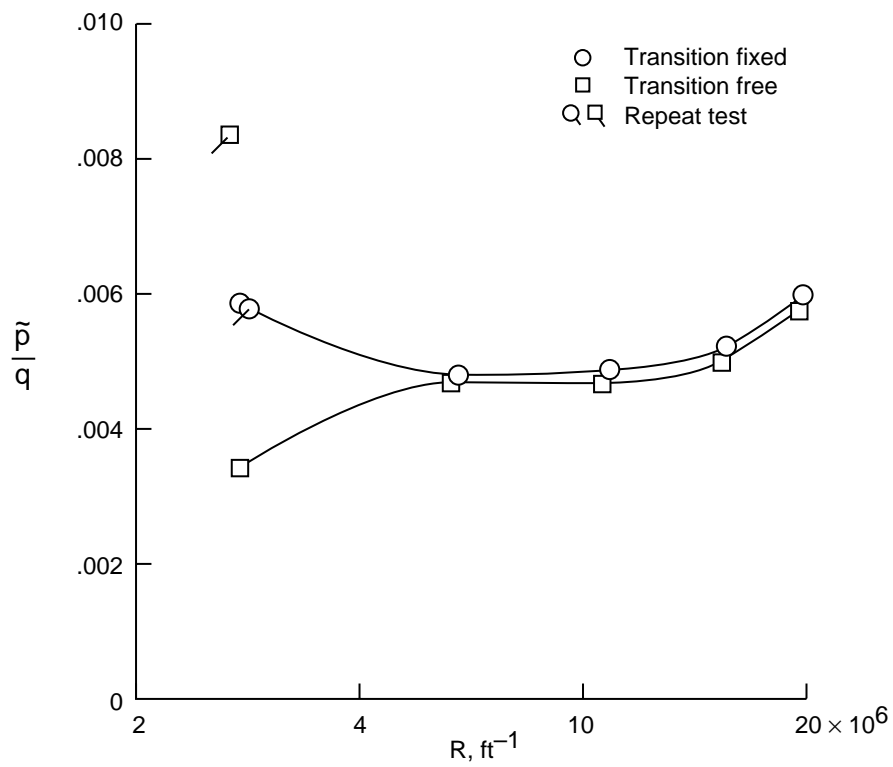
(b) $M = 0.5$; ambient temperature; air mode.

Figure 24. Effect of fixing boundary layer transition on 10.6° cone.
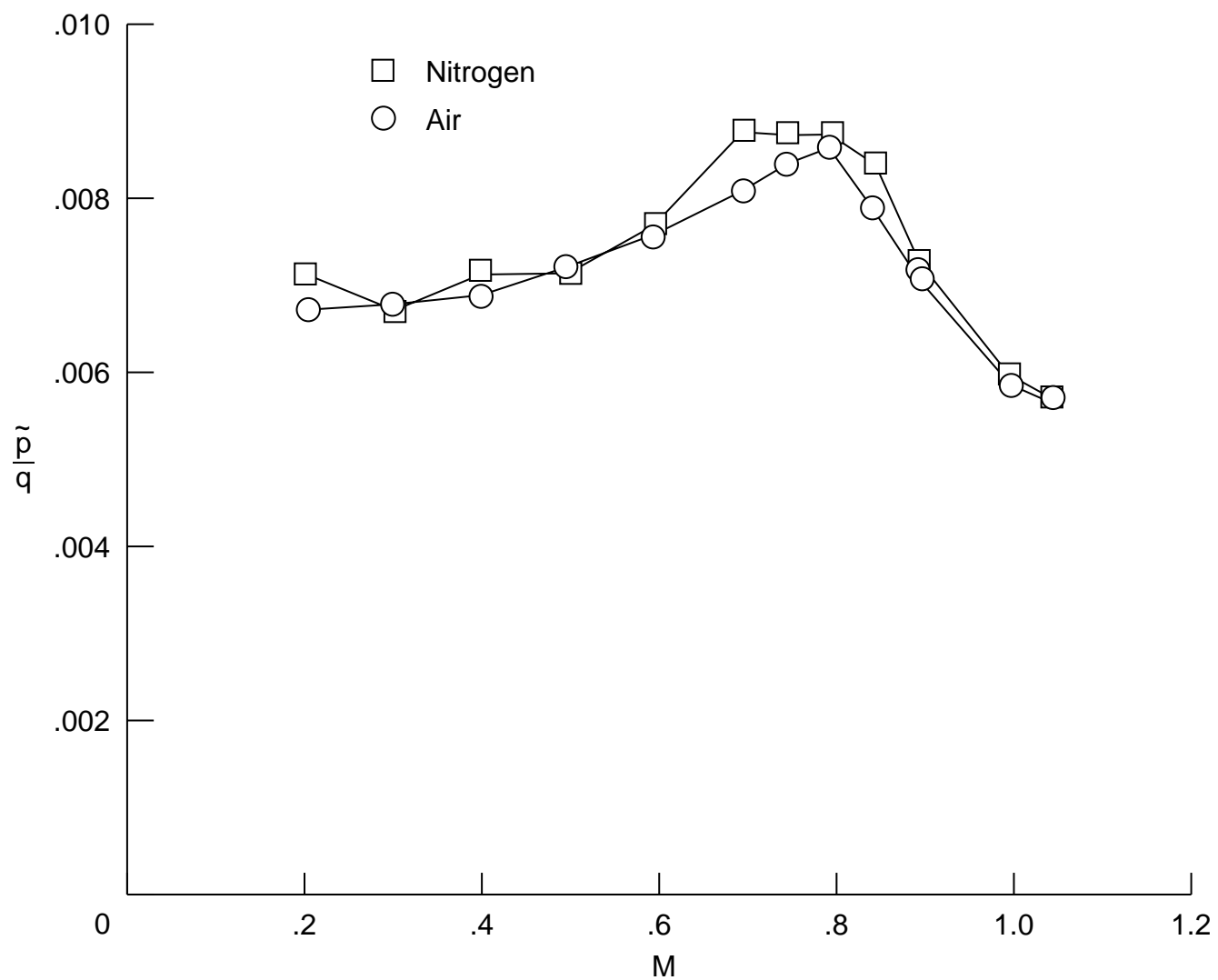
Figure 25. Fluctuating pressure coefficient measured at test section RHS sidewall station 13. $R = 6 \times 10^6$ ft^{-1}; ambient temperature; air and nitrogen modes.
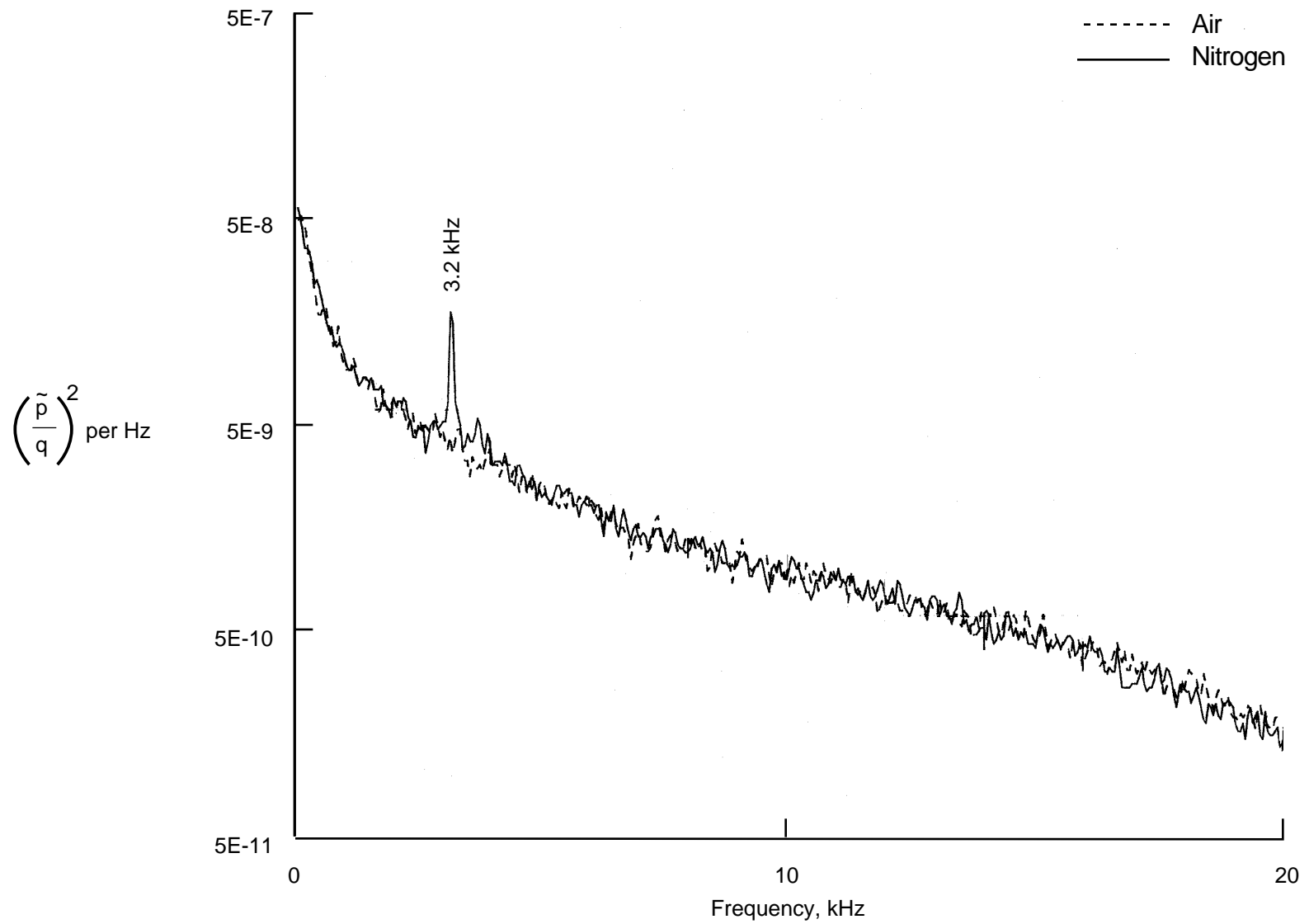
(a) $M = 0.2$.

Figure 26. Power spectra of fluctuating pressure coefficient at test section RHS sidewall station 13. $R = 6 \times 10^6$ ft^{-1}; ambient temperature; air and nitrogen modes.

$$\left(\frac{\tilde{p}}{q}\right)^2 \text{per Hz}$$
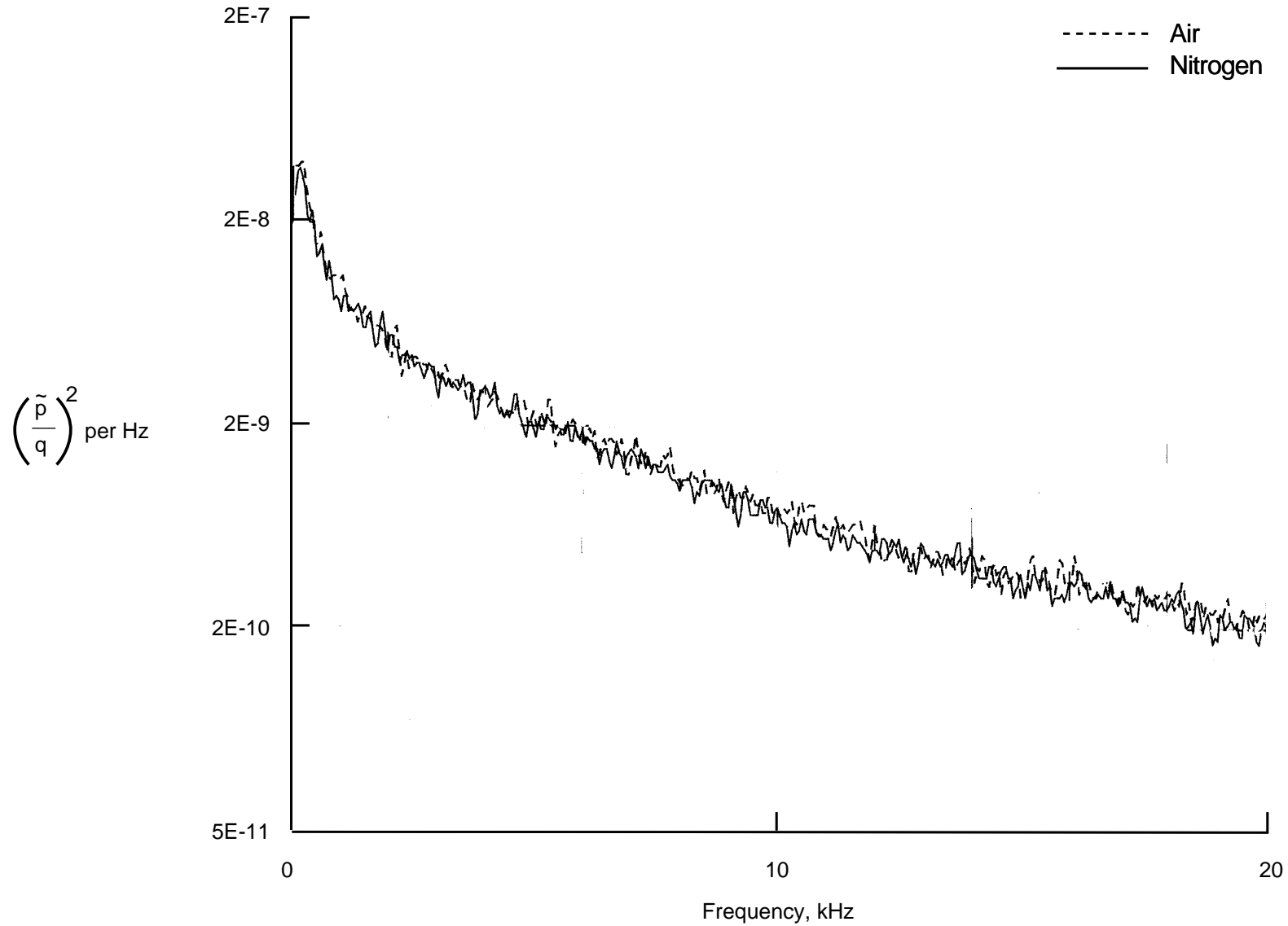
(b) $M = 0.3$.

Figure 26. Continued.
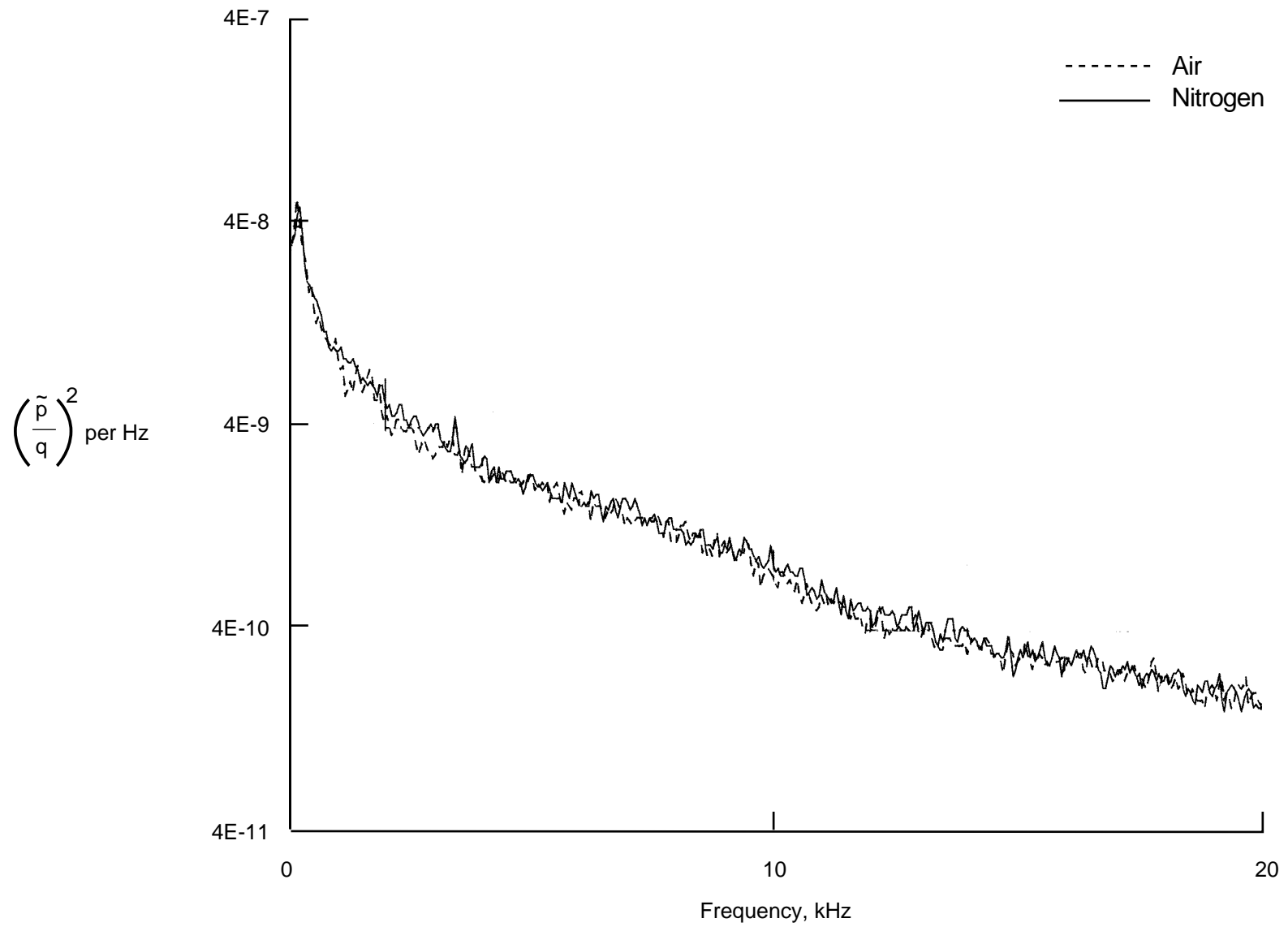
(c) $M = 0.4$.

Figure 26. Continued.
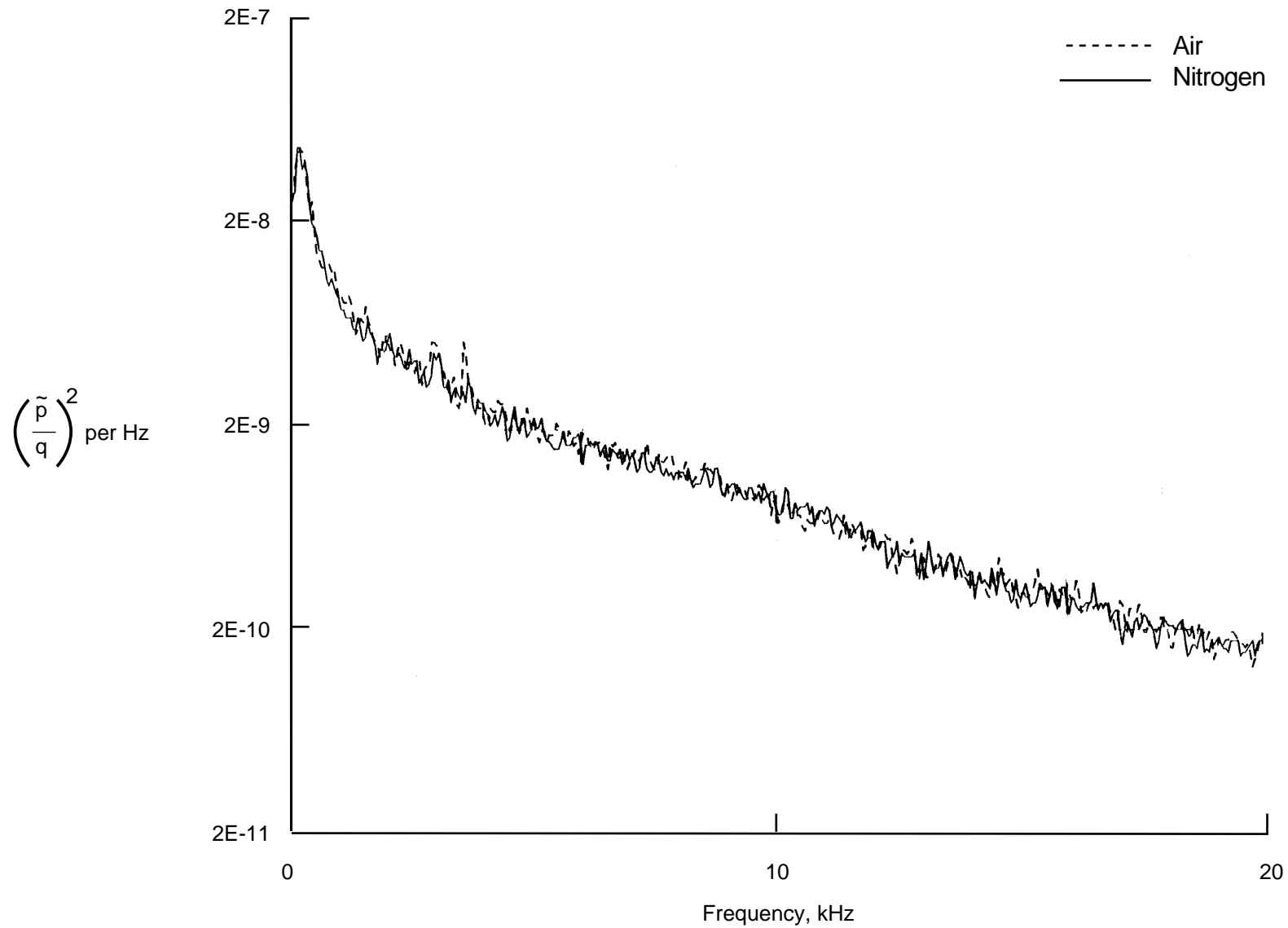
(d) $M = 0.5$.

Figure 26. Continued.
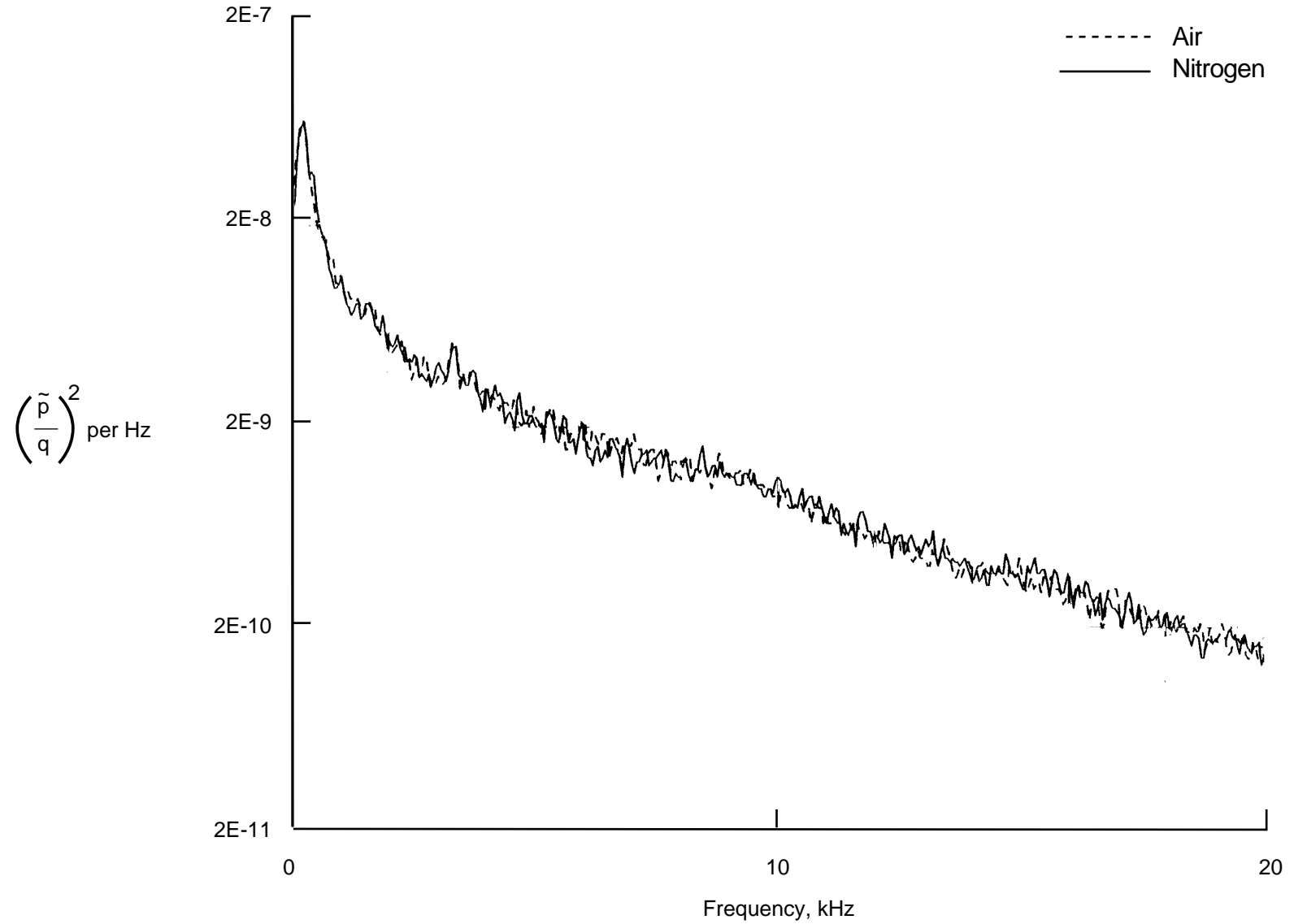
(e) $M = 0.6$.

Figure 26. Continued.
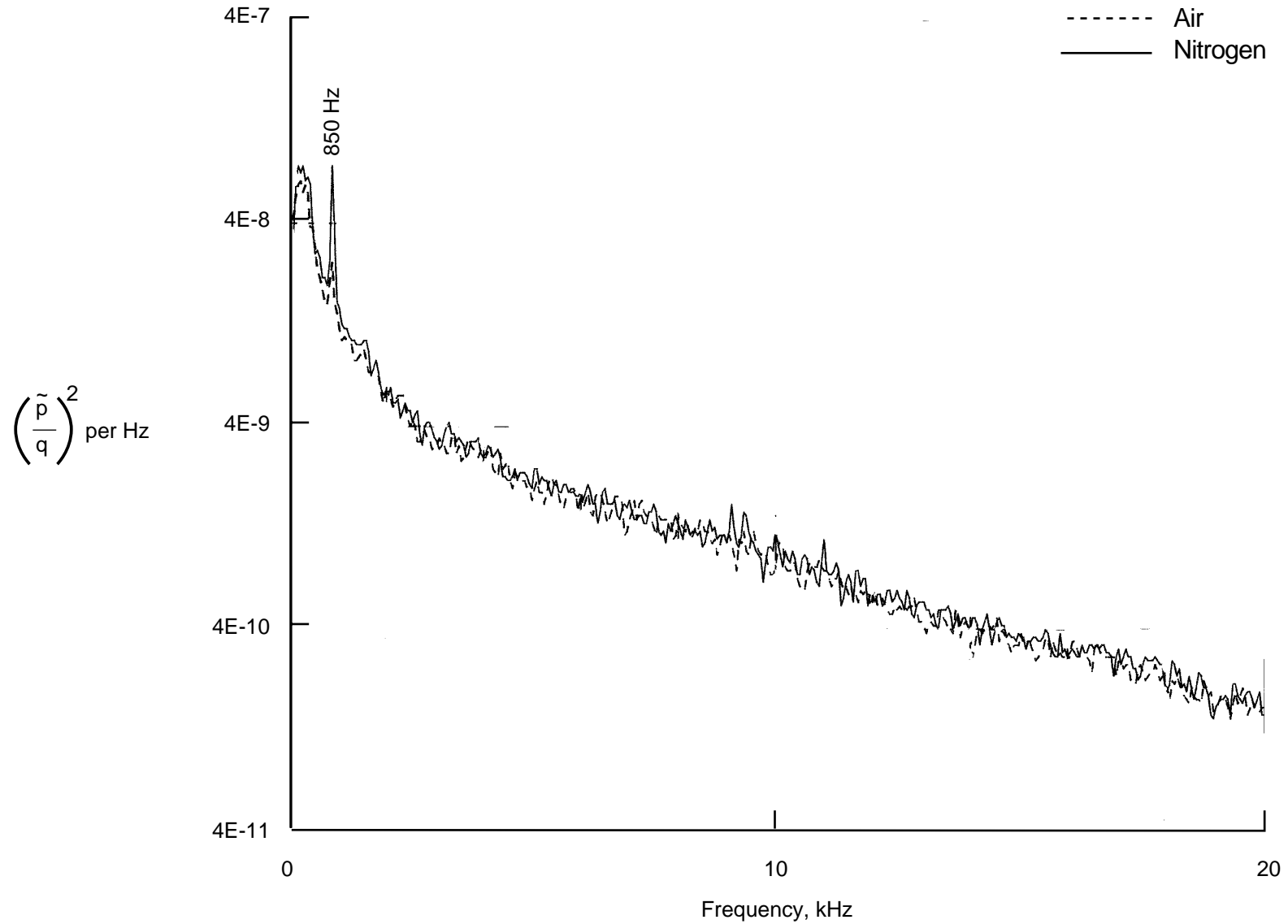
(f) $M = 0.7$.

Figure 26. Continued.
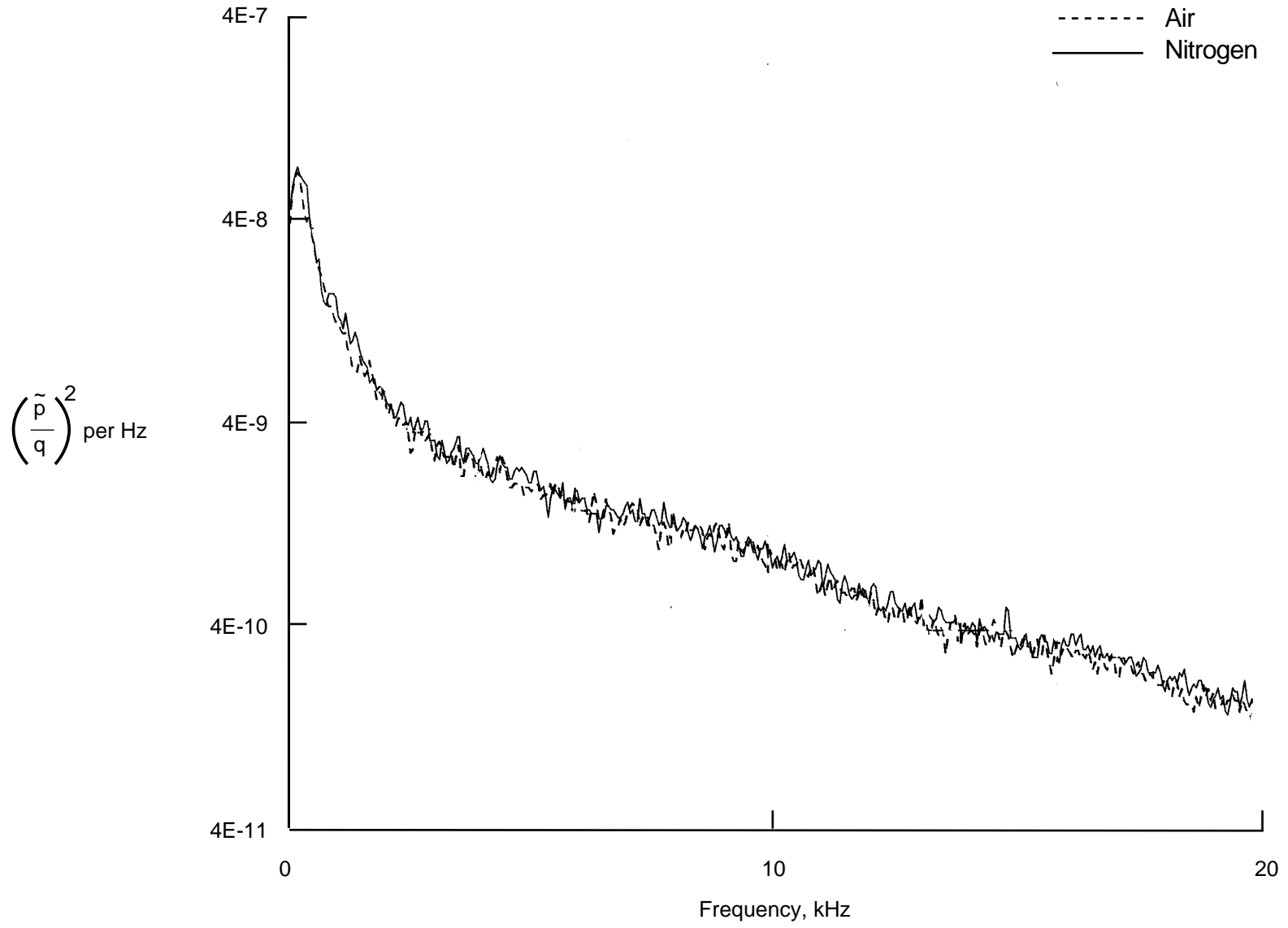
(g) $M = 0.75$.

Figure 26. Continued.

$$\left(\frac{\tilde{p}}{q}\right)^2 \text{per Hz}$$

(h) $M = 0.8$.

Figure 26. Continued.

$$\left(\frac{\tilde{p}}{q}\right)^2 \text{ per Hz}$$

Legend:
- - - - - - Air
———— Nitrogen

Frequency, kHz
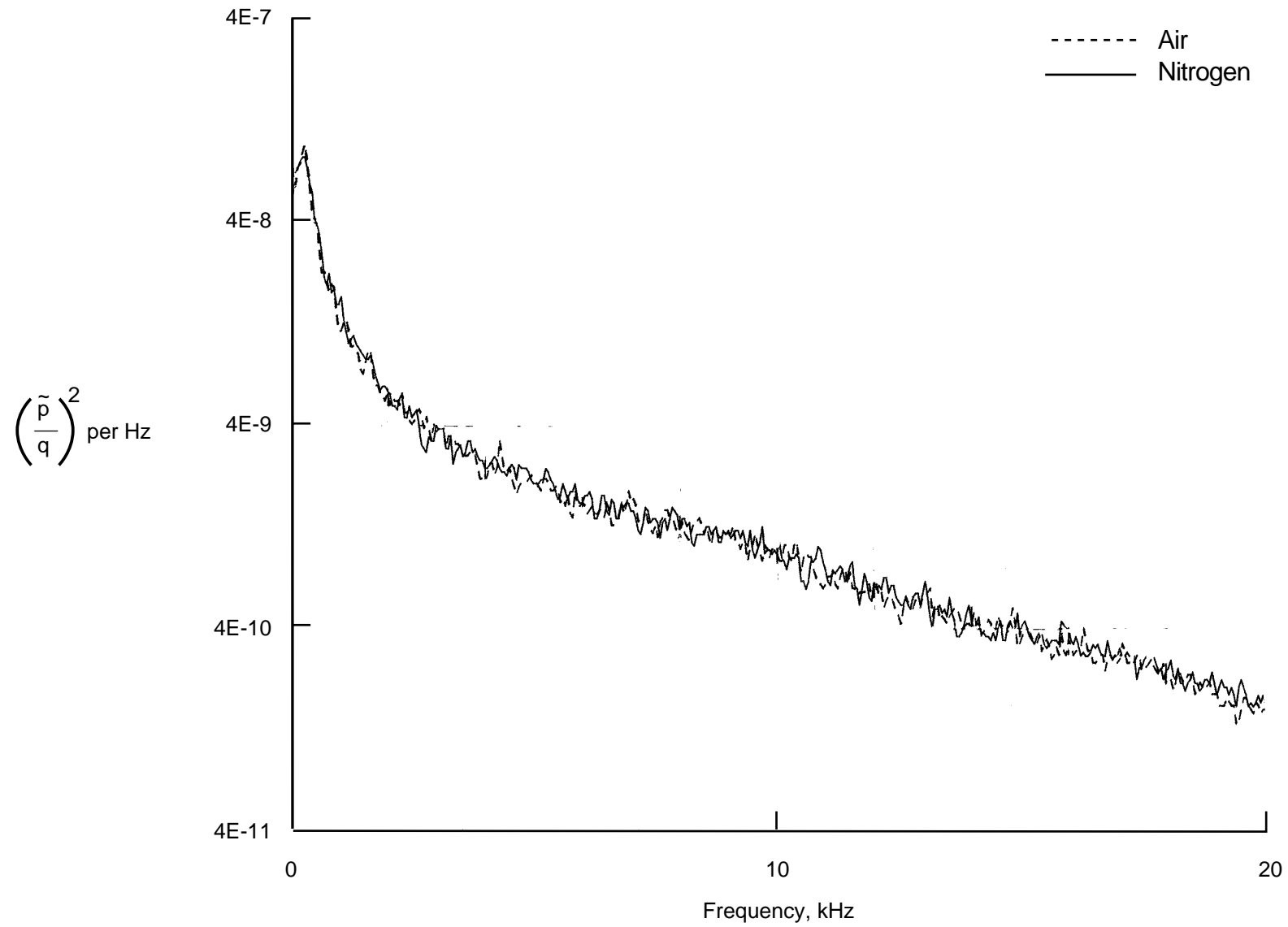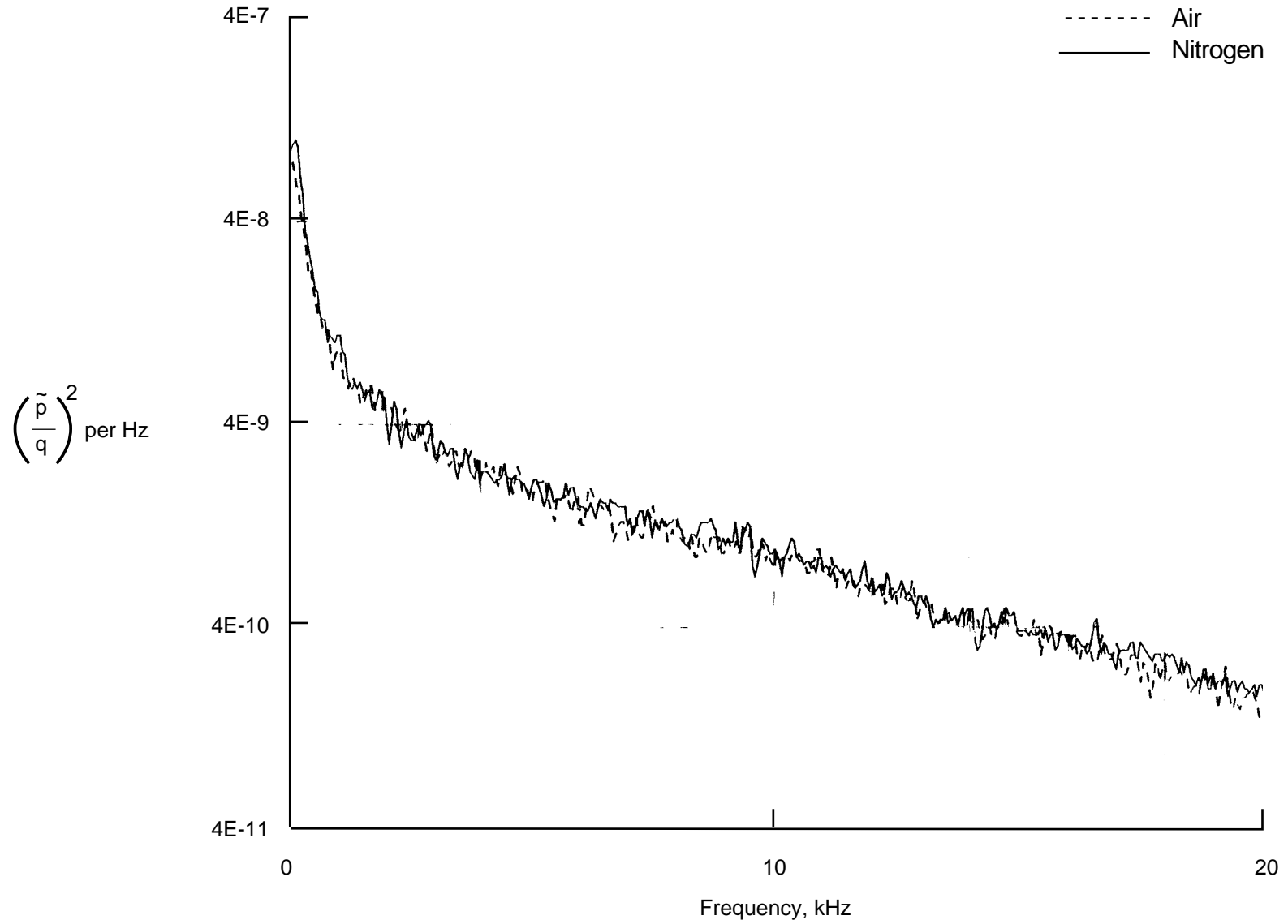
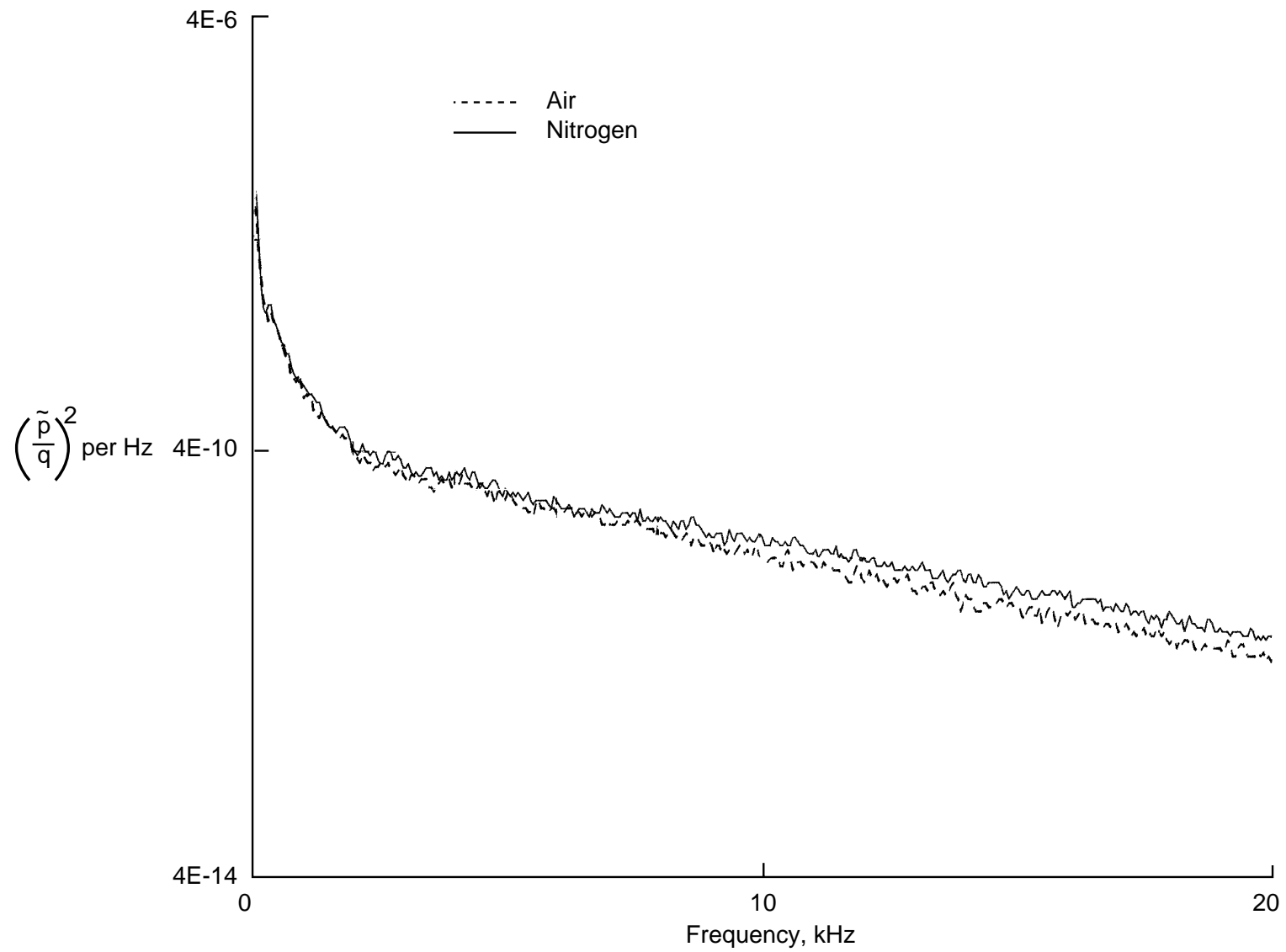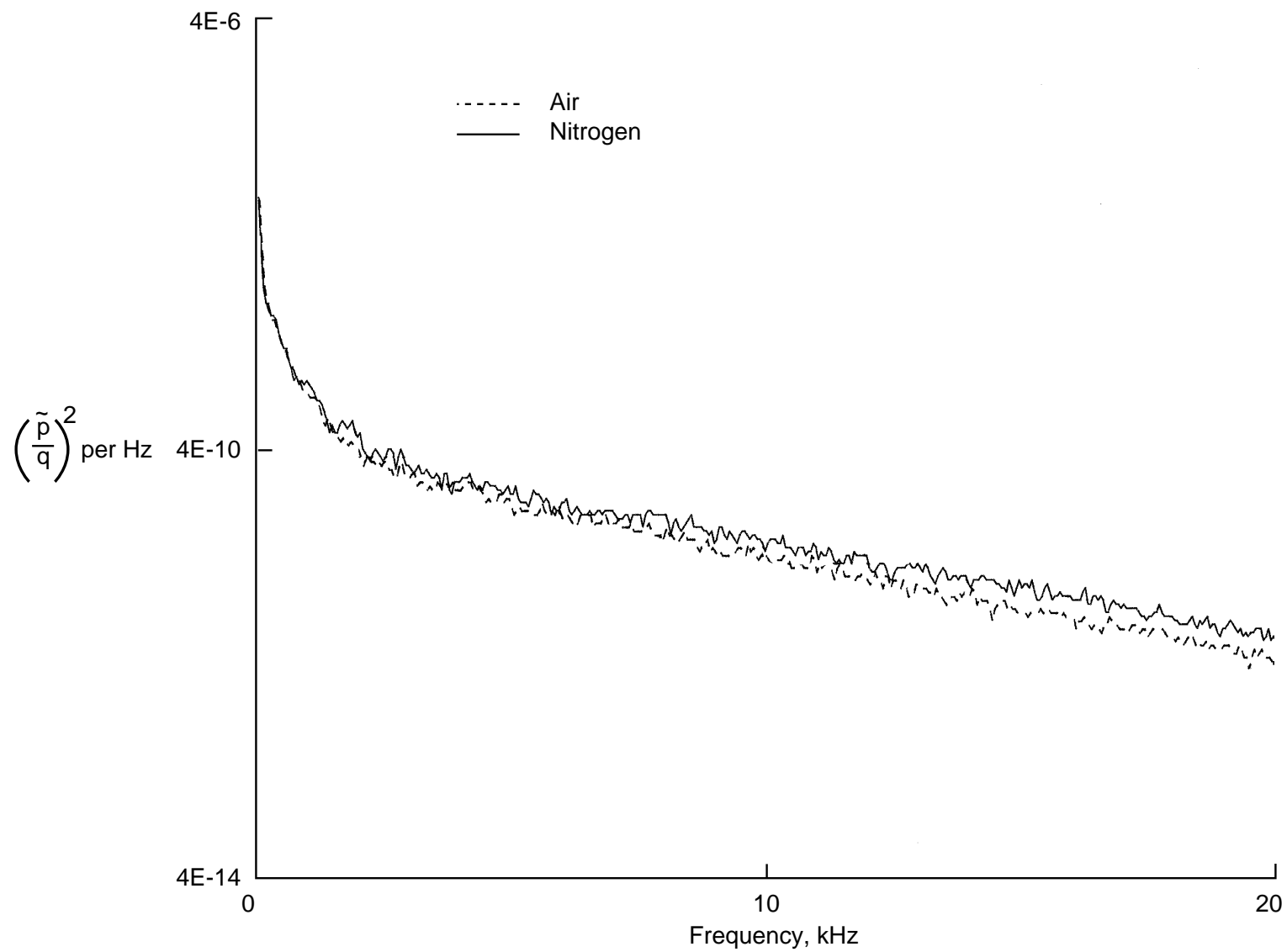(i) $M = 0.85$.

Figure 26. Continued.
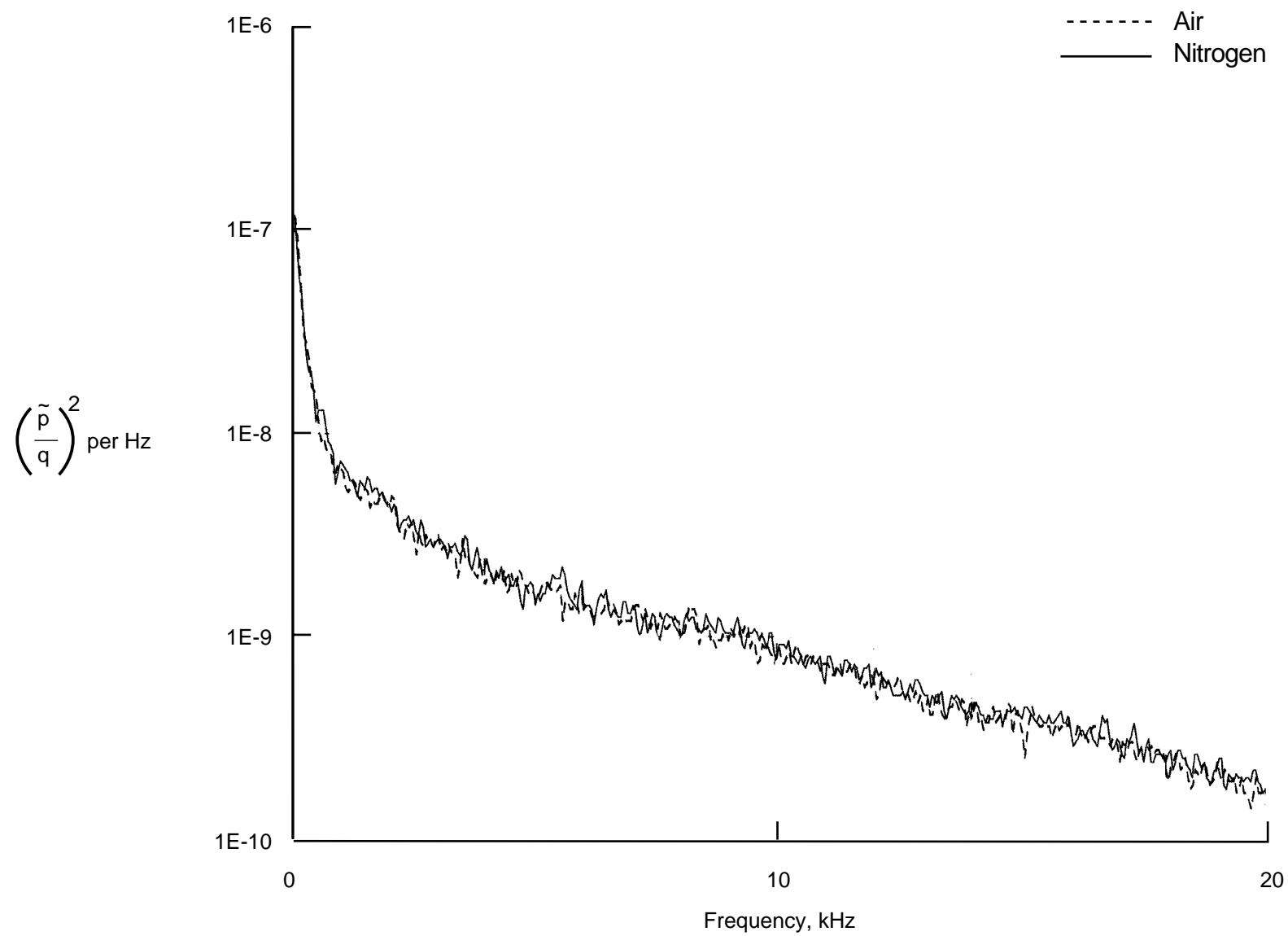
(j) $M = 0.9$.

Figure 26. Continued.
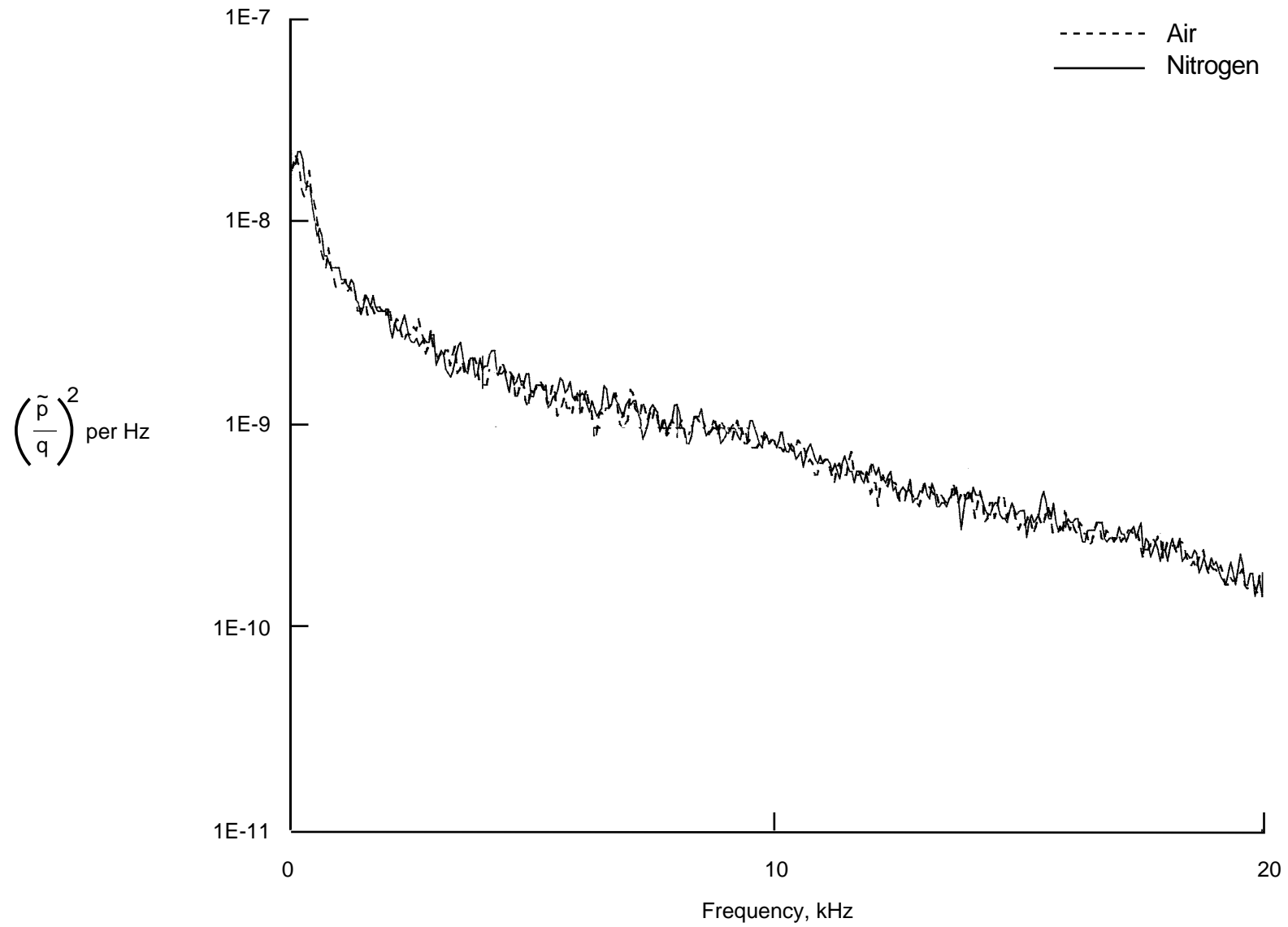
(k) $M = 1.0$.

Figure 26. Continued.
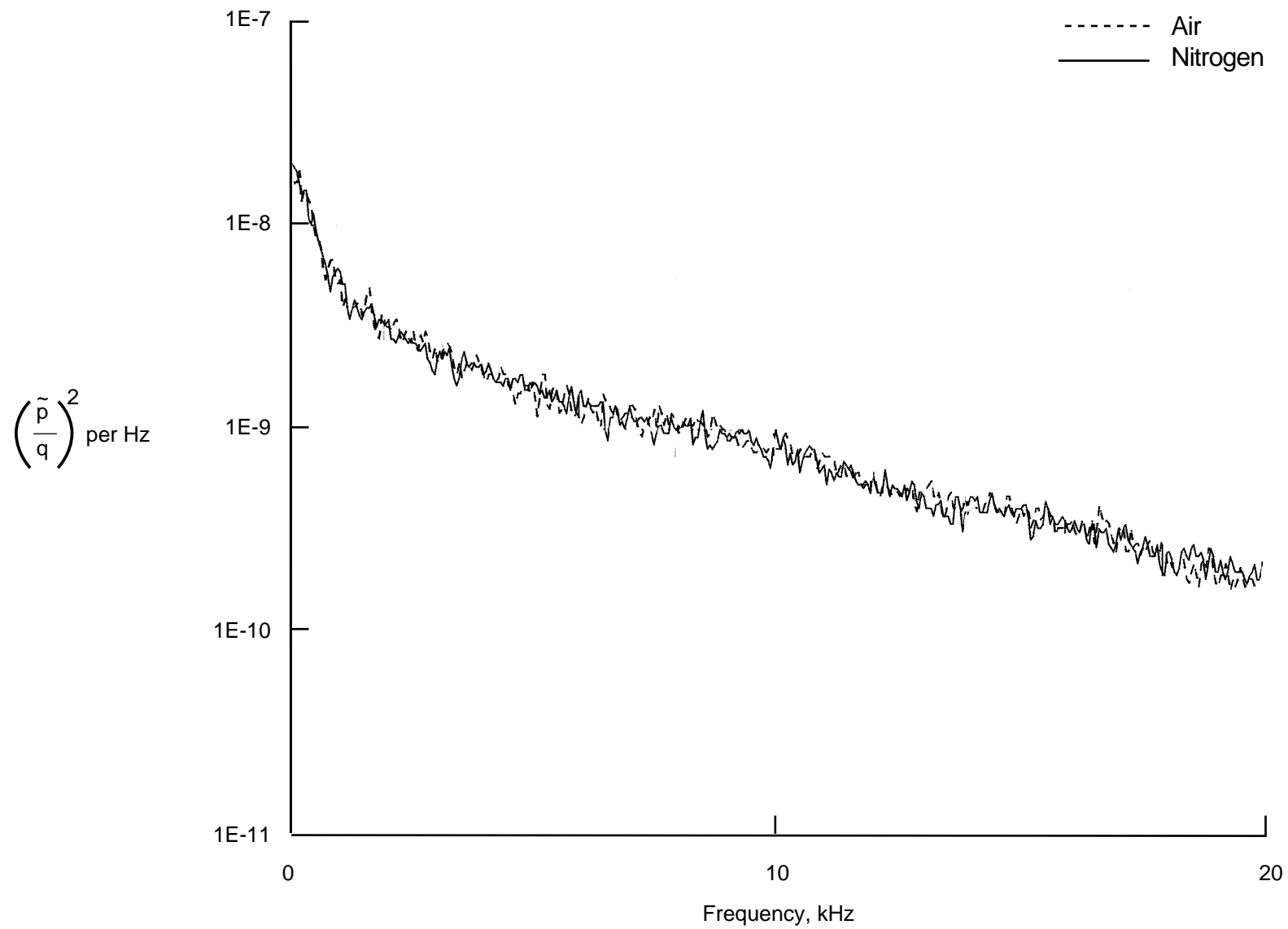
(l) $M = 1.05$.

Figure 26. Concluded.
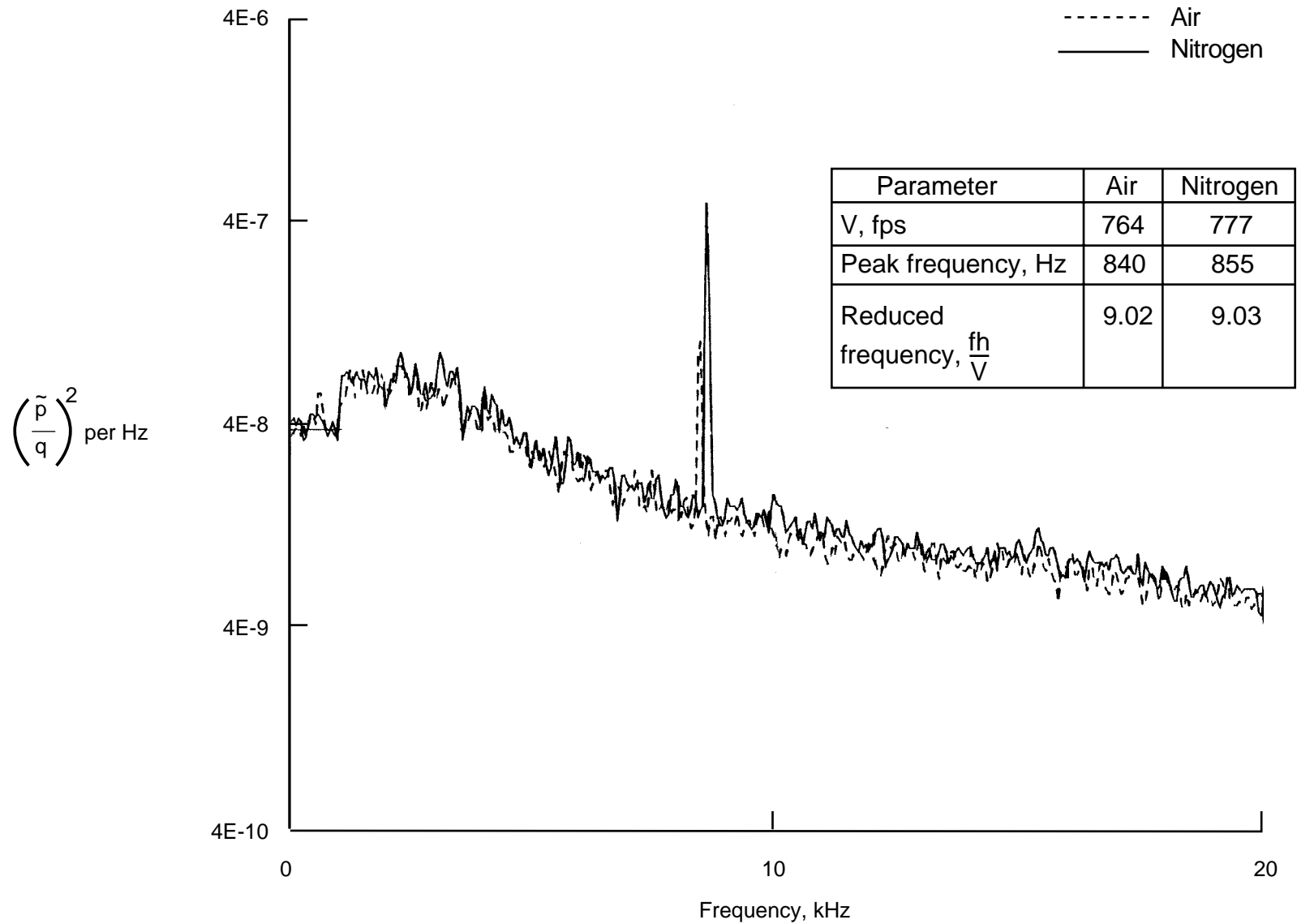
Figure 27. Power spectra of fluctuating pressure coefficient at test section RHS sidewall station 13. $M = 0.7$; $R = 6 \times 10^6$ ft^{-1}; ambient temperature; air and nitrogen modes.
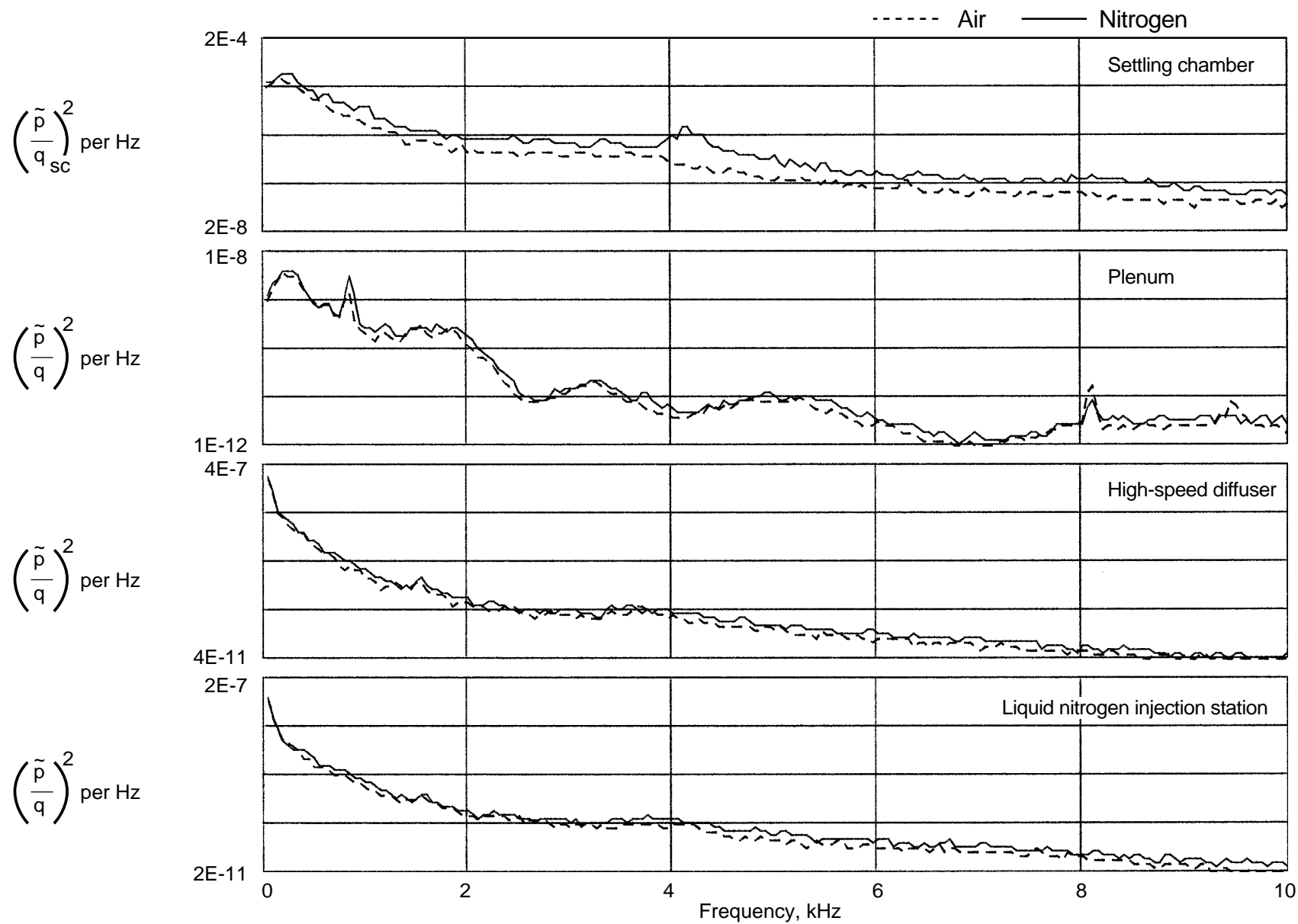
Figure 28. Power spectra of fluctuating pressure coefficient in settling chamber, plenum, high-speed diffuser, and liquid nitrogen injection station. $M = 0.7$; $R = 6 \times 10^6$ ft^{-1}; ambient temperature; air and nitrogen modes.
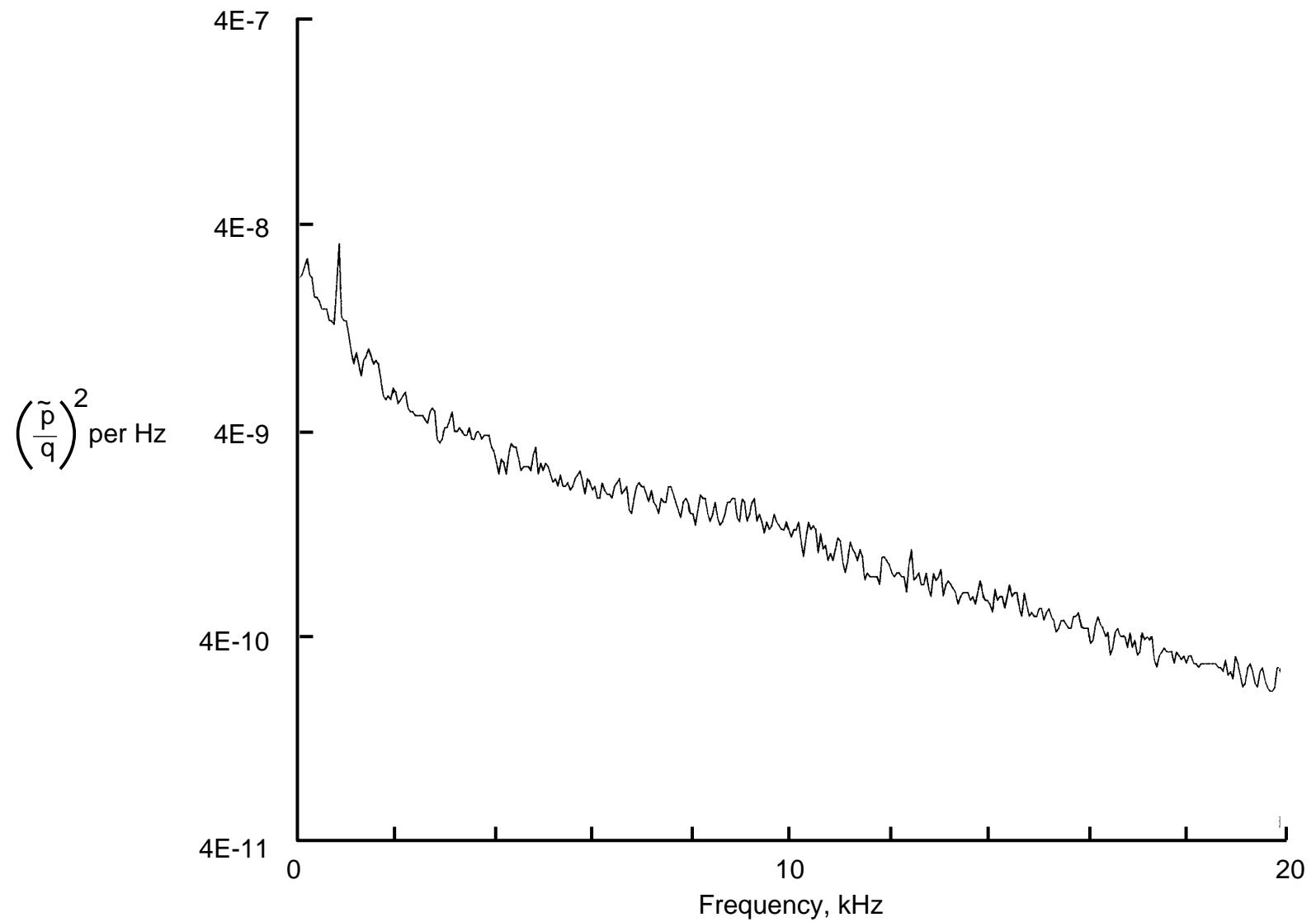
Figure 29. Power spectra of fluctuating pressure coefficient at test section RHS sidewall station 13. $M = 0.7$; minimum Reynolds number boundary; slots covered; air mode.
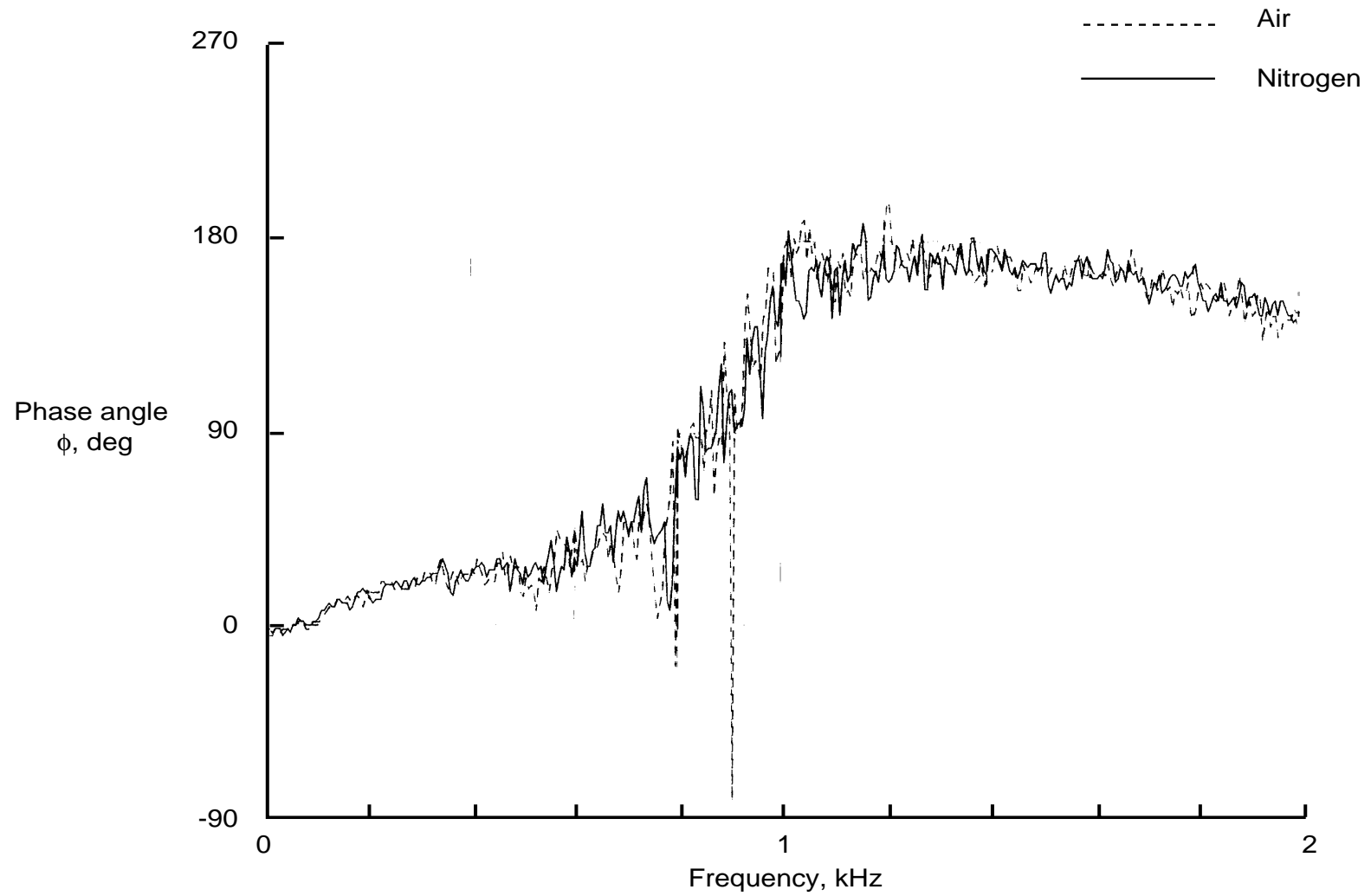
(a) Phase angle.

Figure 30. Phase angle and coherence of disturbance signal between adjacent pressure transducers at test section RHS sidewall station 13. $M = 0.7$; $R = 6 \times 10^6$ ft^{-1}; ambient temperature; comparison of air and nitrogen modes.
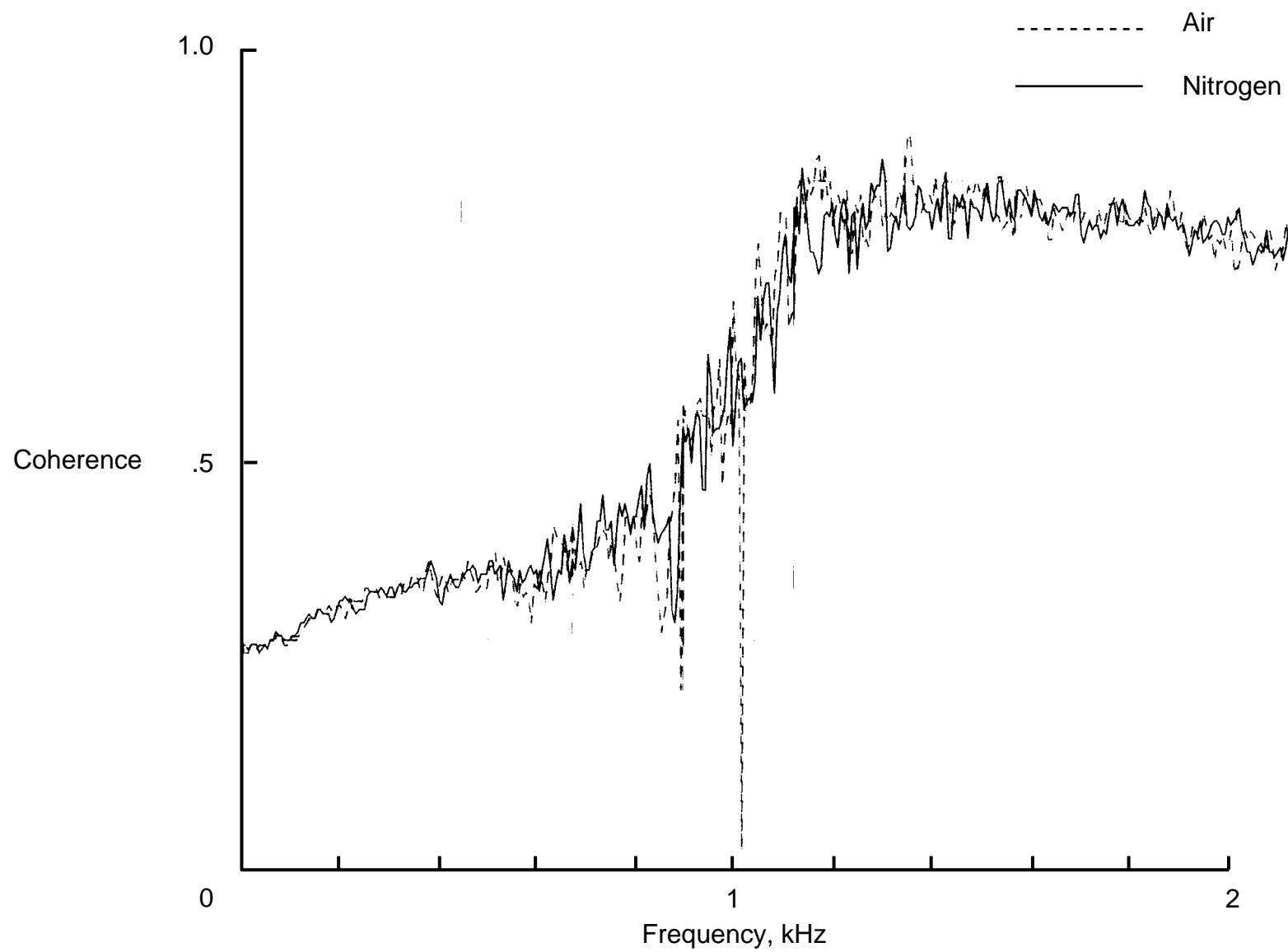
(b) Coherence.

Figure 30. Concluded.
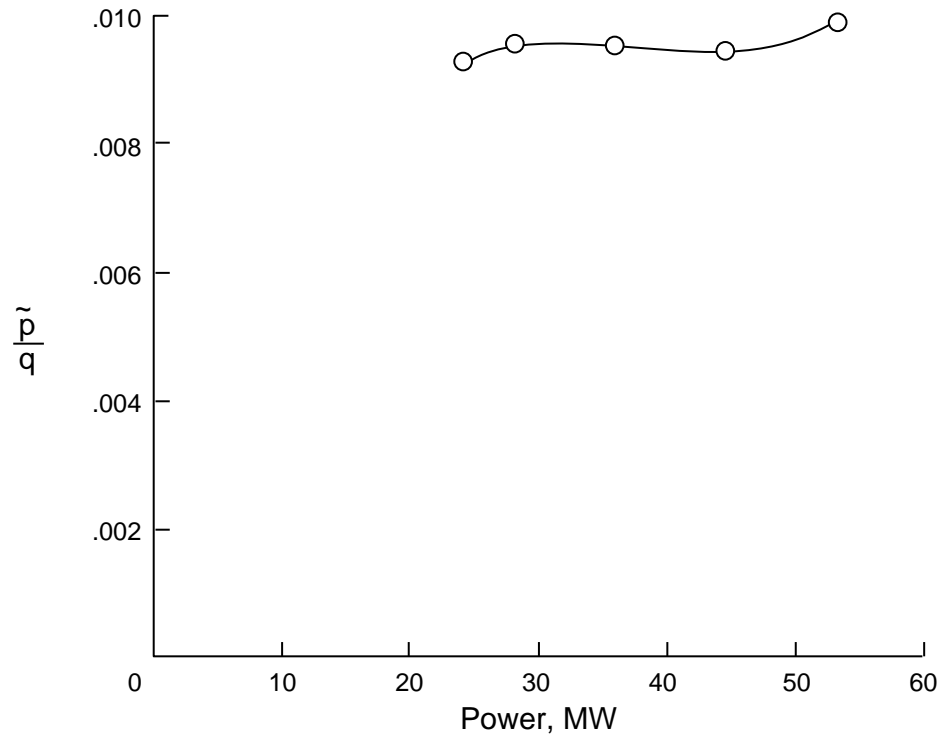
Figure 31. Effect of fan drive power variation on fluctuating pressure coefficient at test section RHS sidewall station 13. $M = 0.8; R = 39.7 \times 10^6$ ft^{-1}.
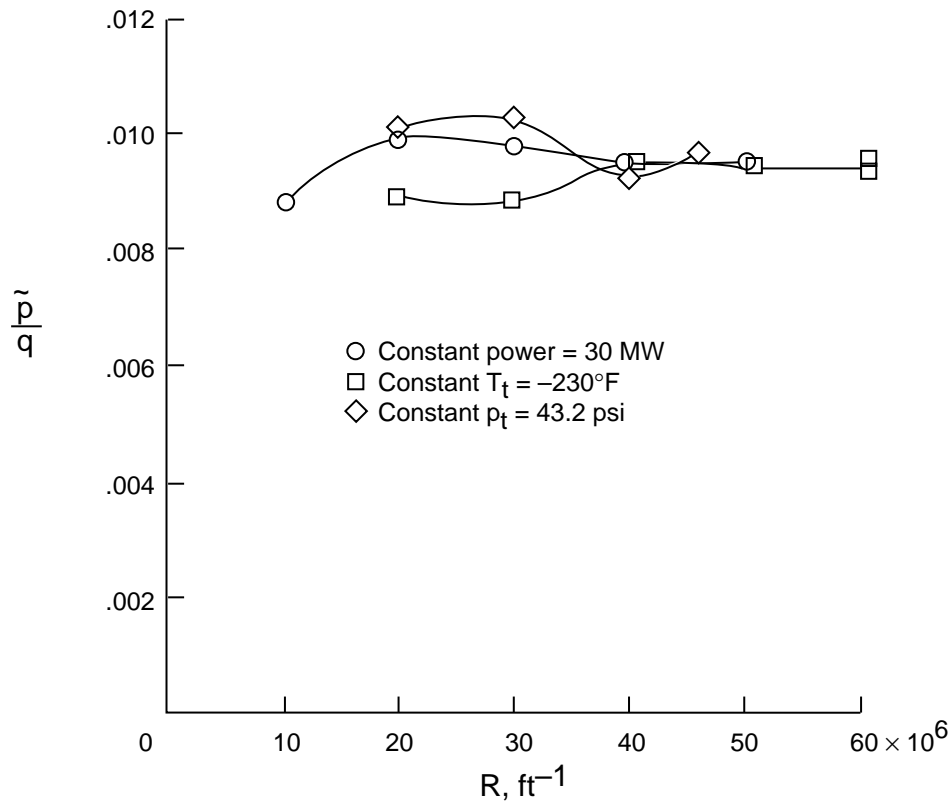
Figure 32. Fluctuating pressure coefficient at test section RHS sidewall station 13. $M = 0.8$; nitrogen mode.
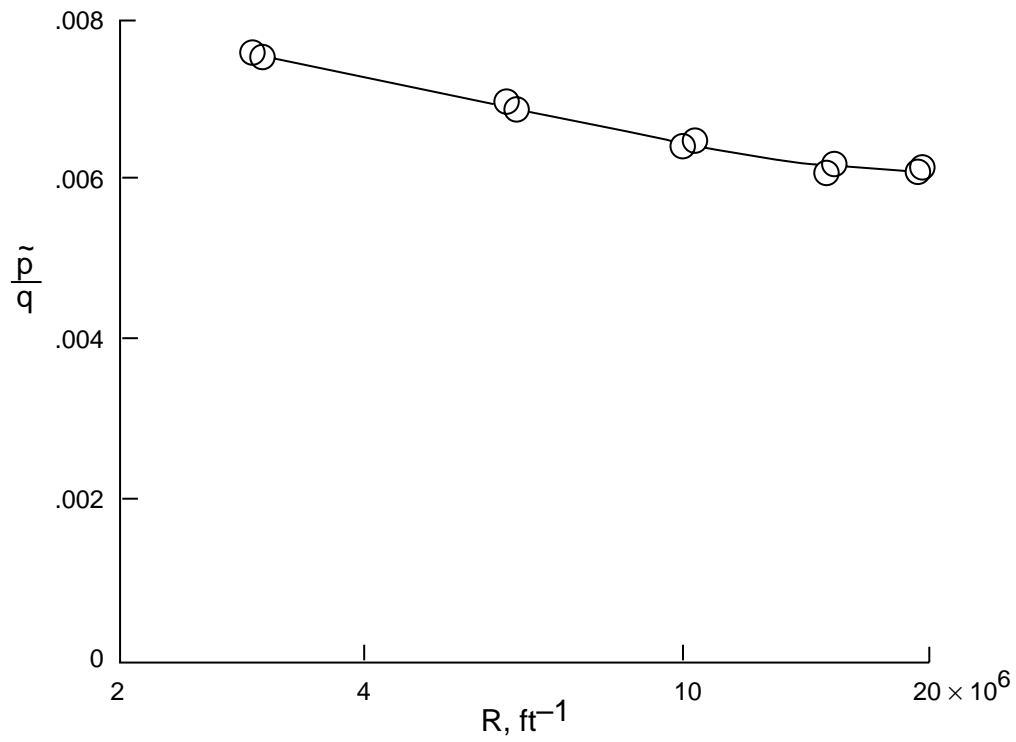
Figure 33. Fluctuating pressure coefficient at test section RHS sidewall station 13. $M = 0.5$; air mode; ambient temperature.
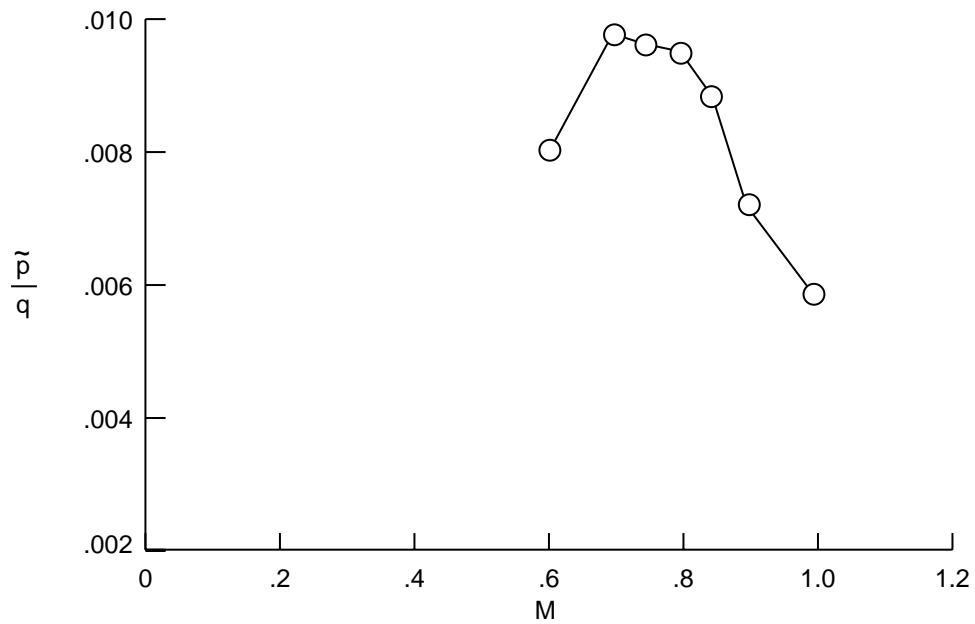
Figure 34. Fluctuating pressure coefficient at test section RHS sidewall station 13. $R = 40 \times 10^6$ ft^{-1}; fan drive power = 30 MW.
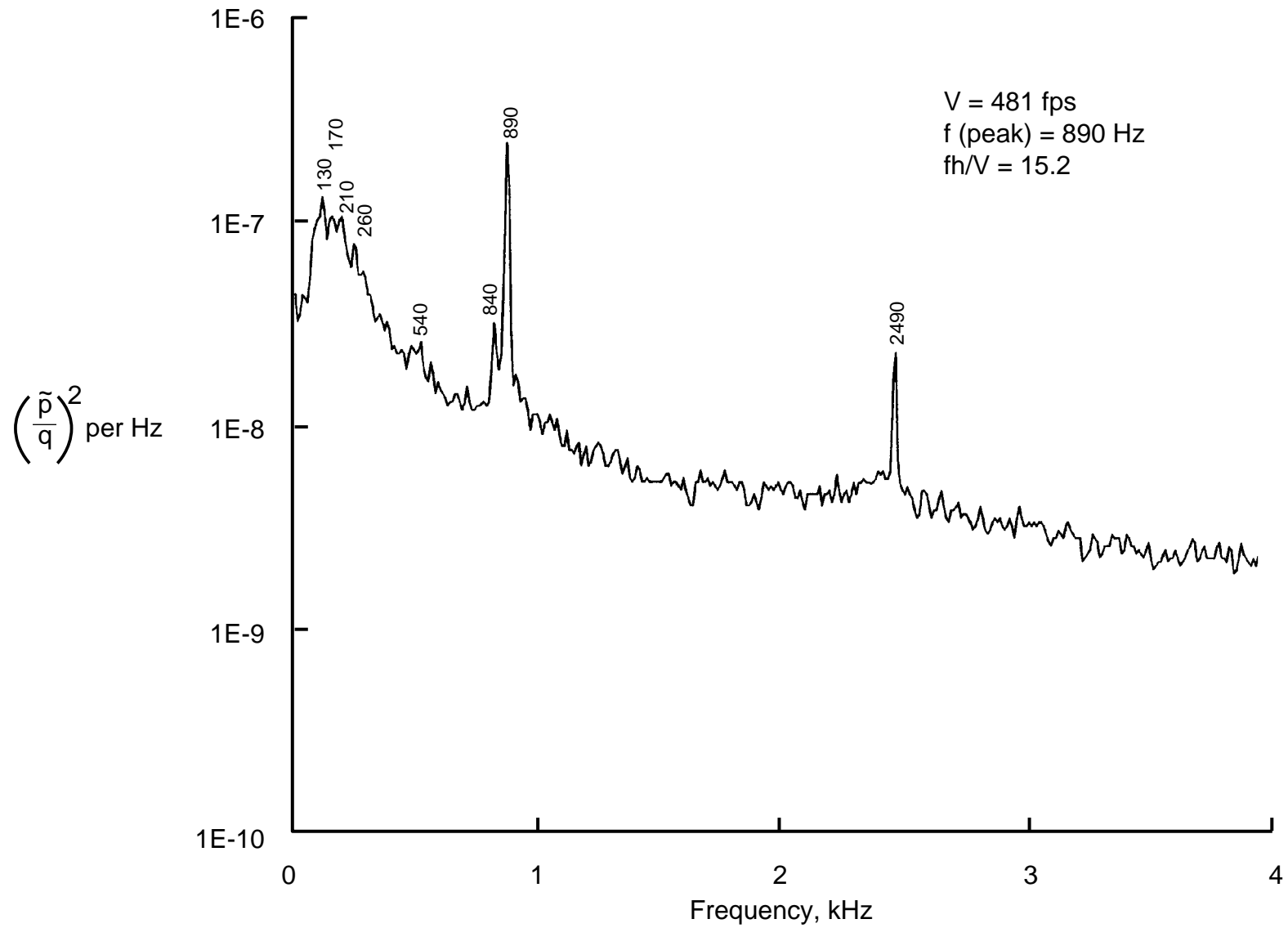
(a) $M = 0.598.$

Figure 35. Power spectra of fluctuating pressure coefficient at test section RHS sidewall station 13. $R = 40 \times 10^6$ ft^{-1}; fan drive power = 30 MW.
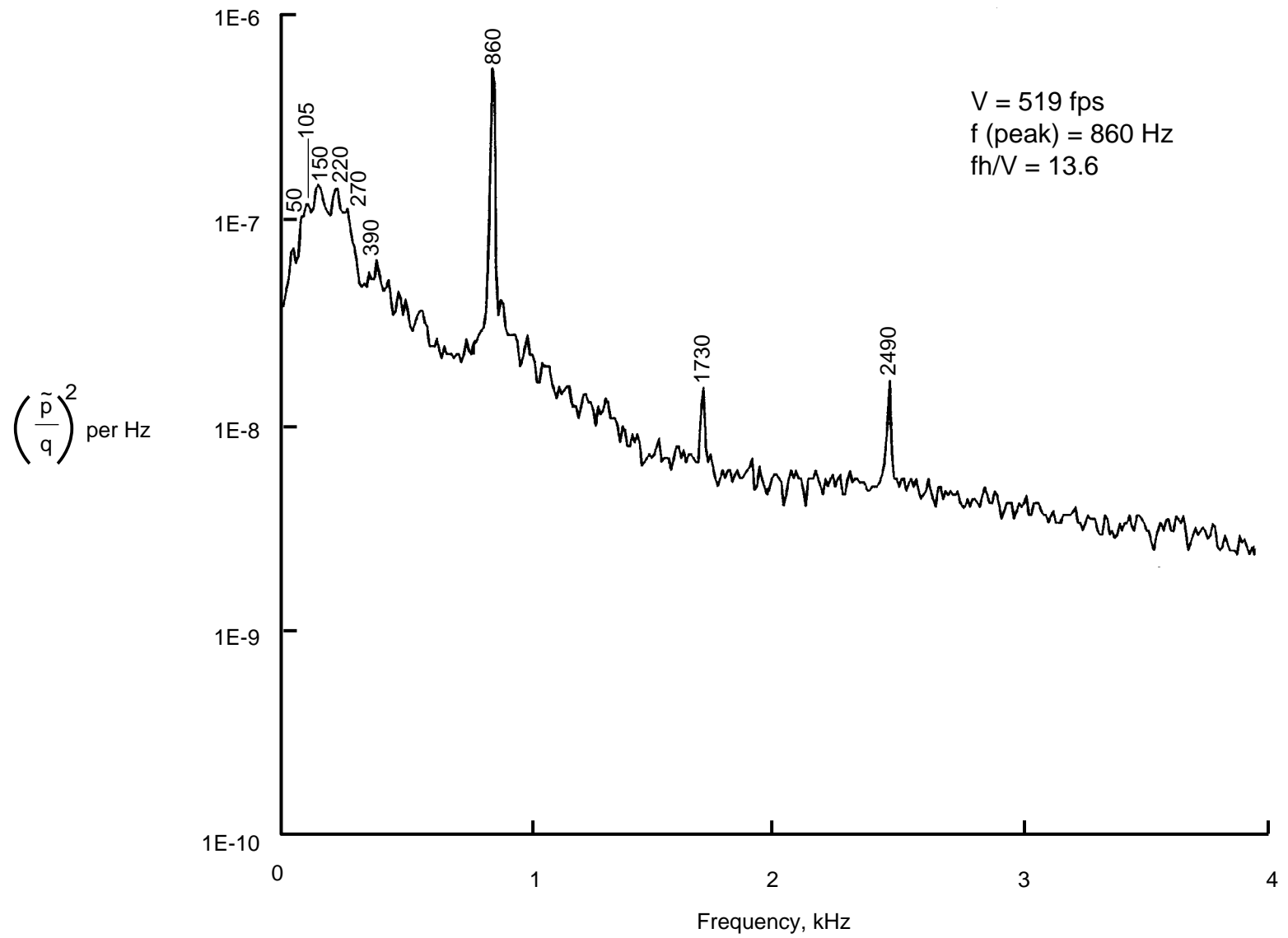
(b) $M = 0.694$.

Figure 35. Continued.
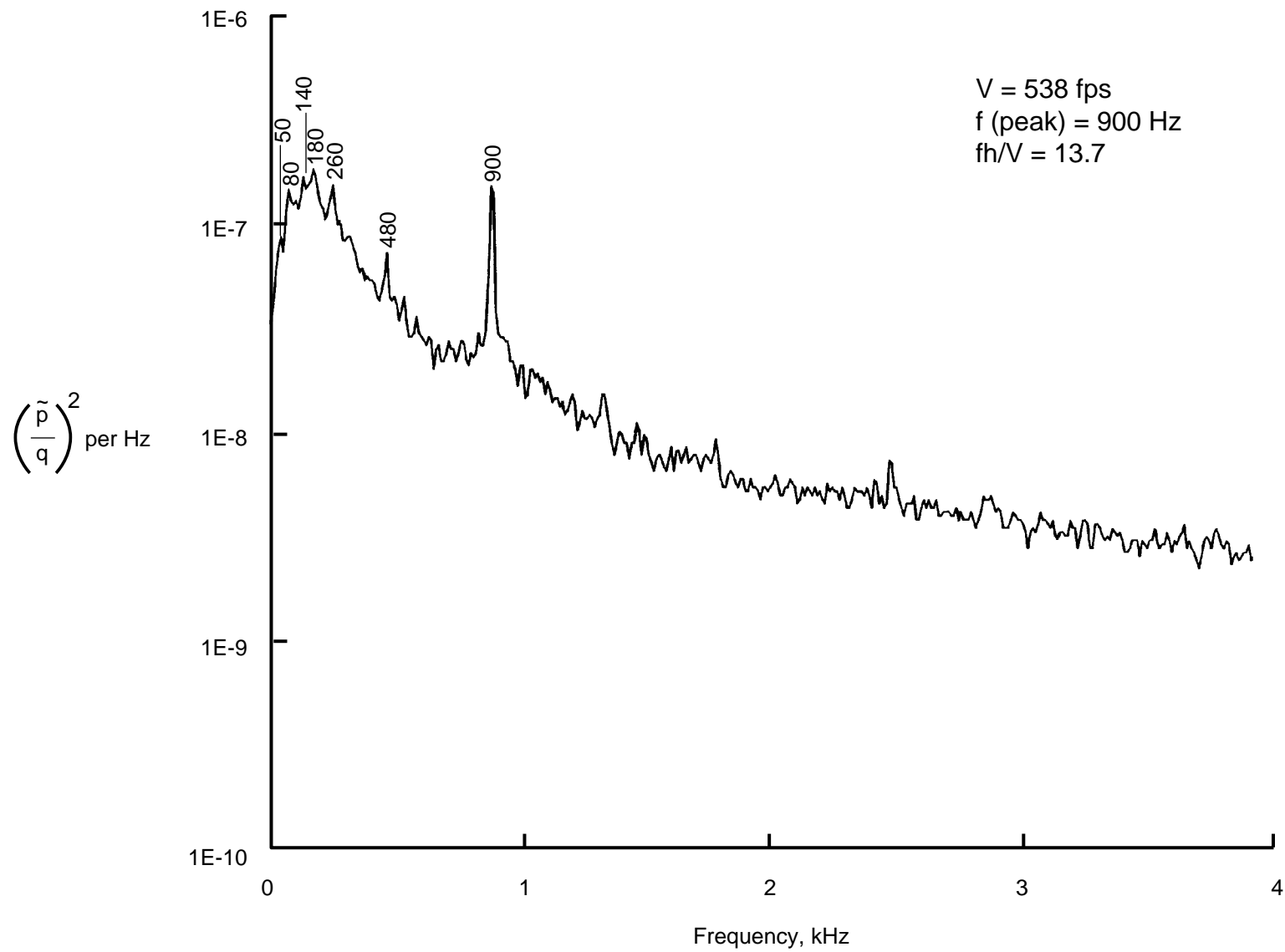
(c) *M* = 0.742.

Figure 35. Continued.
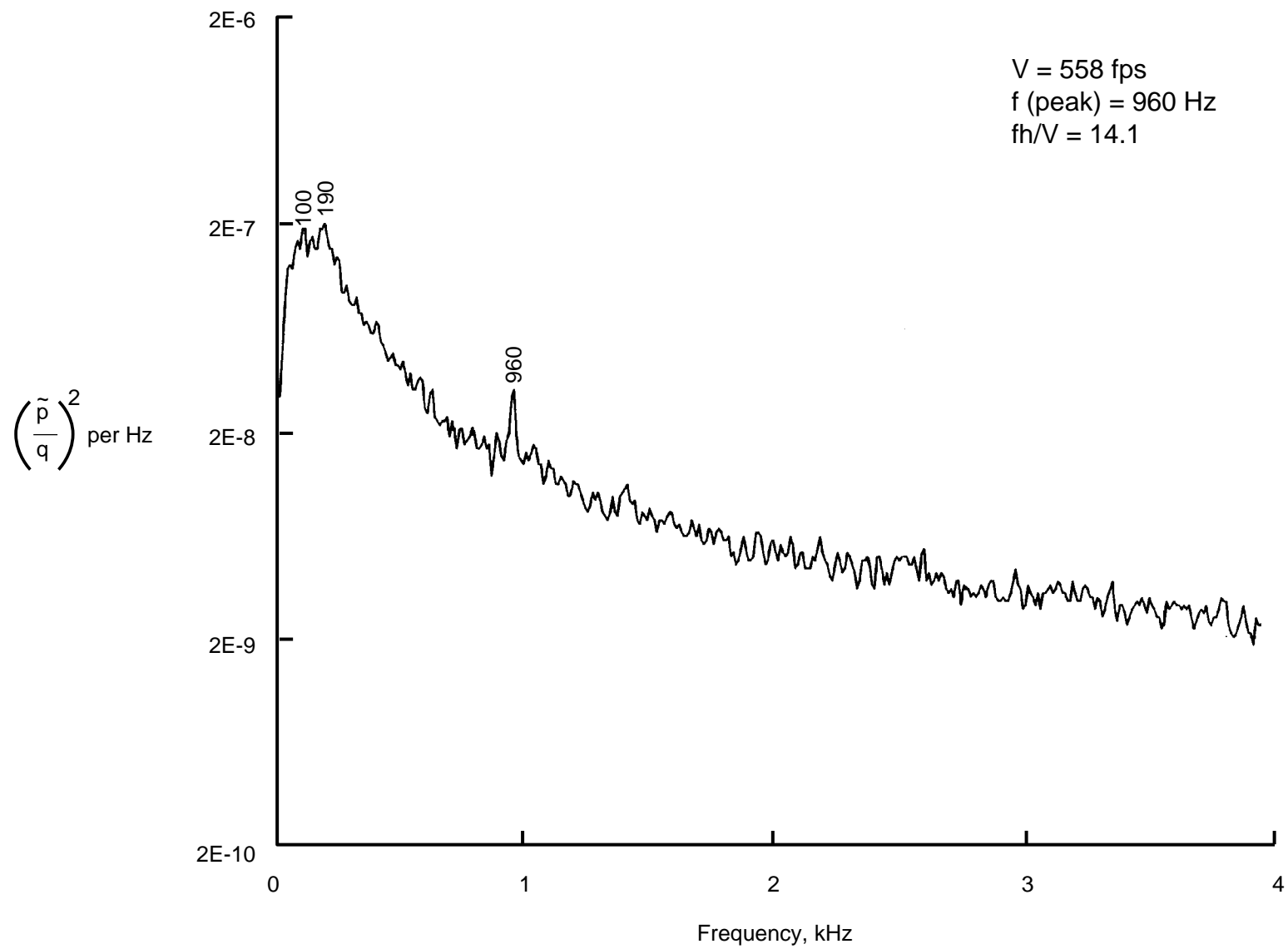
(d) $M = 0.793$.

Figure 35. Continued.
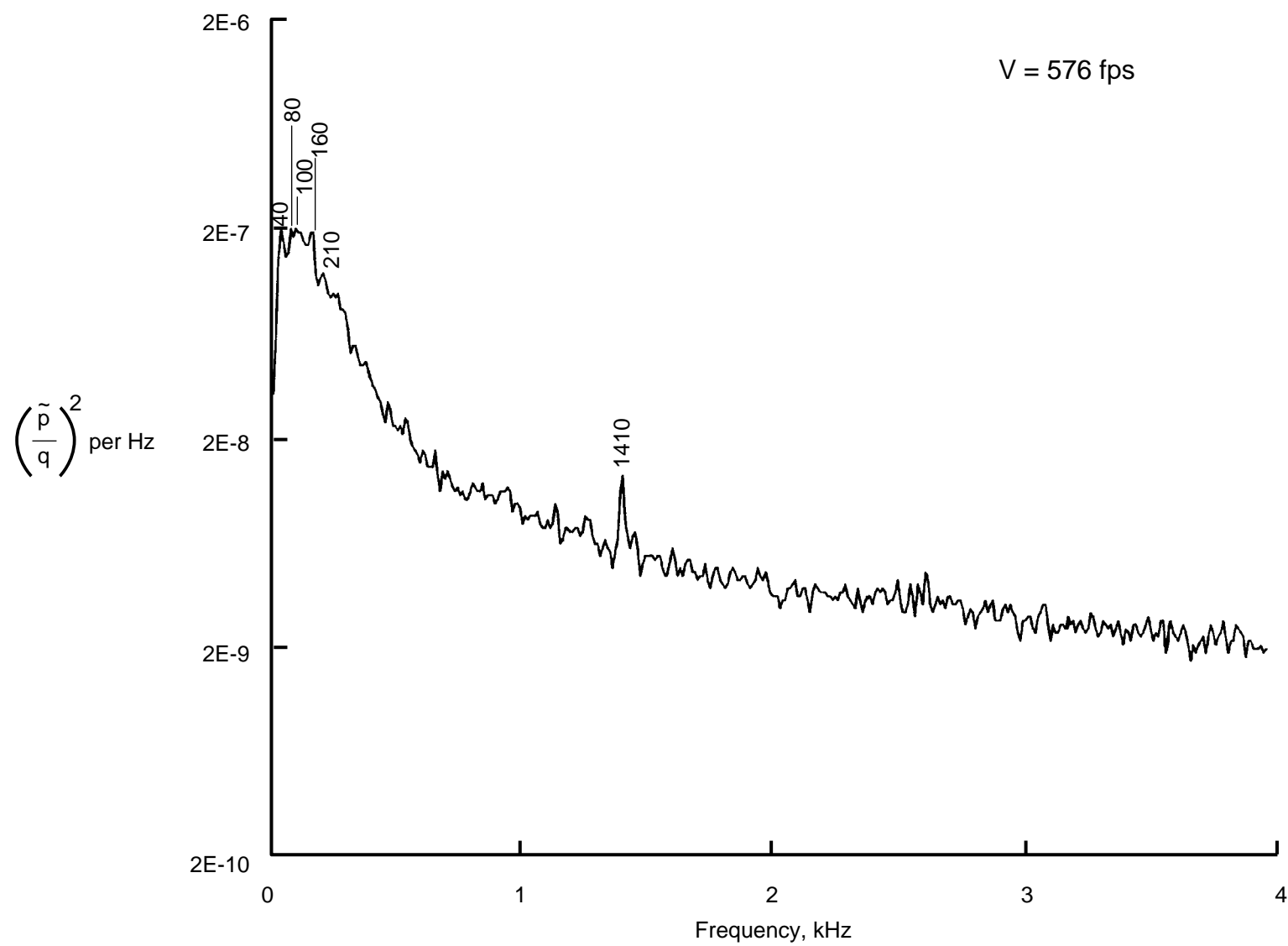
(e) *M* = 0.839.

Figure 35. Continued.
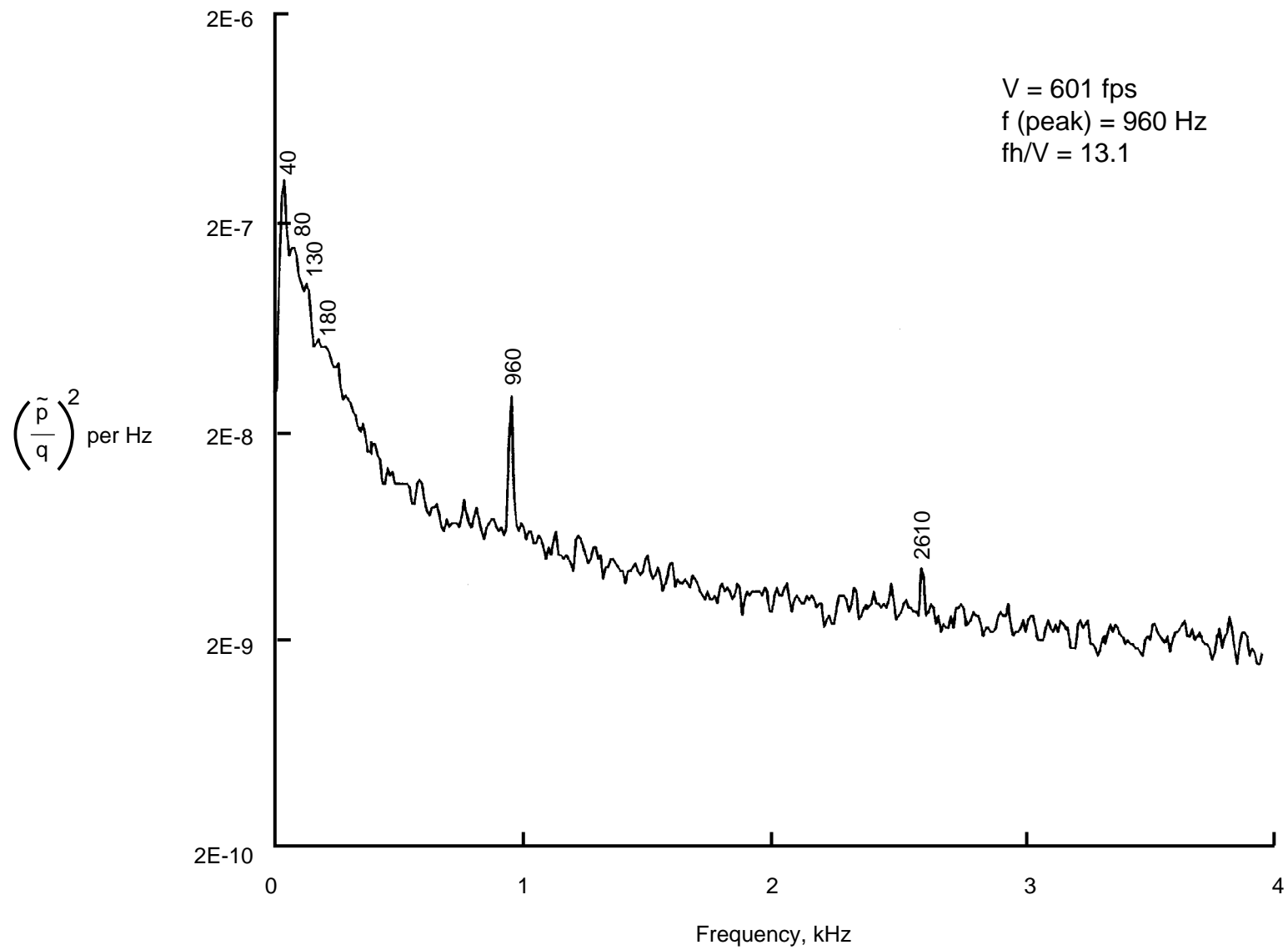
(f) $M = 0.892$.

Figure 35. Continued.
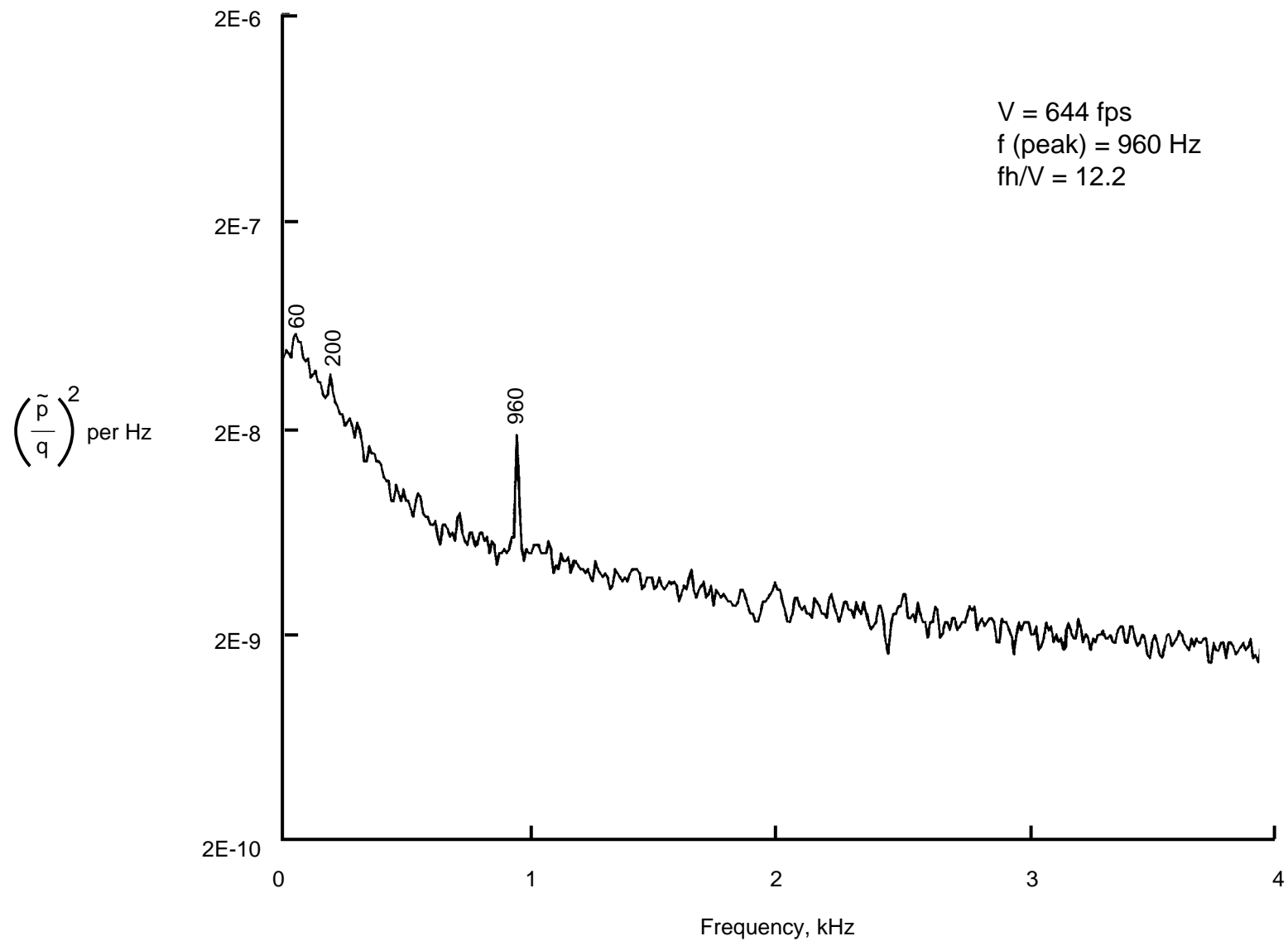
(g) $M = 0.992$.

Figure 35. Concluded.
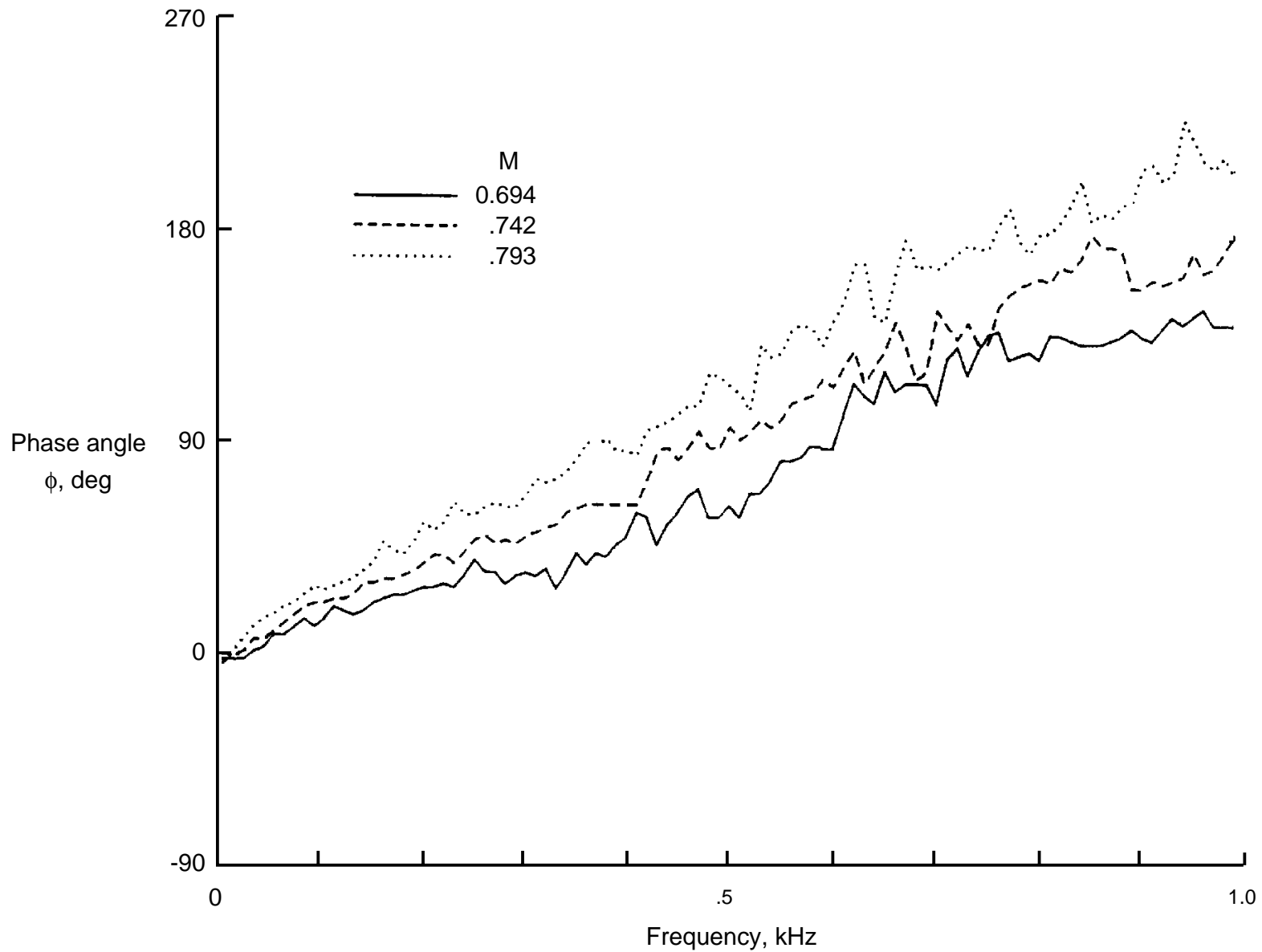
(a) Phase angle.

Figure 36.   Phase angle and coherence of disturbance signals between adjacent pressure transducers at test section RHS sidewall station 13. $R = 40 \times 10^6 \text{ ft}^{-1}$; fan drive power = 30 MW; nitrogen mode.
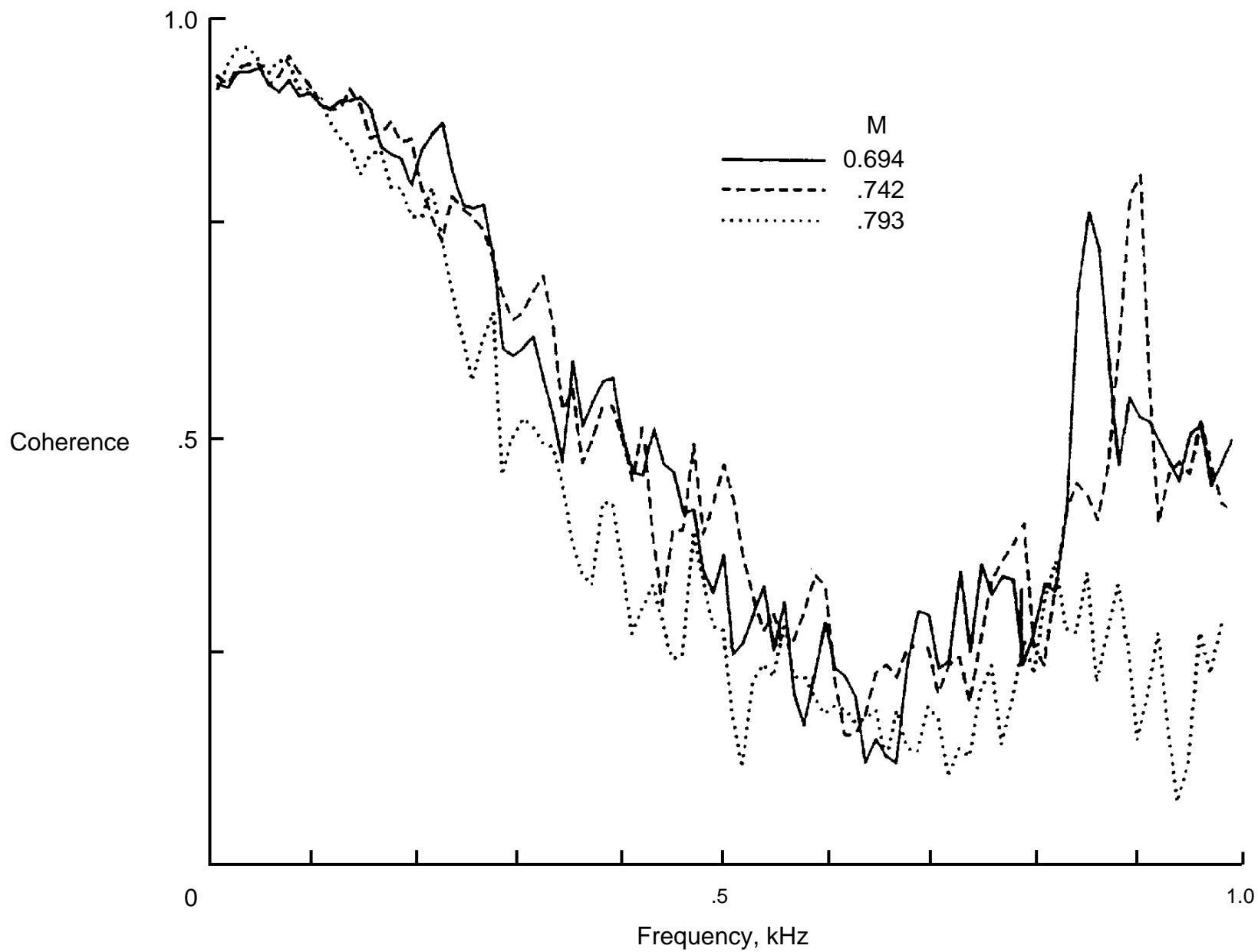
(b) Coherence.

Figure 36. Concluded.
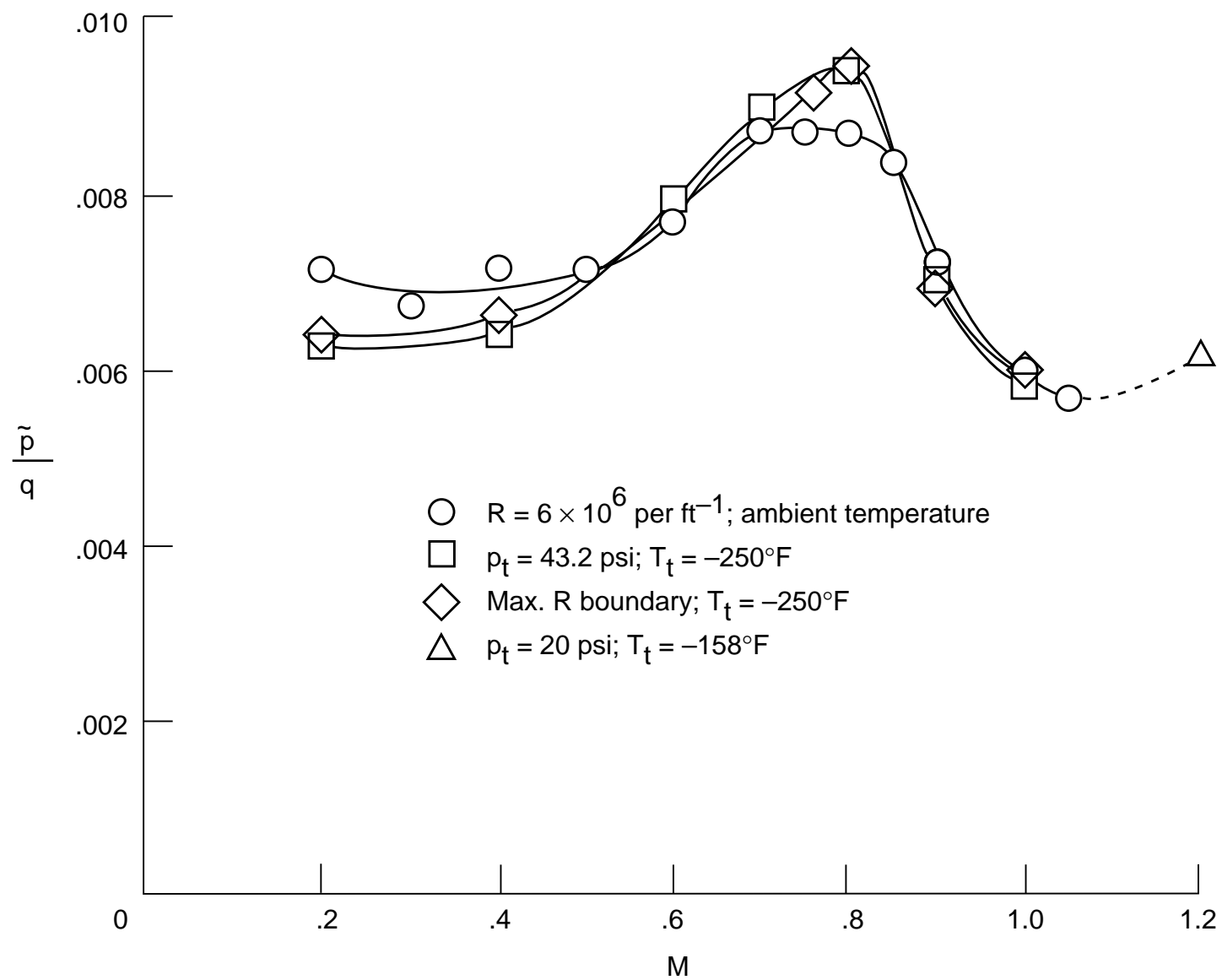
Figure 37. Fluctuating pressure coefficient at test section RHS sidewall station 13. Nitrogen mode.

Max. R boundary
p_t = 43.2 psi

Arbitrary scale

M = 0.2

M = 0.4

M = 0.6

M = 0.7

Arbitrary scale

M = 0.75

M = 0.8

M = 0.9

M = 1.0

0   Frequency, kHz   20 0   Frequency, kHz   20 0   Frequency, kHz   20 0   Frequency, kHz   20
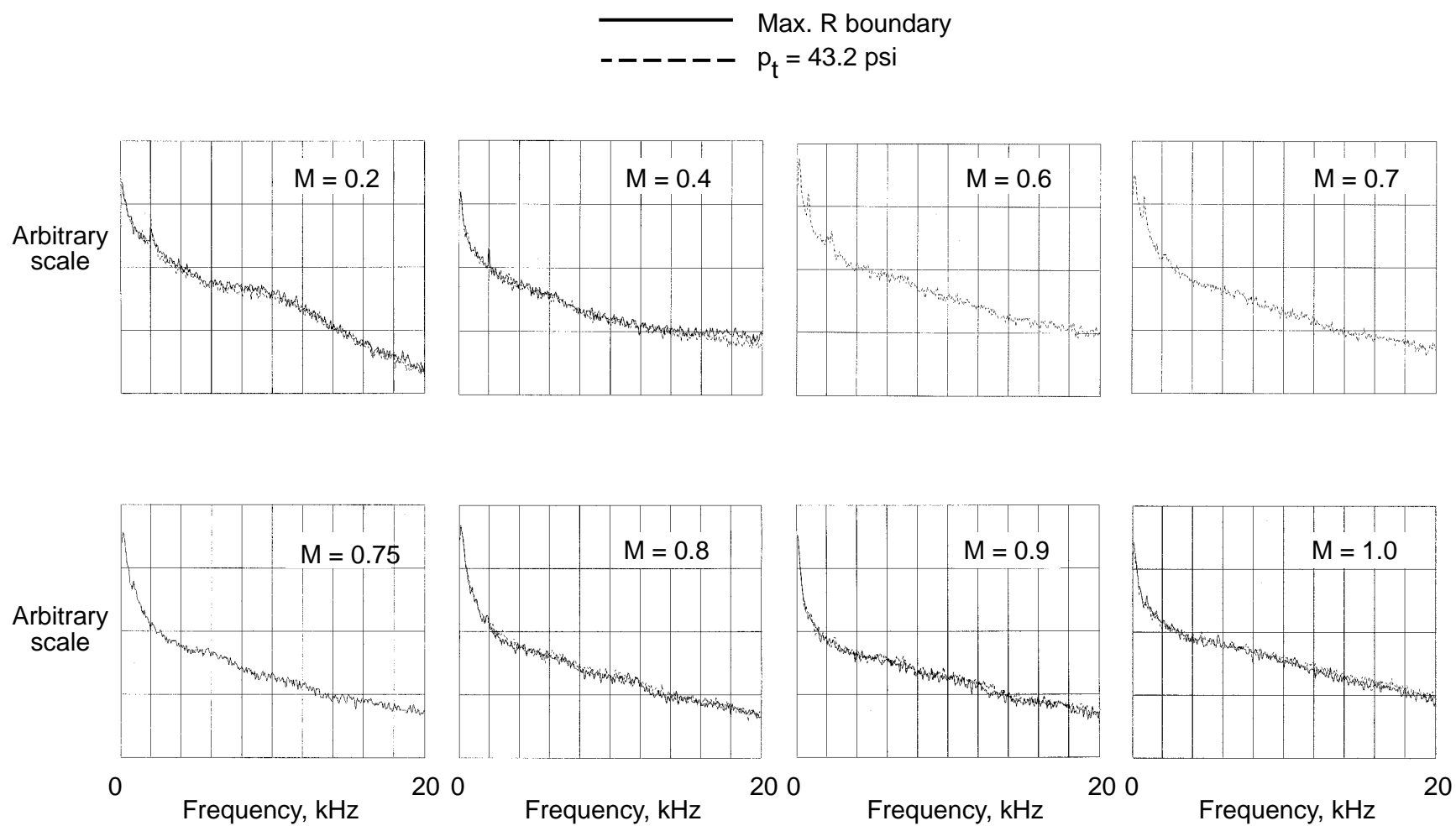
Figure 38. Power spectra of fluctuating pressure coefficient at test section RHS sidewall station 13. $T_t = -250°$F; maximum R boundary and $p_t = 43.2$ psi.
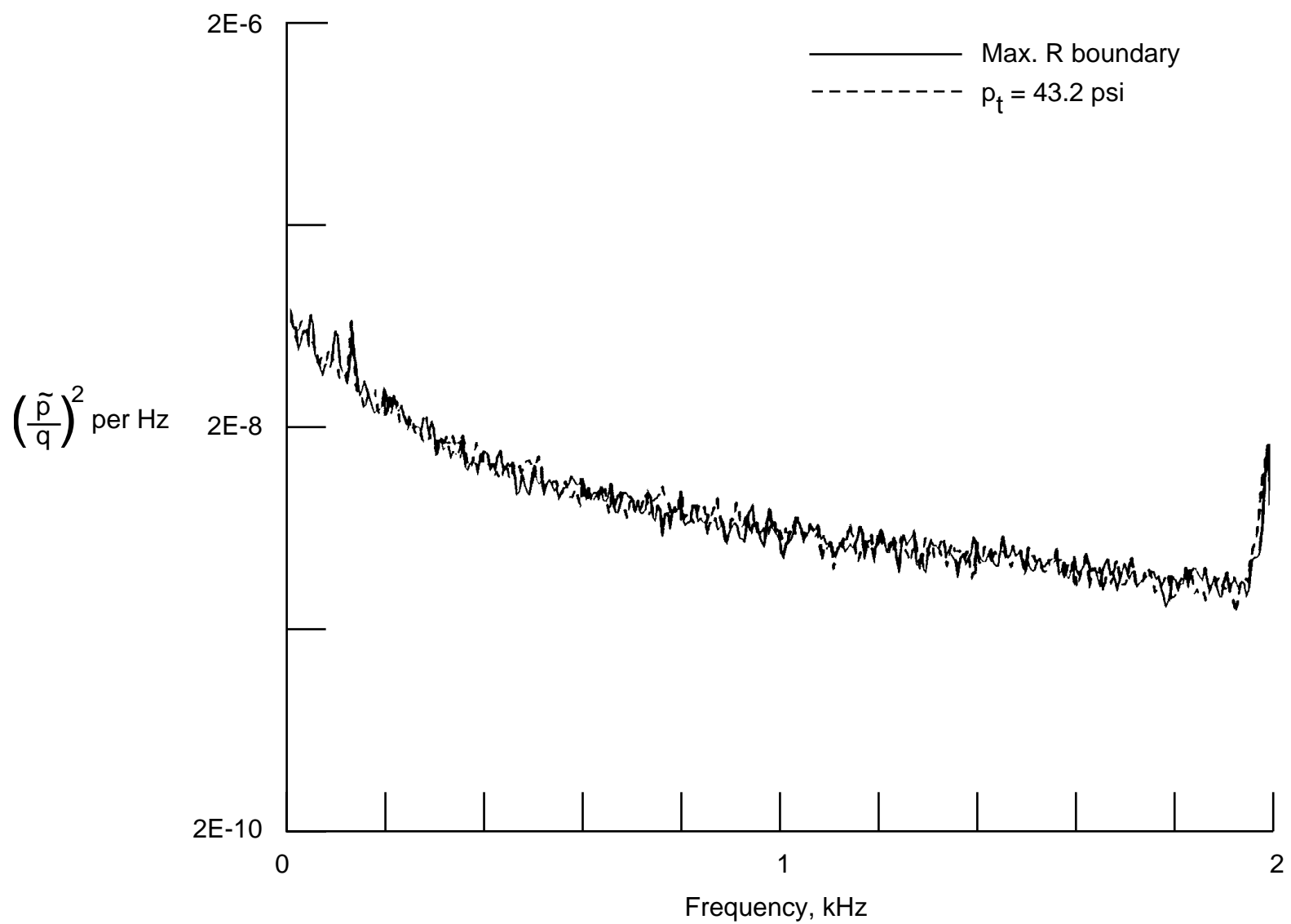
(a) $M = 0.2$.

Figure 39. Power spectra of fluctuating pressure coefficient at test section RHS sidewall station 13. $T_t = -250°F$; maximum R boundary and $p_t = 43.2$ psi; 0- to 2-kHz bandwidth.
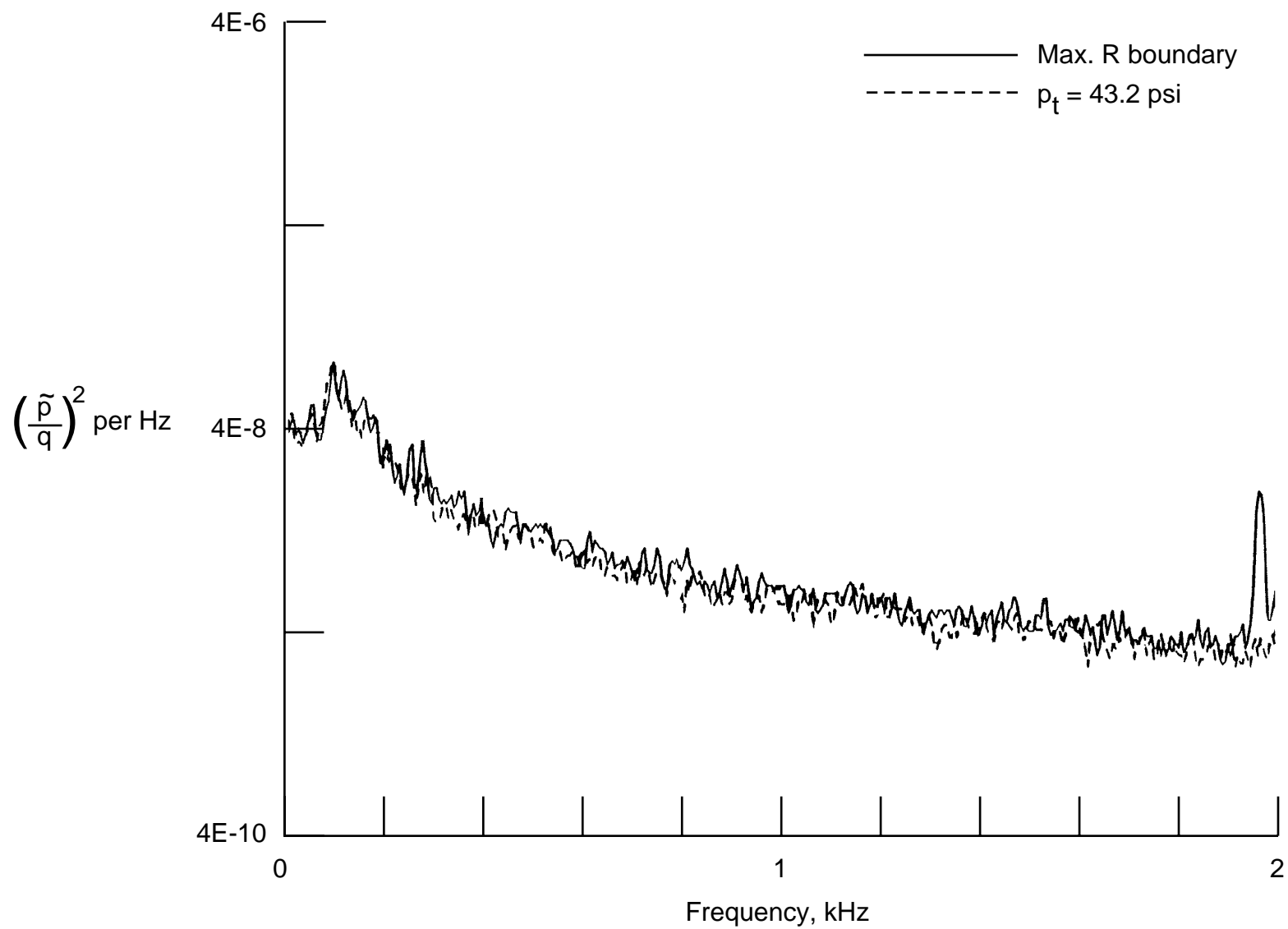
(b) $M = 0.4$.

Figure 39. Continued.
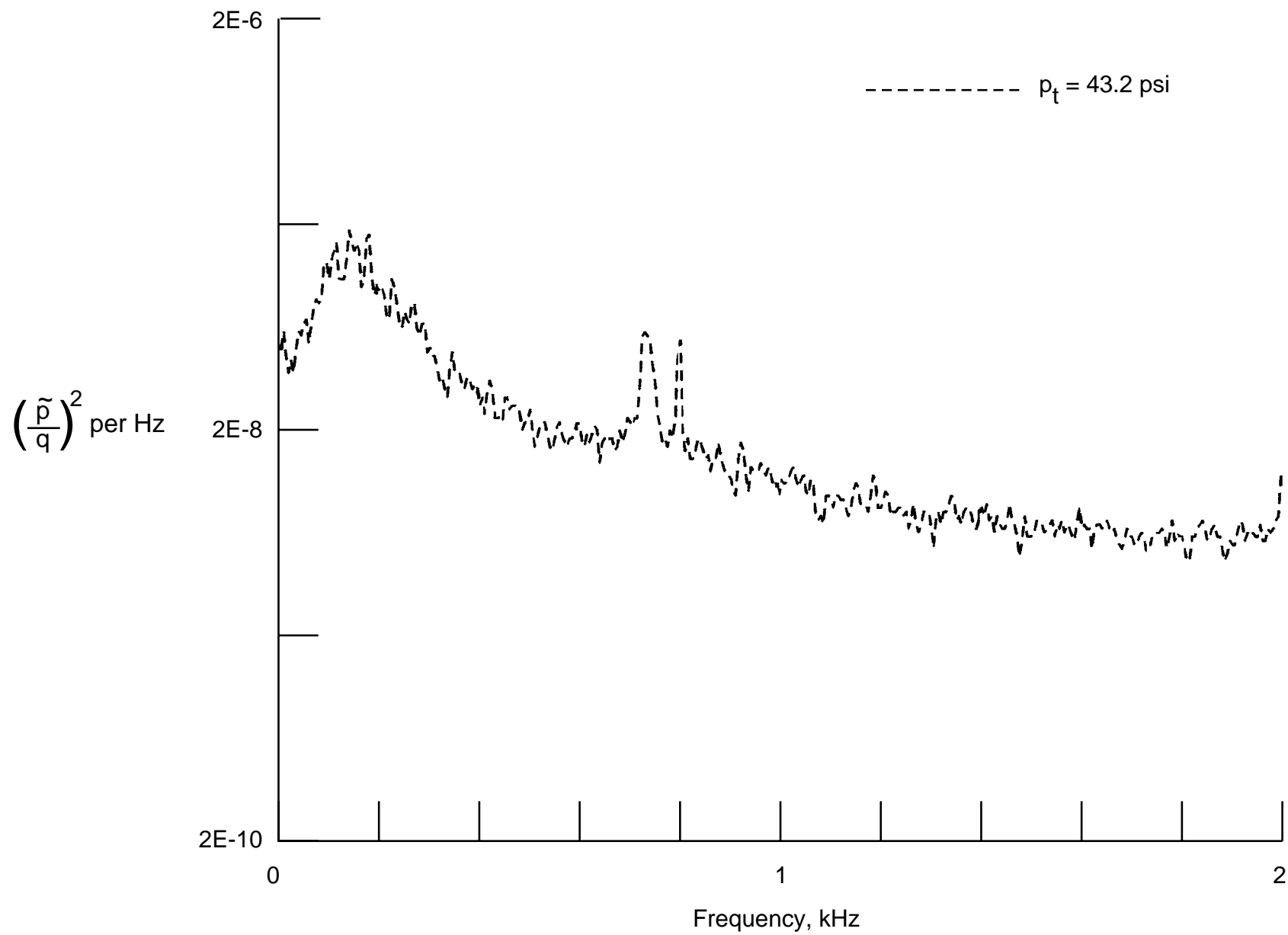
(c) $M = 0.6$.

Figure 39. Continued.
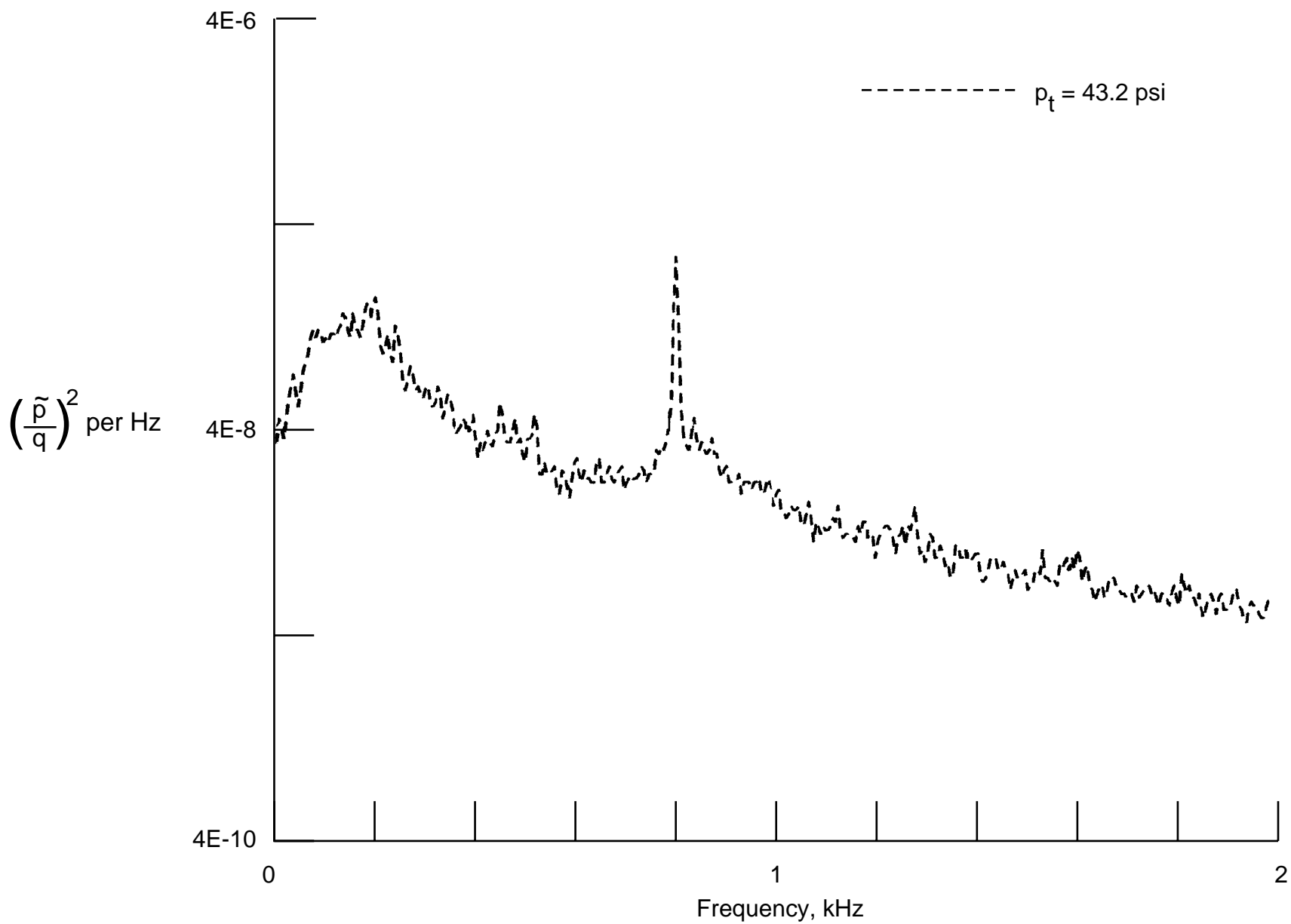
(d) *M* = 0.7.

Figure 39. Continued.
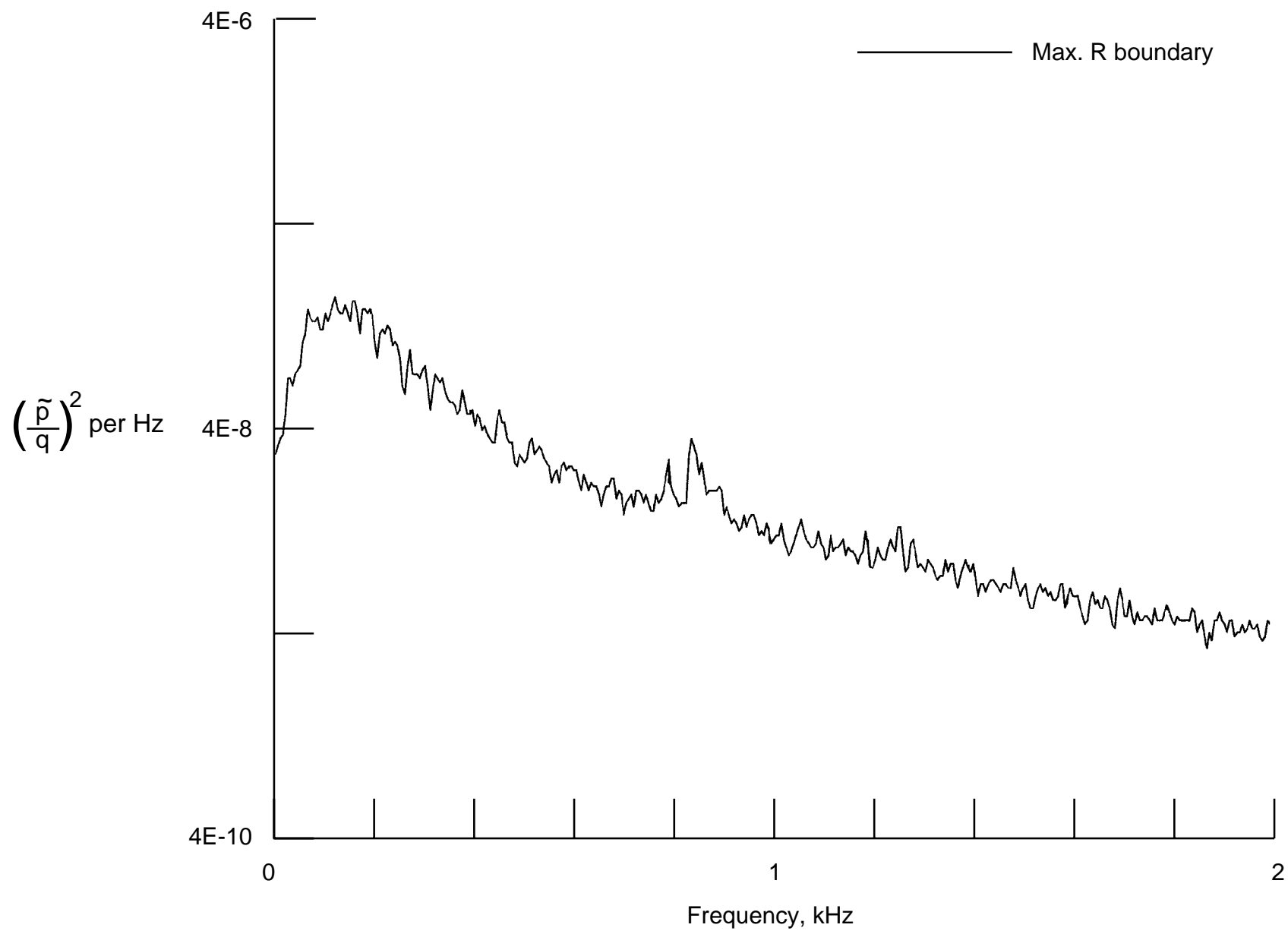
(e) $M = 0.75$.

Figure 39. Continued.
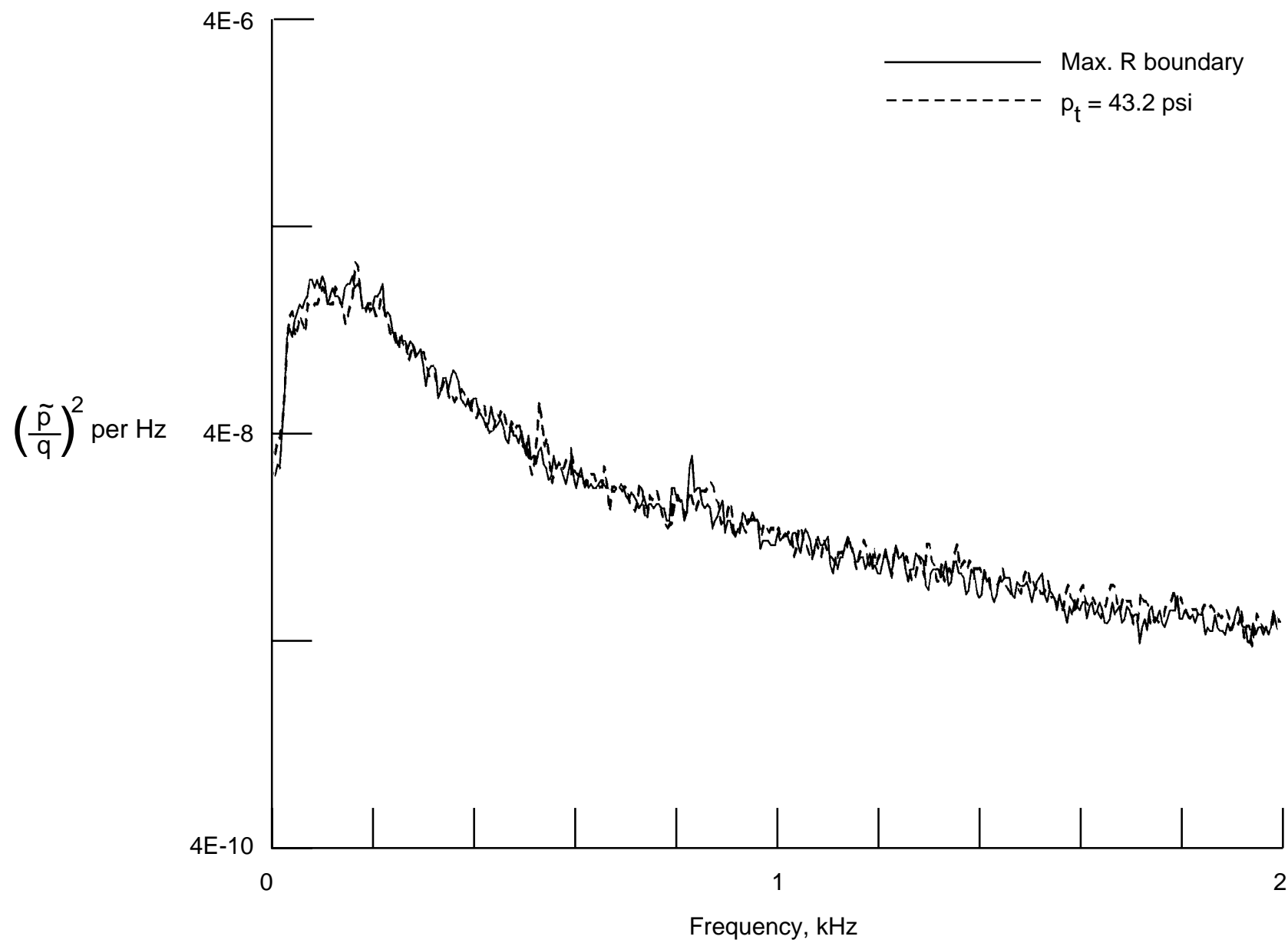
(f) $M = 0.8$.

Figure 39. Continued.
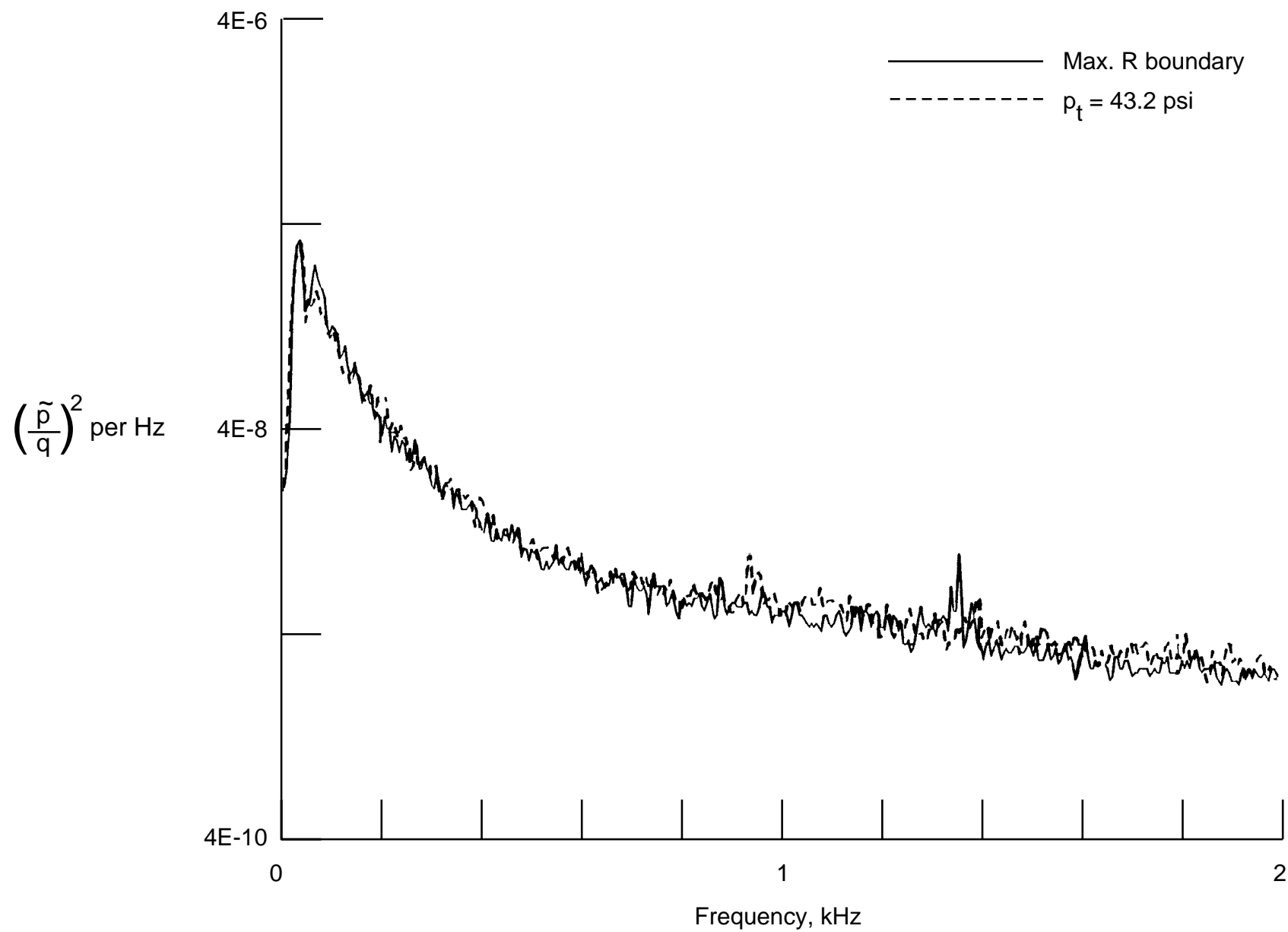
(g) $M = 0.9$.

Figure 39. Continued.
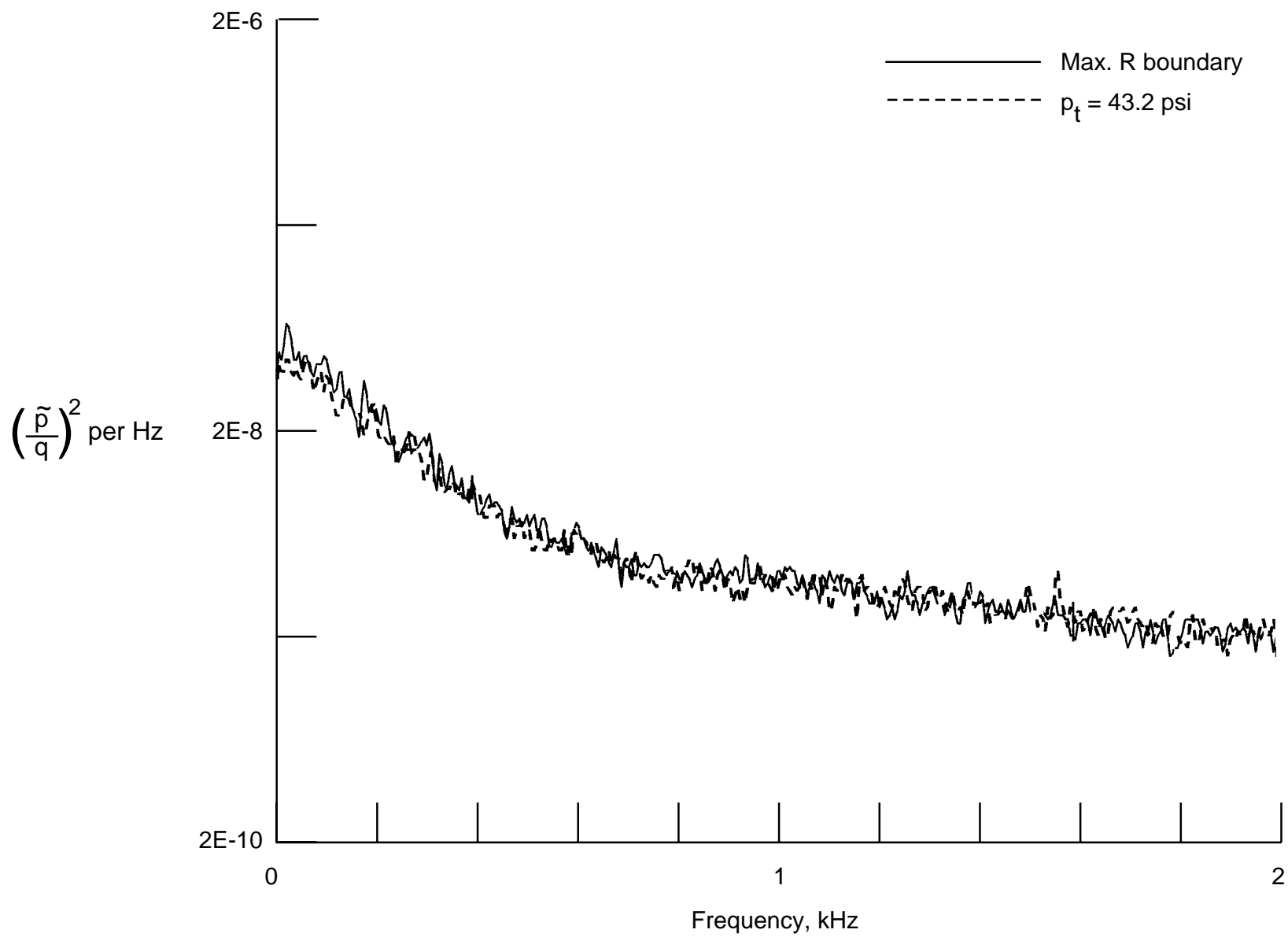
(h) $M = 1.0$.

Figure 39. Concluded.
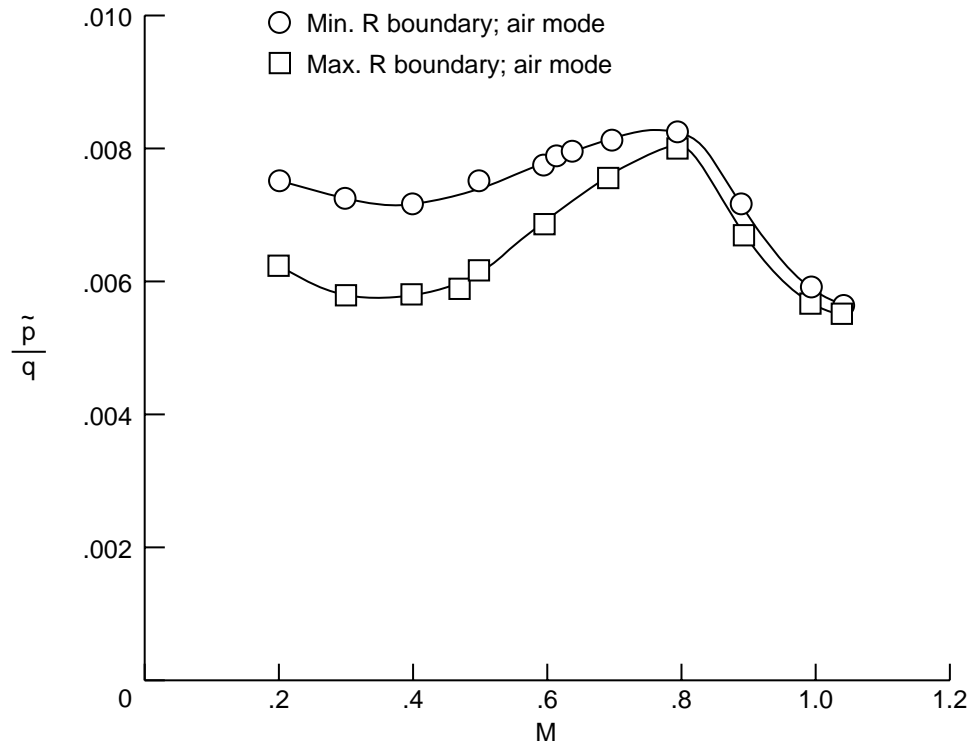
Figure 40. Fluctuating pressure coefficient at test section RHS sidewall station 13. Air mode.
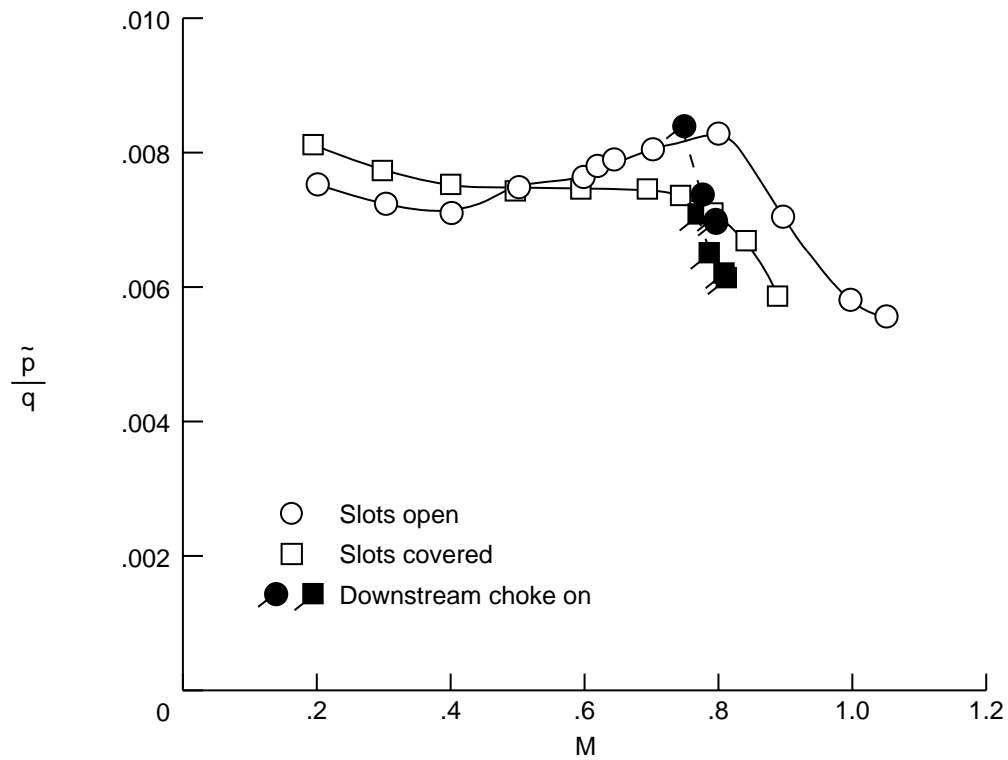
Figure 41. Effect of slot covers and downstream choke on fluctuating pressure coefficient at test section RHS sidewall station 13. Minimum Reynolds number boundary; air mode.
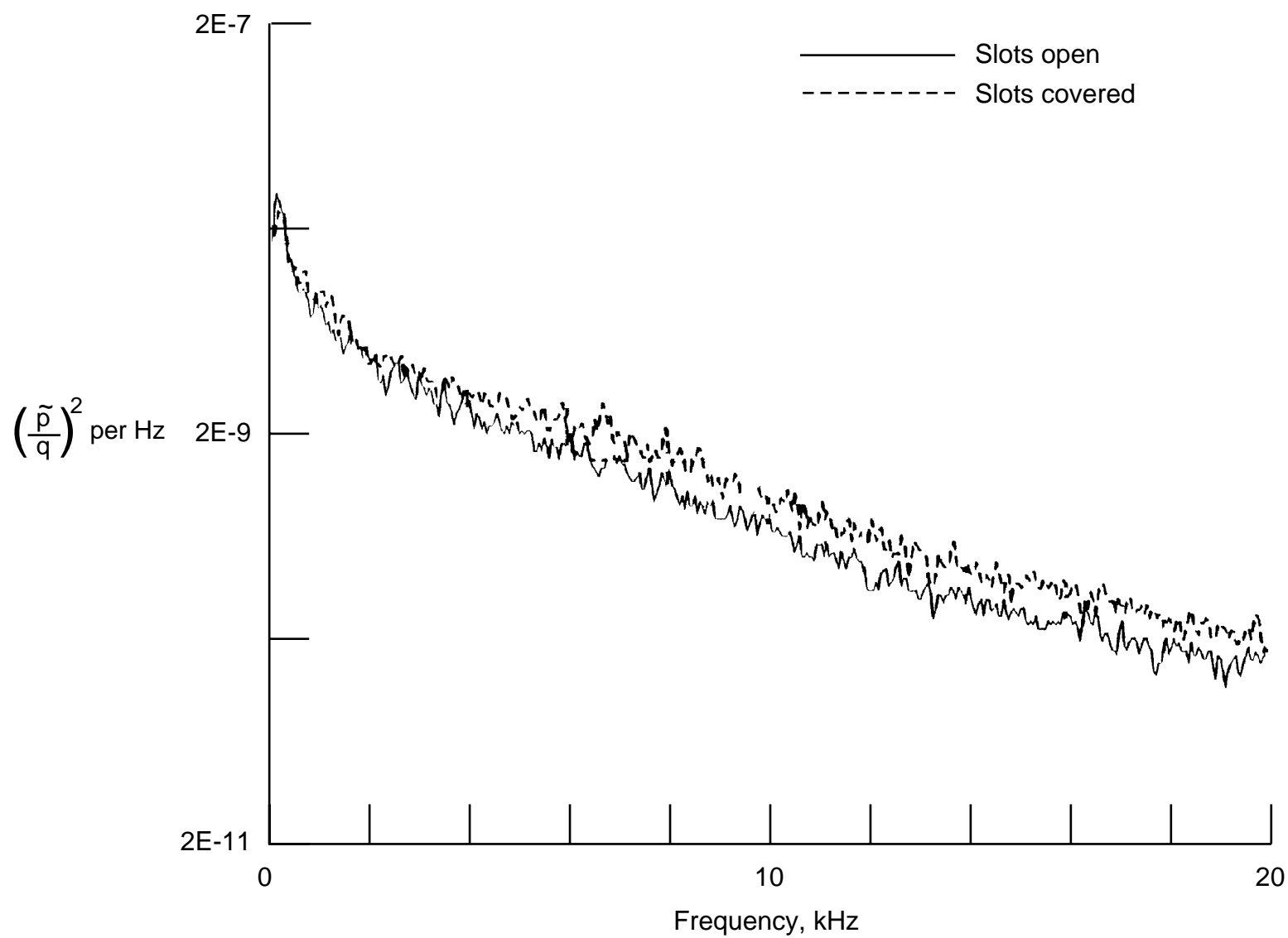
(a) $M = 0.2$.

Figure 42. Power spectra of fluctuating pressure coefficient at test section RHS sidewall station 13. Minimum Reynolds number boundary; air mode; slots open and covered.
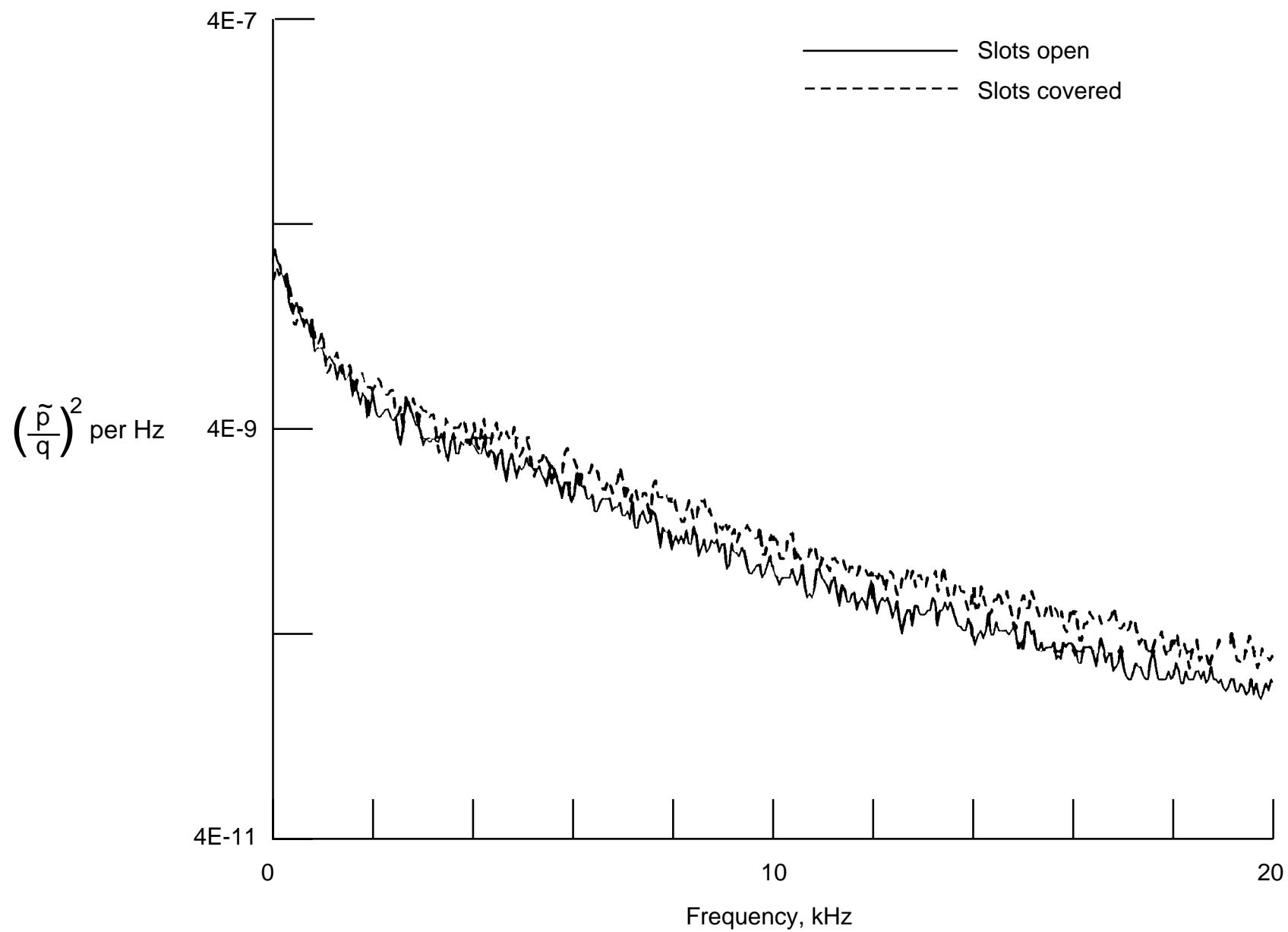
(b) $M = 0.3$.

Figure 42. Continued.
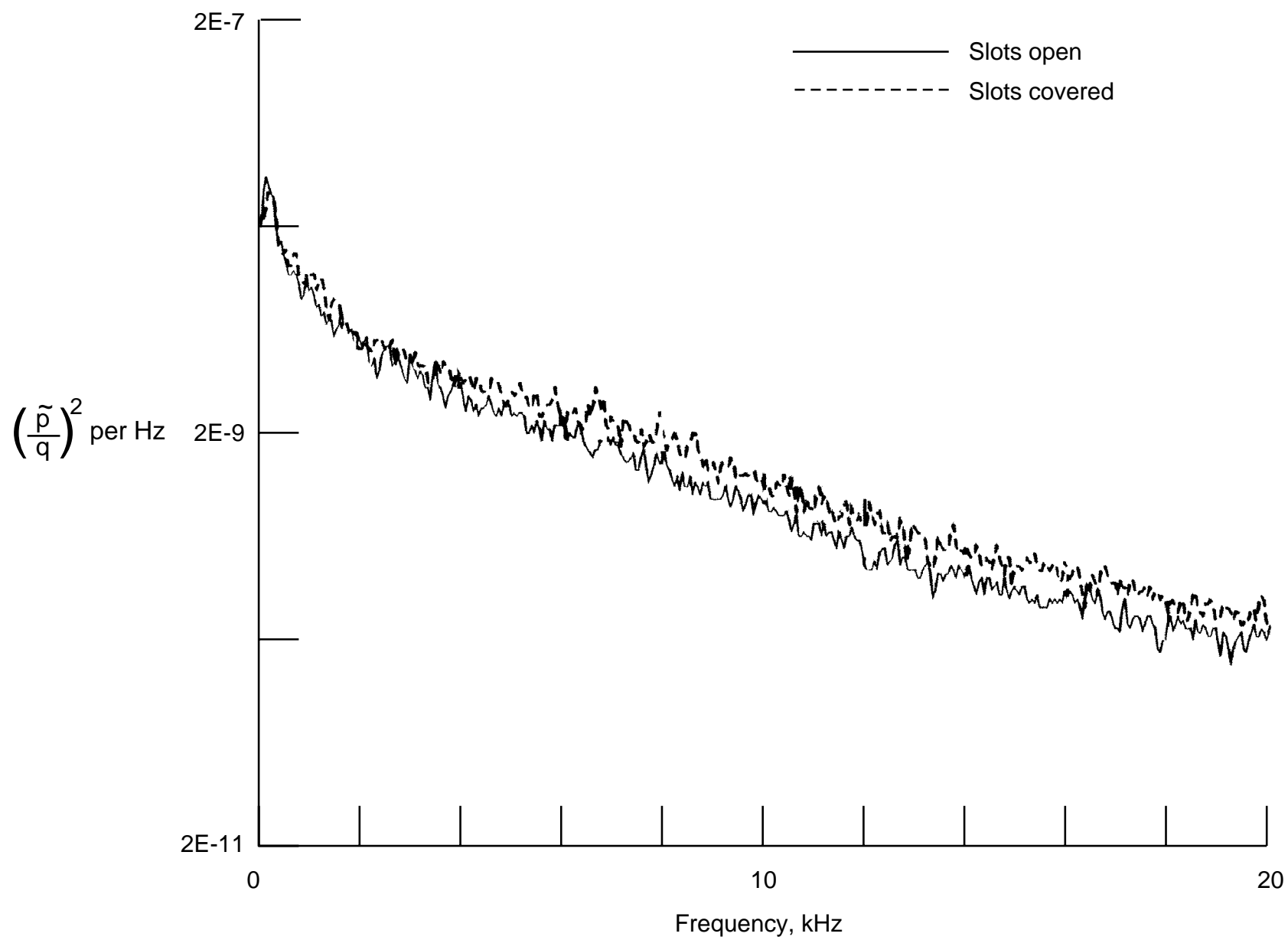
(c) $M = 0.4$.

Figure 42. Continued.
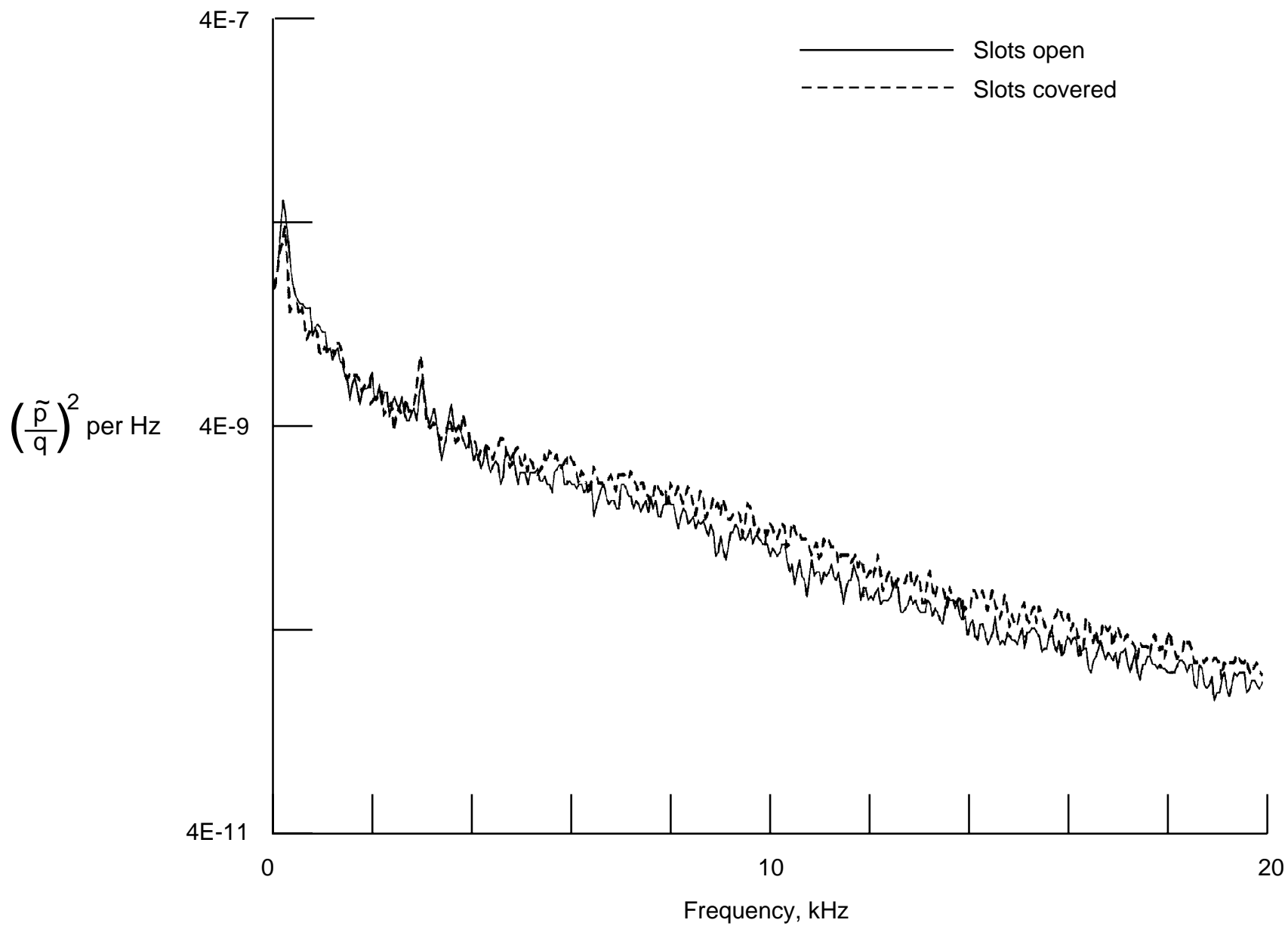
(d) $M = 0.5.$

Figure 42. Continued.
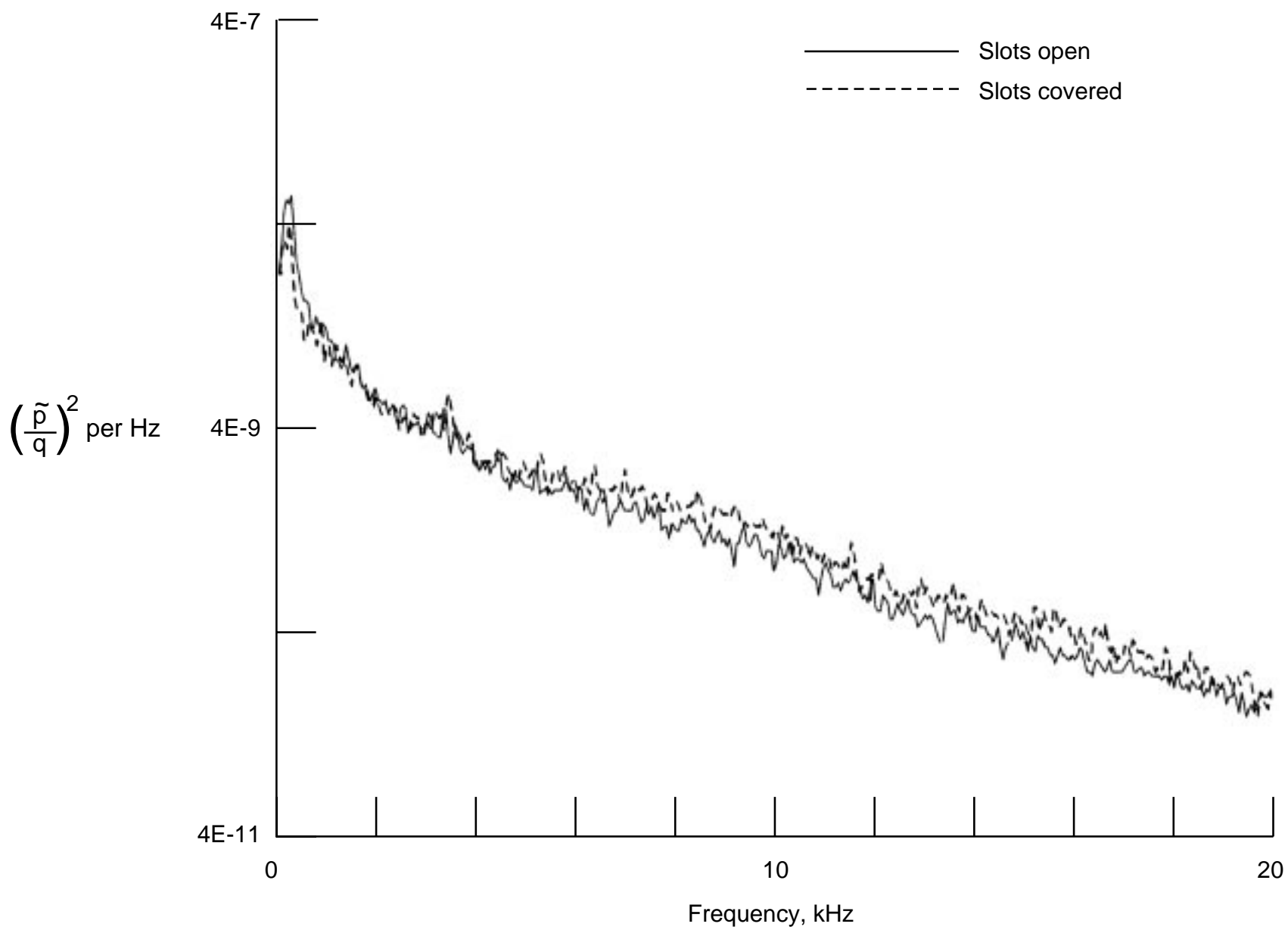
(e) $M = 0.6$.

Figure 42. Continued.
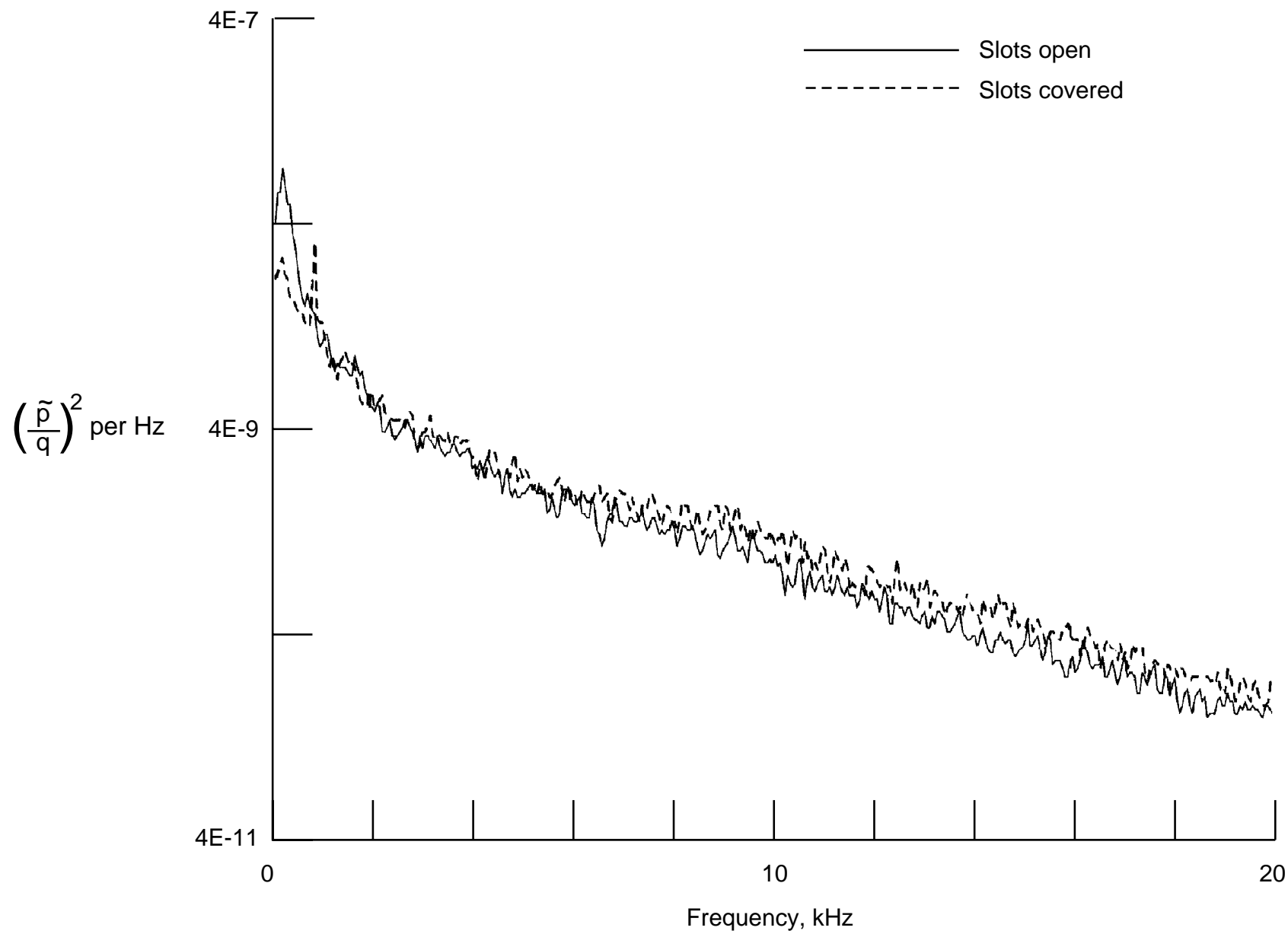
(f) $M = 0.7$.

Figure 42. Continued.
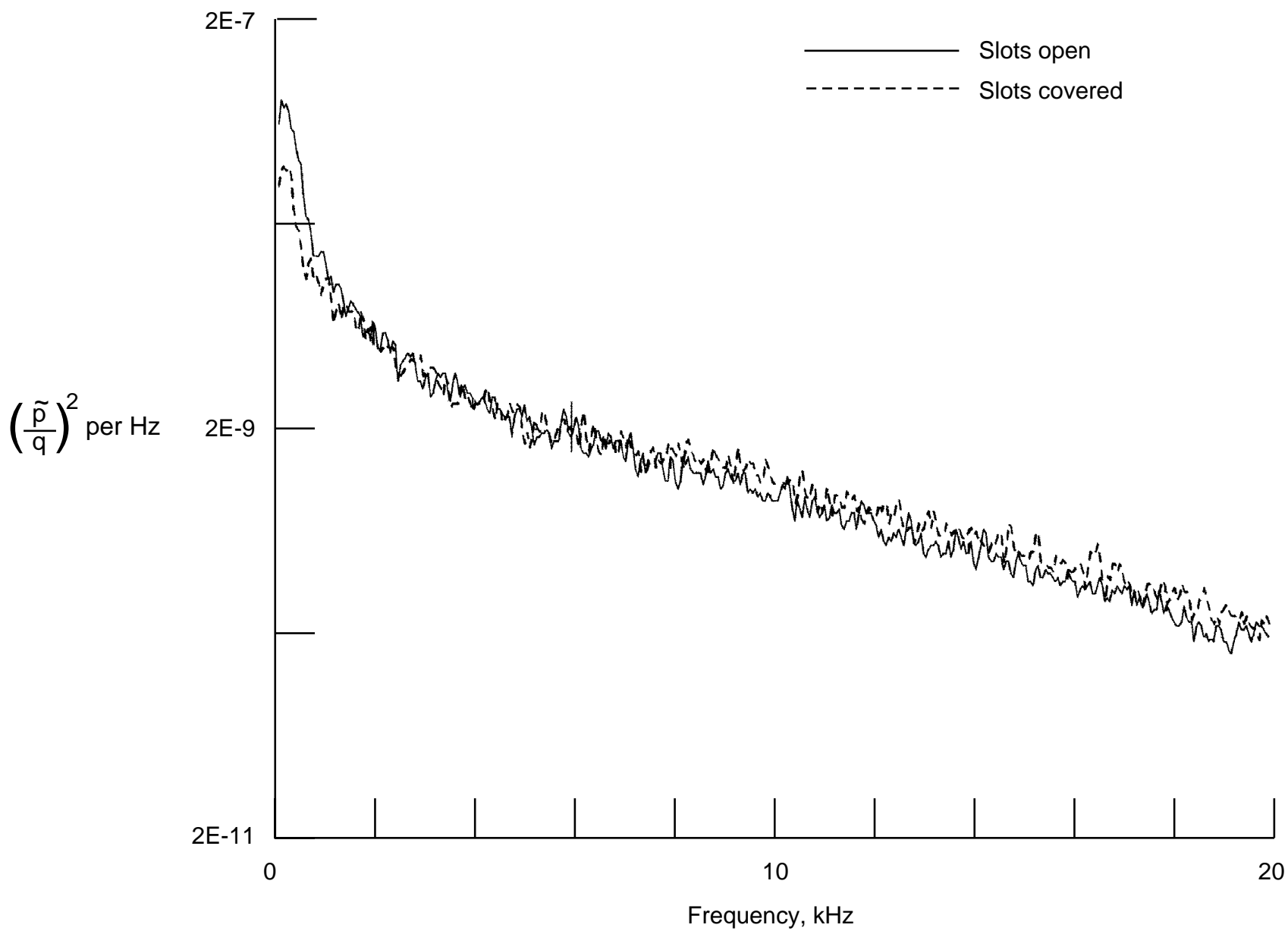
(g) $M = 0.8$.

Figure 42. Continued.
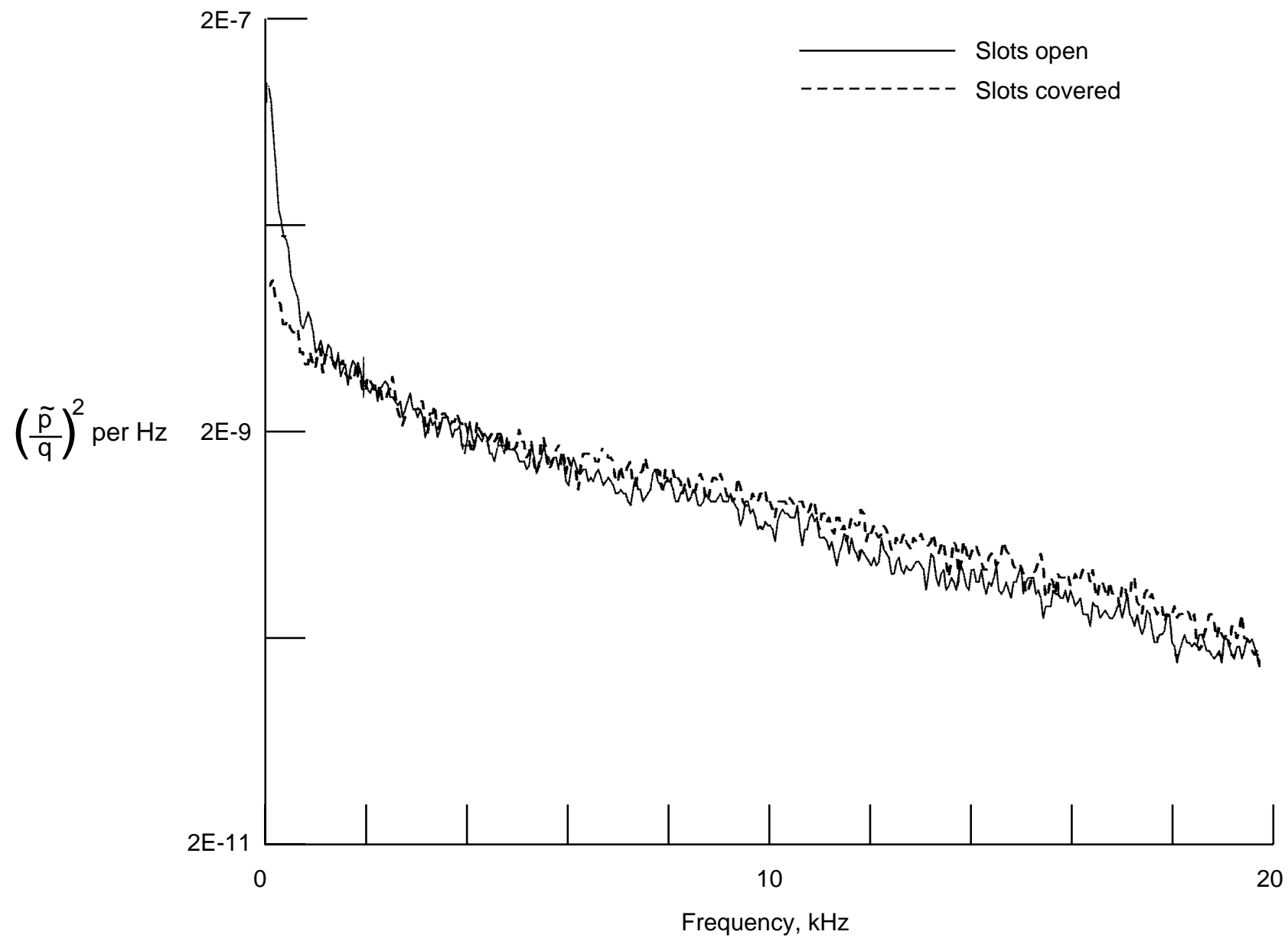
(h) $M = 0.9$.

Figure 42. Concluded.

RHS sidewall
reentry flaps

Downstream
choke location

Bottom wall
reentry flaps
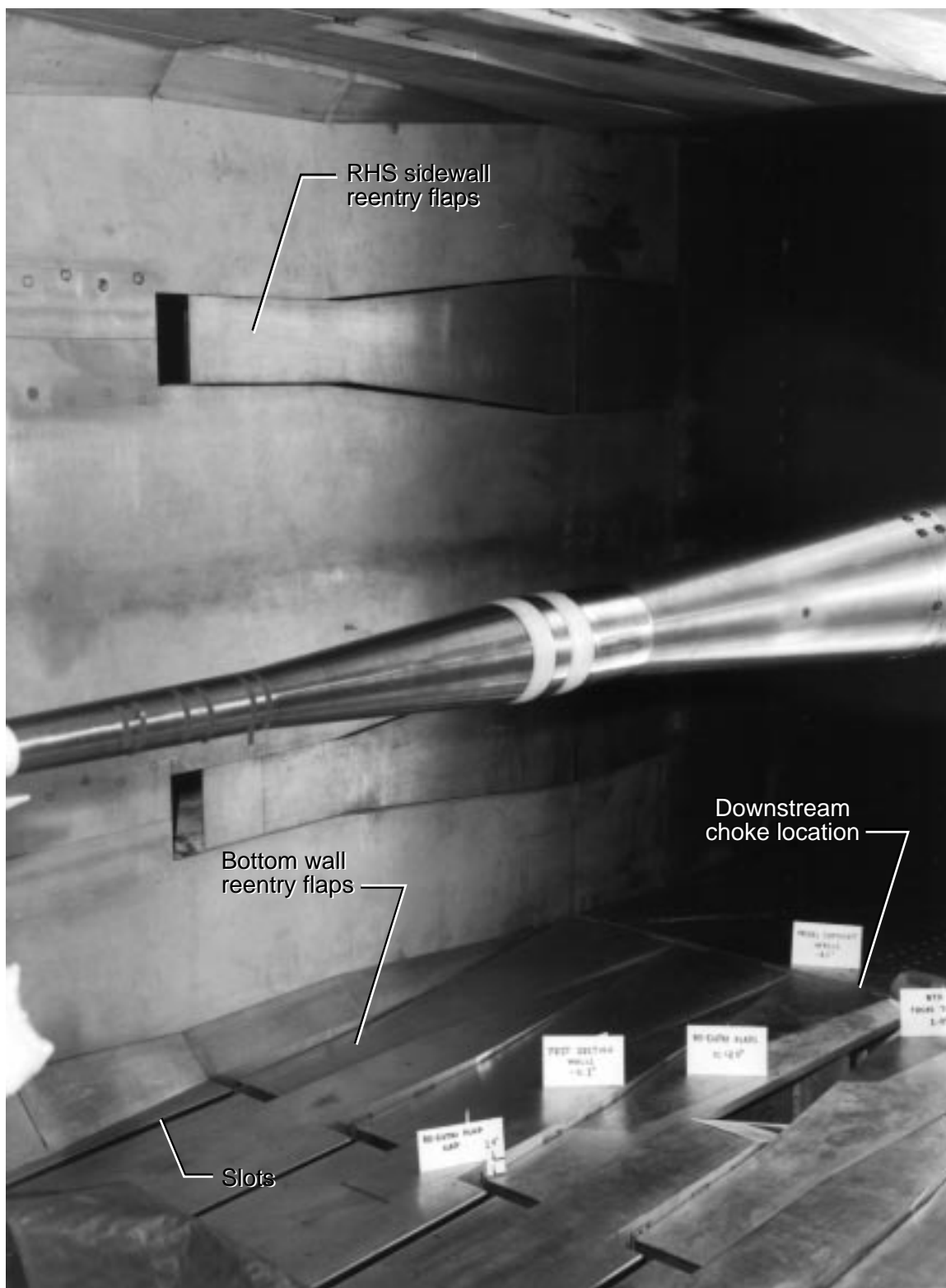
Slots

L-89-00663

Figure 43. NTF test section wall geometry variables for downstream choke with slots open.

126
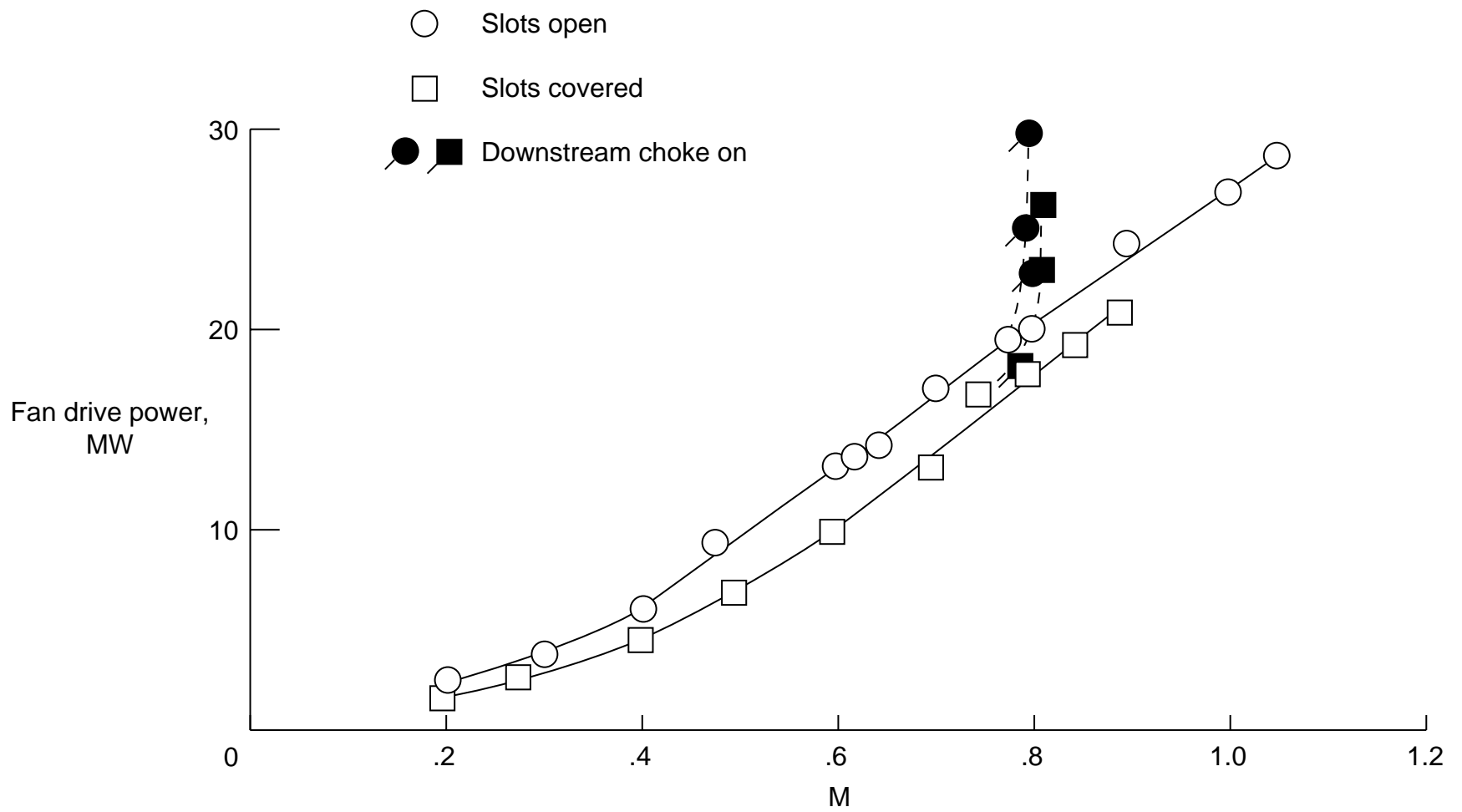
Figure 44. Effect of slot covers and downstream choke on NTF fan drive power. Minimum Reynolds number boundary; air mode.
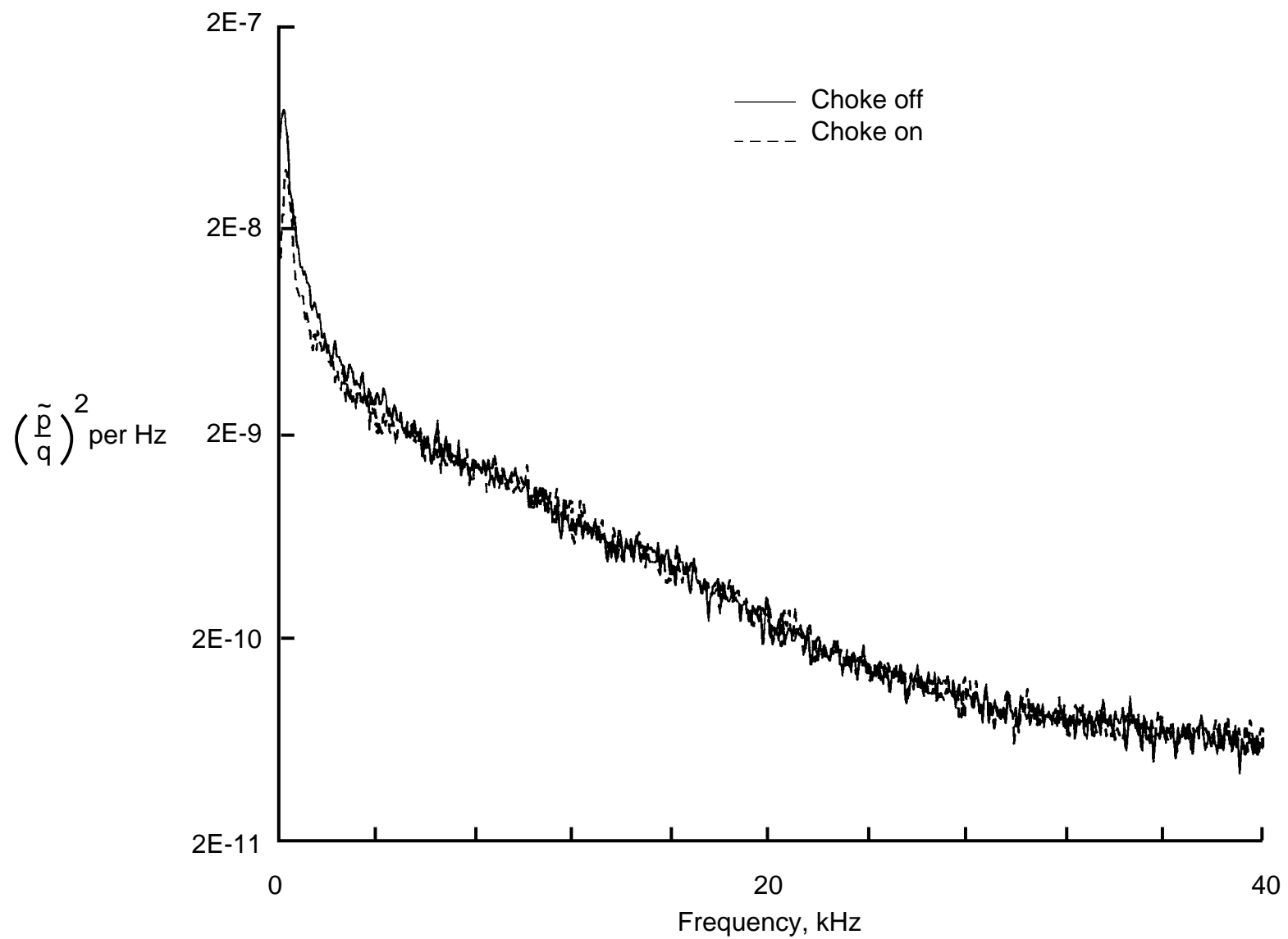
Figure 45. Power spectra of fluctuating pressure coefficient at test section RHS sidewall station 13. Slots open; $M = 0.8$; $R = 4 \times 10^6$ ft^{-1}; air mode.
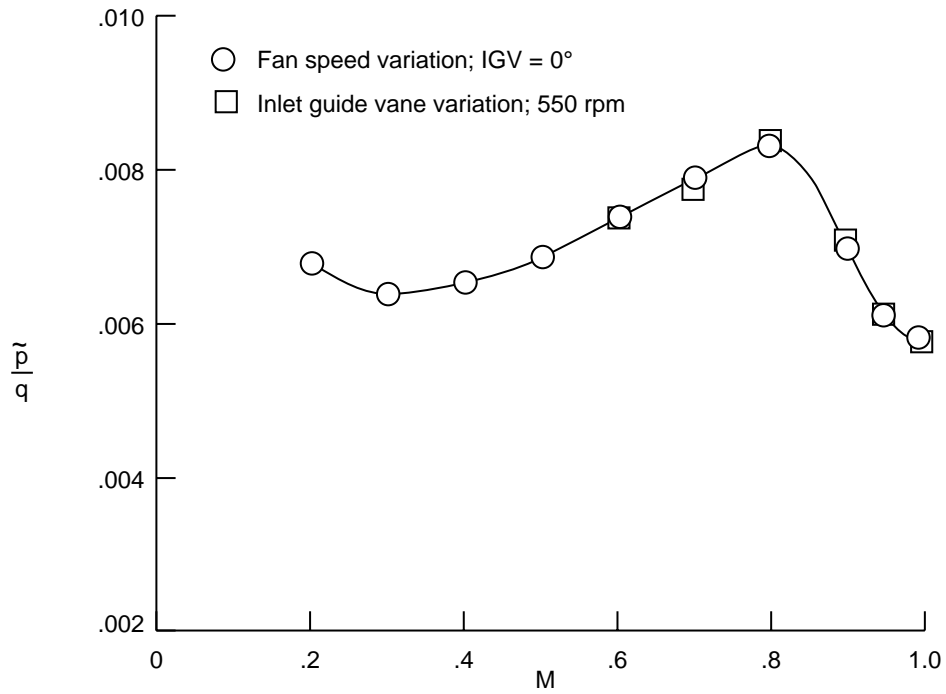
Figure 46. Effect of fan speed and inlet guide vane variation for velocity change on fluctuating pressure coefficient at test section RHS sidewall station 13. $R = 6 \times 10^6$ ft^{-1}; ambient temperature; air mode.
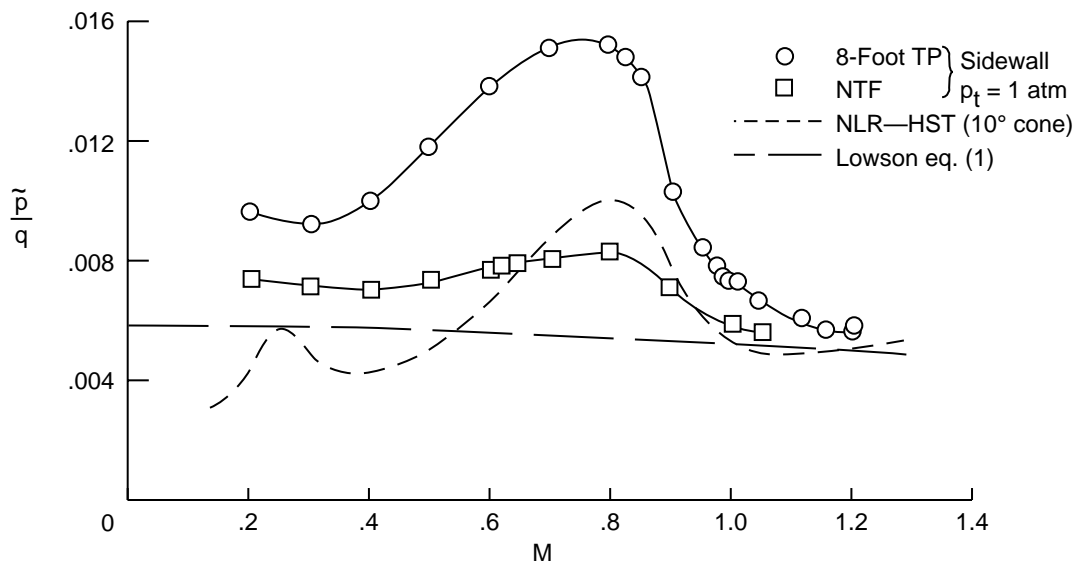
Figure 47. Comparison of NTF and 8-Foot TPT fluctuating pressure coefficient on test section sidewall. Atmospheric stagnation pressure; ambient temperature; air mode.

(a) $\alpha_{rf} = 0°$; $\delta_{msw} = -1.76°$.

(b) $\theta_{tsw} = 0°$; $\delta_{msw} = -1.76°$.

(c) $\theta_{tsw} = 0°$; $\alpha_{rf} = 0°$.
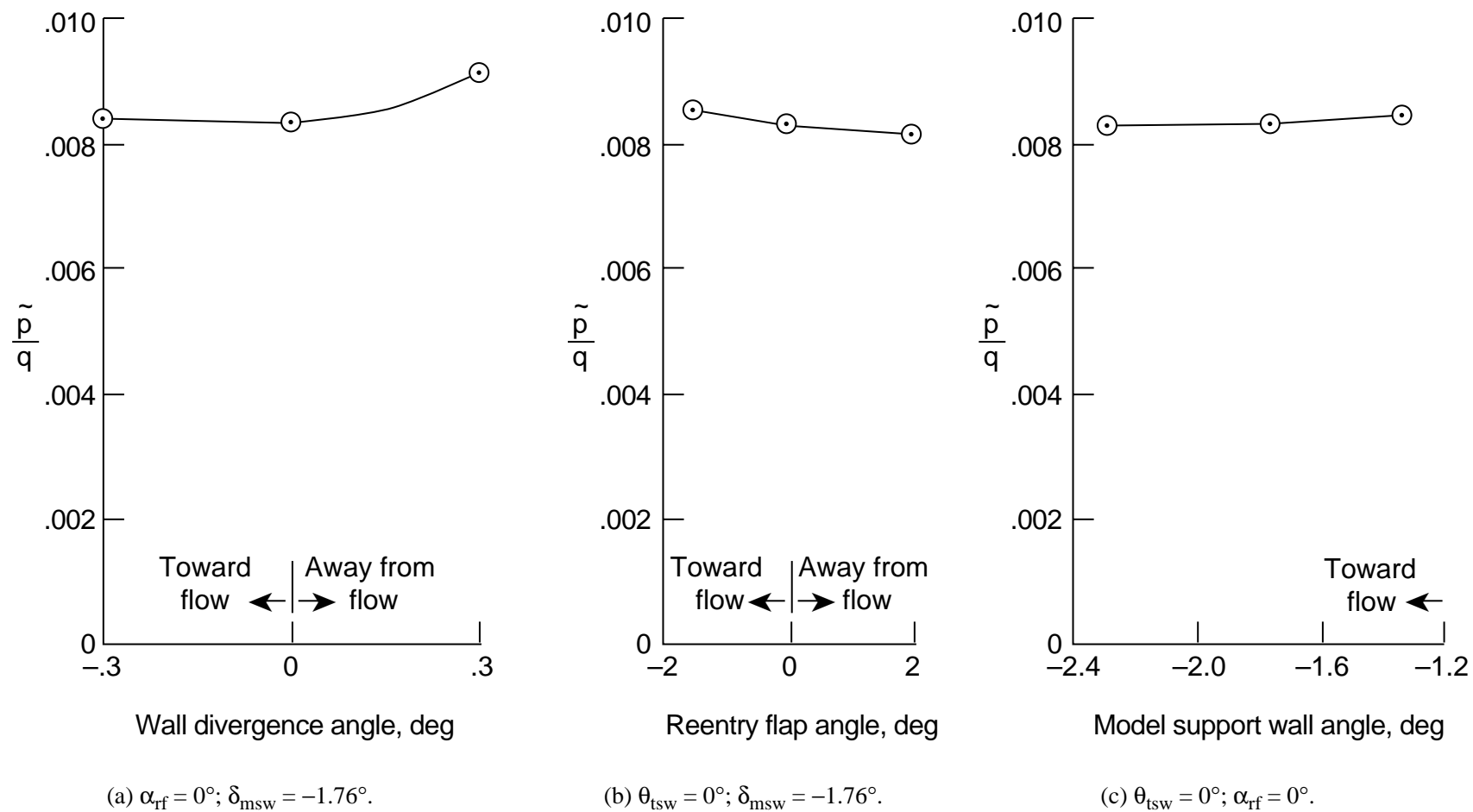
Figure 48. Effect of test section geometry variables on fluctuating pressure coefficient at test section RHS sidewall station 13. $M = 0.8$.; $R = 6 \times 10^6$ ft^{-1}; ambient temperature; air mode.
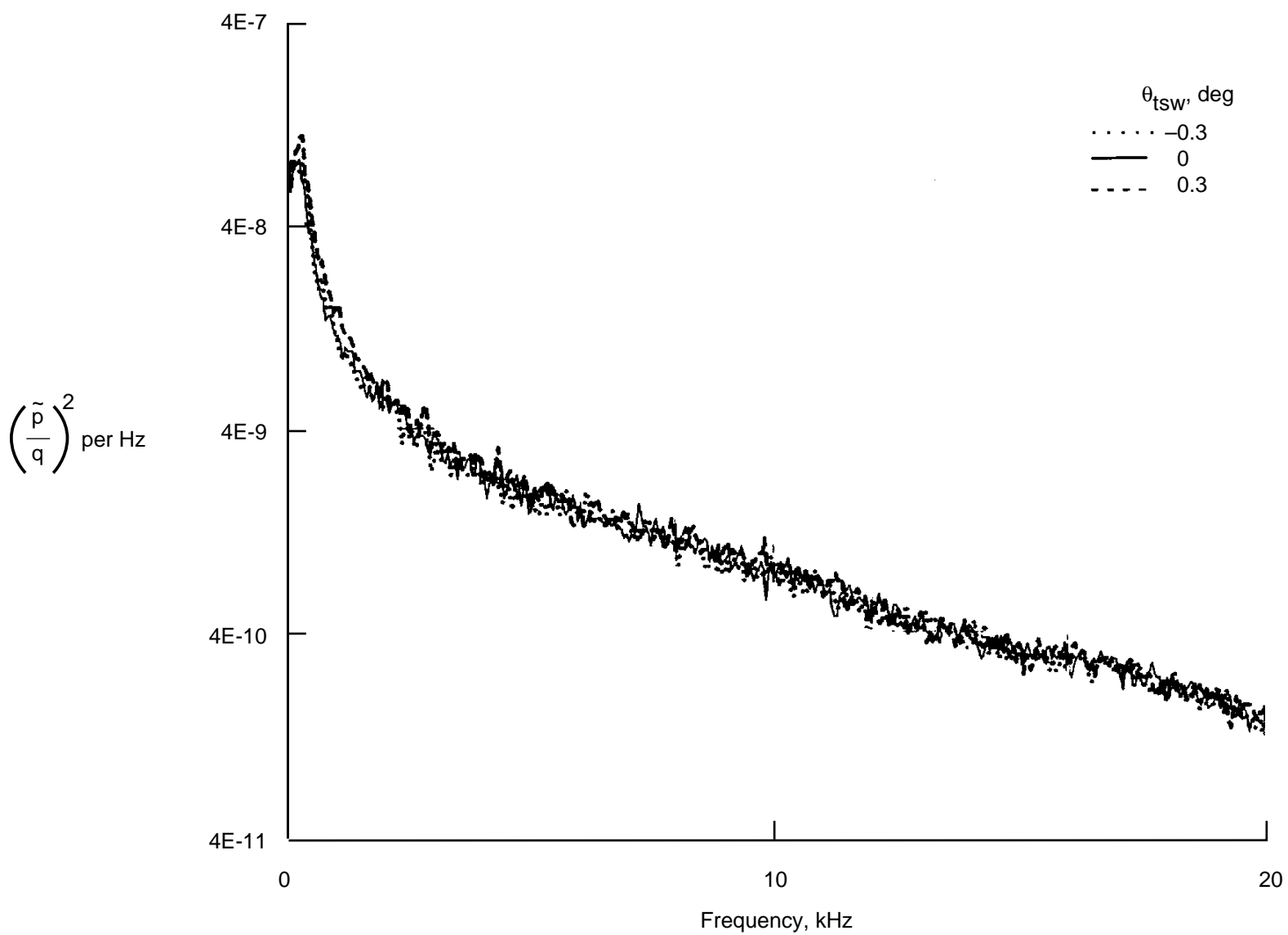
(a) Wall divergence angle; $\alpha_{rf} = 0°$; $\delta_{msw} = -1.76°$.

Figure 49. Effect of test section geometry variables on power spectra of fluctuating pressure coefficient at test section RHS sidewall station 13. $M = 0.8$.; $R = 6 \times 10^6$ ft^{-1}; ambient temperature; air mode.
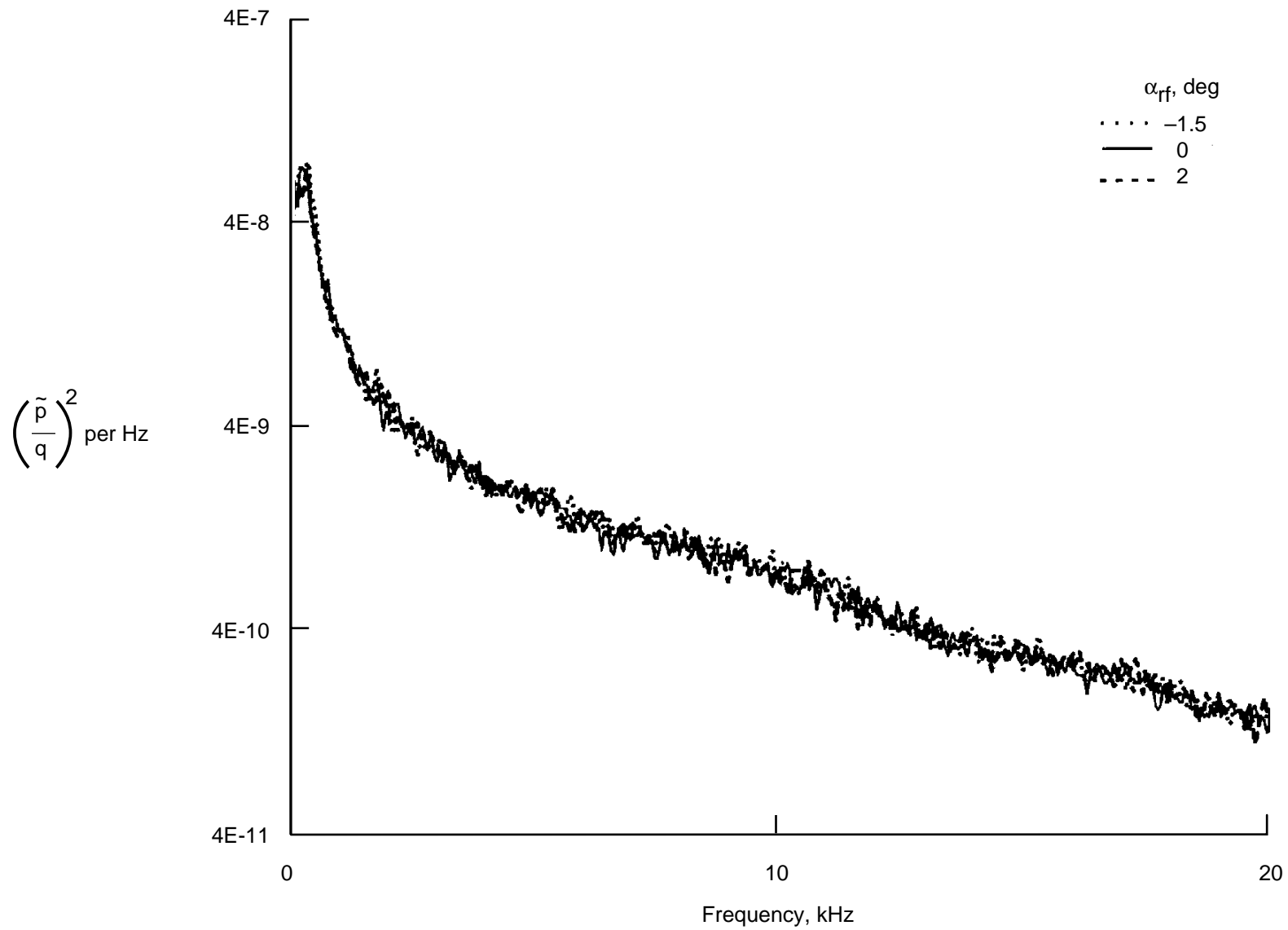
(b) Reentry flap angle; $\theta_{tsw} = 0°$; $\delta_{msw} = -1.76°$.

Figure 49. Continued.
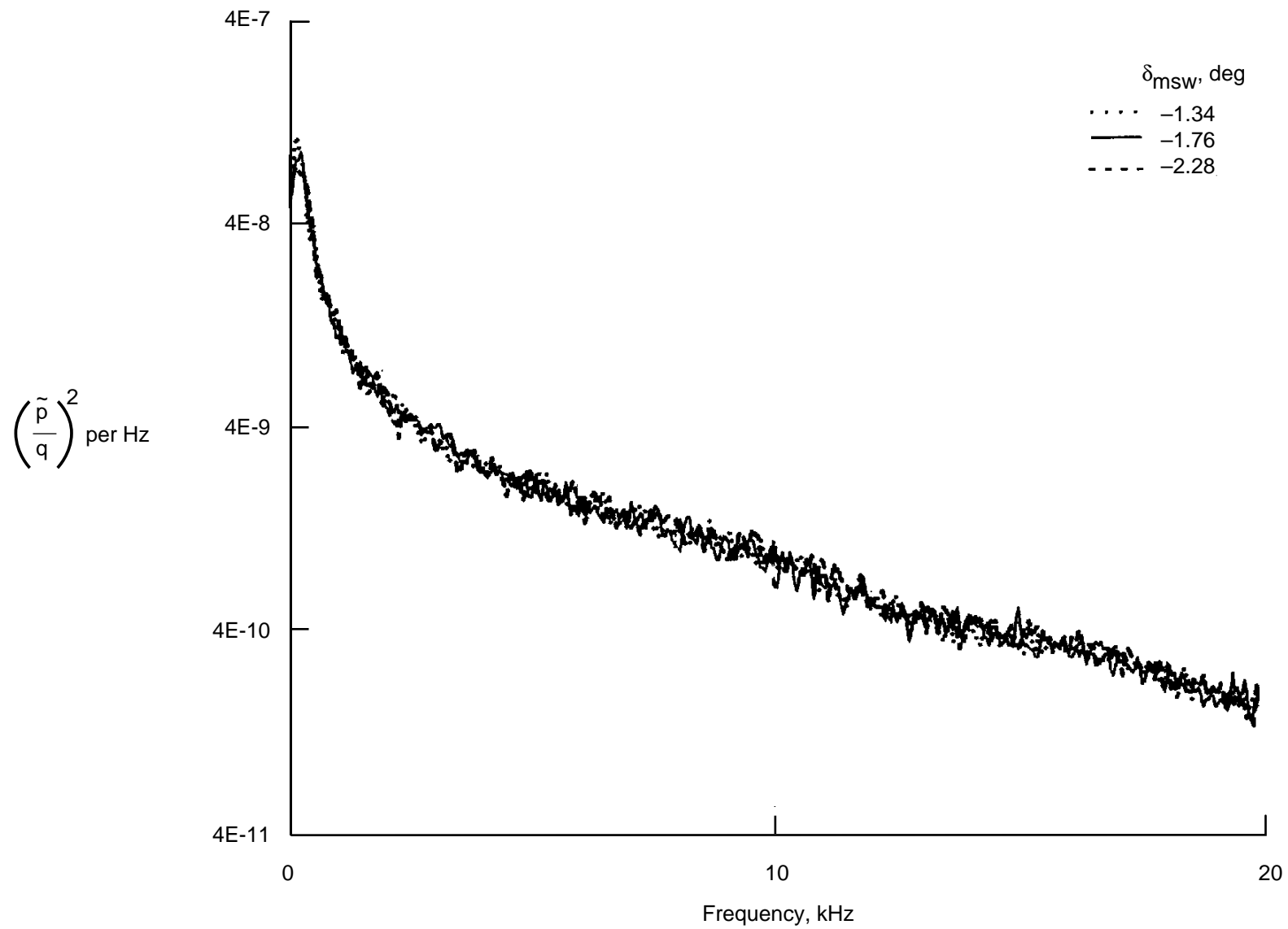
(c) Model support wall angle; $\theta_{tsw} = 0°$; $\alpha_{rf} = 0°$.

Figure 49. Concluded.
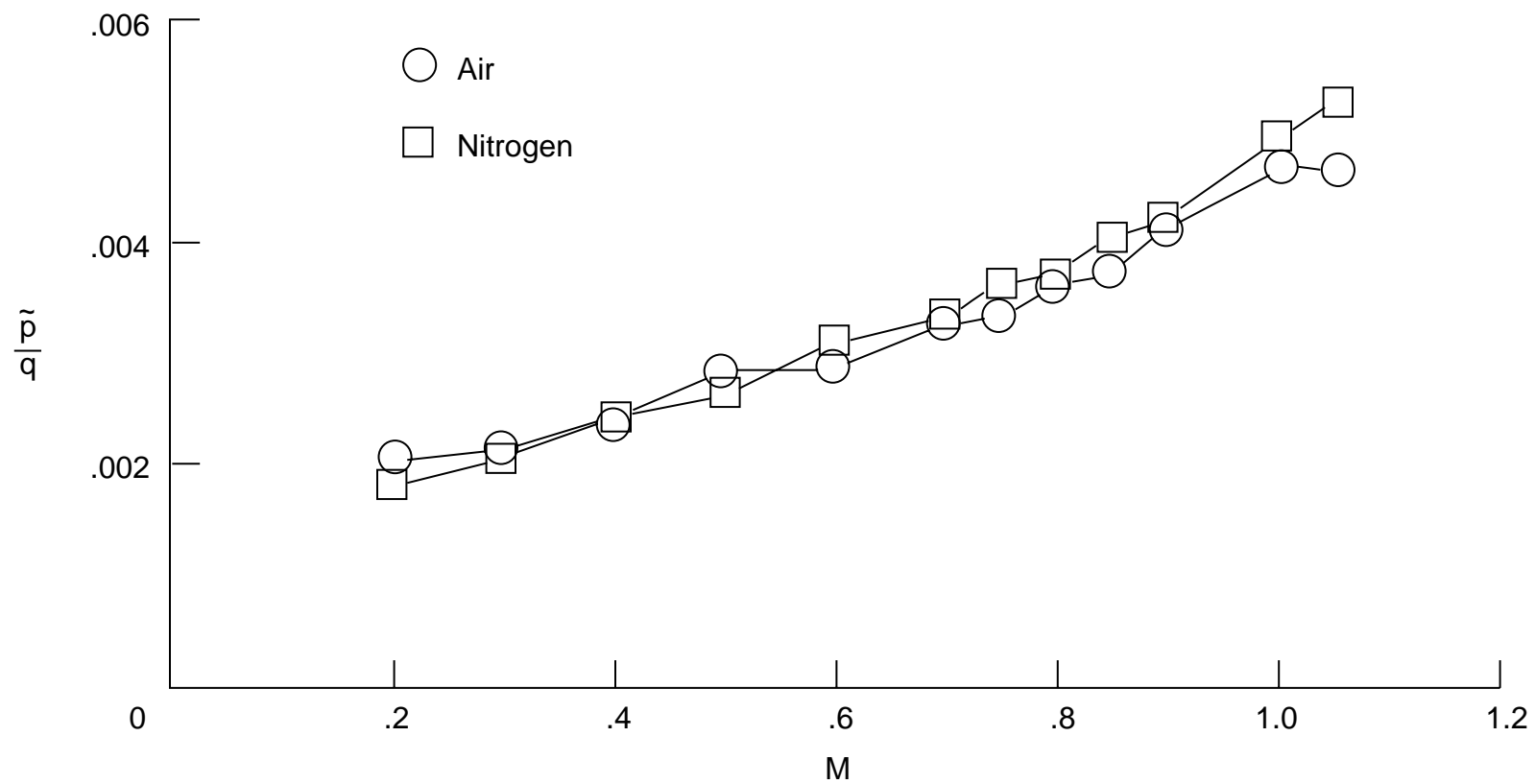
Figure 50. Fluctuating pressure coefficient at liquid nitrogen injection station. $R = 6 \times 10^6$ ft^{-1}; ambient temperature; air and nitrogen modes.
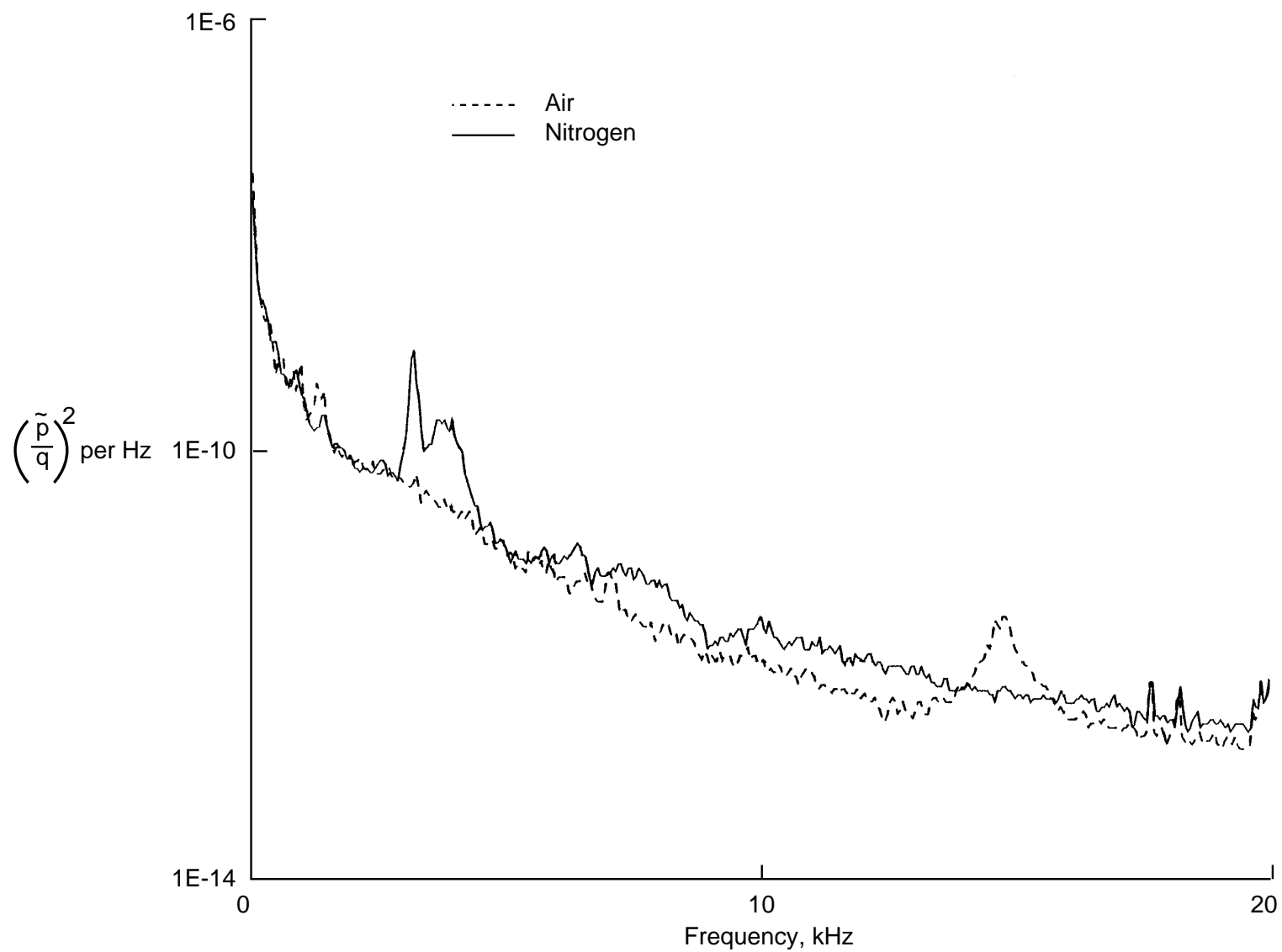
(a) $M = 0.2$.

Figure 51. Power spectra of fluctuating pressure coefficient at liquid nitrogen injection station. $R = 6 \times 10^6$ ft^{-1}; ambient temperature; air and nitrogen modes.
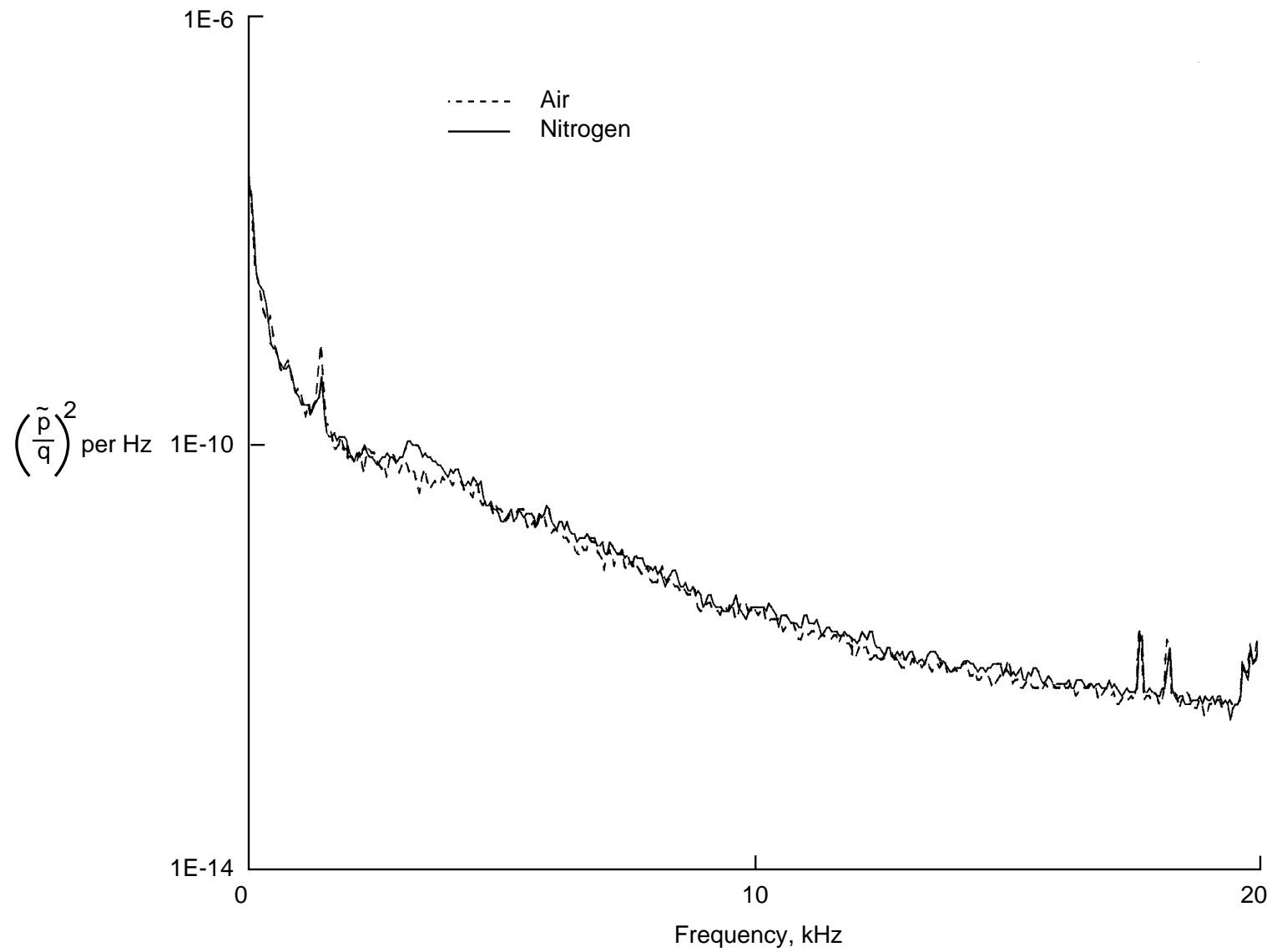
(b) $M = 0.3$.

Figure 51. Continued.
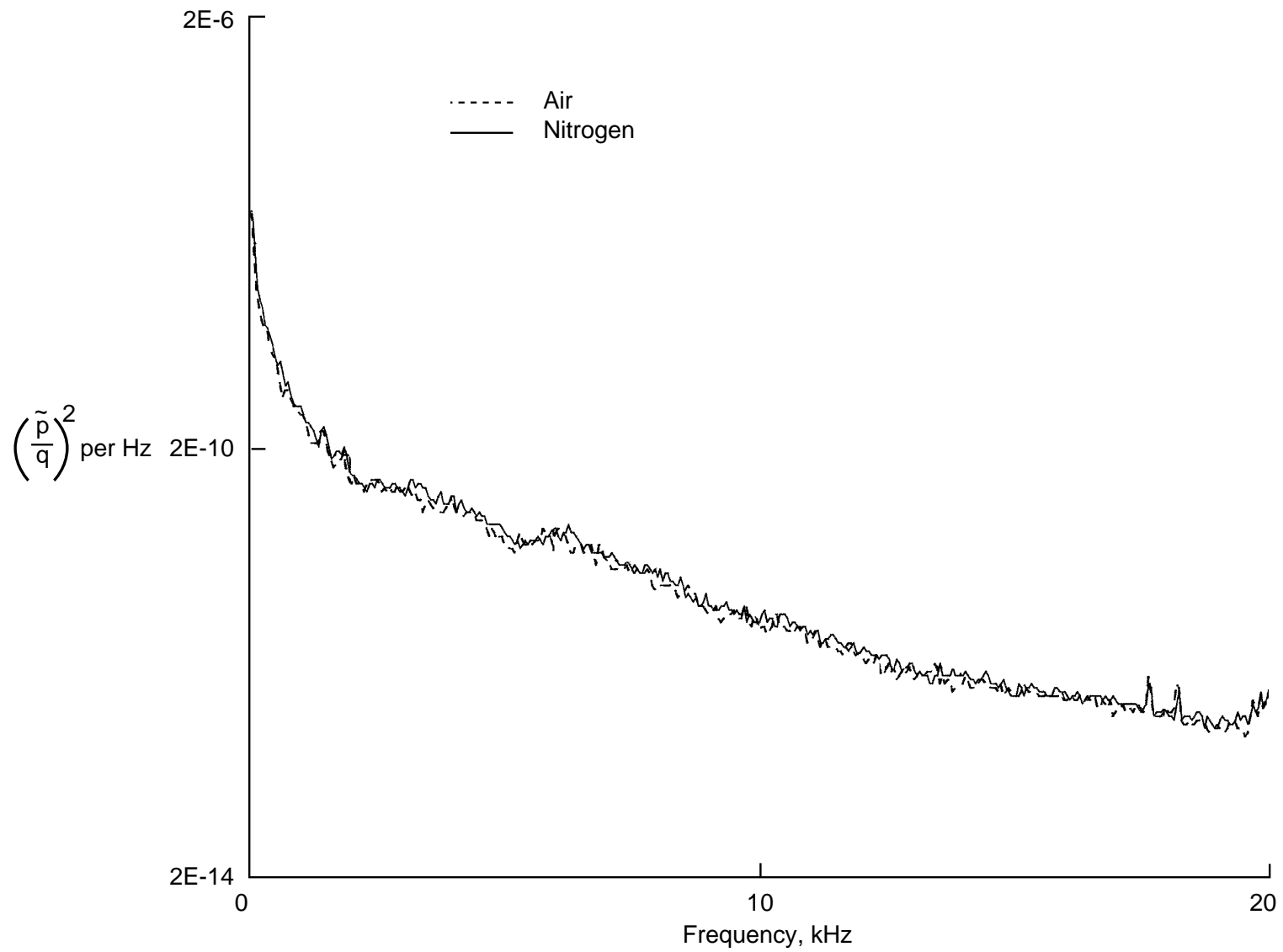
(c) $M = 0.4$.

Figure 51. Continued.
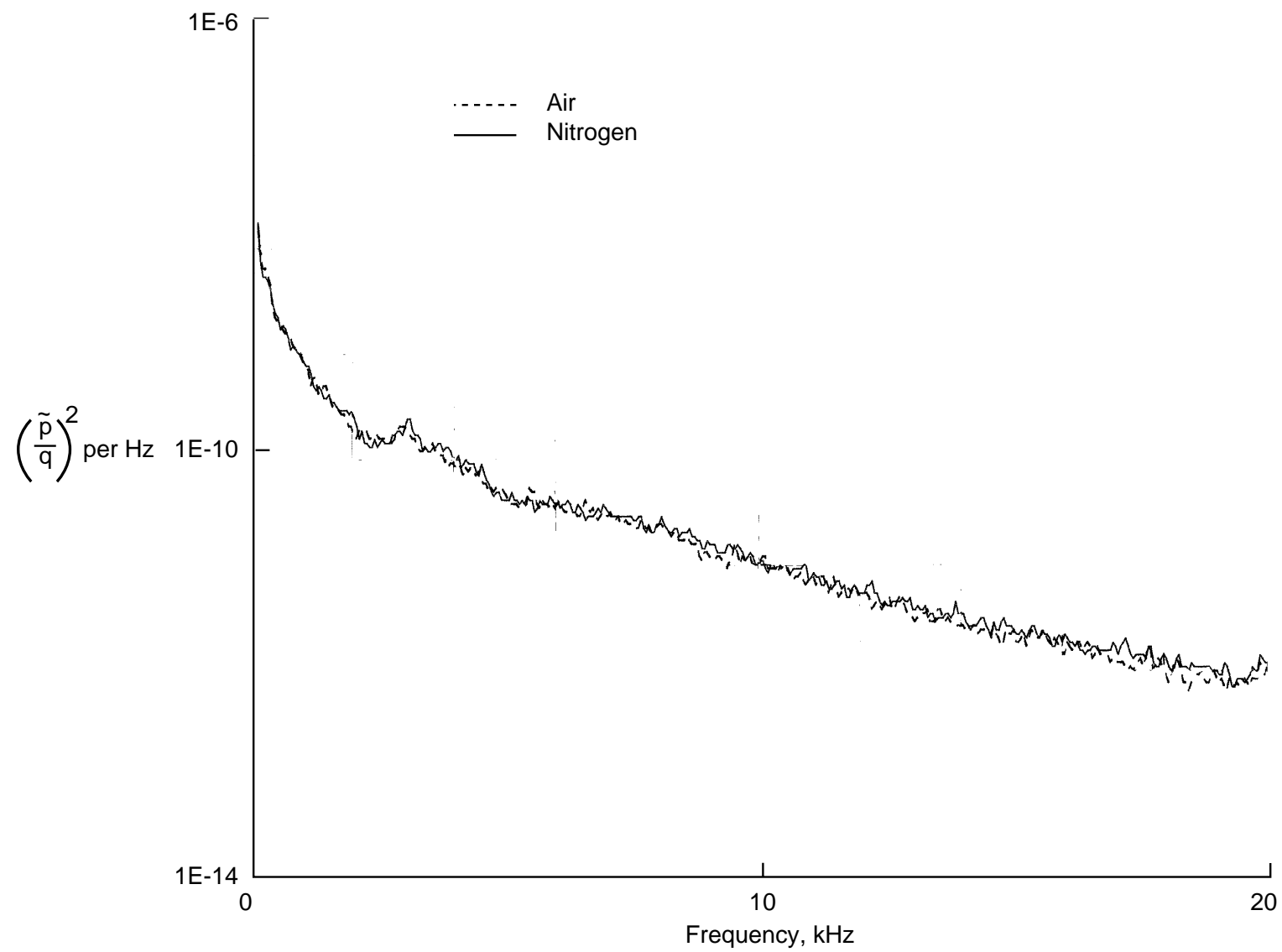
(d) $M = 0.5$.

Figure 51. Continued.
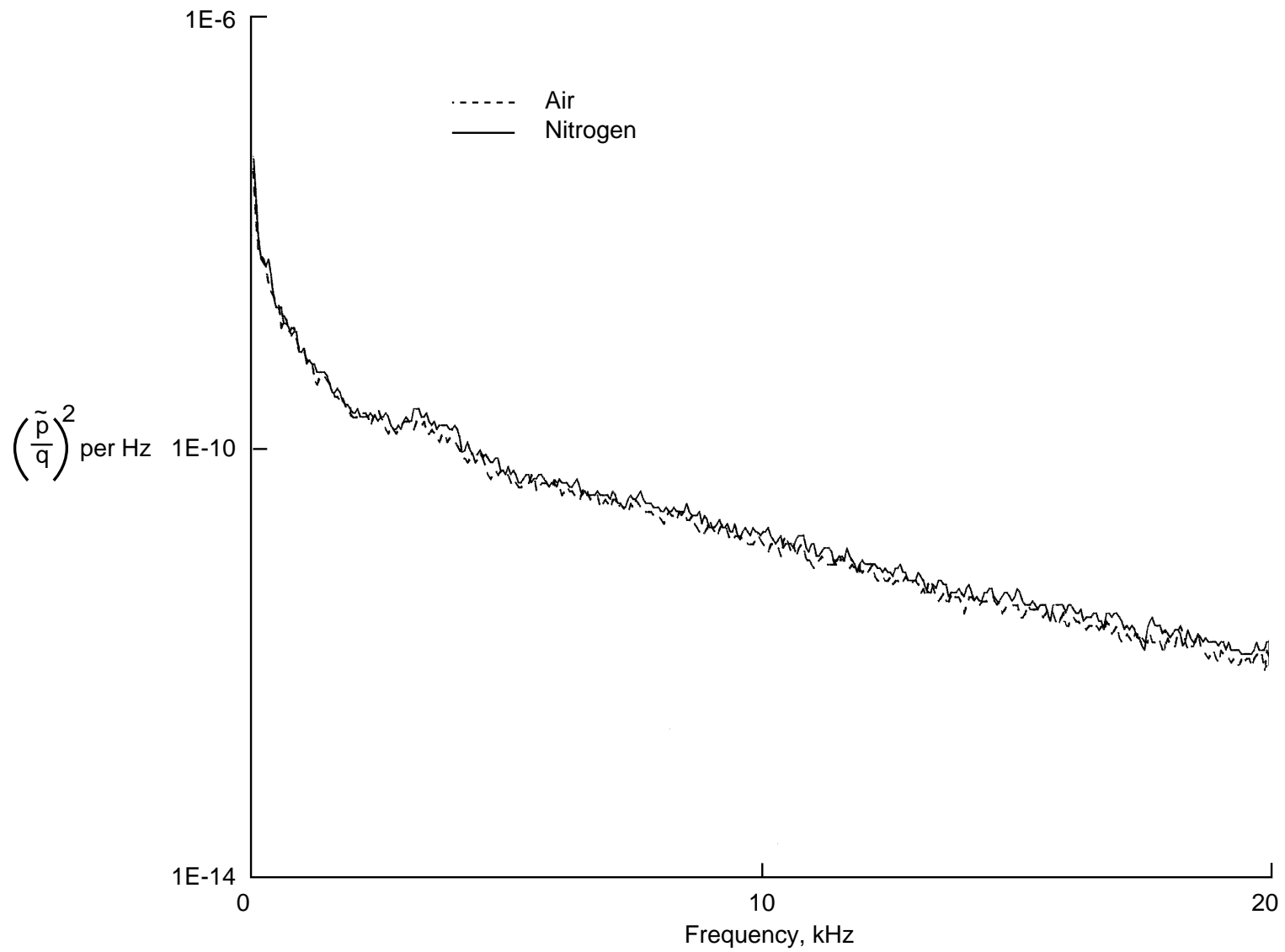
(e) $M = 0.6$.

Figure 51. Continued.
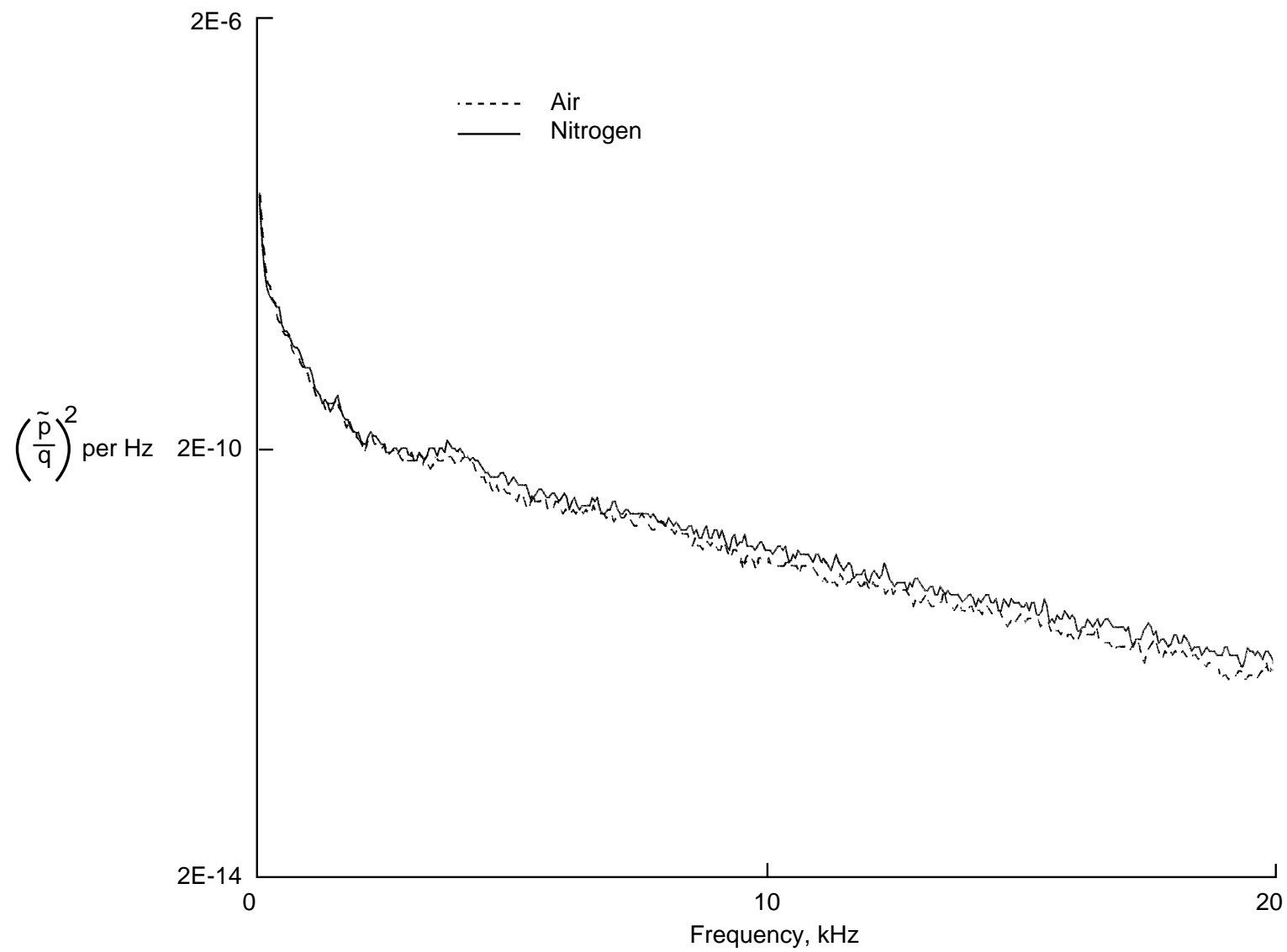
(f) $M = 0.7$.

Figure 51. Continued.
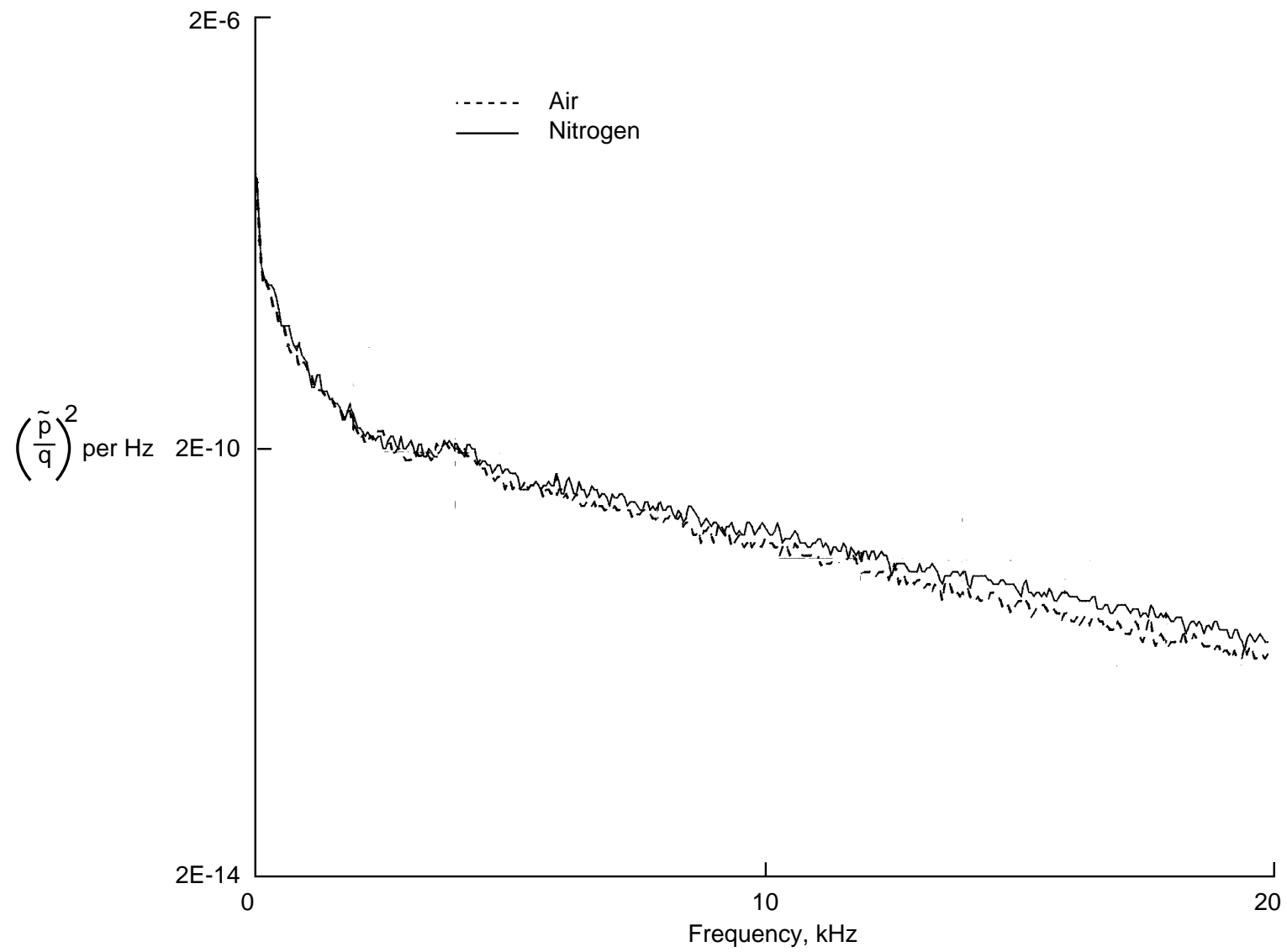
(g) $M = 0.75$.

Figure 51. Continued.
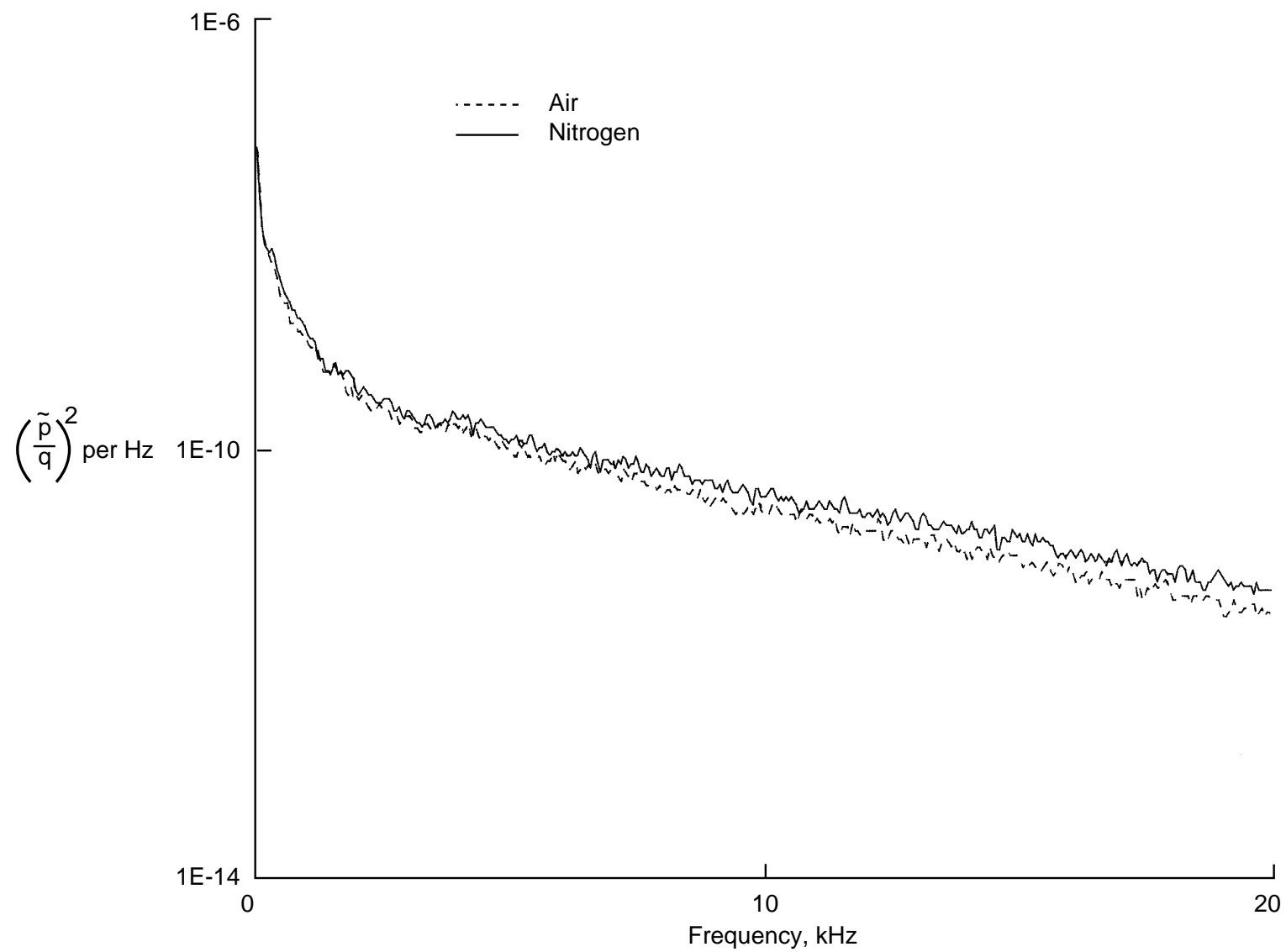
(h) $M = 0.8$.

Figure 51. Continued.

(i) $M = 0.85$.

Figure 51. Continued.

(j) $M = 0.9$.

Figure 51. Continued.
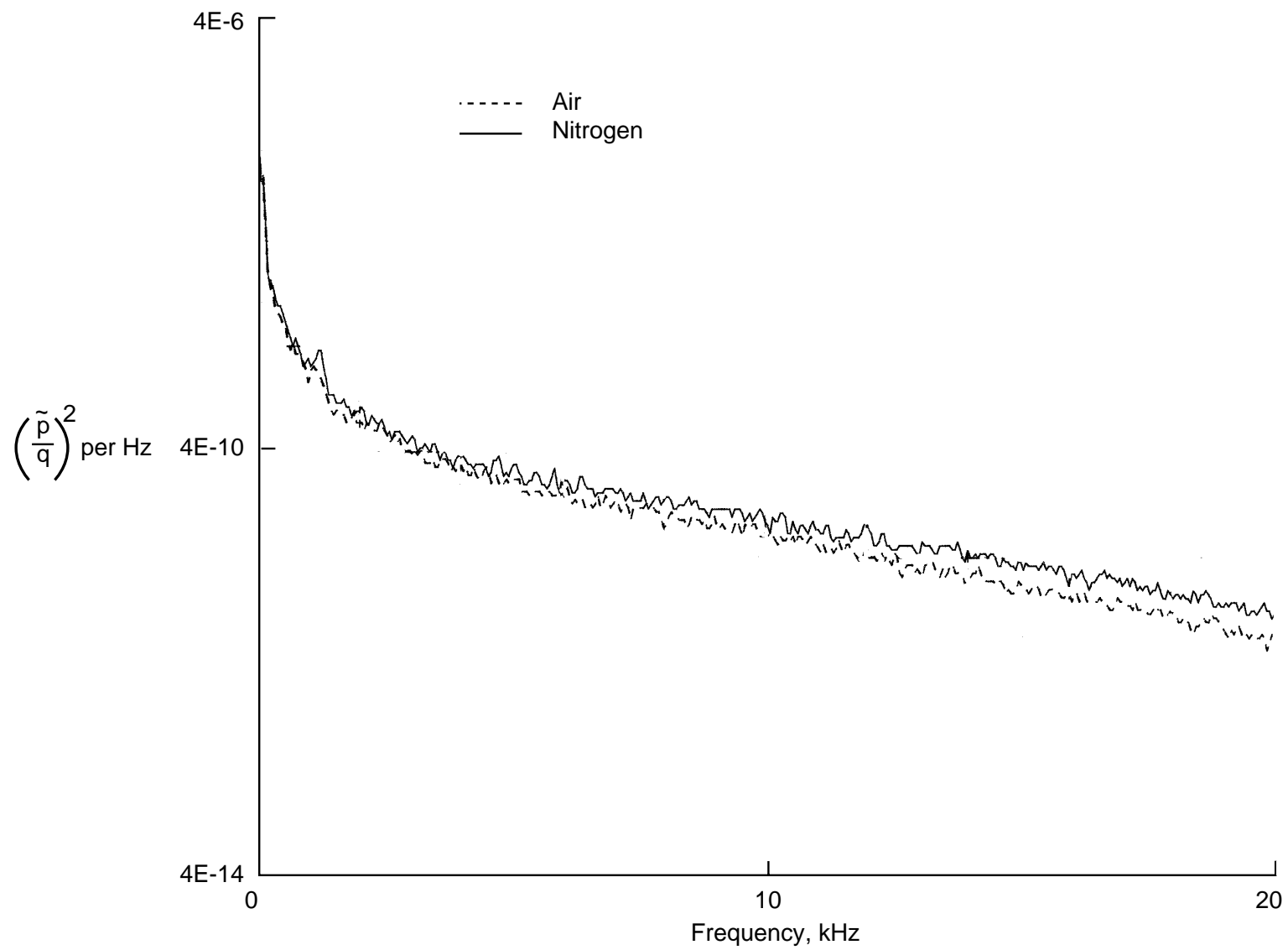
(k) $M = 1.0$.

Figure 51. Continued.
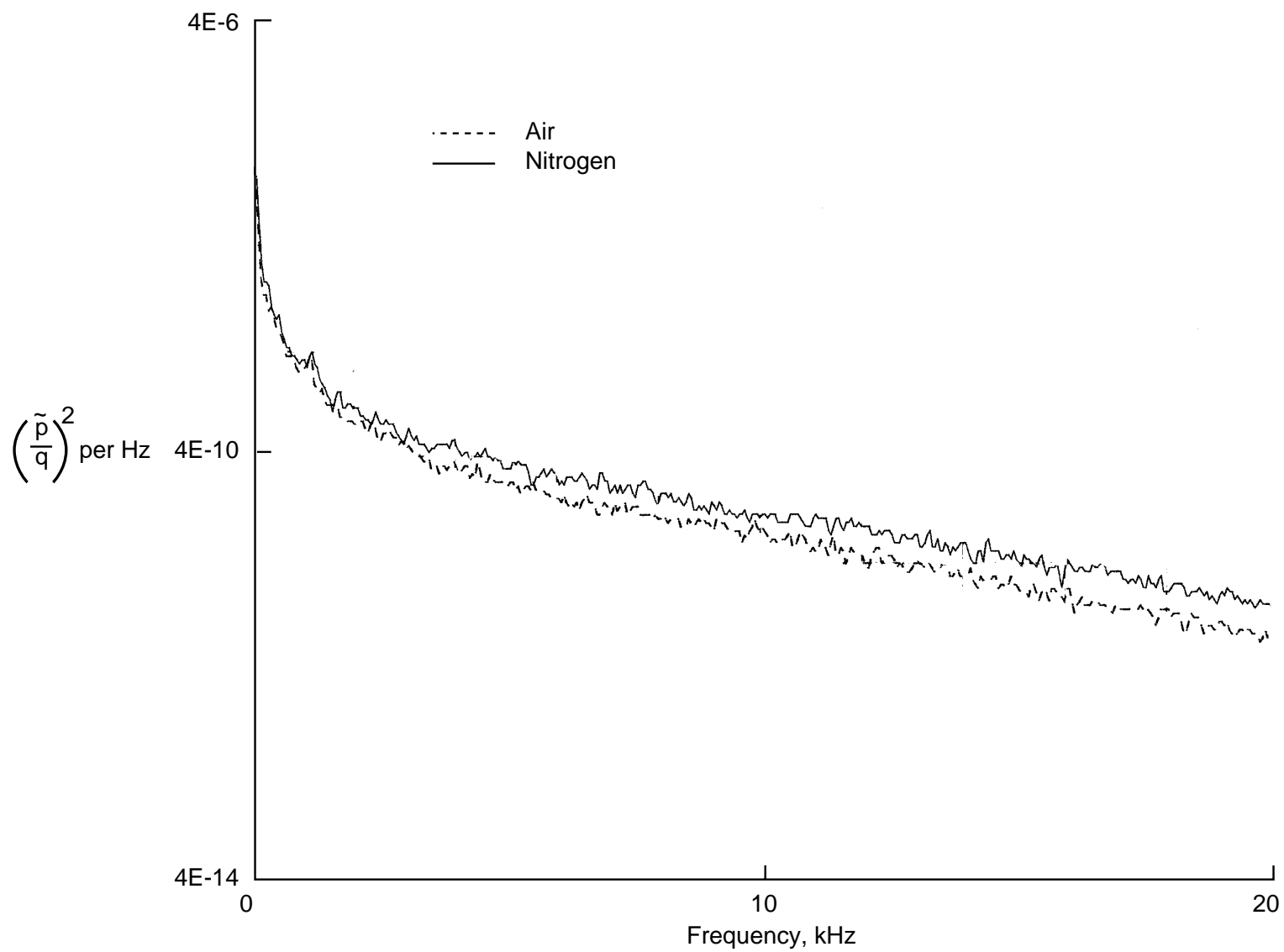
(l) $M = 1.05$.

Figure 51. Concluded.
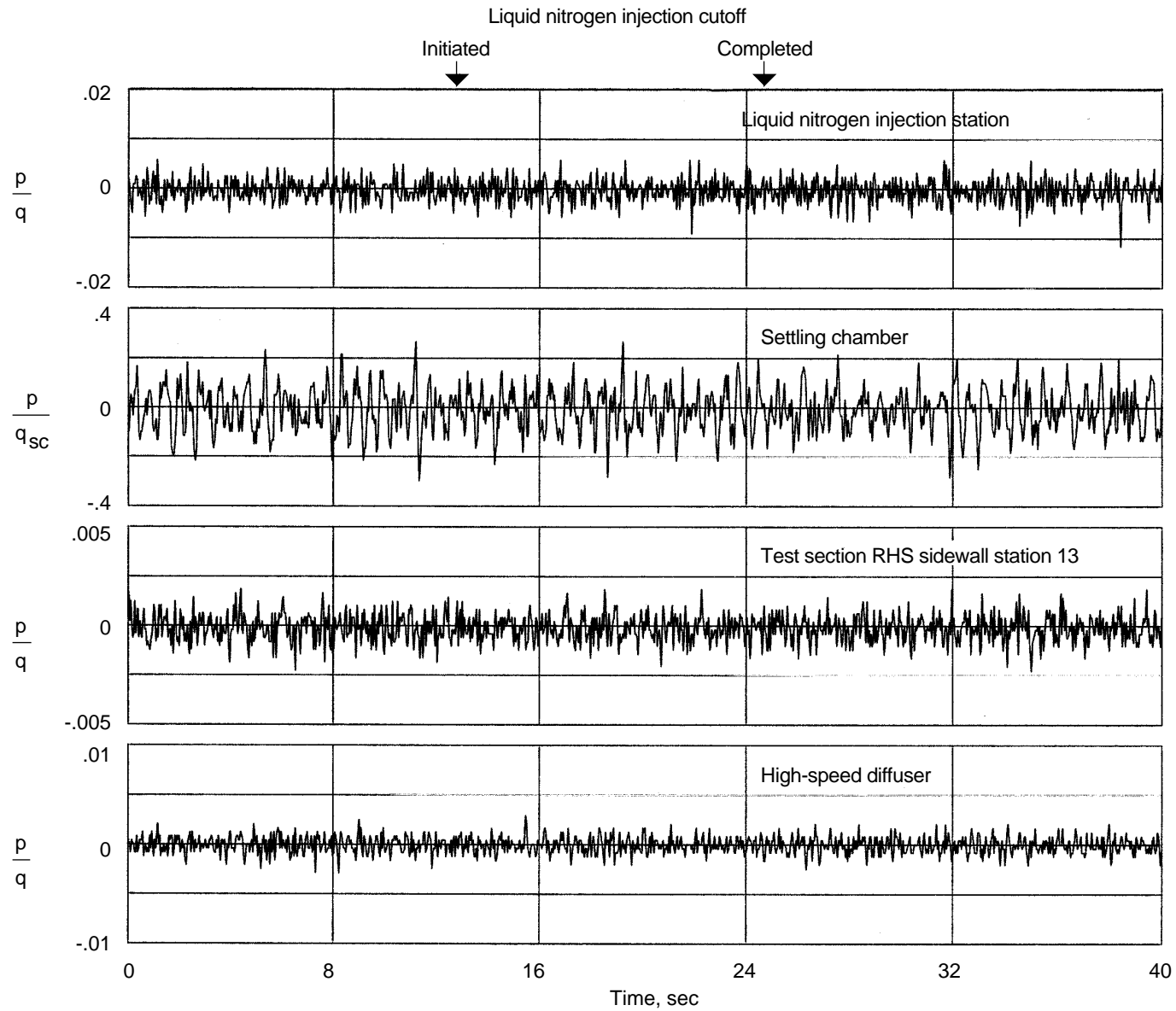
Figure 52. Time history traces of fluctuating static pressure coefficient at four tunnel stations during cutoff of liquid nitrogen injection. $M = 0.8$; $p_t = 20$ psi; and $T_t = -160°F$ at initiation.
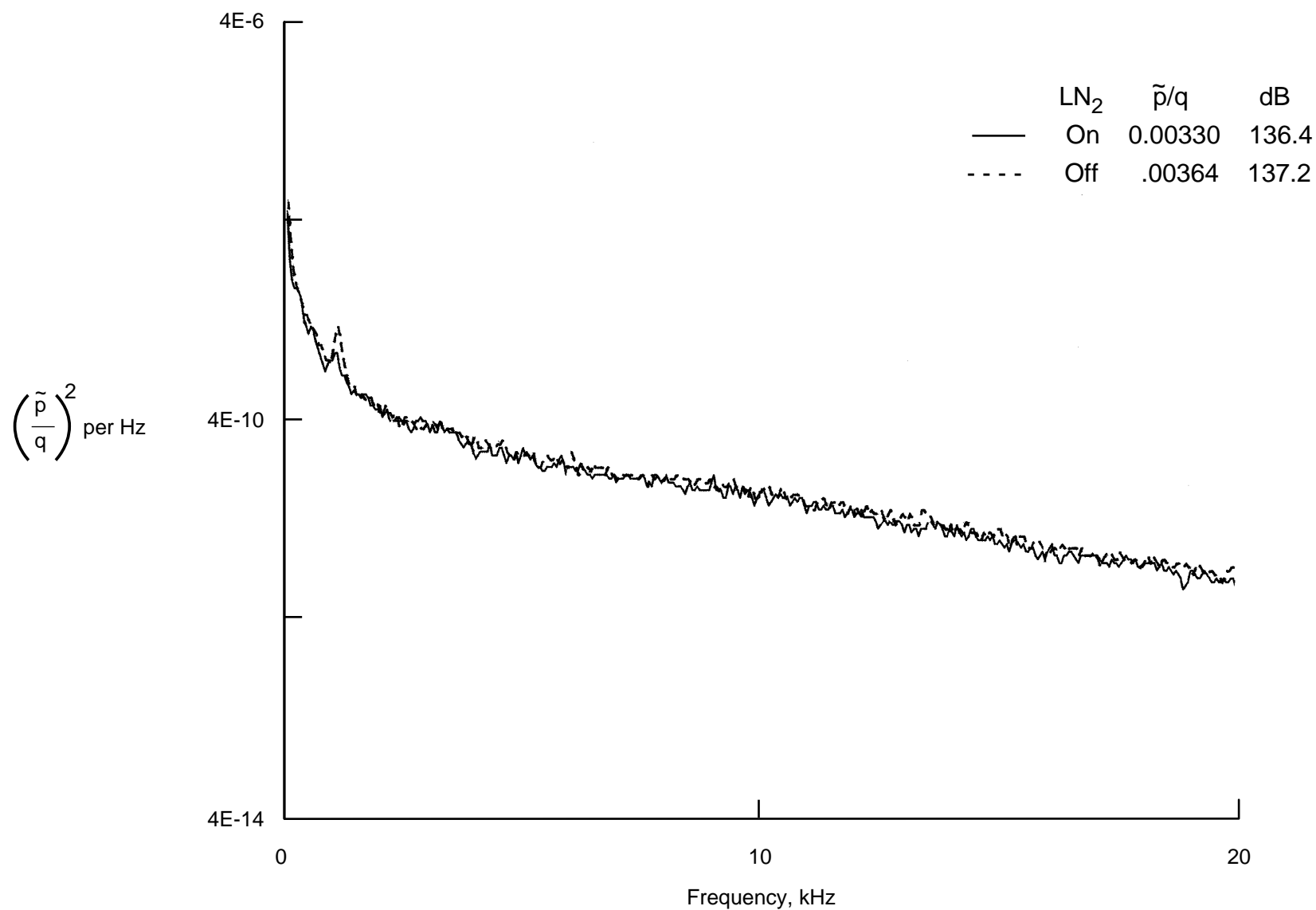
(a) Liquid nitrogen injection station.

Figure 53. Power spectra of fluctuating pressure coefficient before and after cutoff of liquid nitrogen injection. $M = 0.8$; $p_t = 20$ psi; $T_t = -160°F$ before cutoff; and dB re 20 μPa.
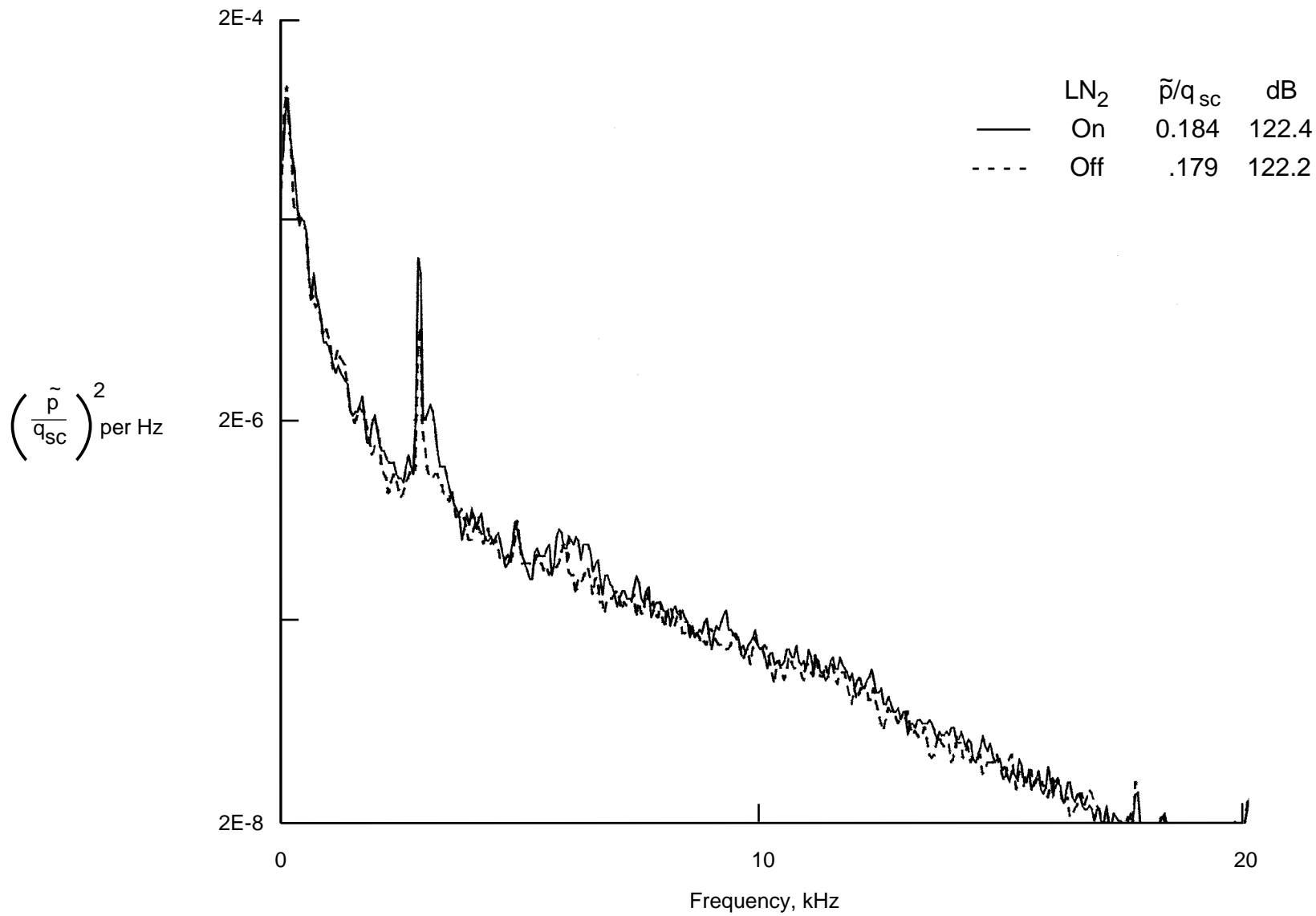
(b) Settling chamber.

Figure 53. Continued.
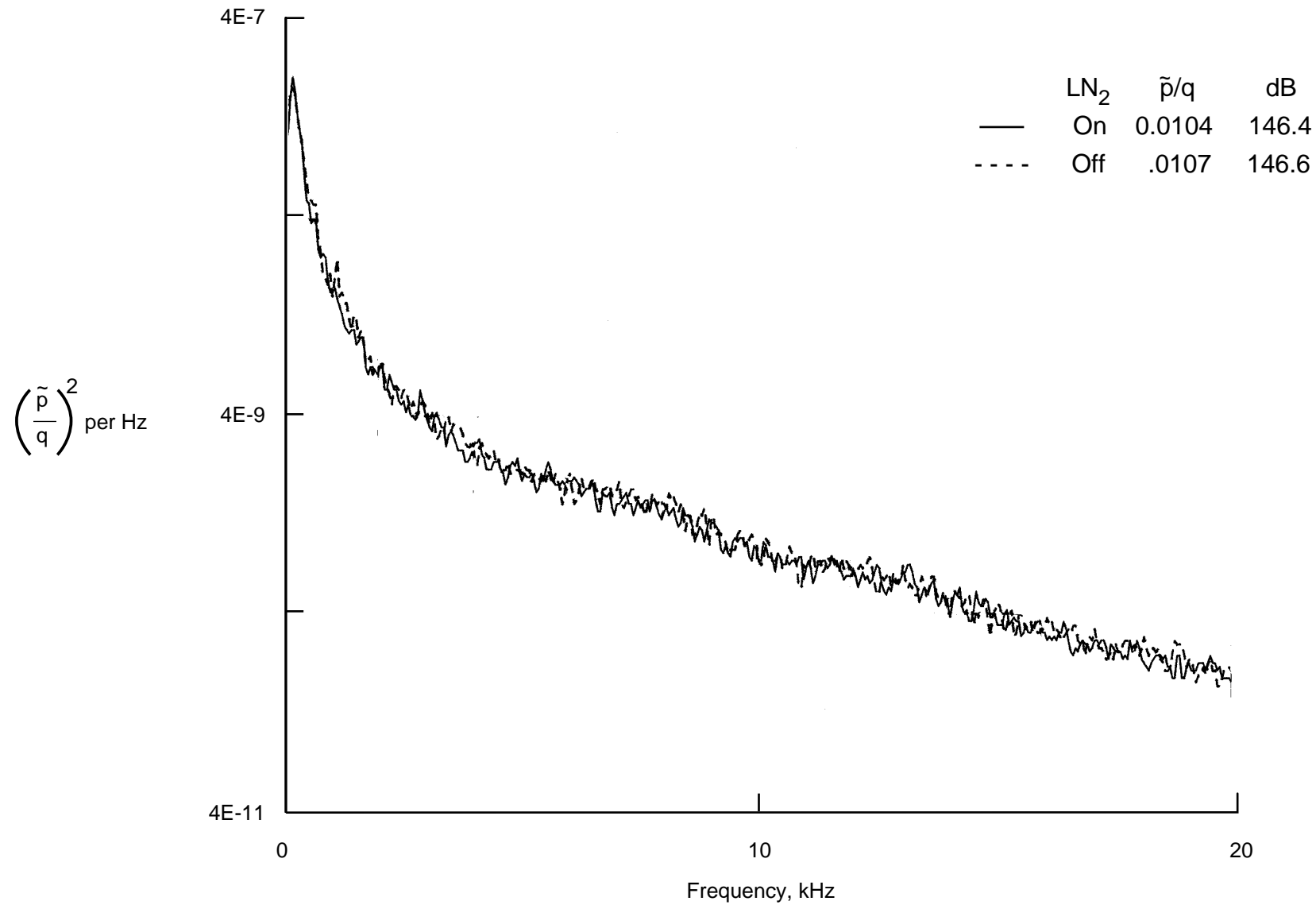
(c) Test section RHS sidewall station 13.

Figure 53. Continued.
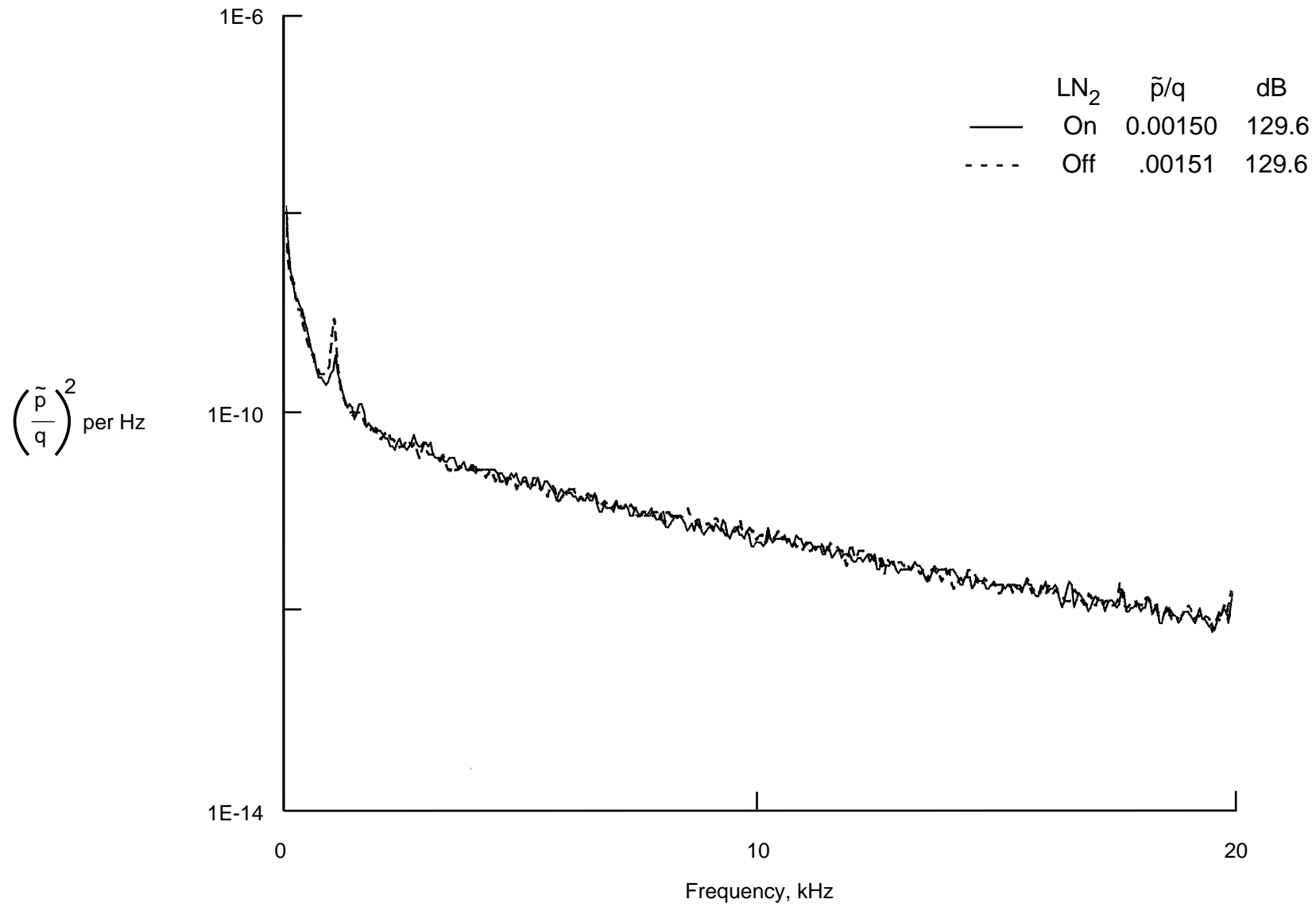
(d) High-speed diffuser.

Figure 53. Concluded.
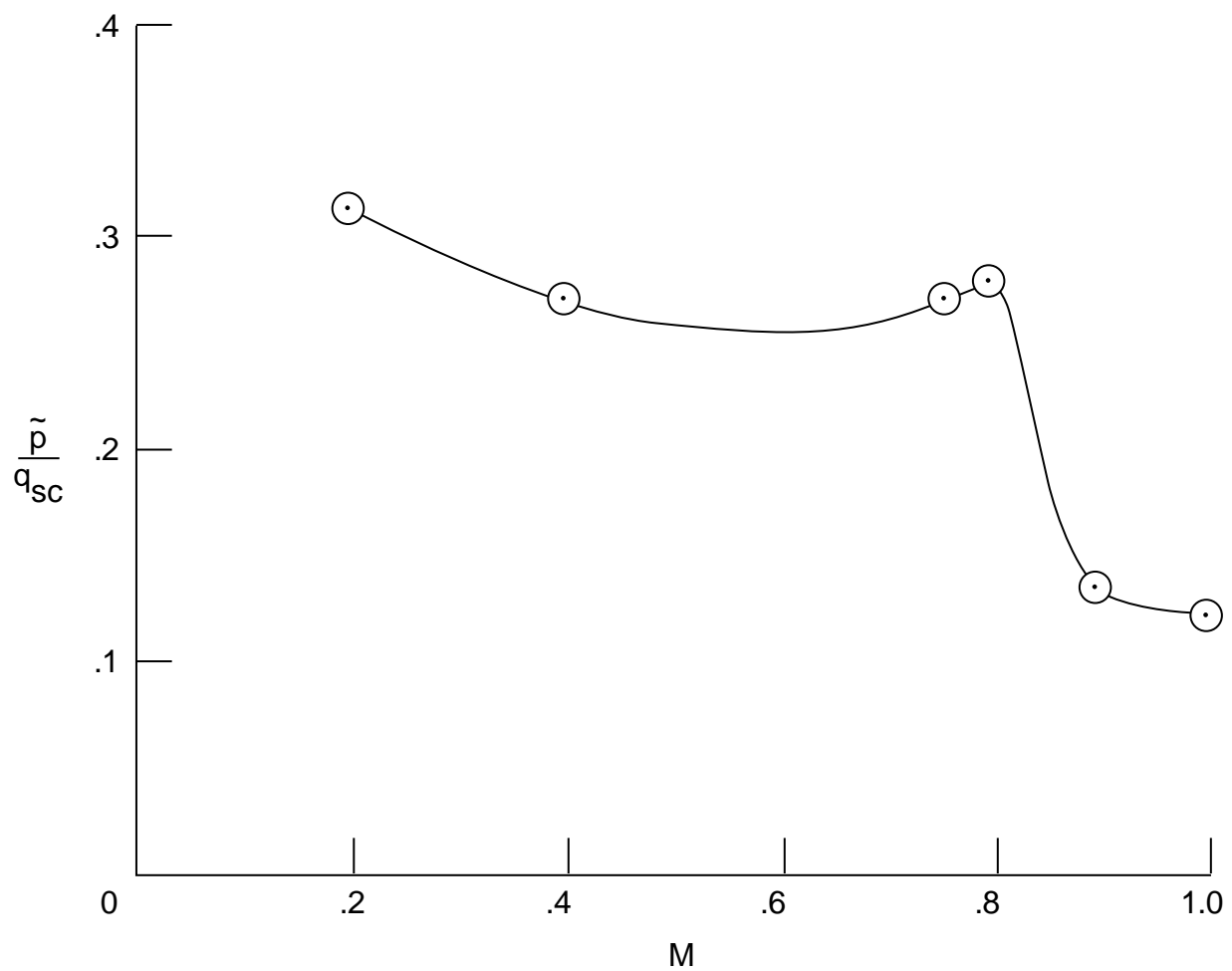
Figure 54. Fluctuating pressure coefficient in settling chamber for maximum Reynolds number boundary in nitrogen mode.
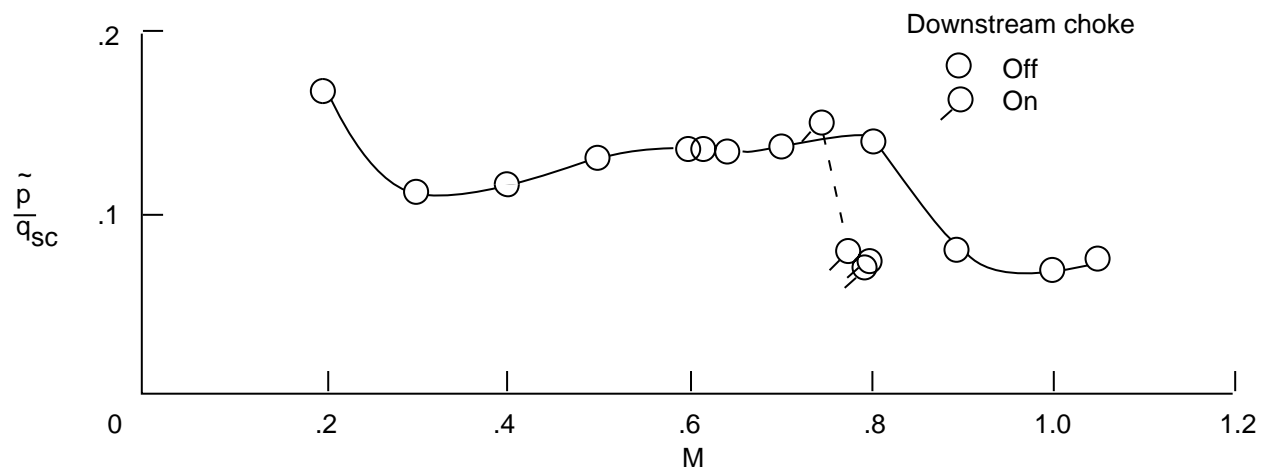
(a) Test section slots open.
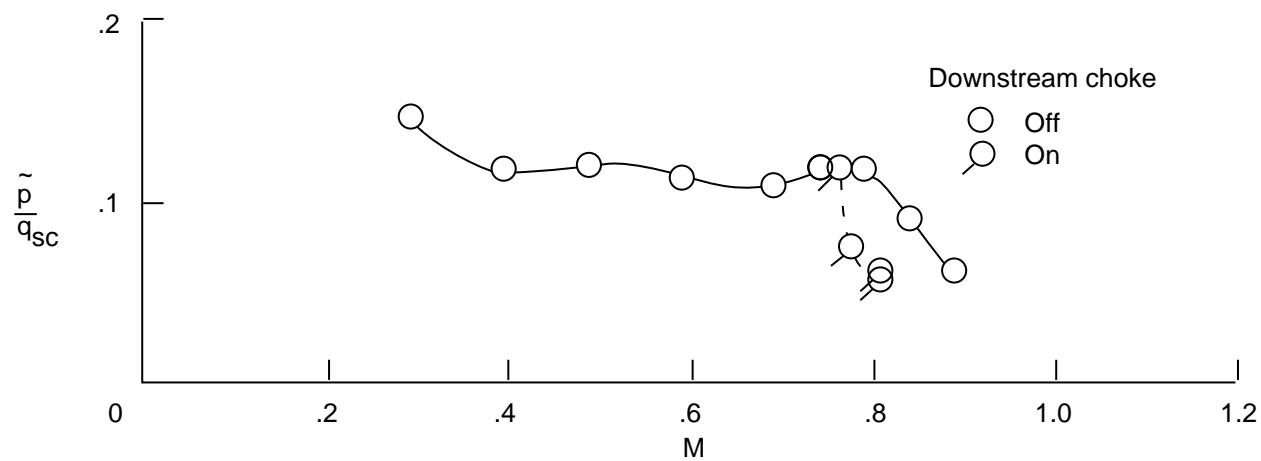
(b) Test section slots covered.

Figure 55. Fluctuating pressure coefficient in settling chamber. Minimum Reynolds number boundary; air; choked and unchoked.
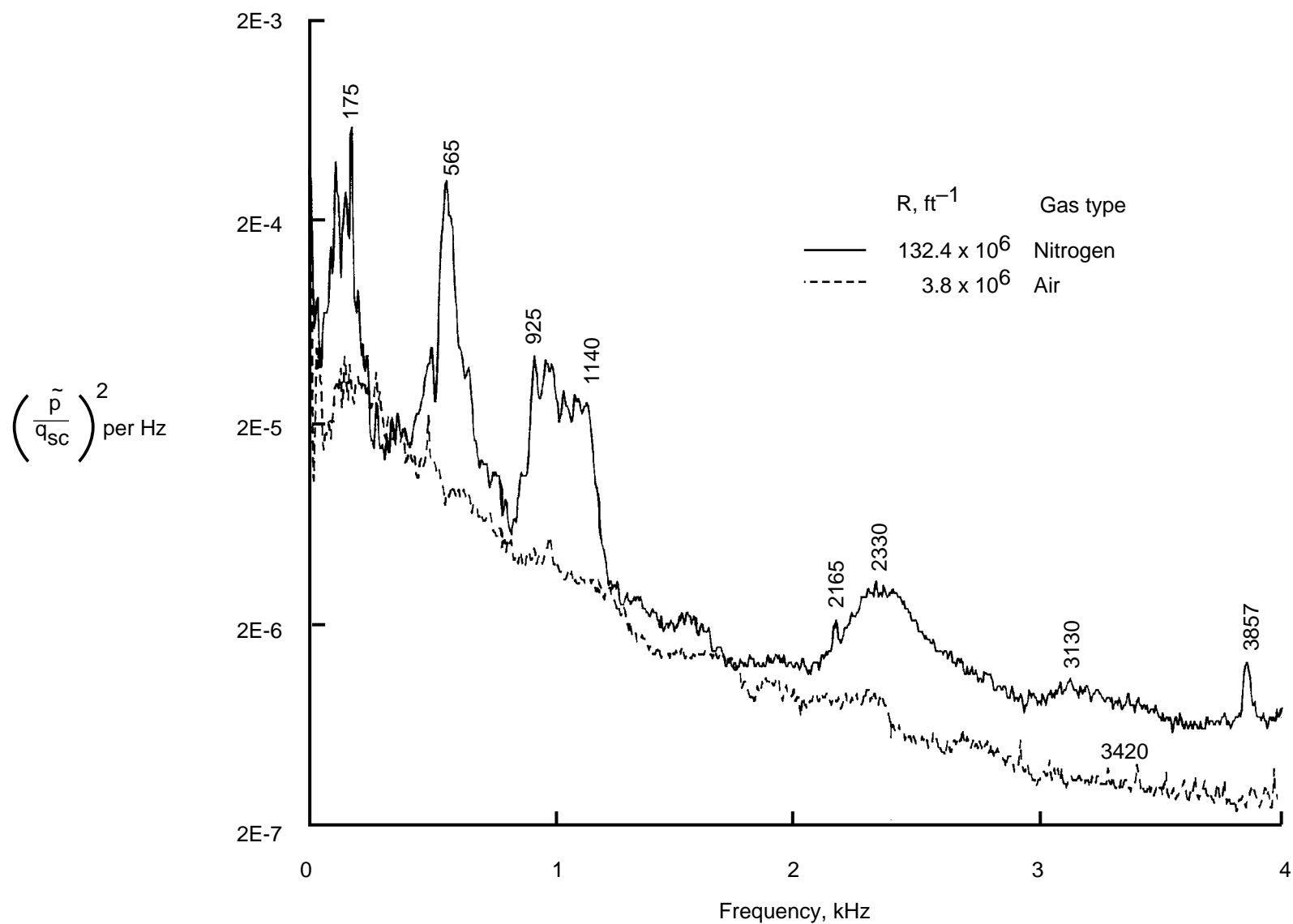
(a) Linear frequency scale.

Figure 56.   Power spectra of fluctuating pressure coefficient in settling chamber. $M = 0.8$; minimum and maximum Reynolds number boundaries.
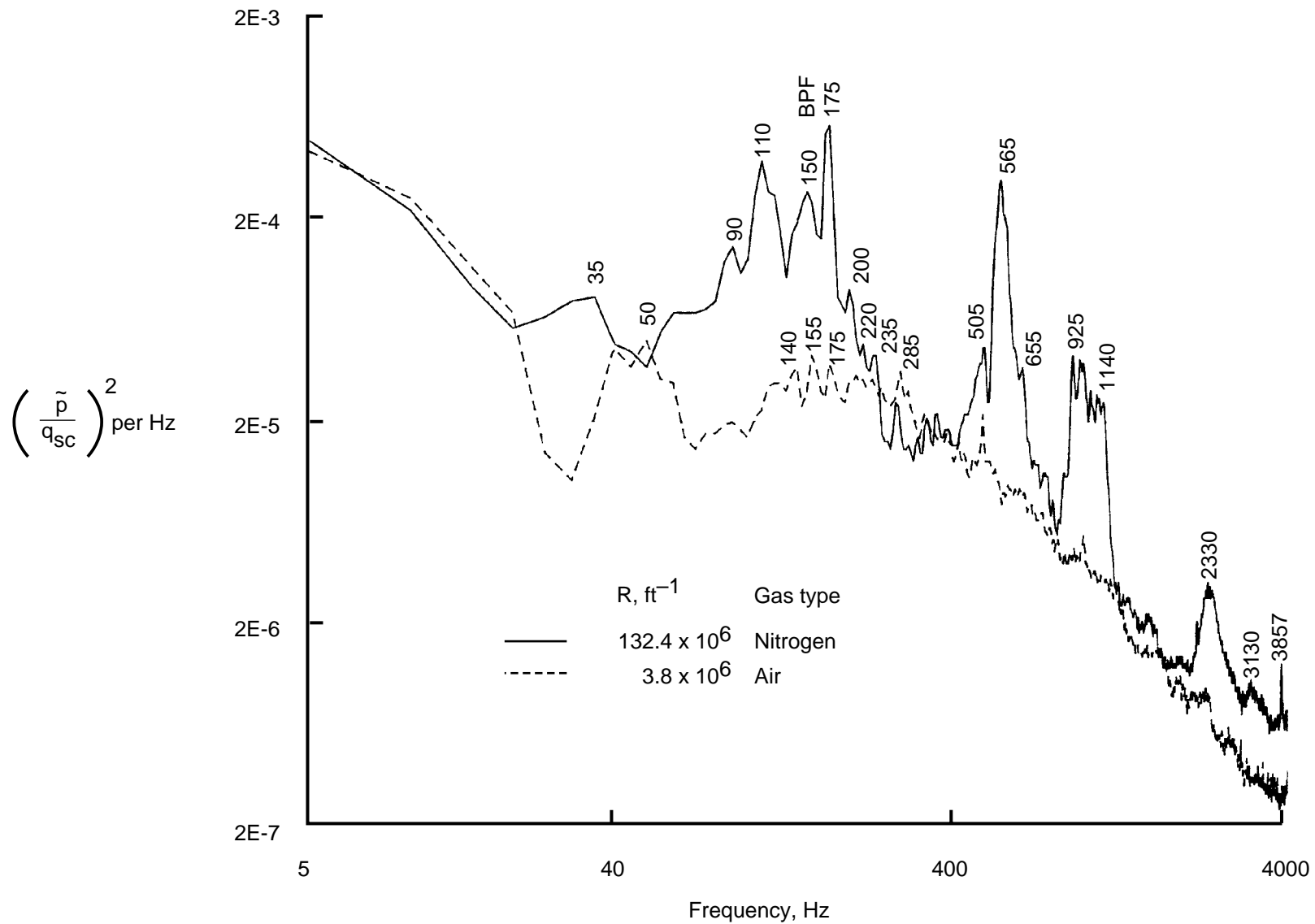
(b) Logarithmic frequency scale.

Figure 56. Concluded.
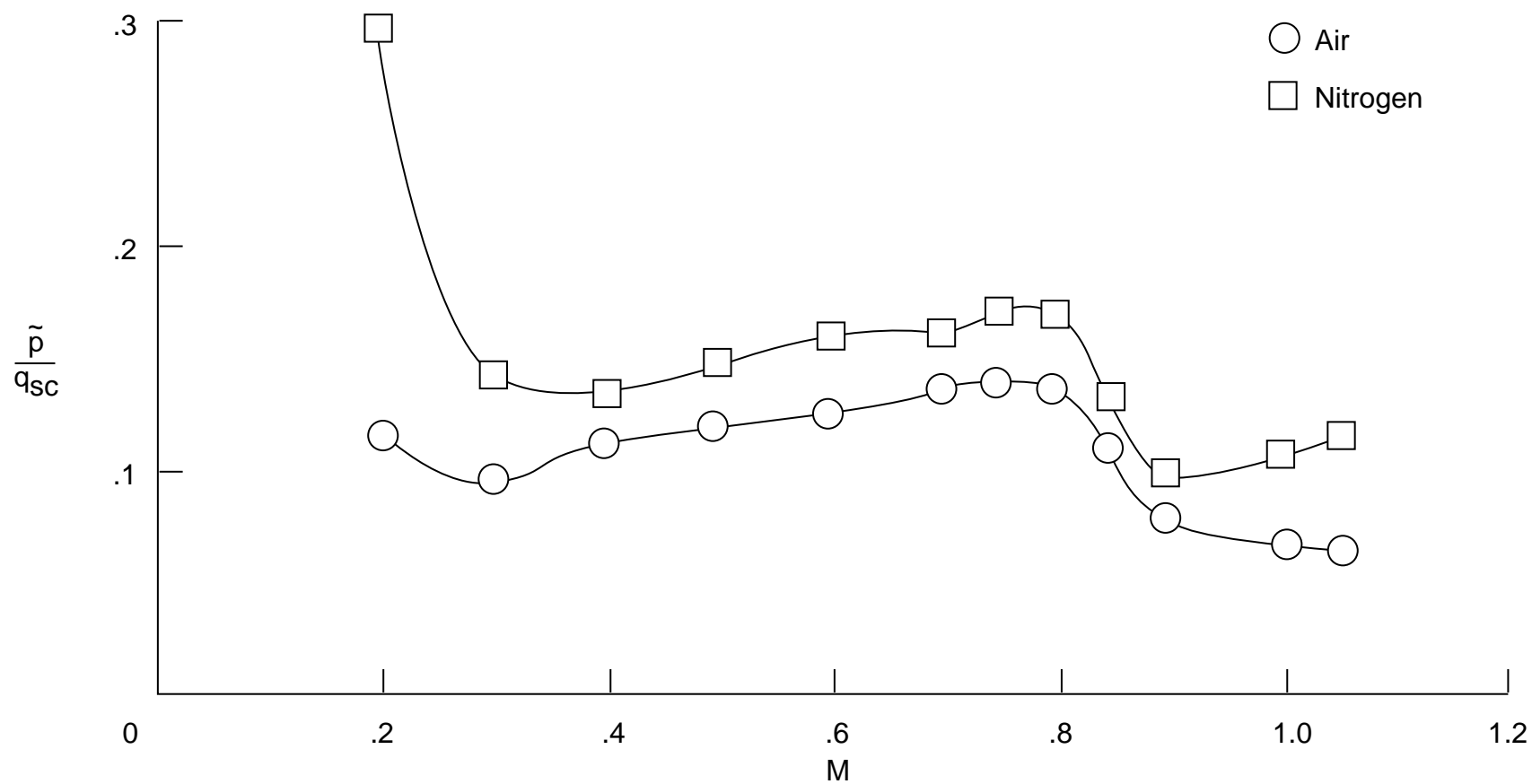
Figure 57. Fluctuating pressure coefficient in settling chamber. $R = 6 \times 10^6$ ft^{-1}; ambient temperature; air and nitrogen modes.
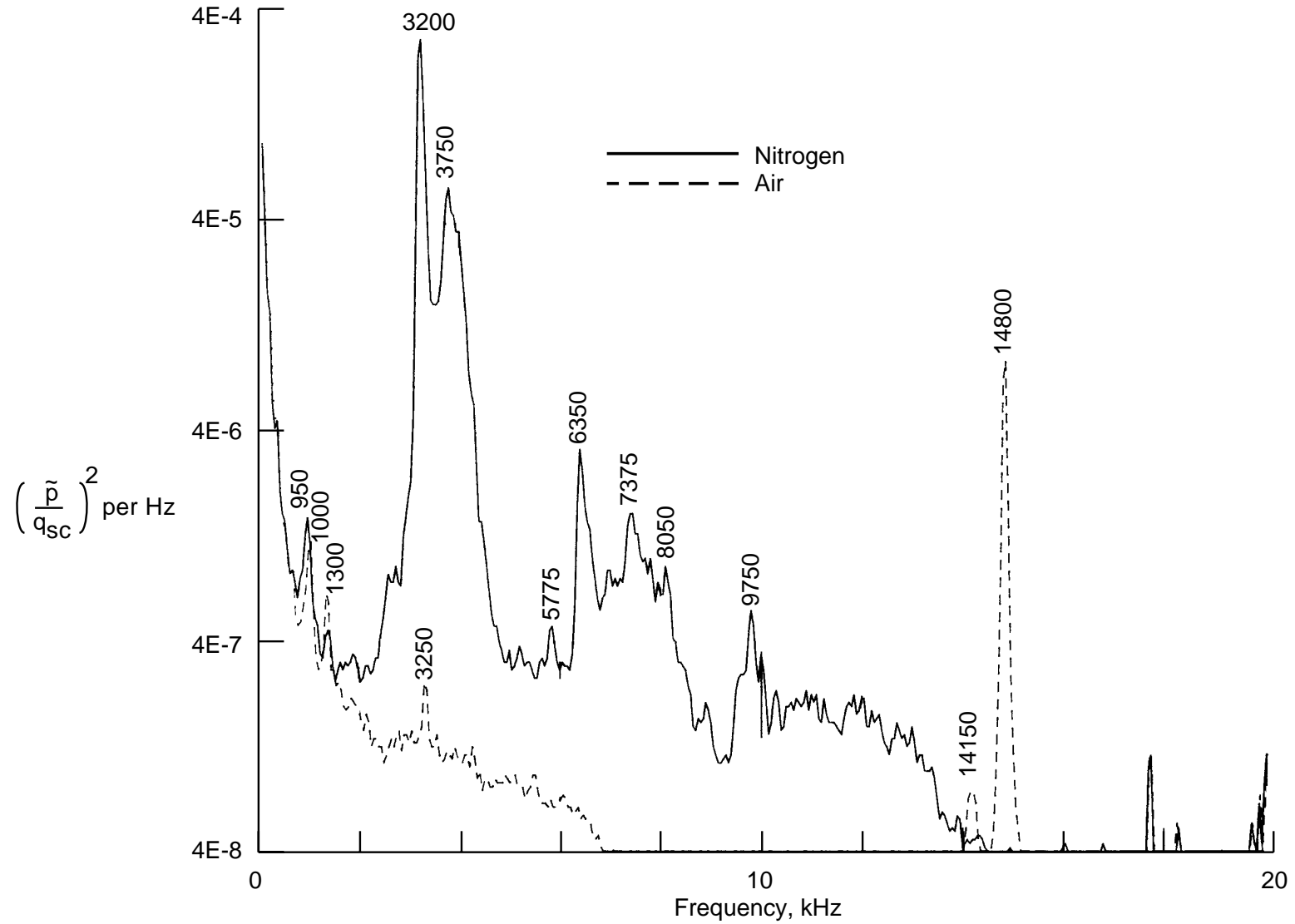
(a) $M = 0.2$.

Figure 58. Power spectra of fluctuating pressure coefficient in settling chamber. $R = 6 \times 10^6$ ft^{-1}; ambient temperature; air and nitrogen modes.
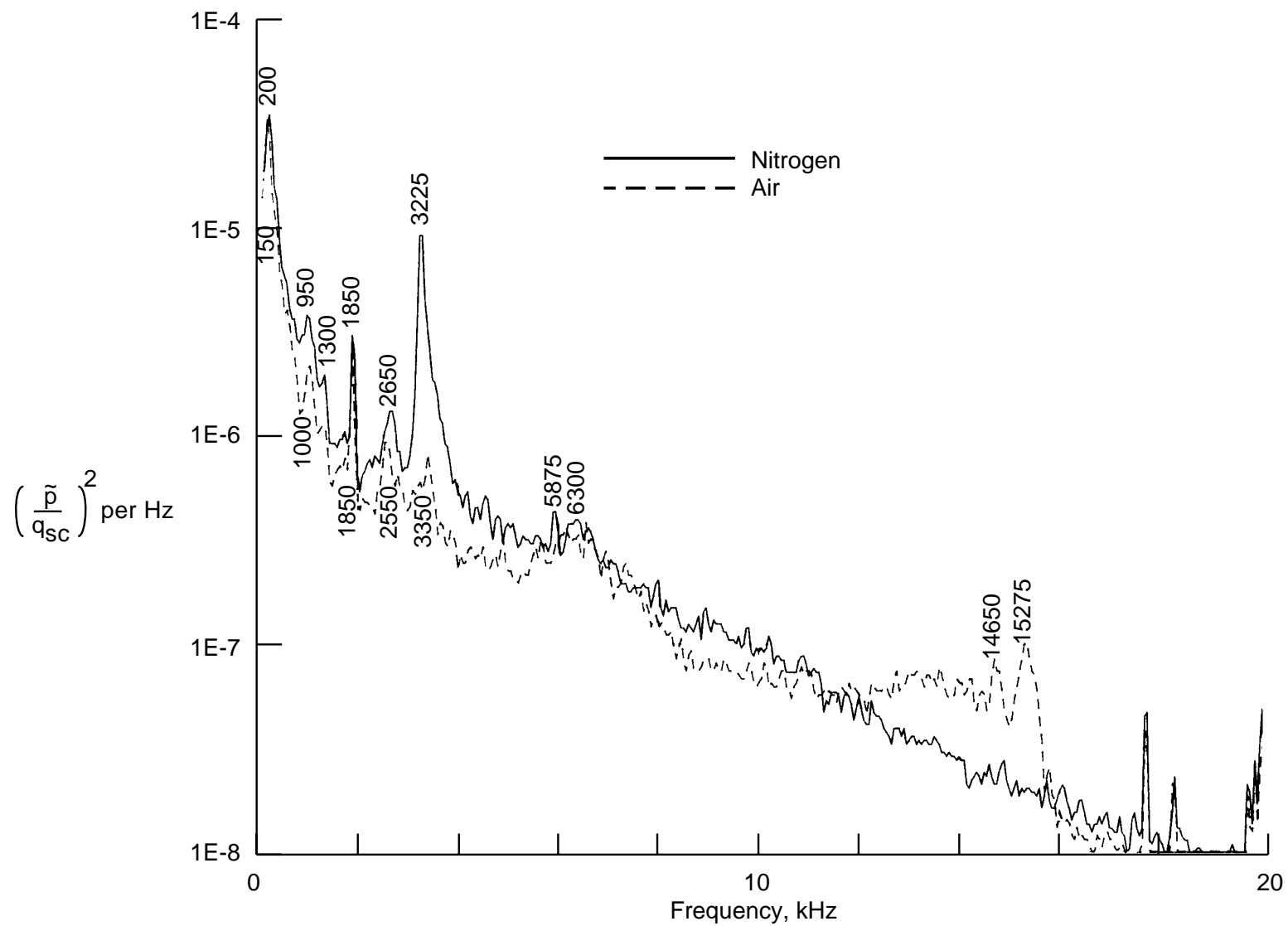
(b) $M = 0.4$.

Figure 58. Continued.
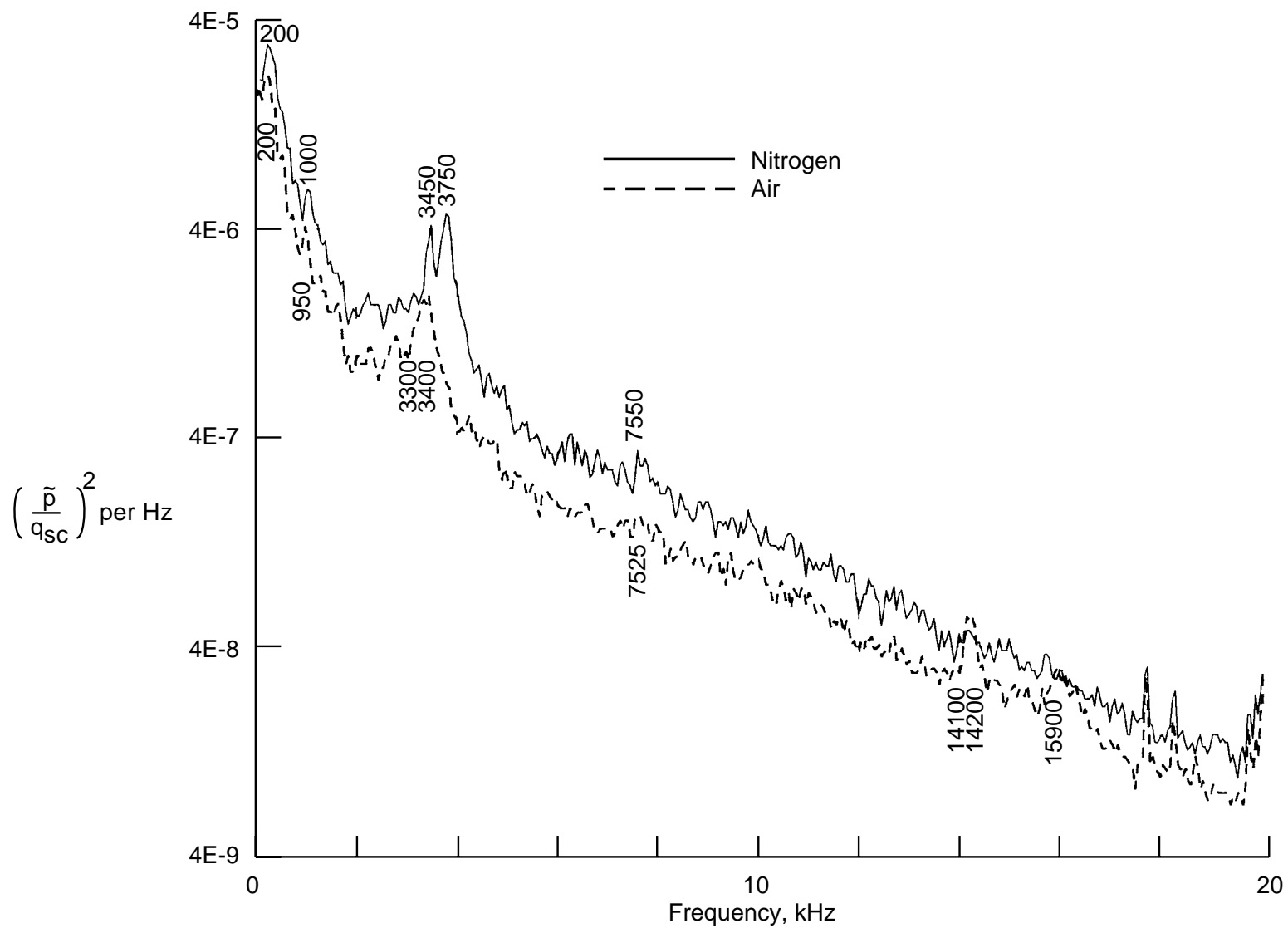
(c) $M = 0.6$.

Figure 58. Continued.
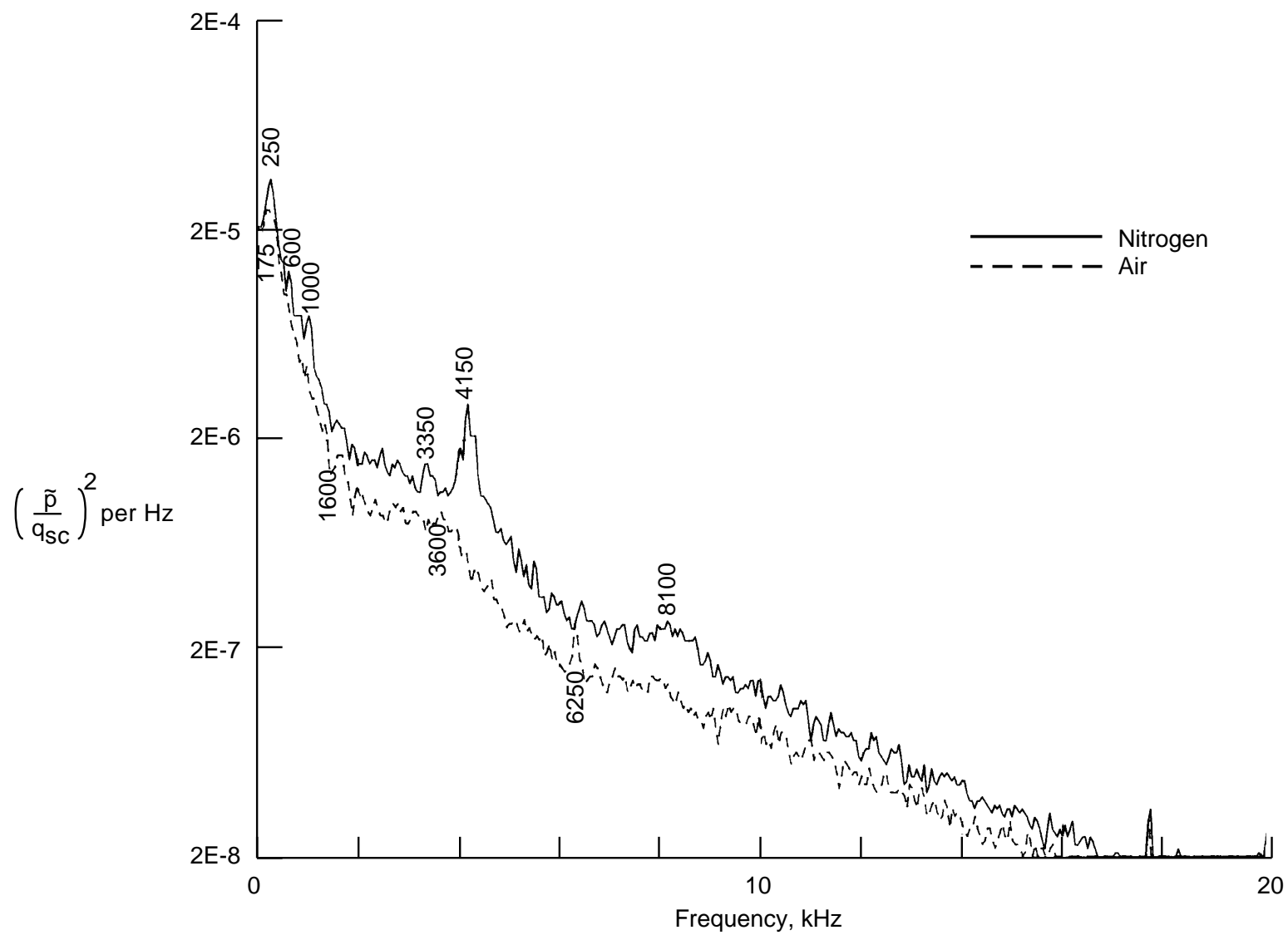
(d) $M = 0.7$.

Figure 58. Continued.
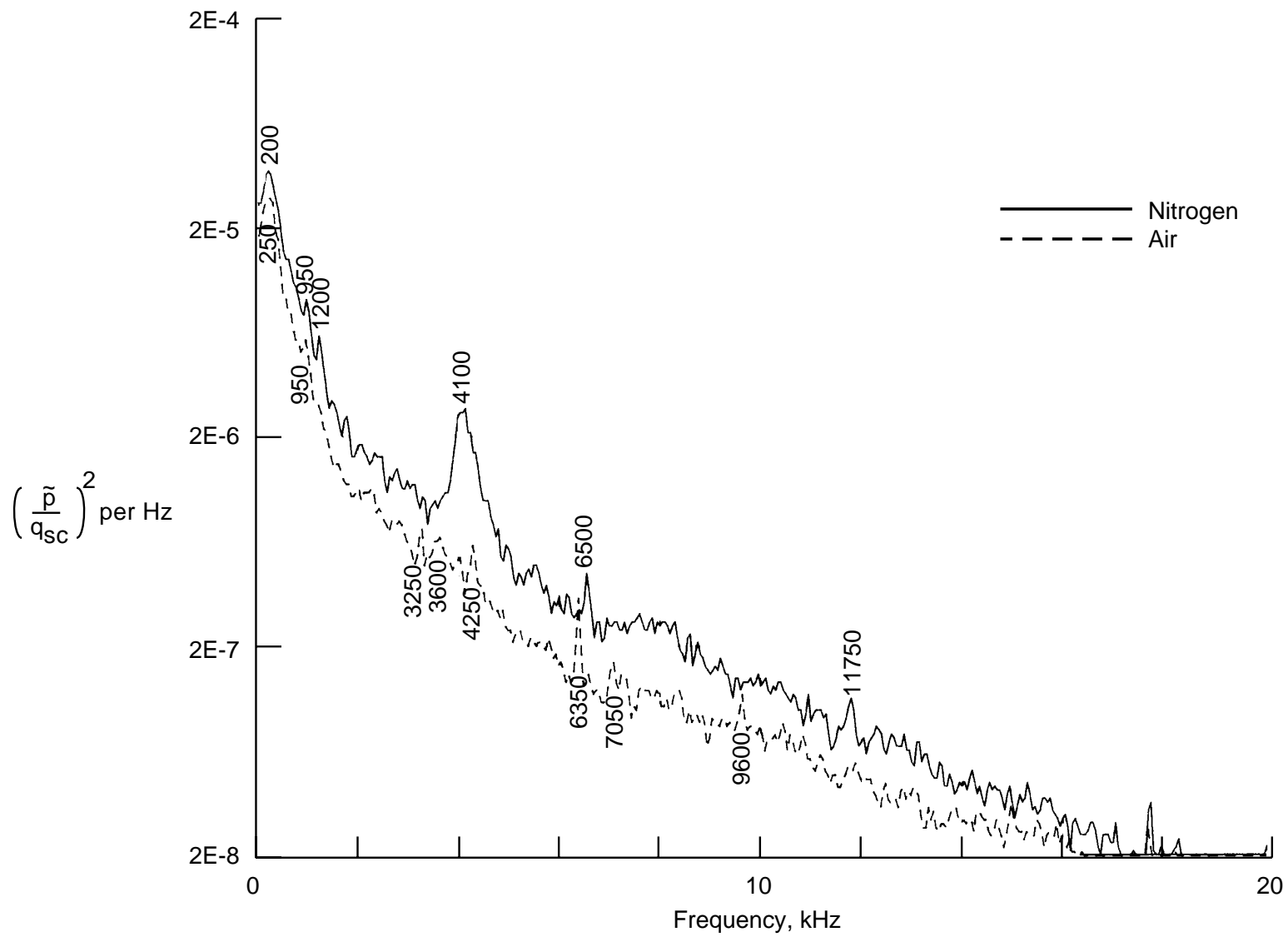
(e) $M = 0.75$.

Figure 58. Continued.
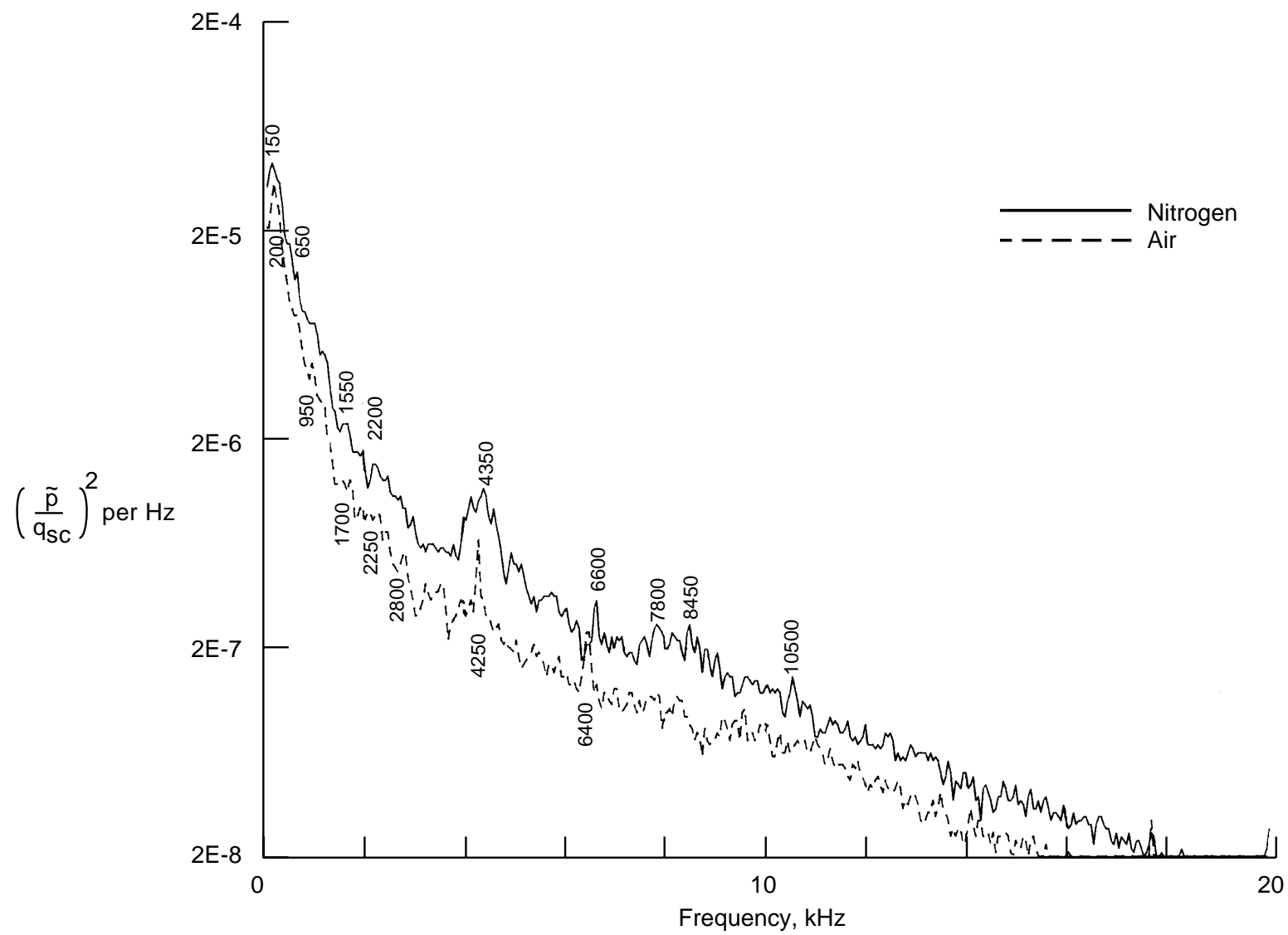
(f) $M = 0.8$.

Figure 58. Continued.
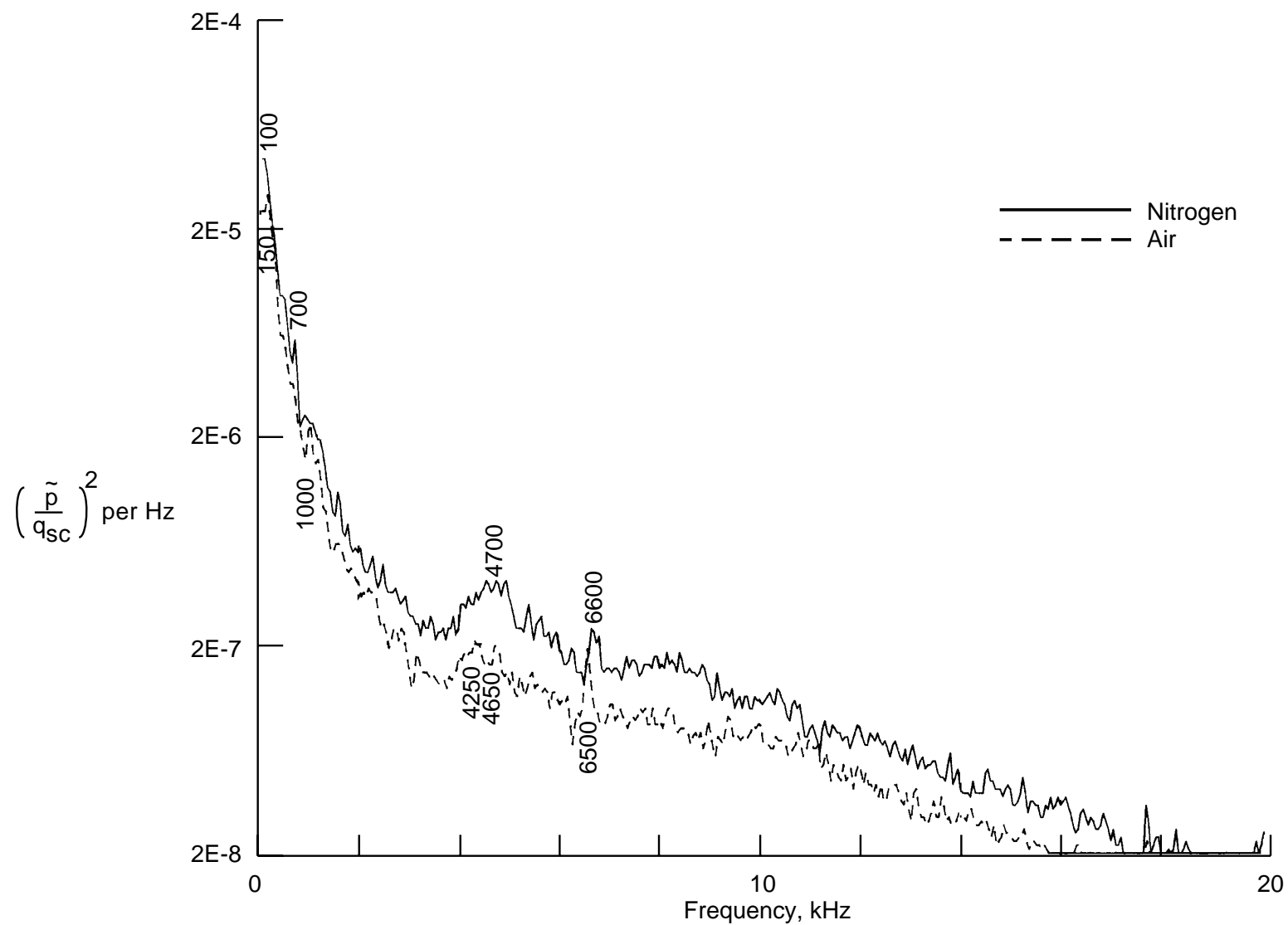
(g) $M = 0.85$.

Figure 58. Continued.
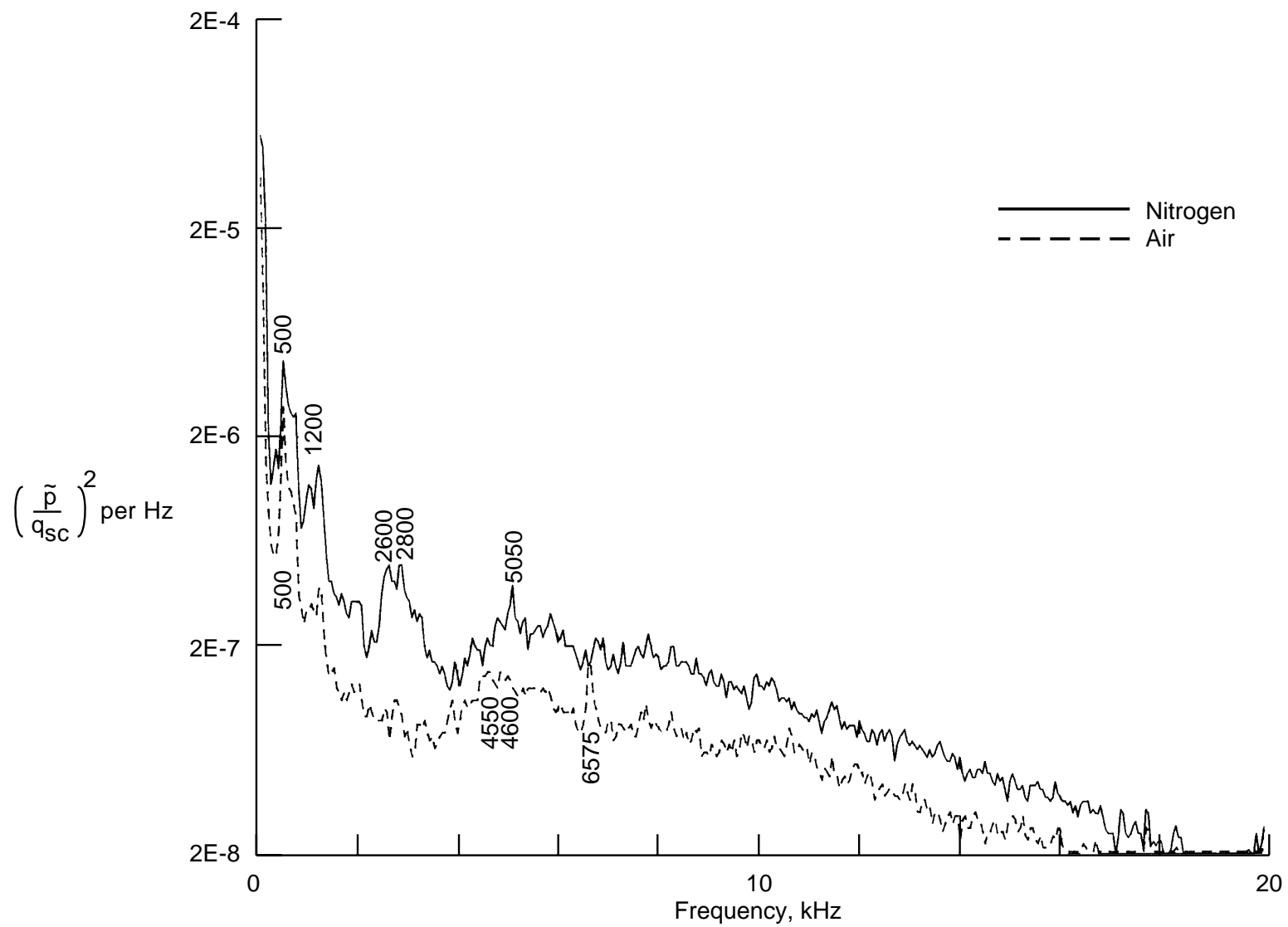
(h) $M = 1.0$.

Figure 58. Continued.
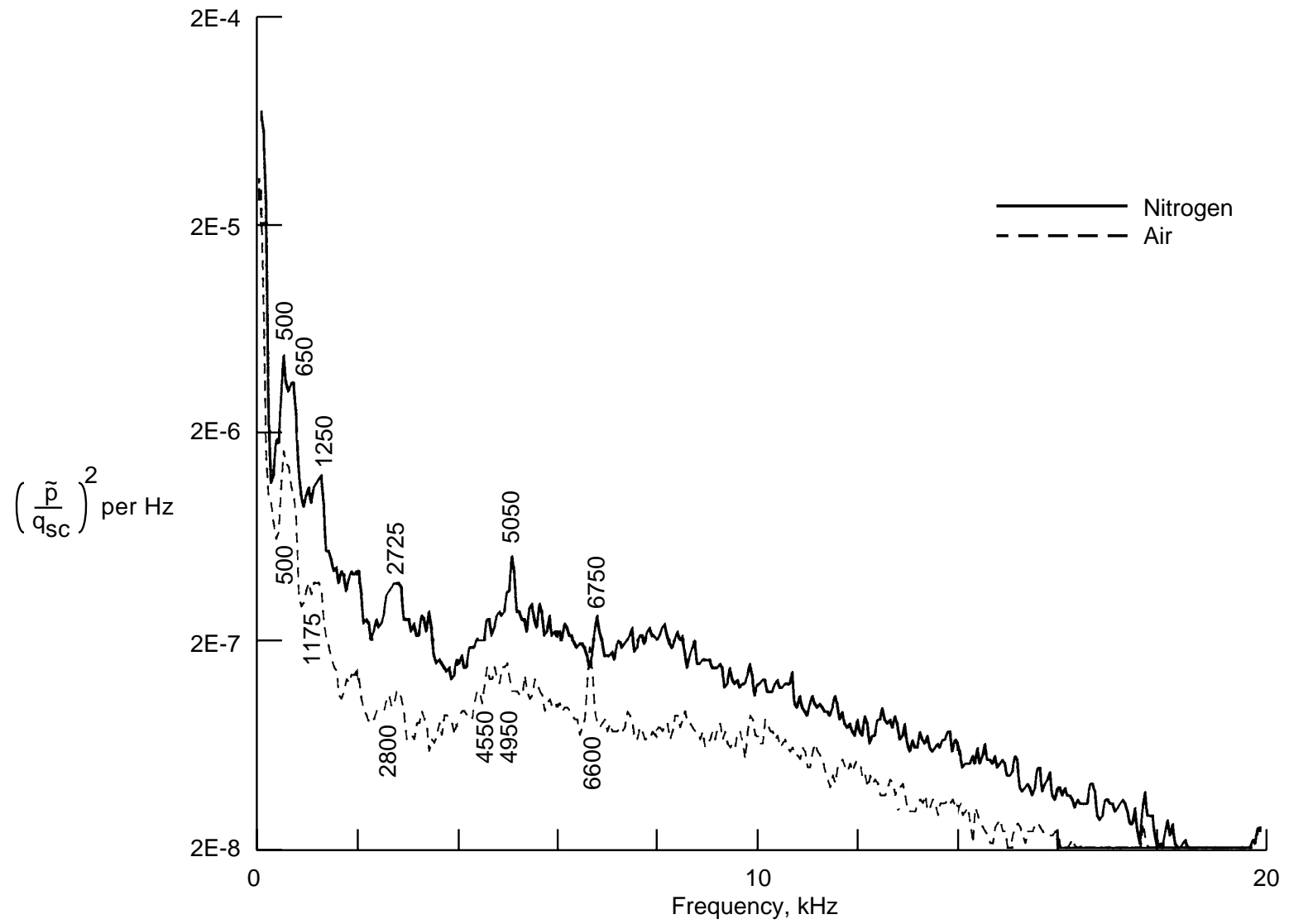
(i) *M* = 1.05.

Figure 58. Concluded.
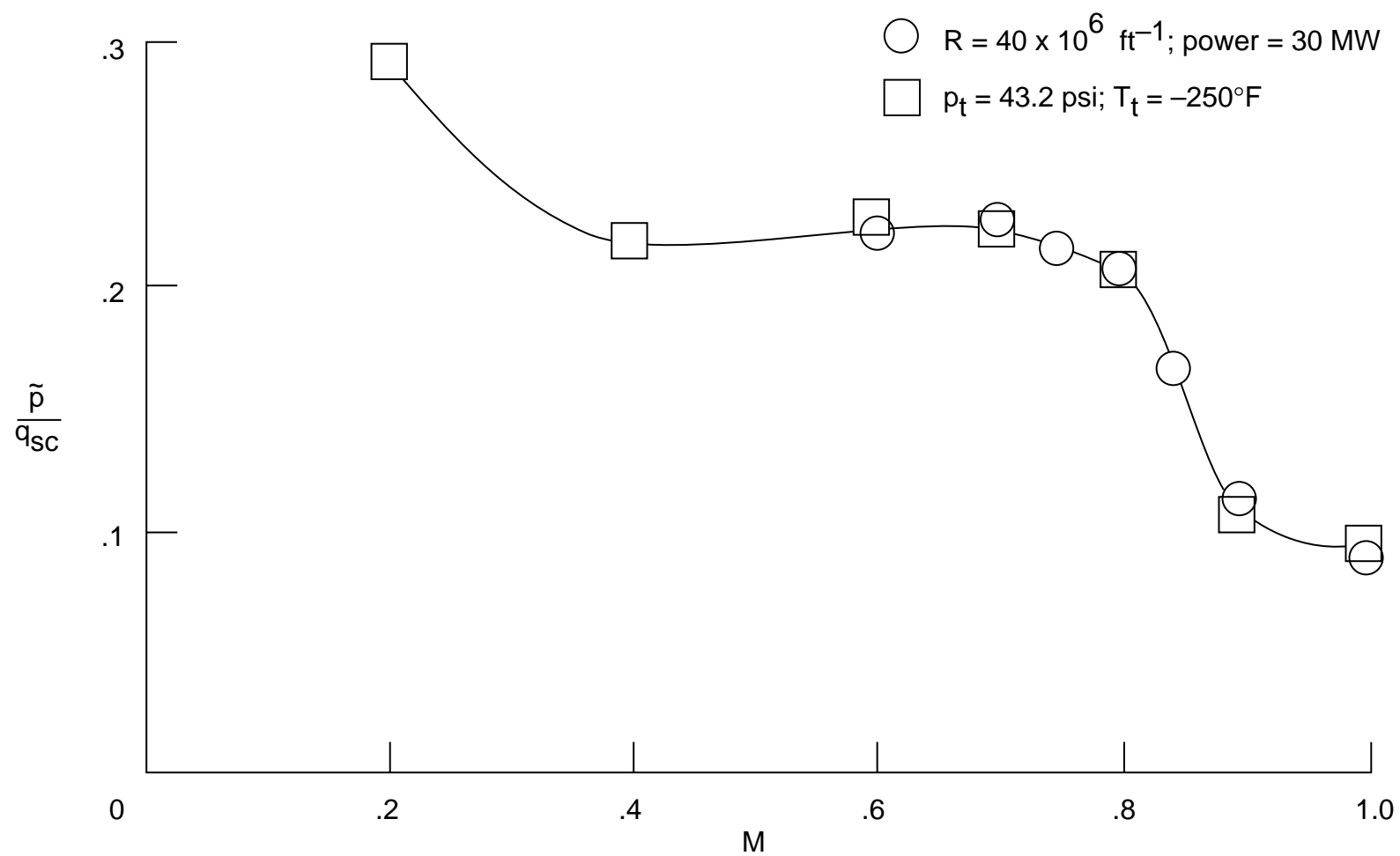
Figure 59. Fluctuating pressure coefficient in settling chamber as function of test section Mach number in nitrogen mode.
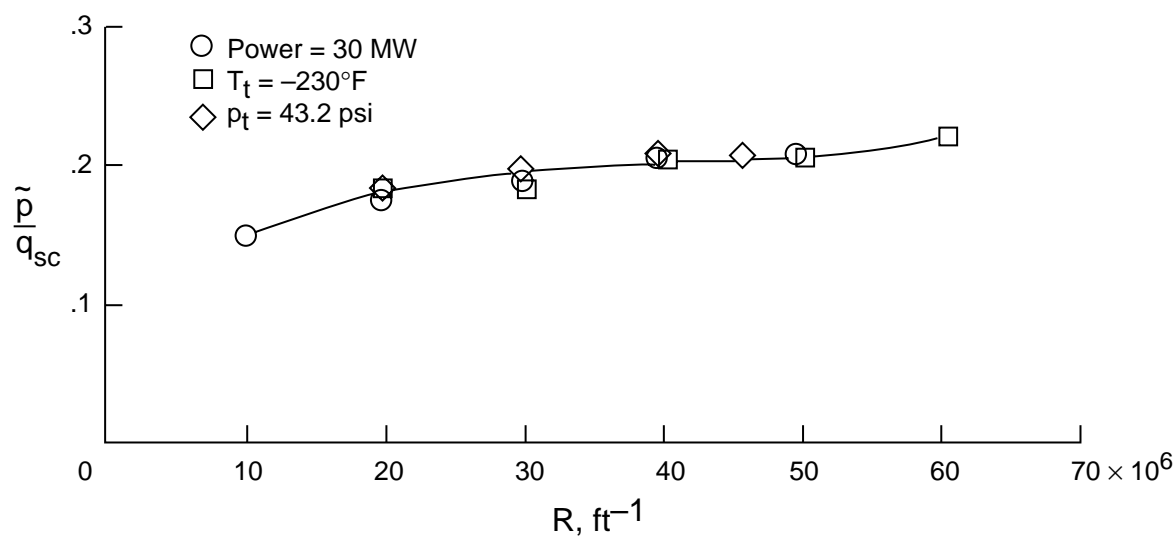
Figure 60. Fluctuating pressure coefficient in settling chamber as function of test section Reynolds number at $M = 0.8$.
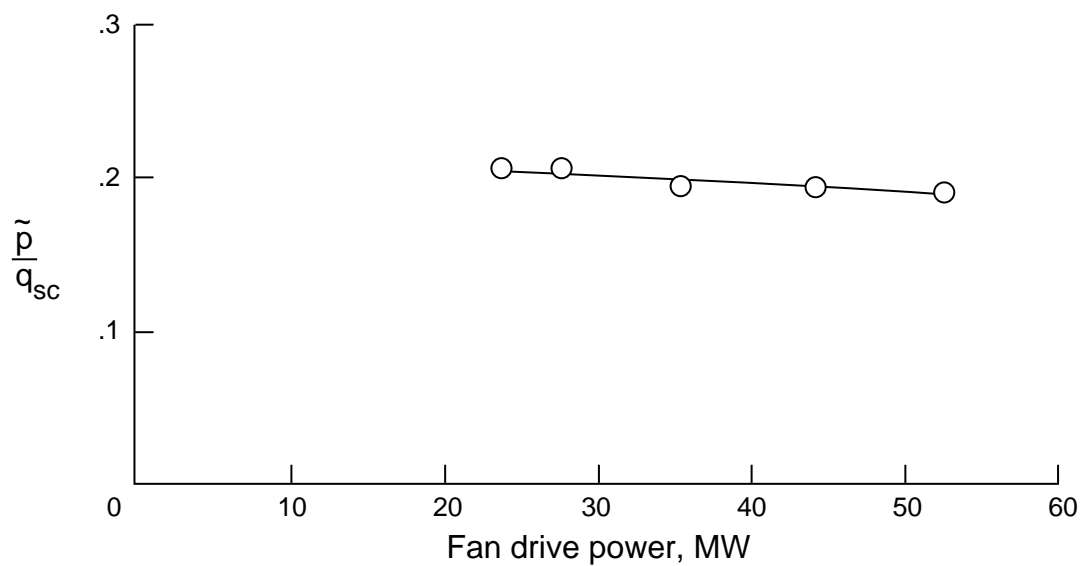
Figure 61. Effect of fan drive power on fluctuating pressure coefficient in settling chamber. $M = 0.8$; $R = 40 \times 10^6$ ft^{-1}.
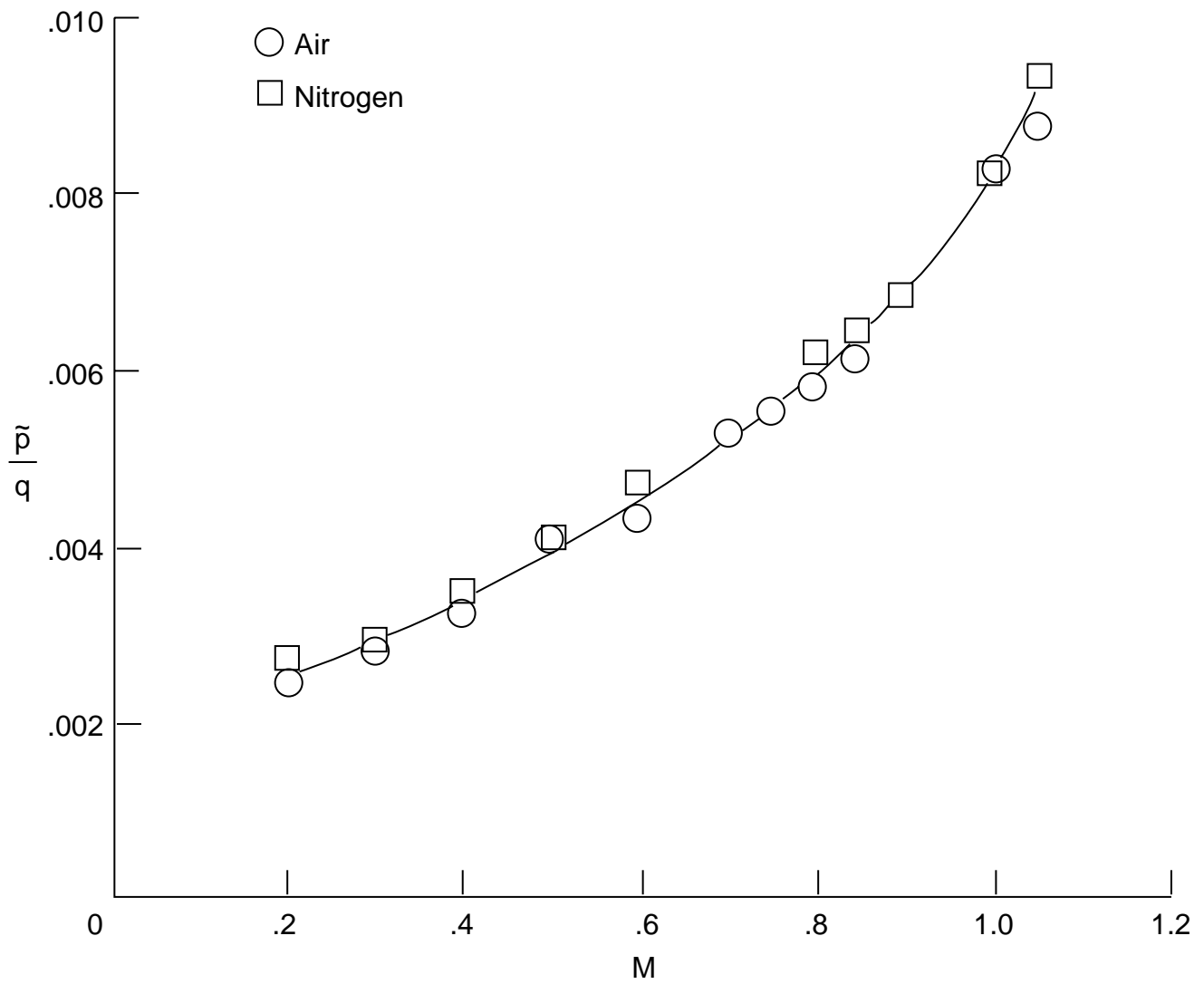
Figure 62. Fluctuating pressure coefficient in high-speed diffuser as function of test section Mach number. $R = 6 \times 10^6$ ft^{-1}; air and nitrogen modes; and ambient temperature.
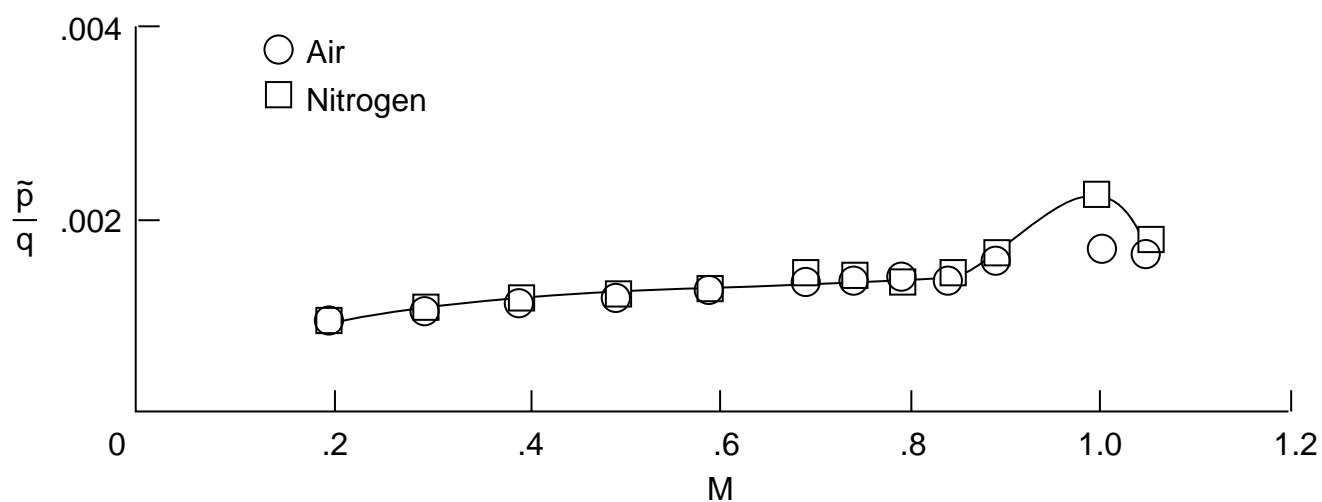
(a) $R = 6 \times 10^6$ ft^{-1}.
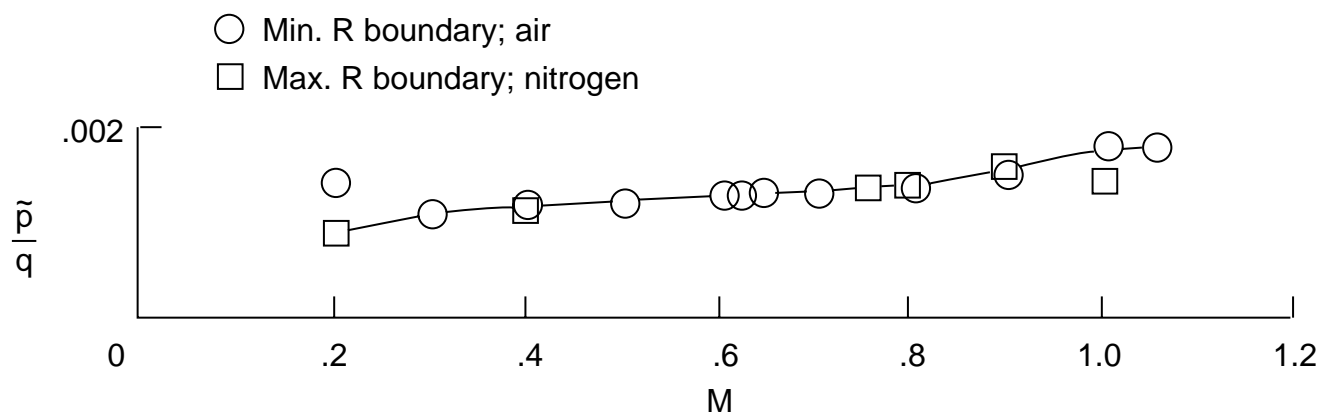
(b) Minimum and maximum Reynolds number boundary.

Figure 63. Fluctuating pressure coefficient in plenum.
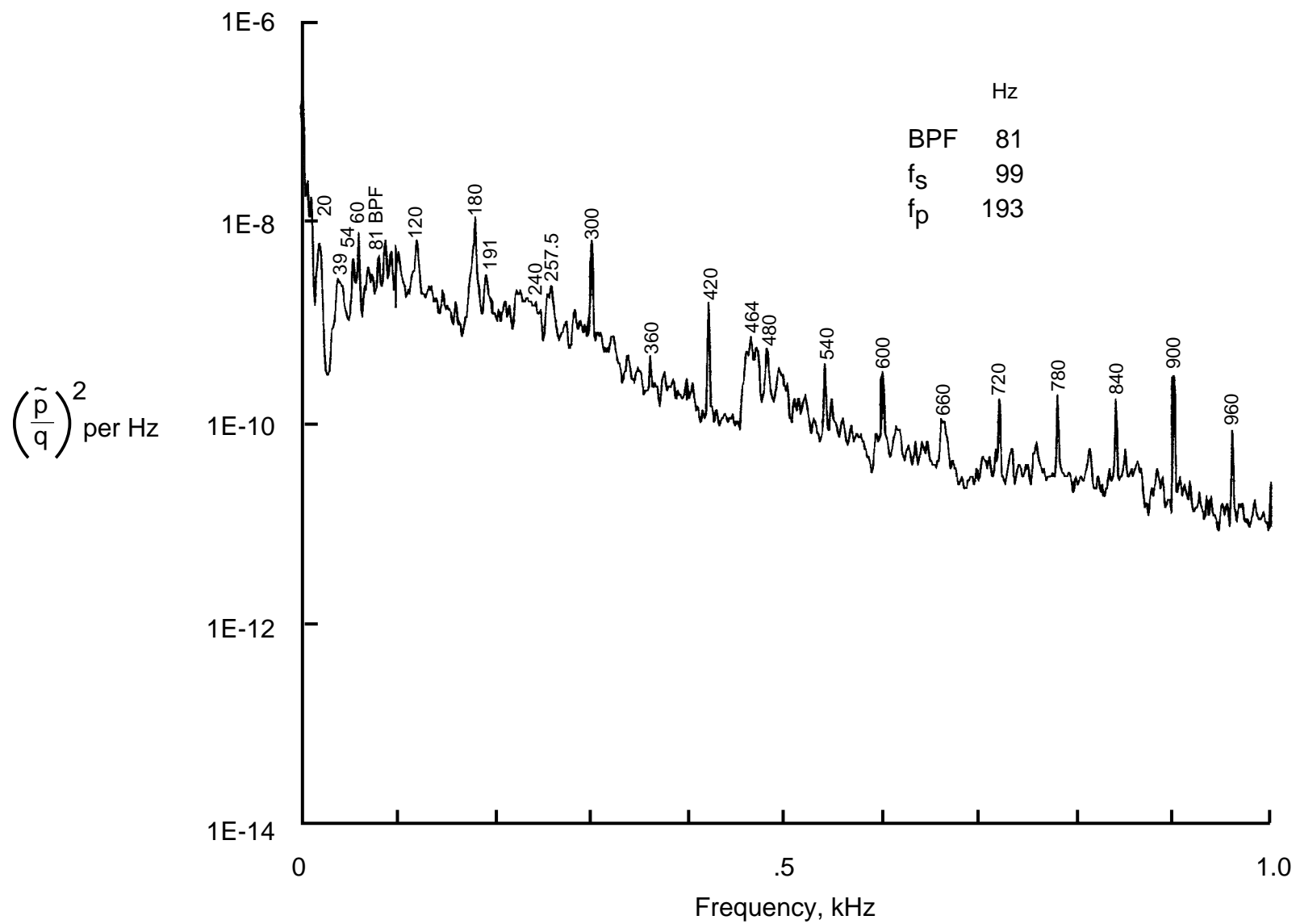
(a) $M = 0.2$.

Figure 64. Power spectra of fluctuating pressure coefficient in plenum. Minimum Reynolds number boundary; air mode.
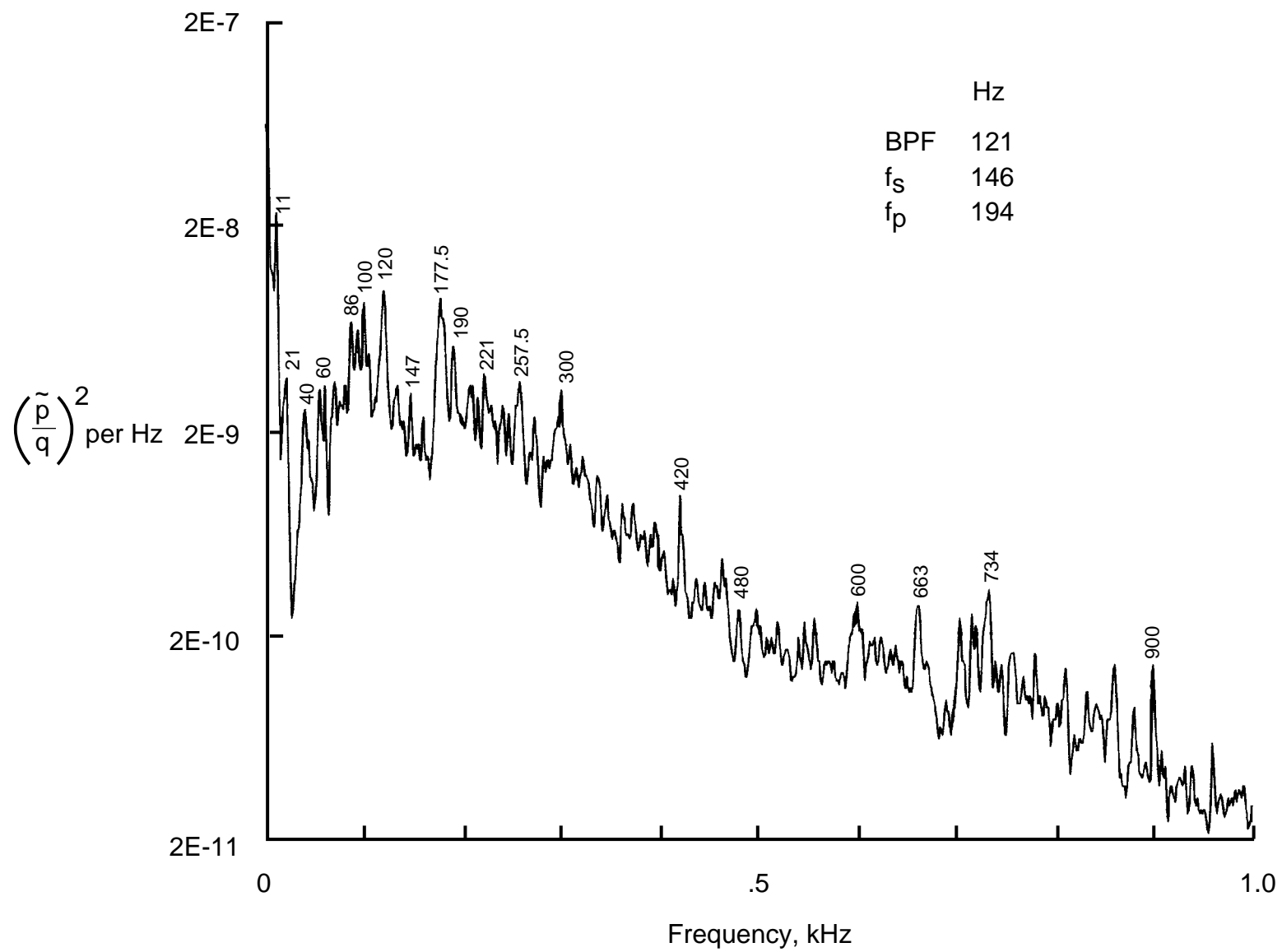
(b) $M = 0.3$.

Figure 64. Continued.
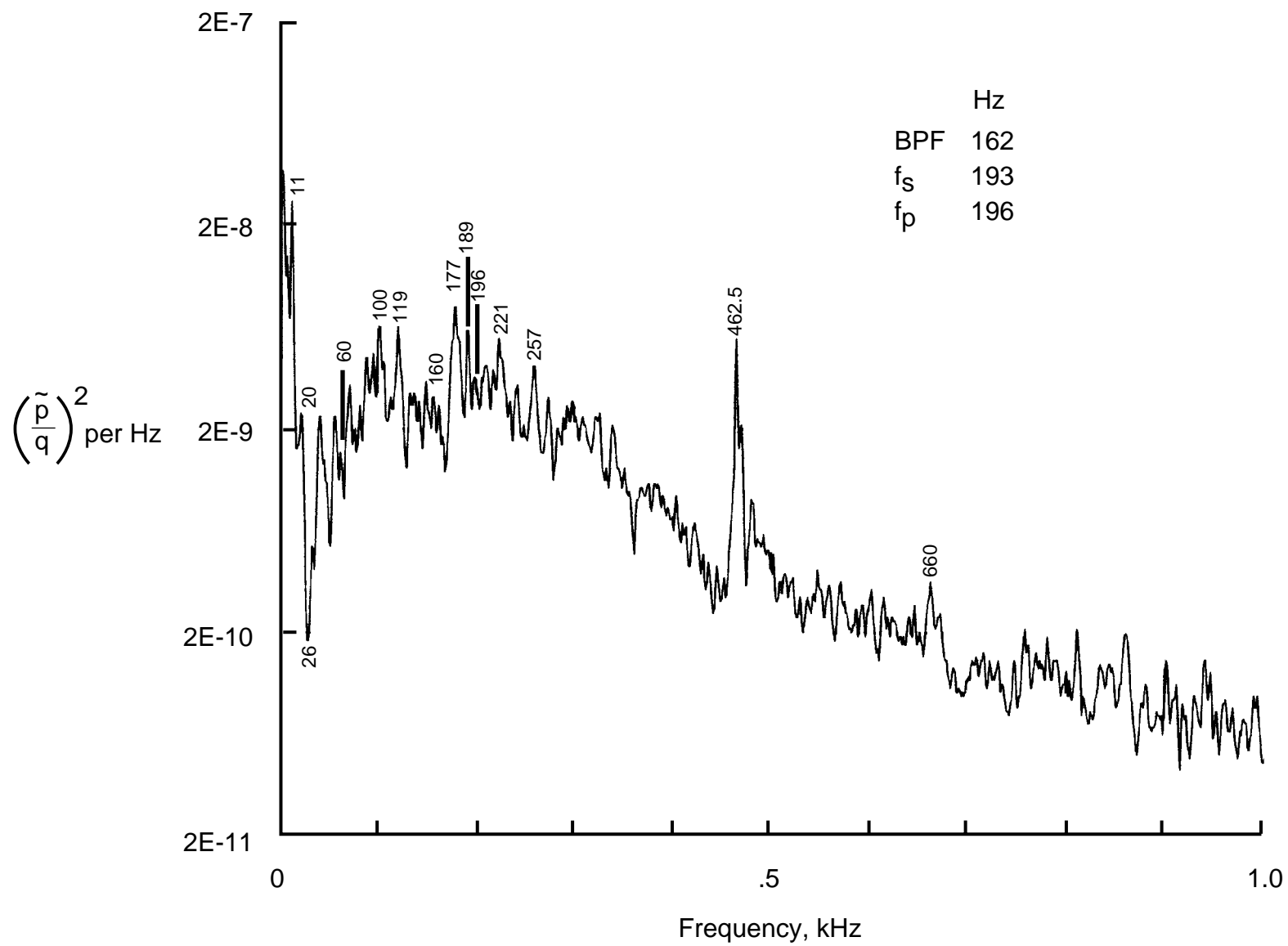
(c) $M = 0.4$.

Figure 64. Continued.
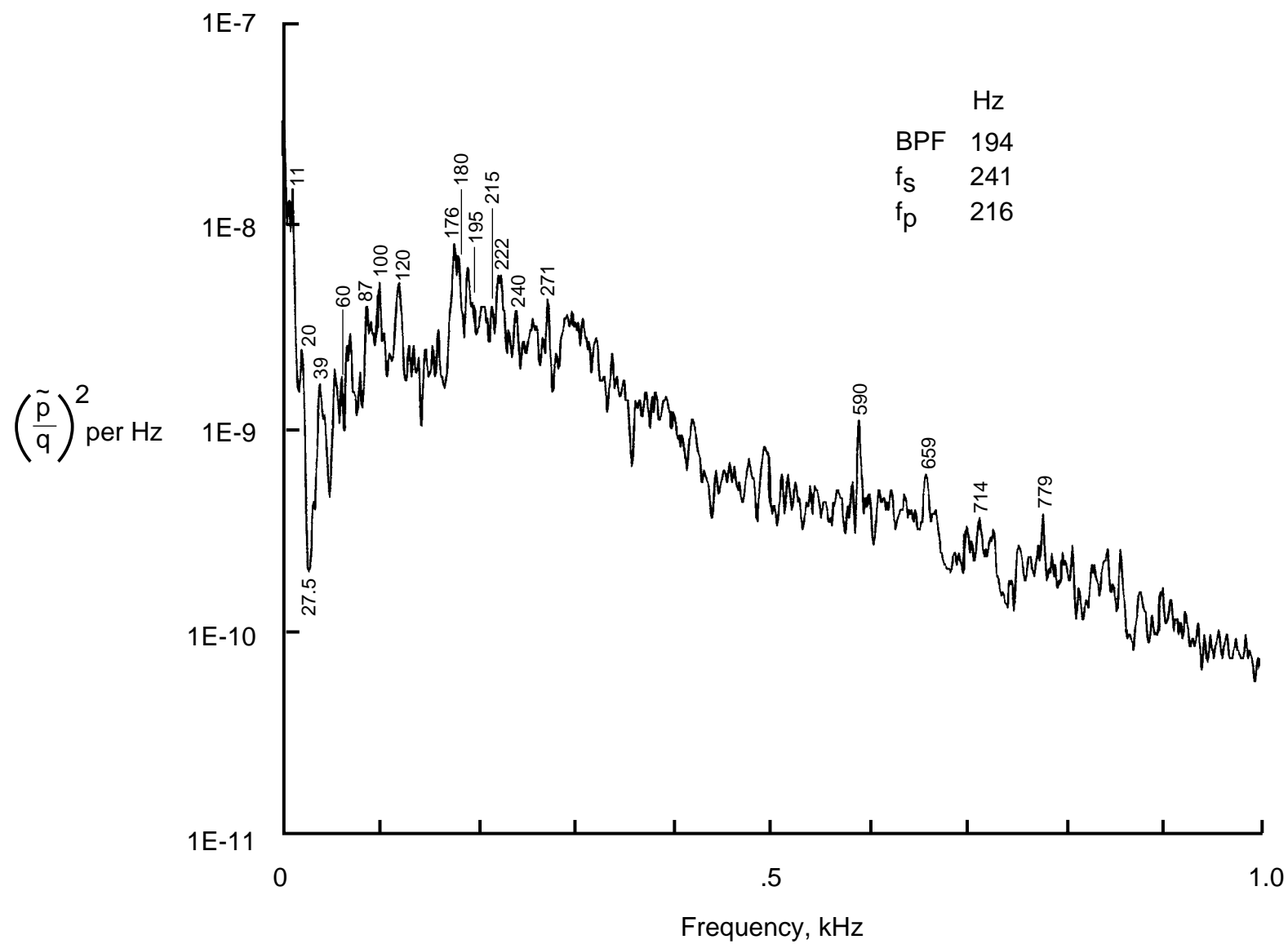
(d) $M = 0.5$.

Figure 64. Continued.
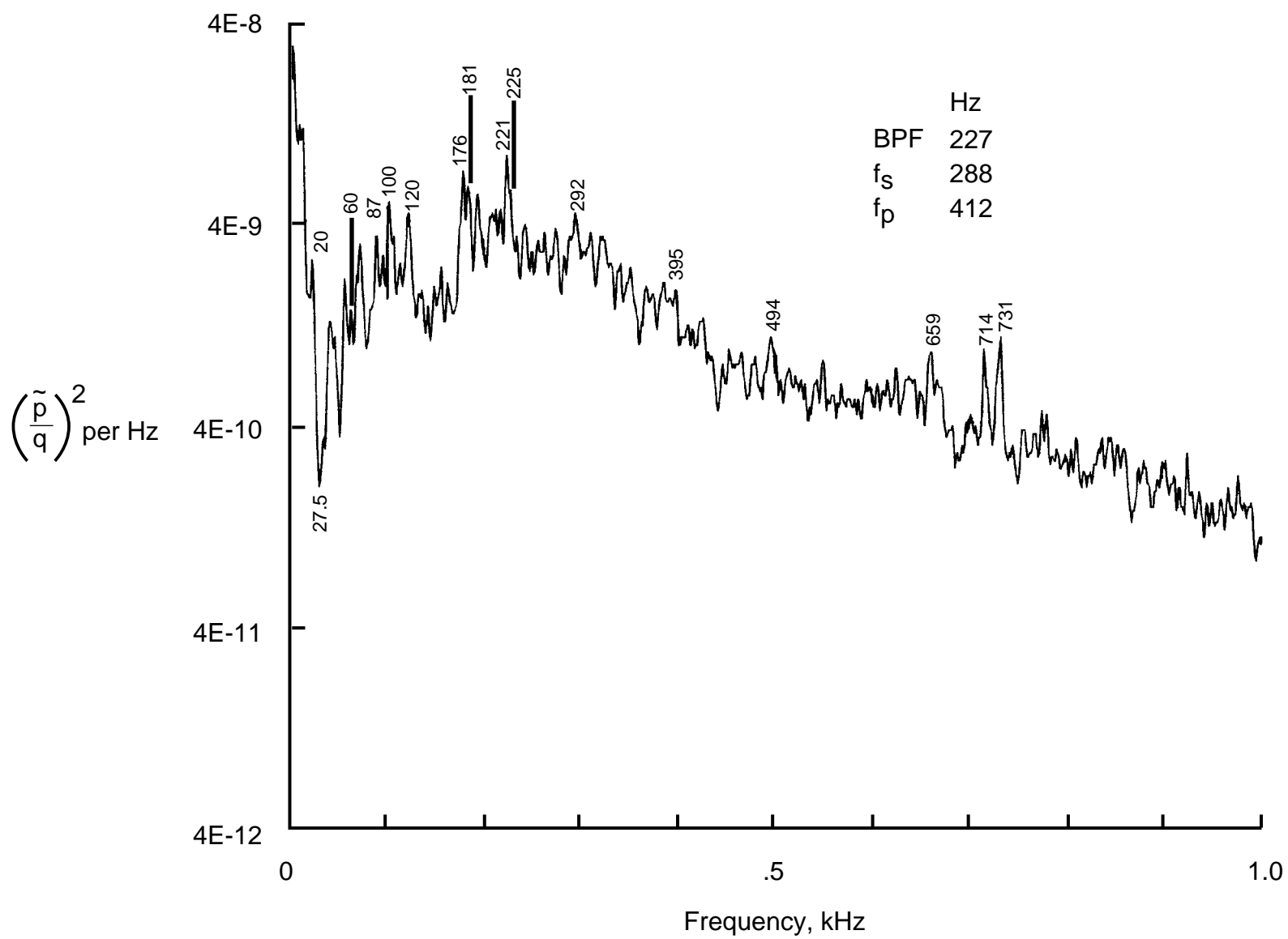
(e) $M = 0.6$.

Figure 64. Continued.
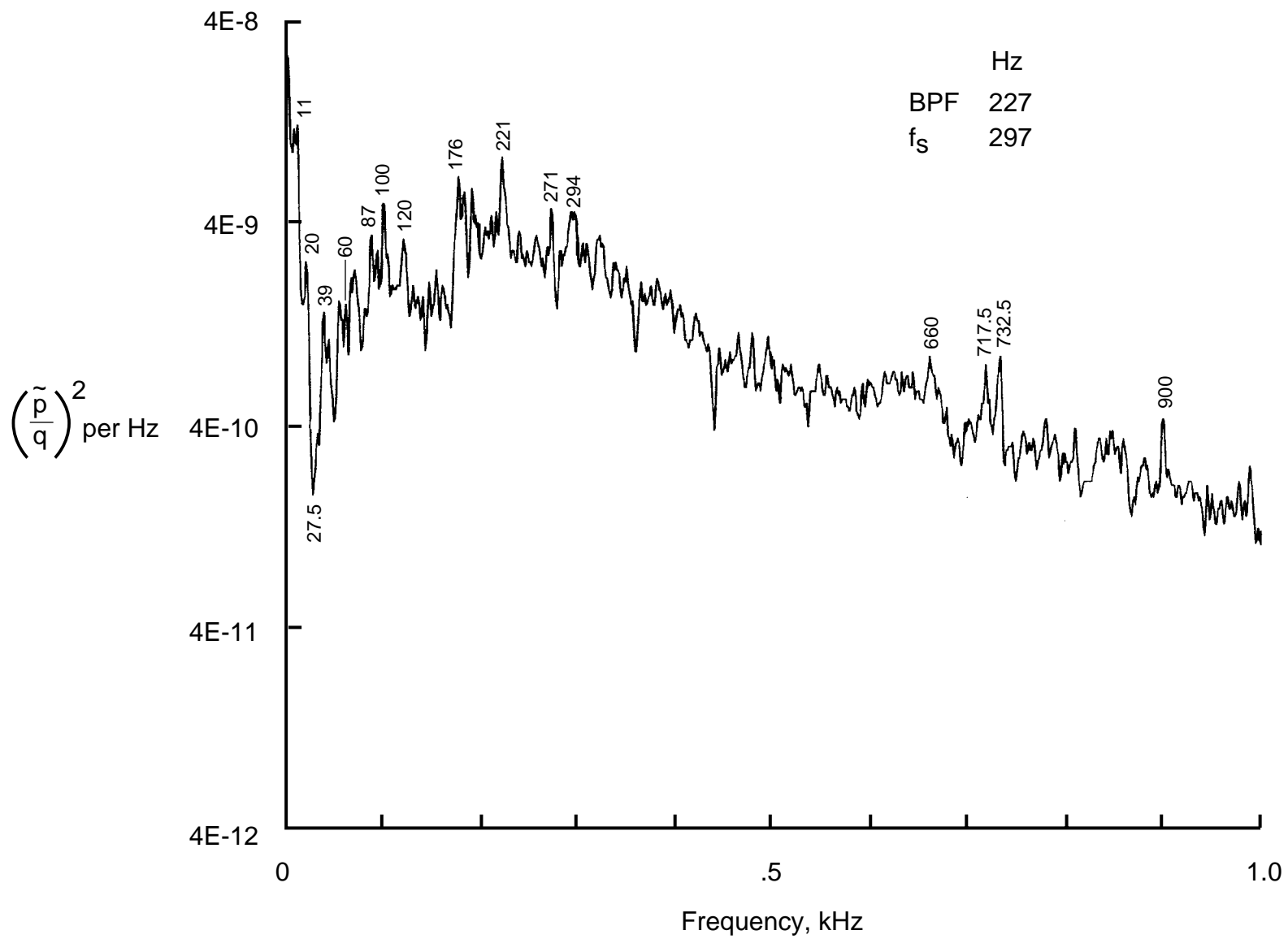
(f) $M = 0.618$.

Figure 64. Continued.
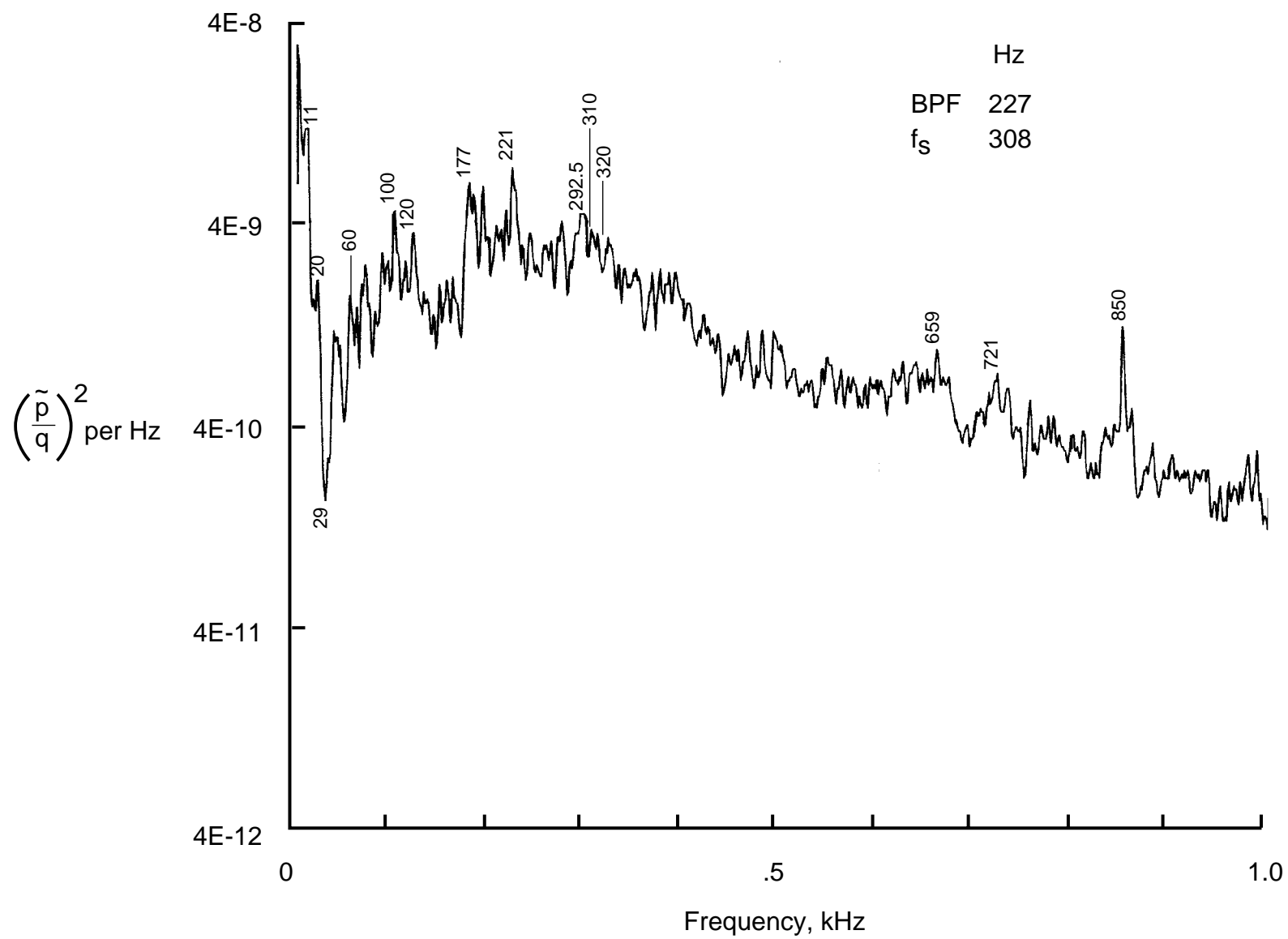
(g) $M = 0.642$.

Figure 64. Concluded.
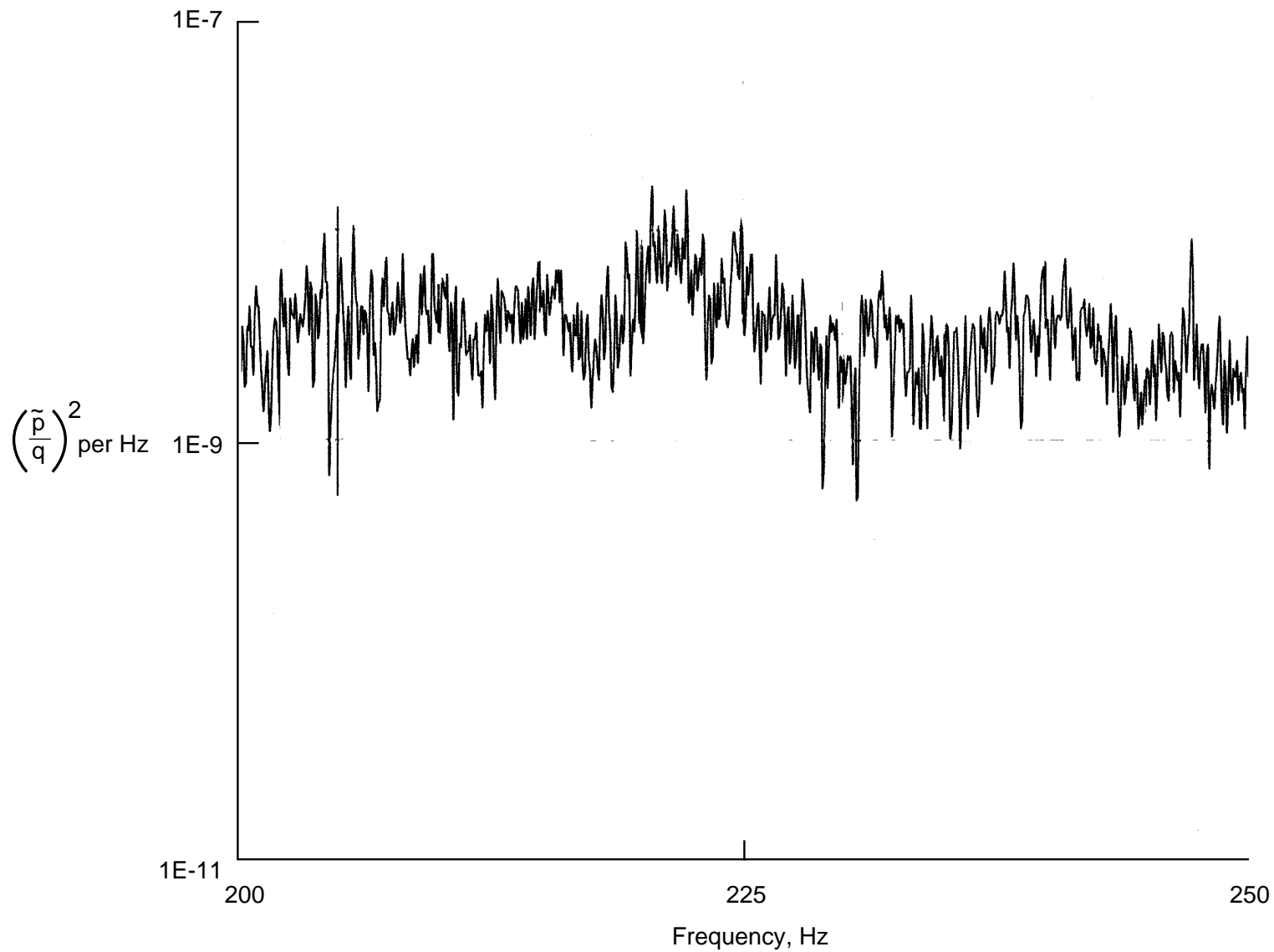
Figure 65. High frequency resolution power spectrum of fluctuating pressure coefficient in plenum. $M = 0.6$; minimum Reynolds number boundary; air mode; and BPF = 227 Hz.
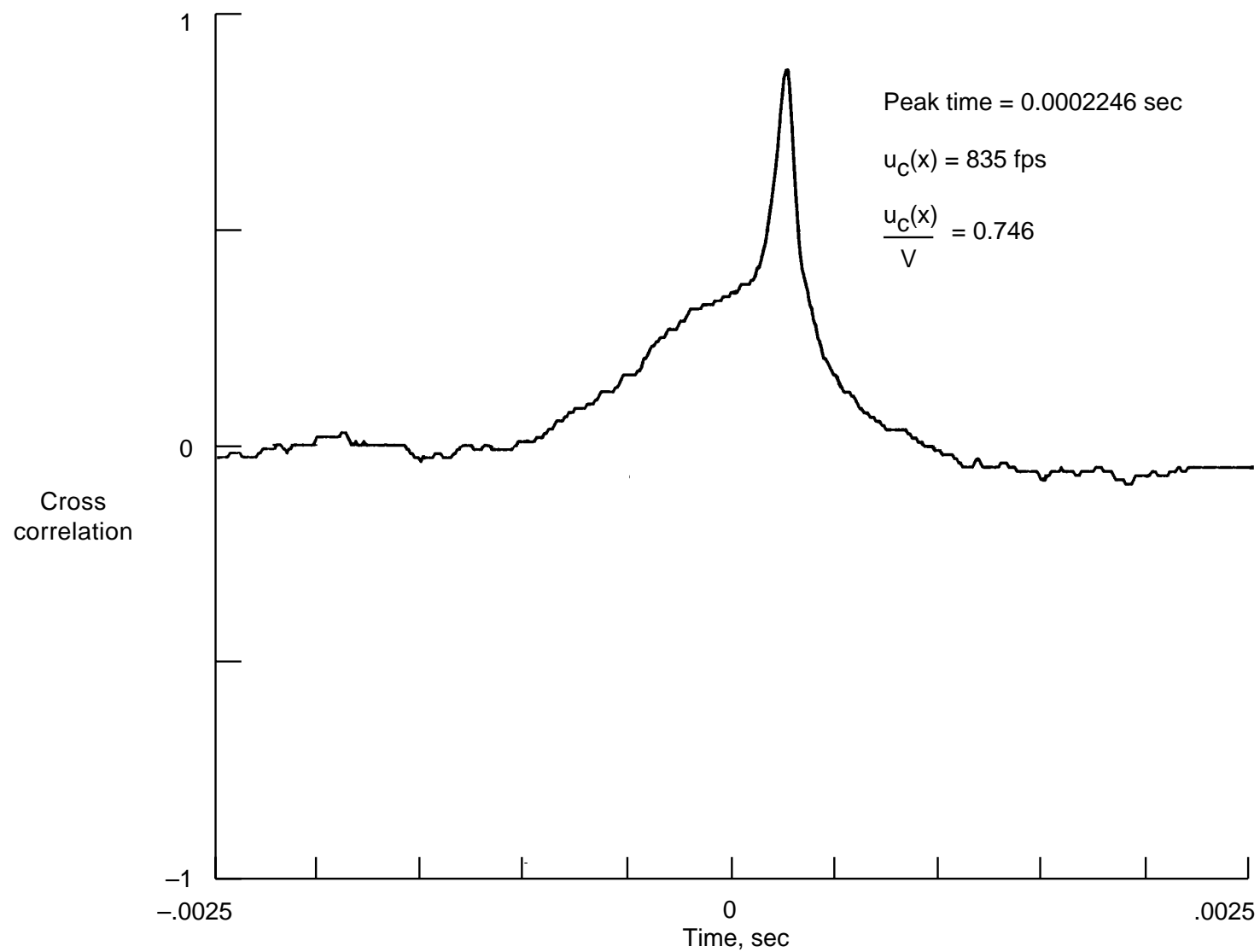
Figure 66.   Cross correlation of adjacent pressure transducer signals at test section RHS sidewall station 13. $M = 0.998$; $R = 6.1 \times 10^6$ ft^{-1}; nitrogen mode; ambient temperature; and transducer separation distance 2.25 in.
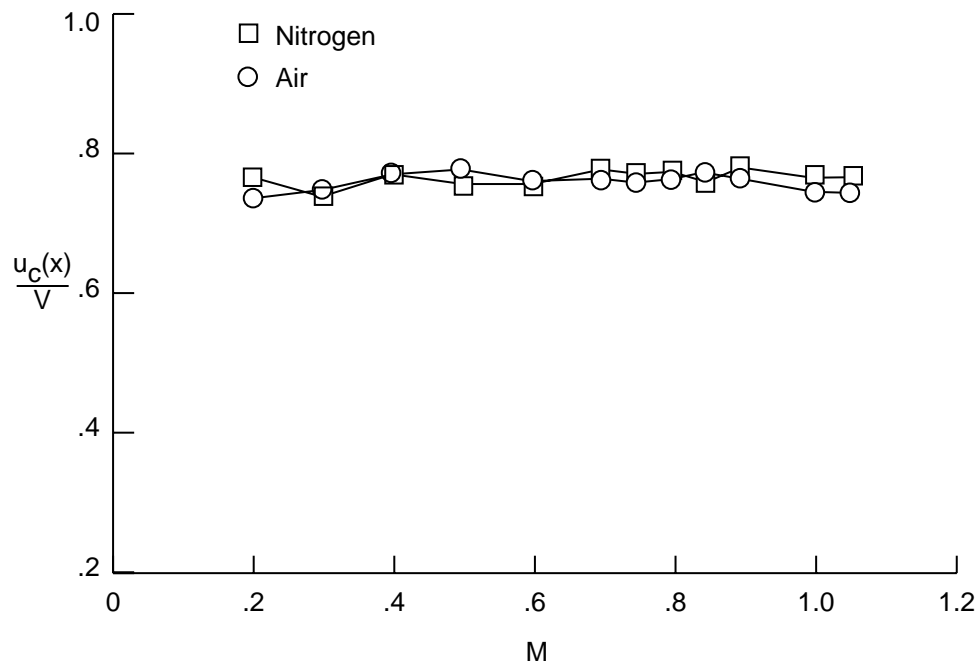
Figure 67. Convection velocity ratio at test section RHS sidewall station 13. $R = 6 \times 10^6$ ft^{-1}; ambient temperature; air and nitrogen modes.
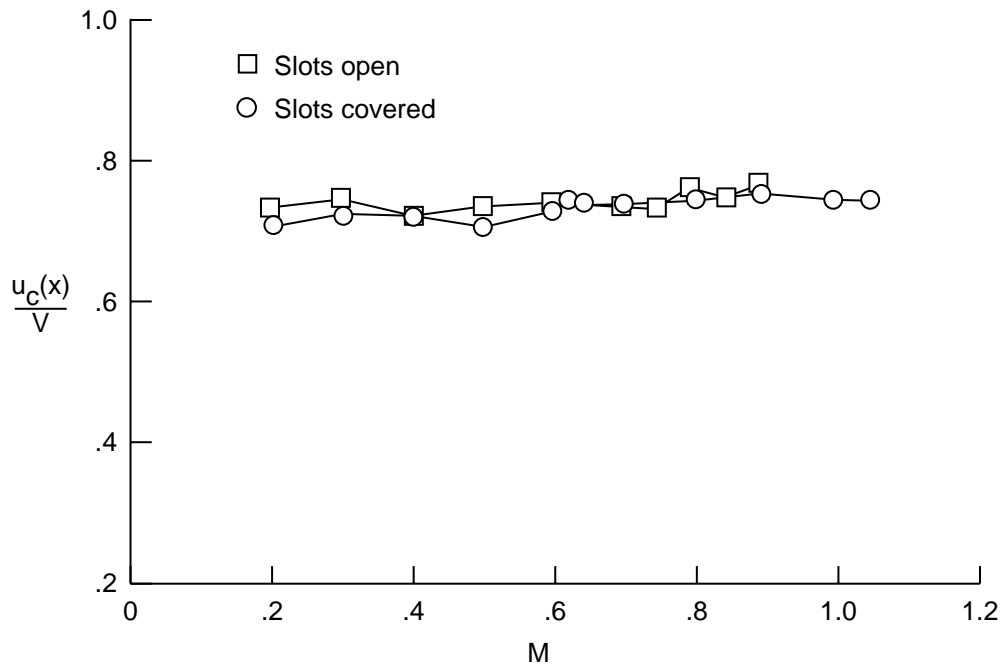

Figure 68. Convection velocity ratio at test section RHS sidewall station 13. Minimum Reynolds number boundary; air mode; ambient temperature; and slots open and covered.
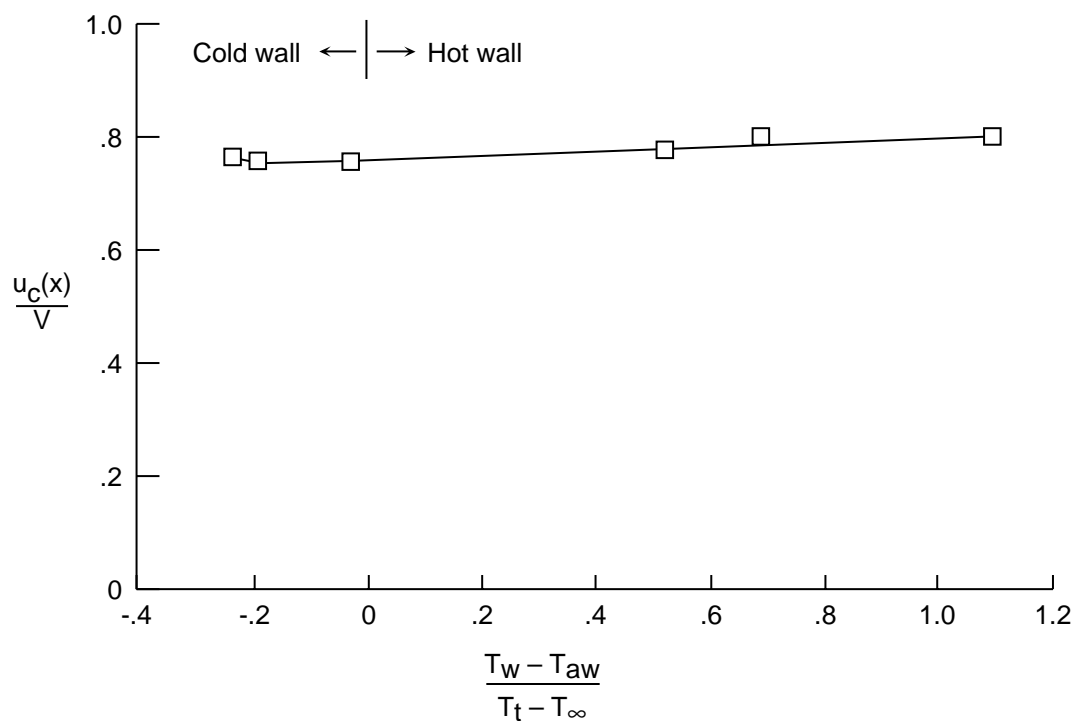
Figure 69. Effect of hot and cold walls on convection velocity ratio at test section sidewall station 13. $M = 0.8$; nitrogen mode.
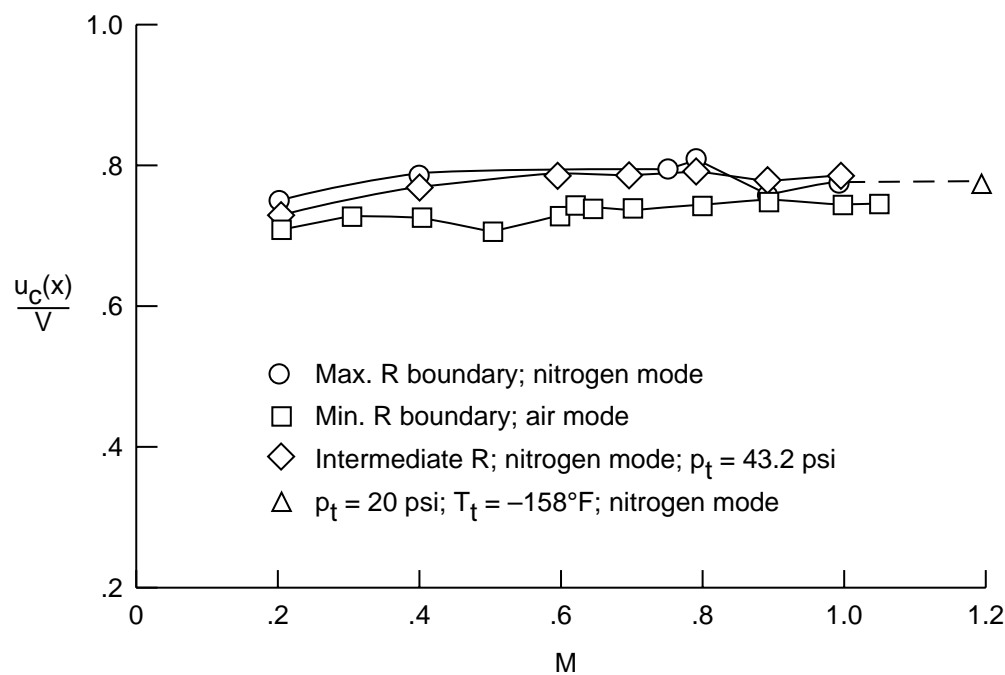

Figure 70. Effect of Reynolds number on convection velocity ratio at test section sidewall station 13.

REPORT DOCUMENTATION PAGE

Form Approved
OMB No. 0704-0188

1. AGENCY USE ONLY *(Leave blank)*	2. REPORT DATE March 1996	3. REPORT TYPE AND DATES COVERED Technical Paper	

4. TITLE AND SUBTITLE
Analysis of Fluctuating Static Pressure Measurements in the National Transonic Facility

5. FUNDING NUMBERS
WU 505-59-54-01

6. AUTHOR(S)
William B. Igoe

7. PERFORMING ORGANIZATION NAME(S) AND ADDRESS(ES)

NASA Langley Research Center
Hampton, VA 23681-0001

8. PERFORMING ORGANIZATION REPORT NUMBER
L-17371

9. SPONSORING/MONITORING AGENCY NAME(S) AND ADDRESS(ES)

National Aeronautics and Space Administration
Washington, DC 20546-0001

10. SPONSORING/MONITORING AGENCY REPORT NUMBER
NASA TP-3475

11. SUPPLEMENTARY NOTES

12a. DISTRIBUTION/AVAILABILITY STATEMENT

Unclassified–Unlimited
Subject Category 09
Availability: NASA CASI (301) 621-0390

12b. DISTRIBUTION CODE

13. ABSTRACT *(Maximum 200 words)*
Dynamic measurements of fluctuating static pressure levels were taken with flush-mounted, high-frequency response pressure transducers at 11 locations in the circuit of the National Transonic Facility (NTF) across the complete operating range of this wind tunnel. Measurements were taken at test-section Mach numbers from 0.1 to 1.2, at pressures from 1 to 8.6 atm, and at temperatures from ambient to $-250°F$, which resulted in dynamic flow disturbance measurements at the highest Reynolds numbers available in a transonic ground test facility. Tests were also made by independent variation of the Mach number, the Reynolds number, or the fan drive power while the other two parameters were held constant, which for the first time resulted in a distinct separation of the effects of these three important parameters.

14. SUBJECT TERMS
Transonic; Dynamic flow quality; Cryogenic; Pressure fluctuations; High Reynolds number

15. NUMBER OF PAGES
187

16. PRICE CODE
A09

17. SECURITY CLASSIFICATION OF REPORT Unclassified	18. SECURITY CLASSIFICATION OF THIS PAGE Unclassified	19. SECURITY CLASSIFICATION OF ABSTRACT Unclassified	20. LIMITATION OF ABSTRACT

NSN 7540-01-280-5500

Standard Form 298 (Rev. 2-89)
Prescribed by ANSI Std. Z39-18
298-102